# Charge density wave phenomena in trigonal transition metal dichalcogenides

Sayers, Charles

*Award date:*
2020

*Awarding institution:*
University of Bath



# Charge density wave phenomena in trigonal transition metal dichalcogenides

Sayers, Charles

*Award date:*
2020

*Awarding institution:*
University of Bath

# Charge density wave phenomena in trigonal transition metal dichalcogenides

Charles James Sayers

A thesis submitted for the degree of

Doctor of Philosophy

University of Bath

Department of Physics

February 2020

# Copyright and restrictions

# Declaration

### Declaration of any previous submission of the work

The material presented here for examination for the award of a higher degree by research has not been incorporated into a submission for another degree.

Charles James Sayers

Date: .....

Signed: .....

### Declaration of authorship

I am the author of this thesis, and the work described herein was carried out by myself personally, with the exception of that included in the text proceeding this declaration of authorship, in which the names and affiliations of relevant contributors are explicitly stated with reference to their specific input to the work. For published or unpublished journal manuscripts, the author's contribution is clearly outlined in a preceding author statement in each case.

Charles James Sayers

Date: .....

Signed: .....

As outlined in the *Declaration of authorship*, the work described in this thesis was carried out by the author personally, with the exception of that which is explicitly stated. The following provides, to the best of the author's knowledge, a record of the names and affiliations of contributors to this work.

Hall effect measurements of 1$T$-$VSe_2$ [Figure 4.1(b)] were performed by S. Cross and S. Friedemann (University of Bristol, UK). Resistance measurements of 1$T$-$VSe_2$ single crystals in Section 4.3.2 [Fig. 2] and Section 6.3.2 [inset Fig. 3] were performed by L. S. Farrar (University of Bath, UK). PXRD measurements in Section 4.3.2 [Fig. 5] were performed by G. Kociok-Köhn (University of Bath, UK), and investigations of the influence of annealing on the properties of 1$T$-$VSe_2$ using $\mu$XPS in the same work [Fig. 6] were performed by A. J. H. Jones with the assistance of M. Cattelan, and analysed by J. Laverock. Electronic transport measurements of the resistivity and Hall effect of 1$T$-$TiSe_2$ samples in Section 5.3.3 were performed by S. Karbassi and S. Friedemann (University of Bristol, UK). Time-resolved photoemission and reflectivity measurements in Section 5.3.2 were performed by H. Hedayat and D. Bugini, with the assistance of C. Dallera and E. Carpene (Politecnico di Milano, Italy). DFT calculations of the phonon dispersion of 1$T$-$TiSe_2$ [Fig. S4] in Section 5.3.3 were performed by D. Wolverson (University of Bath, UK). Photoemission experiments in Section 6.3.2 were performed by A. J. H. Jones and J. Laverock, with the assistance of the author and M. Cattelan (University of Bristol, UK). Analysis of the experimental data and DFT calculations of the momentum-resolved electronic susceptibility in that work were performed by J. Laverock. The sample of exfoliated 1$T$-$TaSe_2$ encapsulated with h-BN [inset Fig. S3(a)] in Section 7.3.3 was made by L. S. Hart (University of Bath, UK).

Charles James Sayers

Date: .....

Signed: .....

*To all those who have shared the journey.*

# Acknowledgements

First and foremost, I would like to thank my friends and family for their continued support. Great achievements are only possible with great people around you. I had a plan for myself, and I am very fortunate to have the support of others along the way; my parents Ann and Adrian, my brother Harry, and my friends that have stayed close to me over all these years; Jake, Jennifer, Mark, Mike, Matt, Luke and Toby. Acknowledgements are difficult and since it is impossible to mention everyone, I simply say thank you to all the people that have inspired me, the friends I have made, and the experiences that have led me to this point.

Of course, I acknowledge help from colleagues and collaborators who have shared their knowledge and worked alongside me over the past few years. In particular, I thank my PhD supervisor, Enrico Da Como for his guidance and for delving into a field of Physics that was entirely new to both of us. In that way, we learned together and grew to appreciate the fascinating field of charge density waves. Also at the University of Bath, I thank the many academics, technicians and friends, especially; Liam Farrar, Lewis Hart, Phillip Jones, Simon Bending and Daniel Wolverson who directly contributed to some aspect of this work.

At the University of Bristol, I would like to thank past and present members of the correlated electron systems group, and students of the CDT-CMP. In particular, Sven Friedemann for experimental support from his group and valuable discussions throughout my PhD. I thank Mattia Cattelan for sharing his knowledge of photoemission, his unmatched enthusiasm, and for allowing me access to the NanoESCA facility. I thank Jude Laverock for many insightful discussions about photoemission, charge density wave systems, and his important input to this work.

I would like to express my gratitude to all members of the UPhoS group at Politecnico di Milano; Hamoon Hedayat, Davide Bugini, Ariana Ceraso, Claudio Dallera, Giulio Cerullo and Ettore Carpene. During my visits, they were always accommodating and I

thank them for welcoming me into their research group. I learnt a lot from our close collaboration over the years and I appreciate their continued determination to see our work come to fruition. It would be fair to say that without them, much of the experimental work in this thesis would have not been possible, and for that I am most grateful.

Finally, I shall say that one of the best things about undertaking a PhD is the amazing people you meet along the way and the journeys you share together. I will always remember trips for conferences and experiments at home and further afield, my time in Milano, shifts at the synchrotron, and staying in Pepi hotel. In particular, I have fond memories of the adventures in the U.S. for March Meeting; from sunny New Orleans to snowstorms in Boston, -20°C temperatures, flat tyres, and running into the "cops" on our way to Canada.

## Abbreviations & Common symbols

| | |
|---|---|
| **CDW** | Charge density wave |
| **TMD** | Transition metal dichalcogenide |
| **PLD** | Periodic lattice distortion |
| **MIT** | Metal-insulator transition |
| **CVT** | Chemical vapour transport |
| **ARPES** | Angle-resolved photoemission spectroscopy |
| **TR-ARPES** | Time- and angle-resolved photoemission spectroscopy |
| **TRR** | Time-resolved reflectivity |
| **XPS** | X-ray photoemission spectroscopy |
| **XAS** | X-ray absorption spectroscopy |
| **LEED** | Low energy electron diffraction |
| **PXRD** | Powder x-ray diffraction |
| **UHV** | Ultra-high vacuum |
| **BZ** | Brillouin zone |
| **FS** | Fermi surface |
| **EDC** | Energy distribution curve |
| **MDC** | Momentum distribution curve |
| **STM** | Scanning tunnelling microscopy |
| **DFT** | Density functional theory |
| **RRR** | Residual resistance/resistivity ratio |
| **VB** | Valence band |
| **CB** | Conduction band |

| | |
|---|---|
| $\Delta$ | Electronic gap |
| $T_{\mathrm{CDW}}$ | Charge density wave transition temperature |
| $\mathbf{q}_{\mathrm{CDW}}$ | Charge density wave q-vector |
| $\chi^0(\mathbf{q},\omega)$ | Non-interacting electronic susceptibility |
| $E_{\mathrm{F}}$ | Fermi level |
| $\mathbf{k}_{\|\|}$ | Parallel wavevector |
| $h\nu$ | Photon energy |
| $\overline{\Gamma}$, $\overline{\mathrm{M}}$, $\overline{\mathrm{K}}$ | Projected high-symmetry points of the hexagonal BZ |
| $c$ | Speed of light in vacuum ($2.998\times10^{8}$ m s$^{-1}$) |
| $e$ | Elementary charge ($1.602\times10^{-19}$ C) |
| $k_{\mathrm{B}}$ | Boltzmann constant ($1.381\times10^{-23}$ J K$^{-1}$) |
| $h$ | Planck's constant ($6.626\times10^{-34}$ J s). * $\hbar = h/2\pi$ |
| eV | Electronvolt (1 eV = $1.602\times10^{-19}$ J) |
| Å | Angstrom (1 Å = $10^{-10}$ m) |
| fs | Femtosecond (1 fs = $10^{-15}$ s) |
| ps | Picosecond (1 ps = $10^{-12}$ s) |
| THz | Terahertz (1 THz = $10^{12}$ s$^{-1}$) |
| cm$^{-1}$ | Wavenumber (1 cm$^{-1}$ is equivalent to $h\nu = 0.124$ meV) |

# Abstract

The metallic transition metal dichalcogenides (TMDs) are layered, quasi two-dimensional compounds which are host to many strongly-correlated phases of matter. Most notably, they exhibit charge density waves (CDWs); an ordered state consisting of electronic charge density modulation accompanied by a distortion of the underlying crystal lattice. Despite decades of research, there are persisting questions surrounding the origin of charge order in TMDs and numerous scenarios have been proposed.

This thesis presents a study of CDW phenomena in the isostructural, selenium-based TMDs with trigonal ($1\,T$) symmetry; $1\,T$-$TiSe_2$, $1\,T$-$VSe_2$ and $1\,T$-$TaSe_2$. The characteristics of the CDW phase in each compound varies considerably, including; the transition temperature, distorted lattice periodicity, and commensurability. CDW phenomena are often dictated by the electronic band structure, including the shape and composition of the Fermi surface. Angle-resolved photoemission spectroscopy (ARPES) and variants thereof allows direct visualisation of the electronic structure and the signatures of CDW formation, which primarily manifest as electronic gaps, $\Delta$ near the Fermi level. In order to further the understanding of CDW phenomena in these compounds, a unique experimental approach was required in each specific case.

Firstly, a method was developed to grow high quality single crystal TMDs by chemical vapour transport which is discussed in detail with reference to $1\,T$-$VSe_2$ and the influence of growth conditions on the CDW properties. Full-wavevector ARPES measurements of the Fermi surface (FS) in $1\,T$-$VSe_2$ combined with DFT calculations of the electronic susceptibility revealed the importance of FS nesting. The possibility of separate $3q$ and $2q$ CDW states were considered based on the temperature and momentum dependence of the gap. The fluence dependence of photo-induced CDW suppression dynamics in $1\,T$-$TiSe_2$ was investigated using complimentary time- and -angle resolved photoemission spectroscopy (TR-ARPES) and time-resolved reflectivity (TRR) techniques. The experimental results were compared to simulations of the quasiparticle dynamics in order to disentangle the role of excitons and phonons. Finally, investigations of coherent phonon oscillations in the low-temperature phase of $1\,T$-$TaSe_2$ using TR-ARPES showed a modulation of the metal-insulator transition (MIT) gap corresponding to the CDW amplitude mode frequency. Instead, multiple frequencies were triggered by a similar optical pump in TRR, suggesting a selective electron-phonon coupling in the former, shedding light on the interplay between the MIT and CDW in this compound.

# Contents

# Chapter 1

# Introduction

## 1.1 Outline

### 1.1.1 Motivation

At sufficiently low temperatures, a charge density wave (CDW) state will form in certain materials in order to lower the overall energy of the system via a reconstruction of the electronic and lattice structure. The name arises due to the wave-like modulation of electronic charge density found in the new state. CDWs were first theorized to occur in a one-dimensional linear chain metal by Peierls in 1955 [1], and have since been observed in a whole range of low-dimensional solids including; the transition metal dichalcogenides (TMDs) [2], organic charge transfer compounds [3], metal oxides [4], and cuprate superconductors [5], amongst others.

Notably, the metallic TMDs are host to diverse CDW phenomena [2] and exhibit a range of second- and first-order transitions with various critical temperatures, distorted lattice periodicity, and commensurability. In addition, many TMDs are also host to other forms of strongly-correlated behaviour such as metal-insulator transitions (MIT) [6] and superconductivity [7]. As a result of the incredibly rich physics found in this class of materials, they are an excellent platform with which to study potential competition or co-operation between various phases of matter. In particular, since CDWs are found in close proximity to superconductivity in many materials including the cuprates [8, 9] and TMDs [10,11], it has been suggested that these states of matter may be extremely relevant to one another. An ongoing goal of fundamental research is to understand the importance of CDWs in these systems [12, 13], and the possible manipulation of these states [14, 15],

which may prove crucial in achieving high-temperature superconductivity.

Following investigations of TMDs in the 1960s [16], their crystal structure offered the possibility to obtain a single-layer material which could potentially posses dramatically different properties to its bulk counterpart. Although early attempts were made [17], it wasn't until after the discovery of Graphene in 2004 [18], that the surge in research of 2D materials has allowed isolation of single-layer TMDs. The effect of reduced dimensionality has thus far been demonstrated to significantly alter the electronic structure of semiconducting TMDs [19], whereas the impact on strongly-correlated behaviour in the metallic TMDs is comparatively less explored and there are often conflicting reports.

Clearly, if we are to answer these scientific questions, it is crucial to first have a thorough understanding of CDW phenomena and their physical origin in bulk TMDs. However, despite decades of research, questions remain about the formation of CDWs in these materials and numerous scenarios have been proposed [20]. Based on symmetry arguments, and owing to their quasi two-dimensional nature, CDWs in many TMDs have historically been discussed in terms of electronic instabilities such as Fermi surface nesting (FS) [2]. In this scenario, CDW formation is driven by a weak analogue of the Peierls transition [1], and many find it difficult to justify such a situation in any system greater than strictly one dimension [21–23]. Other scenarios suggest interactions with the lattice as the dominant mechanism such as a Jahn-Teller distortion [24] or other forms electron-phonon coupling [25,26]. More unusual mechanisms rely on electron-hole correlations [27] within the excitonic insulator scenario [28]. One of the recurring problems stems from disentangling the dominant electron-electron or electron-phonon processes in driving the phase transition, since typically the experimental signatures of both the electronic order and the underlying lattice distortion occur simultaneously. As such, there can be several different interpretations of fundamentally similar results, and hence the unambiguous determination of the origin of CDWs is notoriously difficult.

The purpose of this thesis is to investigate the isostructural selenium-based TMDs with $1T$ symmetry which, despite having identical crystal structures, exhibit vastly different CDW behaviour. Multiple experimental and theoretical techniques are used to study signatures of CDW formation in both their electronic and lattice structure in an attempt to further the understanding of possible driving mechanisms in this intriguing class of materials.

### 1.1.2 Organisation of the thesis

This chapter begins with an introduction to the concept of charge density waves (CDWs) and relevant theoretical descriptions. An overview of the transition metal dichalcogenides (TMDs) are then presented in the context of the recent surge in research of two-dimensional materials. The chapter culminates in an overview of the specific electronic and structural properties of the 1$T$-TMDs. Chapter 2 describes the experimental techniques used in this work, starting from a theoretical background and eventually the technical details relevant to each specific experimental apparatus are presented. Predominantly, photoemission spectroscopy and variants thereof are discussed, although Raman spectroscopy and electronic transport measurements are also included. Chapter 3 describes the growth of single crystal TMD samples studied in this thesis. It begins with a brief motivation for the growth of crystals by the researcher, as opposed to obtaining samples commercially. This is followed by a detailed description of the specific experimental apparatus and methods used for the growth of high quality single crystal TMDs by chemical vapour transport (CVT). The chapter concludes with general observations about the growth of TMDs by CVT, and some possible means of improving these methods are suggested

The remainder of the thesis is presented in a "portfolio" format. Chapters 5 - 7 report the main results which are included as a document in the style of an academic journal. In each case, the chapter begins with a *preamble* which outlines the motivation, key scientific questions, and a brief summary of the main findings. An *introduction* provides some necessary prerequisites in order to better understand the main work, and in many cases includes some additional results. This is followed by the either a *published journal article* or a *manuscript in preparation* which represents the main work. The chapter concludes with a *discussion* of the results, its implications, and an outlook for the future. Continuing from the methods described in Chapter 3 for the growth of TMD single crystals, Chapter 4 discusses the influence of elevated growth temperature on the CDW properties of 1$T$-$VSe_2$. The origin of defects and doping are investigated using high resolution x-ray photoelectron spectroscopy (XPS) measurements. Based on this work, a method of growing ultra-high purity 1$T$-$VSe_2$ was developed. Chapter 5 reports measurements of the photo-induced suppression of the CDW in 1$T$-$TiSe_2$ using a unique combination of time- and angle-resolved photoemission spectroscopy (TR-ARPES) and time-resolved reflectivity (TRR). A detailed fluence dependence of the dynamics, together with the observation

of coherent phonon oscillation are used to disentangle the contributions of excitons and phonons in driving the CDW. In Chapter 6, full-wavevector ARPES measurements of the Fermi surface (FS) in 1$T$-$VSe_2$ are presented. These results are compared to DFT calculations of the electronic susceptibility in order to investigate the role of FS nesting. A complete temperature and momentum dependent analysis of the CDW gap is discussed. Finally, Chapter 7 investigates the metal-insulator transition (MIT) in 1$T$-$TaSe_2$ and its relationship with the CDW phase by focusing primarily on the strong coherent phonon oscillations in this material observed in both TR-ARPES and TRR measurements.

## 1.2 Charge density waves (CDWs)

In many materials with highly anisotropic crystal and electronic structures, a transition to a new ground state may occur at sufficiently low temperature, known as the charge density wave (CDW), for which there is a modulation of the charge density accompanied by a periodic lattice distortion [29]. As a result of this transition, there is an overall minimisation of the system energy due to a reconstruction of the electronic structure. The new ground state becomes favourable when this gain in electronic energy is greater than the energy cost required to distort the crystal lattice.

In order to describe the idea of a CDW, an understanding of the electronic structure of solids is required, including several fundamental quantum mechanical concepts. Therefore, a simplified theory of electronic structure is presented first, based on the Sommerfeld model of metals. Following this, the CDW will first be introduced in its simplest form as theorised by Rudolf Peierls in 1955 for the case of a one-dimensional (1D) linear chain metal [1]. In short, Peierls mentioned that the electrons of a 1D metal coupled to the underlying lattice is unstable at low temperatures, and the electron-phonon interactions result in a CDW. The effect of Fermi surface topology in driving CDWs is discussed in terms of the electronic susceptibility and phonon dispersion renormalisation as a result of electron-phonon interactions starting from the idealised 1D (Peierls) scenario and then applied to higher dimensions. In more complex systems, alternative driving mechanisms and even multiple competing or co-operating effects may be responsible for the formation of CDWs and these will be discussed in later chapters with regards to specific materials.

### 1.2.1 Electronic structure of solids

The Sommerfeld model is quantum mechanical theory capable of explaining many of the observed electronic properties of metals [30, 31]. Since quantum mechanics dictates that only a certain number of states per unit volume of phase space are allowed, this ultimately leads to the quantisation of electronic energy states within a solid. The model follows a free-electron approach such that there are no electron-ion or electron-electron interactions. Shown in the following is the derivation of the electronic dispersion in solids starting from the Shrödinger equation and assuming a single electron confined to a volume.

The time-independent Schrödinger equation for a single nonrelativistic particle in three dimensions is given by

$$-\frac{\hbar^2\nabla^2}{2m}\psi(\mathbf{r}) + V(\mathbf{r})\psi(\mathbf{r}) = E\psi(\mathbf{r}), \tag{1.1}$$

where $\nabla^2$ is the Laplacian, $m$ is the particle mass, $E$ is the energy of the particle subject to a potential, $V(\mathbf{r})$ and $\psi(\mathbf{r})$ is the particle wavefunction with position $\mathbf{r}$. Then, assuming a free-electron (i.e the potential is zero) Equation 1.1 becomes

$$-\frac{\hbar^2\nabla^2}{2m_e}\psi(\mathbf{r}) = E\psi(\mathbf{r}), \tag{1.2}$$

where $m_e$ is the free-electron mass. If the electrons are confined to a volume $L^3$, the periodic boundary conditions on the wavefunction are defined by $\psi(\mathbf{r}) = \psi(x, y, z) = \psi(x + L, y, z) = \psi(x, y + L, z) = \psi(x, y, z + L)$ and as such, Equation 1.2 is satisfied by the travelling plane wave

$$\psi(\mathbf{r}) = \frac{1}{\sqrt{L^3}}e^{i(\mathbf{k}\cdot\mathbf{r})}, \tag{1.3}$$

where $\mathbf{k} = (k_x, k_y, k_z) = (\frac{2\pi}{L}n_x, \frac{2\pi}{L}n_y, \frac{2\pi}{L}n_z)$ is the three dimensional wavevector and $n$ is an integer. Based on this wavefunction, the solution to Equation 1.2 is then

$$E = \frac{\hbar^2\mathbf{k}^2}{2m} = \frac{\hbar^2}{2m}(k_x^2 + k_y^2 + k_z^2). \tag{1.4}$$

This result shows that the electronic energy is quantised and depends on the wavevector $\mathbf{k}$ in three dimensions. The relationship derived in Equation 1.4 for a single particle can

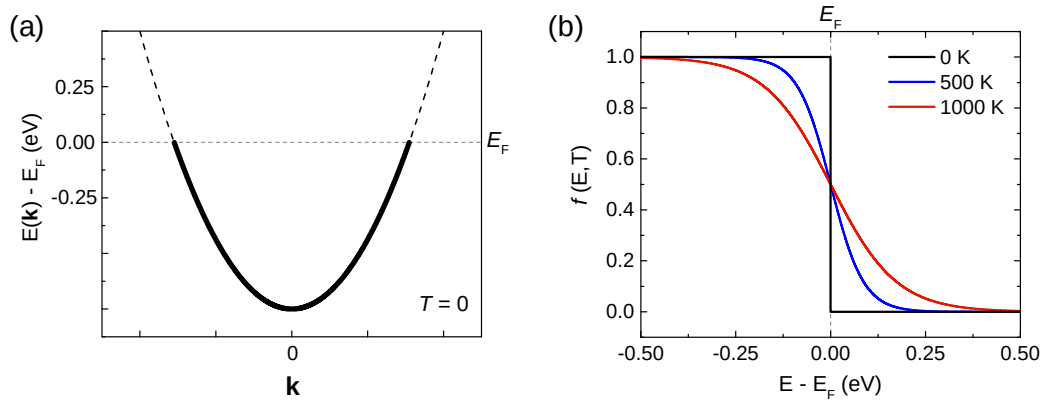


**Figure 1.1:** Electronic structure of solids. (a) Parabolic band at zero temperature with states filled up to the Fermi level, $E_{\mathrm{F}}$ based on the Sommerfeld model. (b) Fermi-Dirac distribution at various temperatures. The energy scale in both panels is for illustrative purposes only.

then be applied to a solid containing $N$ electrons which results in "bands" of allowed energy-momentum states, known as the *electronic dispersion*. For a simple system such as a one-dimensional chain of atoms, this appears as a single parabolic band as illustrated in Figure 1.1(a). The band is filled from the lowest energy state up to $N/2$ since two electrons per state are allowed according to the *Paui exclusion principle*. In more complex systems with many atoms and a three-dimensional crystal structure, there are numerous allowed energy-momentum bands, which leads to the concept of *electronic structure* in solids.

Further to the electronic dispersion, it is also possible to obtain the linear momentum of electrons by acting the momentum operator, $\mathbf{p} = -i\hbar\nabla$ on the electron wavefunction

$$\mathbf{p}\psi(\mathbf{r}) = -i\hbar\nabla\psi(\mathbf{r}) = \hbar\mathbf{k}\psi(\mathbf{r}), \tag{1.5}$$

$$\mathbf{p} = \hbar\mathbf{k}, \tag{1.6}$$

where the result in Equation 1.6 is referred to as the *de Broglie* relation.

Another important consideration of the Sommerfeld model is that electrons must obey *Fermi-Dirac statistics* and the probability of the occupation of states can be described by the Fermi-Dirac (F-D) distribution

$$f(E,T) = \frac{1}{e^{(E-\mu/k_BT)}+1}, \tag{1.7}$$

where $k_B$ is the Boltzmann constant, $T$ is temperature and $\mu$ is the chemical potential,

which is defined as the energy at which the probability of occupation is 1/2. At $T = 0$, $\mu = E_{\mathrm{F}}$ where $E_{\mathrm{F}}$ is the Fermi energy and the F-D distribution is a step function such that states with energy $E > \mu$ have a probability $f(E) = 1$ (completely occupied) and $E < \mu$ have $f(E) = 0$ (completely unoccupied) as shown in Figure 1.1(b). At finite temperature, the F-D is no longer a sharp step function and is instead broadened by $\Delta E \propto k_B T$ around $\mu$. The implication of this is that only electrons with an energy in this range will be able to contribute to electronic transport processes in solids. Note that the notation $E_{\mathrm{F}}$ is regularly used in the literature in place of $\mu$, even at finite temperatures and is usually referred to as the *Fermi level* to make the distinction with the Fermi energy which is only defined at zero temperature. This terminology is adopted throughout this thesis. In a real system at finite temperature, the F-D distribution describes the thermal broadening of the occupation of states around the highest occupied level.

These concepts lead to the idea of a *Fermi surface*. For the simplified situation of an electron confined to a volume $L^3$ in the Sommerfeld model, the Fermi surface is a sphere of occupied states with energy $E_{\mathrm{F}}$. Therefore according to Fermi-Dirac statistics and the implications of Equation 1.7, only electrons that exist on this sphere (or within $\sim k_B T$) have sufficient energy to contribute to the electronic properties. In real solids, the symmetry of the crystal structure, and the particular arrangement of atoms within it, can result in Fermi surfaces with complex topology confined to the boundaries of the reciprocal space (**k**-space) Brillouin zone (BZ). These concepts are discussed in more detail in Section 1.4.3 with reference to specific materials.

### 1.2.2 One-dimensional case: Peierls distortion

CDW formation in a simple one-dimensional system as theorised by Peierls is described here, with a focus on energy considerations related to the electronic structure and the prerequisite of a mean field theory, following the approaching of Grüner [32].

Consider the idealised case of a one-dimensional linear chain metal as depicted in Figure 1.2(a) with an electronic dispersion according to Equation 1.4 derived previously, and initially at zero temperature.

If there are no particle interactions, the ground state is defined by electron states filled up to the Fermi level, $E_{\mathrm{F}}$ and corresponding Fermi wavevector, $k_{\mathrm{F}}$. The lattice is a regular spacing of atoms with separation, $a_0$ and the charge density, $\rho(r)$ is uniform. However, if coupling to the underlying lattice (electron-phonon interactions) is considered,

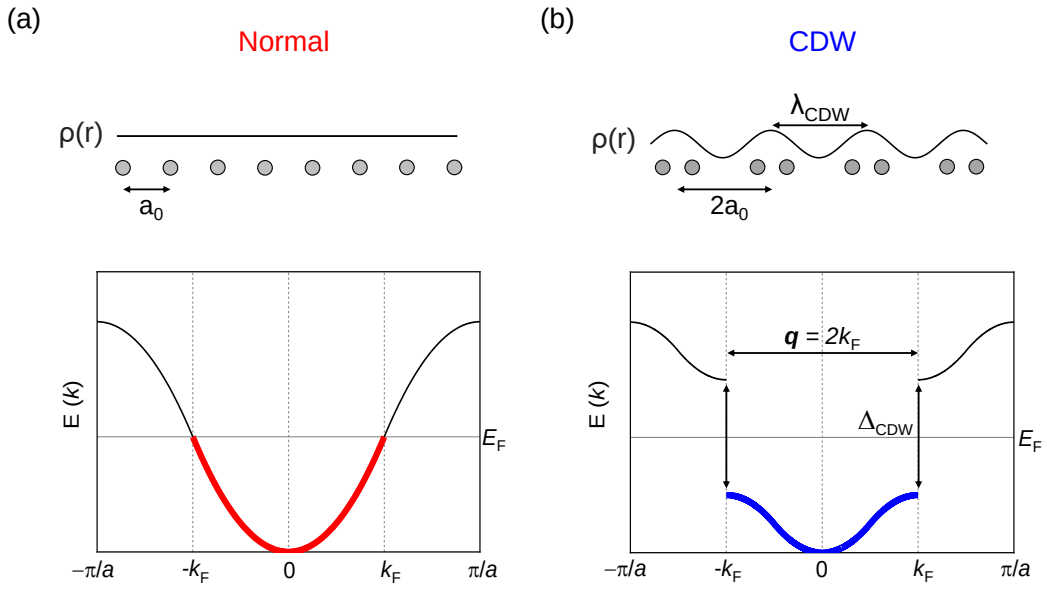


**Figure 1.2:** Peierls distortion in a 1D linear chain metal with a half-filled band. (a) In the normal state, there is a regular atomic spacing, $a_0$ and uniform electron density, $\rho$(r). Electrons are filled up to the Fermi level, $E_\mathrm{F}$ (solid red line). (b) As a result of electron-phonon interactions, a lattice (Peierls) distortion occurs leading to a periodic modulation in the electron density with wavelength, $\lambda_\mathrm{CDW}$ and is known as a charge density wave (CDW) state. A gap, $\Delta_\mathrm{CDW}$ opens in the electronic dispersion around $E_\mathrm{F}$ which lowers the overall system energy.

it may be energetically favourable to form a periodic lattice distortion (PLD) as shown in Figure 1.2(b) known as the *Peierls distortion* [1]. For the particular case of a half-filled band, the lattice constant has doubled to $2a_0$. As a result, there is modulation in the charge density with period, $\lambda_\mathrm{CDW}$ related to the Fermi wavevector, $k_\mathrm{F}$:

$$\lambda_\mathrm{CDW} = \frac{\pi}{k_\mathrm{F}}. \tag{1.8}$$

Since the real-space unit cell has doubled, the reciprocal space BZ has halved and results in a gap, $\Delta$ opening in the single-particle electron dispersion around the Fermi level, $E_\mathrm{F}$ at the new BZ boundary, forming an insulator known as the *Peierls insulator*. As a consequence, there is a decrease in the electronic energy, $E_\mathrm{el}$ as the occupied portion of the band is lowered below $E_\mathrm{F}$. Conversely, there is an increase in the elastic energy of the lattice, $E_\mathrm{lat}$ in order to make the distortion. Thus, the total change in energy of the system is simply given by the sum of electronic and lattice components whereby

$$E_{\mathrm{el}} = n(E_{\mathrm{F}}) \left[ -\frac{\Delta^2}{2} - \Delta^2 \log\left(\frac{2E_{\mathrm{F}}}{\Delta}\right) \right], \tag{1.9}$$

$$E_{\mathrm{lat}} = \frac{n(E_{\mathrm{F}})\Delta^2}{\lambda}, \tag{1.10}$$

and hence

$$E_{\mathrm{tot}} = E_{\mathrm{el}} + E_{\mathrm{lat}} = n(E_{\mathrm{F}}) \left[ -\frac{\Delta^2}{2} - \Delta^2 \log\left(\frac{2E_{\mathrm{F}}}{\Delta}\right) + \frac{\Delta^2}{2\lambda} \right], \tag{1.11}$$

where $n(E_F)$ is the electron density at the Fermi level and $\lambda$ is the dimensionless electron-phonon coupling constant. For $\lambda \ll 1$, minimisation of the total energy in Equation 1.11 leads to a gap, $\Delta = 2E_{\mathrm{F}}e^{-1/\lambda}$ and shows that the net energy of the system is lowered from the normal state, $E_{\mathrm{norm}}$ to the new state, $E_{\mathrm{CDW}}$ and the difference is given by the condensation energy

$$E_{\mathrm{con}} = E_{\mathrm{norm}} - E_{\mathrm{CDW}} = \frac{1}{2} n(E_{\mathrm{F}})\Delta^2. \tag{1.12}$$

The modification of the electron dispersion, leads to a periodic potential for electrons to occupy, and the periodic charge modulation in one dimension, $\rho(x)$ is given by:

$$\rho(x) = \rho_0 + \frac{\Delta\rho_0}{\hbar v_F k_F \lambda} \cos(2k_F x + \varphi), \tag{1.13a}$$

$$= \rho_0 + \rho_1 \cos(2k_F x + \varphi), \tag{1.13b}$$

where $v_{\mathrm{F}}$ is the Fermi wavevector and $\rho_0$ is the charge density in the absence of electron-phonon interactions which is given by $\rho_0 = \frac{\pi}{k_F}$ in one dimension. $\rho_1$ and $\varphi$ are the amplitude and phase of the charge modulation respectively.

The result of these processes, driven by electron-phonon interactions, causes charge carriers involving the wave vector $\mathbf{q} = 2k_F$ to condense into a collective mode. This condensate is associated with the charge density modulation given by Equation 1.13a and together the state is known as a charge density wave (CDW). Similar to other condensates, this state can be described by the complex order parameter

$$\Delta = |\Delta| \, e^{i\varphi}, \tag{1.14}$$

where $|\Delta|$ is the amplitude and $\phi$ is the phase of the mode (similar to those in Equation 1.13a). $|\Delta|$ is related to the magnitude of the single-particle CDW gap (written $\Delta$ previously) and the notation is used interchangeably. In later chapters, this will appear as $\Delta_{\mathrm{CDW}}$ in order to distinguish it from other order parameters.

Now the case at finite temperatures is considered. Electrons that are thermally excited across the single-particle gap screen the electron-phonon interaction which results in a reduction of the magnitude of the CDW gap, and size of the lattice distortion. This means the CDW state can exist at non-zero temperatures, and is characterised by a second-order phase transition which occurs at the critical temperature, $T_{\mathrm{CDW}}$. According to mean field theory, the temperature dependence of the CDW gap is

$$\Delta(T) \propto \Delta(0)\sqrt{1 - T/T_{\mathrm{CDW}}}, \tag{1.15}$$

where $\Delta(0)$ is the zero temperature (maximum) gap and $T_{\mathrm{CDW}}$ in this case is the mean-field CDW transition temperature.

Although the theory presented here is strictly for a one dimensional system, the concept of a CDW can be generalised for higher dimensions by considering the position vector, $\mathbf{r}$:

$$\rho(\mathbf{r}) = \rho_0 + \rho_1 \cos(2k_F \cdot \mathbf{r} + \varphi). \tag{1.16}$$

Finally, it should be noted that a charge density wave can be defined by its commensurability, whereby it is *commensurate* (CCDW) when the period of the density wave modulation, $\lambda_{\mathrm{CDW}}$ is some multiple of the period of the underlying distorted lattice, $a$ and therefore obeys $\lambda_{\mathrm{CDW}} = (n/m)a$, where $n$ and $m$ are integers. Conversely, it is *incommensurate* (ICCDW) when the charge density does not match the underlying lattice periodicity in this way. Commensurability is discussed further in Section 1.4.1 with reference to specific materials.

### 1.2.3 Higher dimensions: Fermi surface nesting

An alternative approach to understanding CDW formation is to study the Fermi surface topology and evaluate its electronic stability.

Starting from the ideal 1D case discussed previously in Section 1.2.2, there is an open Fermi surface consisting of two parallel sheets at $\pm\, k_{\mathrm{F}}$ as depicted in Figure 1.3(a). It is

then possible to define a single wavevector, $\mathbf{q}$ which spans the Fermi surface, linking states in opposite sheets. The response of the electrons to a perturbation with wavevector $\mathbf{q}$ and frequency $\omega$ can then be approximated using the Lindhard response function, $\chi(\mathbf{q},\omega)$ [32]. Within the free-electron model, is it possible to obtain the non-interacting electronic susceptibility

$$\chi^0(\mathbf{q},\omega) = \sum_k \frac{f(E_\mathbf{k}) - f(E_{\mathbf{k}+\mathbf{q}})}{E_\mathbf{k} - E_{\mathbf{k}+\mathbf{q}} - \hbar\omega - i\delta} \left|M(\mathbf{q})\right|^2, \tag{1.17}$$

where $f$ is the F-D function for energies $E_\mathbf{k}$ and $E_{\mathbf{k}+\mathbf{q}}$ at the original, $\mathbf{k}$ and perturbed, $\mathbf{k}+\mathbf{q}$ wavevectors respectively. $M(\mathbf{q})$ is a matrix element which describes the effect of the perturbation on the electron wavefunction [33]. This complex function can be expressed in terms of the real and imaginary parts $\chi^0(\mathbf{q},\omega) = \mathrm{Re}\,\chi^0(\mathbf{q},\omega) + i\,\mathrm{Im}\,\chi^0(\mathbf{q},\omega)$. To illustrate the effect of dimensionality on the susceptibility in an idealised case, Equation 1.17 can be estimated within the static (zero energy transfer) limit ($\omega \to 0$) and the constant matrix element approximation. The real part, $\mathrm{Re}\,\chi^0(\mathbf{q})$ can then be evaluated for the one-, two- and three-dimensional cases [23]. The results are plotted in Figure 1.4(a) and shows a strong divergence at $\mathbf{q} = 2k_\mathrm{F}$ in 1D.

By considering electron-phonon interactions, it was noticed by Kohn [34] that any divergence in the electronic susceptibility will also be reflected in the phonon dispersion, resulting in a significant renormalisation. For the one-dimensional case near $\mathbf{q} = 2k_\mathrm{F}$, this will cause a phonon softening to zero energy known as the *Kohn anomaly* [3]. The renormalised phonon dispersion as a result of this interaction is given by

$$\omega(\mathbf{q})^2 = \omega_0(\mathbf{q})^2 + 2\omega_0(\mathbf{q})^2 g^2\,\mathrm{Re}\,\chi(\mathbf{q},\omega), \tag{1.18}$$

where $\omega_0$ is the bare phonon dispersion, $g$ is an interaction constant and $\mathrm{Re}\,\chi(\mathbf{q},\omega)$ is now the interacting susceptibility. Equation 1.18 can be approximated using the bare electronic susceptibility and the results for $\omega(\mathbf{q})$ in one, two and three-dimensional cases are shown in Figure 1.4(b).

In Equation 1.17, the most significant contribution to the function is pairs of states with the same energy but differ in momentum by exactly $\mathbf{q} = 2k_\mathrm{F}$, which is responsible for the divergence in the susceptibility. The implication of this analysis is that a 1D metal at zero temperature is always unstable, confirming the result of Peierls. This instability

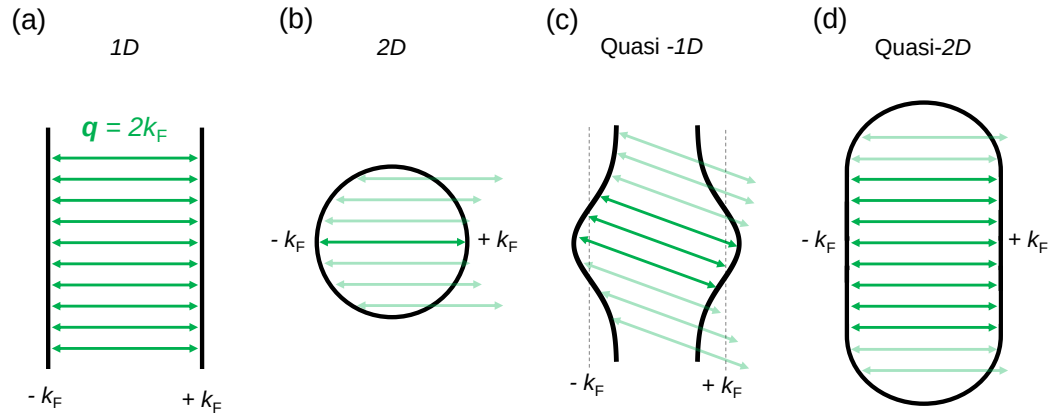


**Figure 1.3:** Fermi surface nesting in different dimensions. (a) 1D system with open Fermi surface consisting of two parallel sheets at $\pm\ k_{\mathrm{F}}$. The wave-vector of length $\mathbf{q} = 2k_{\mathrm{F}}$ spans the entire Fermi surface, leading to perfect nesting. (b) 2D system with cylindrical Fermi surface. Due to its shape, only an infinitesimally small portion of the Fermi surface is linked by $\mathbf{q}$ and thus nesting is poor. (c) In a quasi-1D system with warped parallel sheets, there are finite portions that are nested by the same $\mathbf{q}$ vector allowed by a small rotation. (d) In a quasi-2D system with elliptical Fermi surface, there can exist large parallel regions of the fermi surface that are well-nested.

is referred to as *Fermi surface nesting* and for the 1D case, perfect nesting is achieved since the entire Fermi surface can be linked by a translation with a single nesting vector of $\mathbf{q} = 2k_{\mathrm{F}}$. In higher dimensions, such as the 2D Fermi surface shown in Figure 1.3(b), there exists only an infinitesimally small portion of states that are matched by $\mathbf{q} = 2k_{\mathrm{F}}$ (poor nesting). This means that the contribution to the total response in Equation 1.17 is small and the divergence is greatly reduced as shown in Figure 1.4. With more complicated FS topology however, it may be possible to achieve an intermediate nesting condition. For a quasi-1D system with warped FS sheets as sketched in Figure 1.3(c), there is some finite nesting by allowing a rotation of $\mathbf{q}$. In a quasi-2D system, an elliptical FS such as that sketched in Figure 1.3(d) may posses large parallel portions similar to the 1D case and near-perfect nesting can be achieved.

Referring to Equation 1.12, it is straightforward to see why the degree of Fermi surface nesting dictates the amount of energy gained by the system in undergoing the transition. As a larger portion of the FS becomes nested by $\mathbf{q}$, a greater density of carriers, $n(E_{\mathrm{F}})$ are involved in the transition and contribute to the condensation energy for a fixed gap, $\Delta$ i.e. a greater number of states are lowered in energy and thus removed from the Fermi

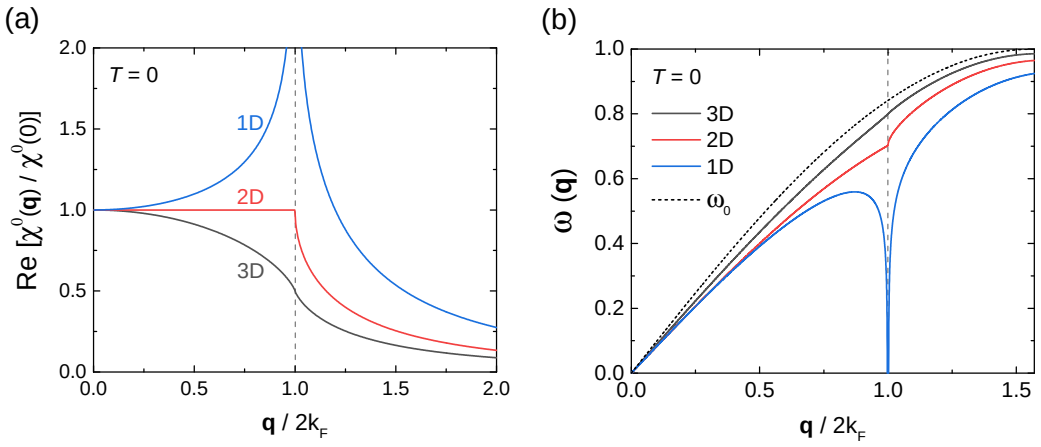


**Figure 1.4:** Evaluating instabilities in metals. (a) Bare electronic susceptibility, $\chi^0(\mathbf{q})$ and (b) Renormalised acoustic phonon dispersion, $\omega(\mathbf{q})$ for one, two and three-dimensional Fermi surfaces at zero temperature, exhibiting a divergence at $\mathbf{q} = 2k_\mathrm{F}$. The dashed line is the bare phonon dispersion, $\omega_0$.

surface. It is therefore expected that Fermi surfaces which allow a significant degree of nesting are more likely to form a CDW via this mechanism.

The theoretical treatment presented in this section successfully describes how an idealised case of a 1D metal would be unstable to CDW formation as a result of FS nesting, evidenced by the strong divergence in the electronic susceptibility and phonon dispersion near the nesting vector, $\mathbf{q} = 2k_\mathrm{F}$. Although arguments about the weak divergence in $\mathrm{Re}\,\chi^0(\mathbf{q})$ for higher dimensions have been discussed, the situation is not as simple in real materials. The static limit is rarely applicable i.e. $\omega \neq 0$ and as such, both the real and imaginary parts of the susceptibility are important to describe the total influence of Fermi surface nesting [23]. By evaluating Equation 1.17, a 'true nesting' is achieved if there is a peak in $\mathbf{q}$ for $\mathrm{Re}\,\chi^0(\mathbf{q})$ which translates into divergence of the full electronic susceptibility (as discussed previously), and is also matched by a corresponding peak in $\mathrm{Im}\,\chi^0(\mathbf{q})$ at the same $\mathbf{q}$, responsible for the low energy excitations near $E_\mathrm{F}$ [22]. For a particular FS topology, the peaks in $\mathbf{q}$ can be compared to suspected CDW wavevectors $\mathbf{q}_\mathrm{CDW}$ in order to determine if nesting is significant.

## 1.3 Transition metal dichalcogenides (TMDs)

### 1.3.1 An overview

Graphene is a single atomic layer of carbon atoms and was the first 2D material to be isolated experimentally by means of mechanical exfoliation from graphite in 2004 [18]. It has since been found to exhibit excellent mechanical and electronic properties such as extremely high carrier mobilities at room temperature, making it a prime candidate for use in future high performance electronic devices [35]. Later, Andre Geim and Konstantin Noveselov were awarded the 2010 Nobel Prize in Physics for "groundbreaking experiments regarding the two-dimensional material graphene". Following these important discoveries, an entire field of research into 2D materials has emerged.

Recently, researchers have turned their attention to other quasi-2D layered materials to see if similar methods could be used to obtain single layers (*monolayers*) from a bulk crystal. Among the primary candidates in this effort are the family of transition metal dichalcogenides (TMDs) which exist in the form $MX_2$, composed of transition metal (M) and chalogen (X) elements as shown in Figure 1.5(a). These materials are formed of stacks of thin layers held together by van der Waals (vdW) forces. Each individual layer is comprised of three atomic planes in an X-M-X configuration whereby a single plane of transition metal atoms is sandwiched between two planes of chalcogen atoms as shown in Figure 1.5(b). Interest in these materials is mainly due to their extremely diverse range of properties depends on the particular combination of transition metal and chalcogen. The variety of material classification within this family includes and is not limited to; *semiconductors* (e.g., $MoS_2$ , $WS_2$), *semimetals* (e.g., $WTe_2$, $TiSe_2$), *true metals* (e.g., $NbS_2$, $VSe_2$), and *superconductors* (e.g., $NbSe_2$, $TaS_2$) [36]. Many of these properties also vary between structural polytypes (see Section 1.3.2) of one particular compound. For example, $2H$-$MoS_2$ is semiconducting, whereas $1T$-$MoS_2$ is metallic [37].

TMDs have been known to the research community for many years and their bulk properties have been studied since the 1960s [16]. However, isolating monolayer or few-layer samples has not been possible until recently, and it is expected to have a profound effect on the behaviour on fundamental particles and quasiparticles (e.g. electrons, phonons, excitons) as a result of quantum confinement. This effect can influence electronic transitions within a system, the density of states, and strength of interactions. One of the most

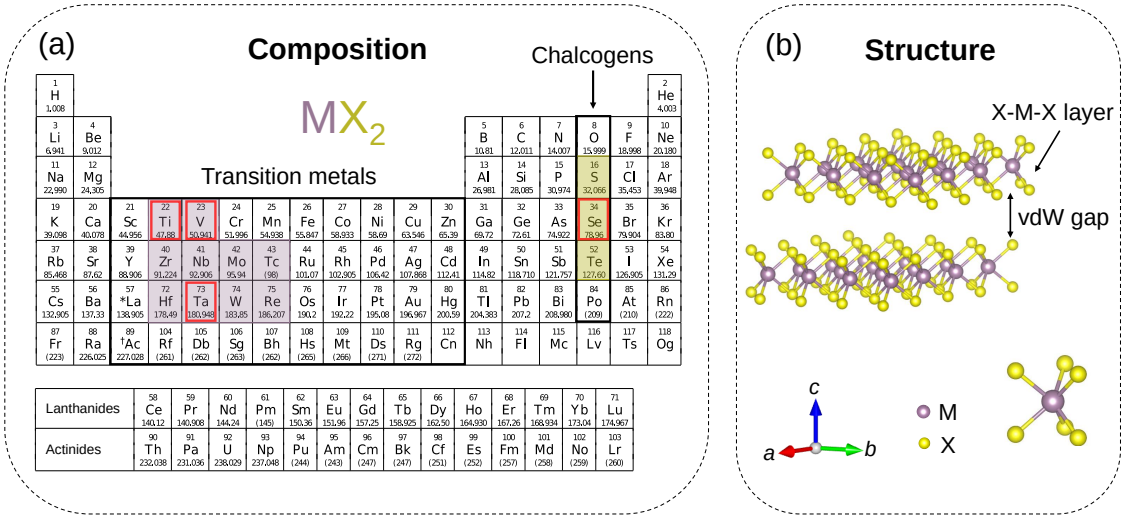


**Figure 1.5:** Composition and crystal structure of transition metal dichalcogenides (TMDs). (a) Periodic table highlighting the position of the transition metals and chalcogens (black boxes). The shaded areas highlight the specific transition metals (M) and chalcogens (X) which form the compounds ($MX_2$). The red squares indicate the elements present in the specfic compounds investigated in this thesis. (b) Diagram of the crystal structure consisting of layers made from three atomic planes (X-M-X) each, separated by a van der Waals (vdW) gap.

readily studied TMDs to date is molybdenum disulphide ($MoS_2$) in the $2H$ polytype which normally exists as a semiconductor with an indirect band gap in the bulk. However, by mechanically exfoliating a bulk crystal down to a monolayer, it has been shown to become a direct band gap semiconductor with an enhancement of the photoluminescence quantum yield by a factor of $10^4$ [19]. In addition, these properties were shown to shift progressively with decreasing thickness as the material goes from 3D to the 2D limit. Therefore, the incredible range and tunability of TMD properties has already been demonstrated and makes them excellent candidates for a number of applications [38]. This diversity has also opened up the possibility of constructing nanoscale devices known as *van der Waals heterostructures*, whereby the desired properties can be obtained by stacking individual layers of 2D materials such as graphene, TMDs and hexagonal boron nitride (h-BN) with a particular arrangement [39].

Although the revival of interest in TMDs has been driven mainly by the emerging field of 2D materials, there remains important questions surrounding their bulk properties which must be fully explored in order to understand physical phenomena in the 2D limit. Since the first studies of these materials in the 1960s, there has been a great advancement

in experimental techniques available to researchers, which justifies revisiting this field of Physics.

### 1.3.2 Crystal structure and polytypism

TMDs have been found to exist with numerous structural polytypes [40] although there are three commonly occurring types; $1T$, $2H$ and $3R$ where the letter refers to the *trigonal*, *hexagonal* and *rhombohedral* symmetry of the unit cells respectively, and the number indicates the layers found within the cell [41]. Presented in Figure 1.6 is the crystal structure of the two most stable polytypes for many TMDs and these will be discussed in the following section. The polytypes can also be defined by their metal coordination in the layered structure; either *octahedral* or *trigonal prismatic* for the case of $1T$ and $2H$ which refers to the arrangement of the six chalcogen atoms around the central metal atom as shown in Figure 1.6(b). The octahedral coordination has a rotation between the topmost chalogen atoms with respect to the bottom such that all chalcogens are visible when viewed from above (along $c$). By contrast, the chalcogen atoms of the trigonal prismatic coordination have the same orientation between top and bottom such that it exhibits the honeycomb structure when viewed from above, similar to graphene.

Both the trigonal and hexagonal crystal systems belong to the hexagonal family and therefore all TMDs are defined by a unit cell consisting of two equal axes ($a = b$) separated by an angle $\gamma = 120°$ and a third axis ($c$) which is perpendicular to the $a$-$b$ plane and may not be equal in length to the other axes as shown in Figure 1.6(c). In Hermann-Mauguin notation, the $2H$ and $1T$ symmetries belong to the $P6_3/mmc$ (no. 194) and $P\bar{3}m1$ (no. 164) spacegroups respectively [41]. In relation to the crystal structure, the $a$- and $b$-axes lie within the layer plane along the minimal chalcogen-chalogen distance, and the $c$-axis is perpendicular to the layers. The lattice parameters of the $1T$ compounds are typically in the range; $a = b \approx$ (3 - 4) Å and $c \approx$ (6 - 7) Å. The $2H$ polytypes therefore have approximately double the $c$-axis length in the range (12 - 14) Å [see Figure 1.6(c)].

## 1.4 Metallic TMDs with trigonal symmetry

In this section, an overview of the CDW properties of the metallic TMDs with trigonal ($1T$) symmetry is provided, followed by the basic structural and electronic characteristics of these compounds.

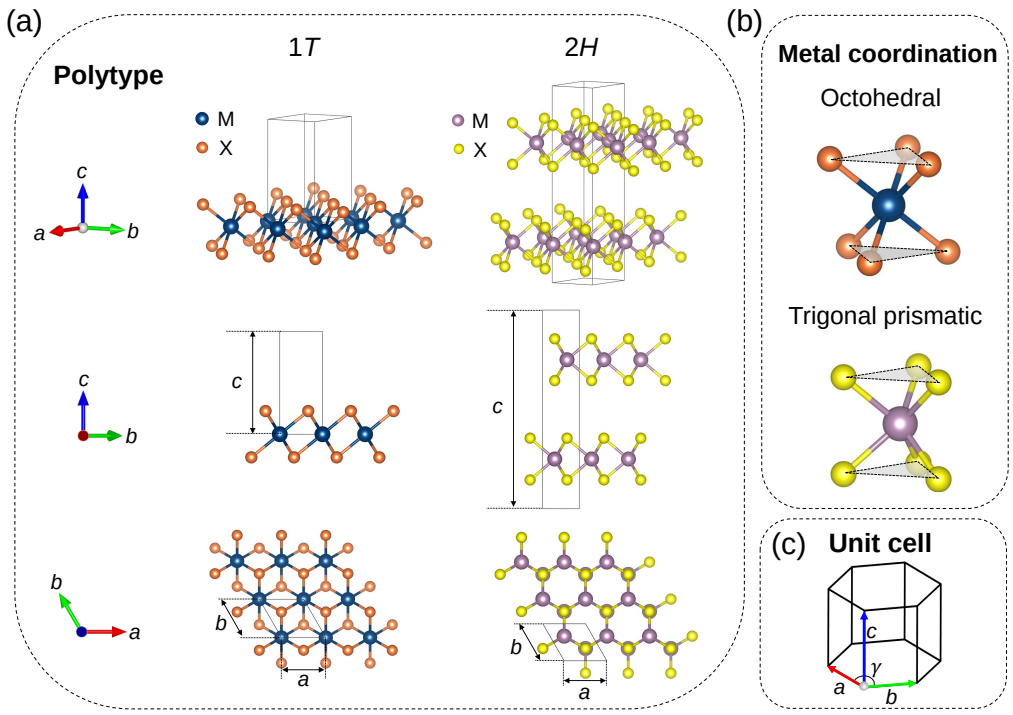


**Figure 1.6:** Structural polytypes of TMDs. (a) The 1$T$ (*trigonal*) and 2$H$ (*hexagonal*) polytypes shown at an angle to the layer-plane, and along the $a$- and $c$- axes as indicated by the coloured compass. The grey frame shows the lattice parameters of the primitive cell (b) Metal coordination; either *octohedral* or *trigonal prismatic* for the 1$T$ and 2$H$ polytypes respectively. (c) Unit cell of the hexagonal crystal family

### 1.4.1 CDW properties

Following early experimental studies of the metallic TMDs, it was noticed that the vast majority exhibited anomalies in the temperature-dependence of electronic [6,42,43], magnetic [44] and thermal [45] transport properties, suggestive of phase transitions in these compounds. Based on coinciding observations of superlattice formation in diffraction experiments [2,46], related to distortions of the underlying crystal lattice, the behaviour was explained by transitions to a CDW state. In the decades following these discoveries, various scenarios have been proposed to explain the mechanism behind CDW formation [20].

This thesis specifically focuses on understanding CDW phenomena in the isostructural, selenium-based TMDs with trigonal (1$T$) symmetry; 1$T$-$TiSe_2$, 1$T$-$VSe_2$ and 1$T$-$TaSe_2$. The only significant variation is the transition metal (M = Ti, V or Ta) yet the CDW properties in each compound varies considerably, including; the transition temperature, distorted lattice periodicity, and commensurability [2,47], as summarised in Table 1.1.

| Compound | $T_{\mathrm{CDW}}$ | PLD | Commensurability |
|---|---|---|---|
| $1T$-$TiSe_2$ [42] | 202 K | $2a_0 \times 2a_0 \times 2c_0$ | CCDW |
| | - | - | - |
| $1T$-$VSe_2$ [48] | 110 K | $4a_0 \times 4a_0 \times 3.18c_0$ | ICCDW |
| | 85 K | $3.25c_0$ | - |
| $1T$-$TaSe_2$ [49] | 600 K* | - | ICCDW |
| | 473 K | $\sqrt{13}a_0 \times \sqrt{13}a_0$ | CCDW |

**Table 1.1:** Summary of the CDW properties of the Se-based TMDs with $1T$ symmetry. *Predicted normal state to ICCDW transition temperature since an interpolytypic transformation ($1T \rightarrow 3R$) at 530 K makes it experimentally inaccessible.

The main differences in CDW behaviour can mostly be attributed to subtle variations in the electronic structure, governed by the transition metal as will be discussed in Section 1.4.3. The $1T$-TMDs have been demonstrated to posses particularly two-dimensional Fermi surfaces with large parallel portions which theoretically should be prone to electronic instabilities (FS nesting) [2, 50–52], similar to the quasi-2D case shown previously in Figure 1.3(d). However, such a situation is not straightforward [21, 53], and both the electron-electron and electron-phonon interactions have to be considered. The precise driving mechanism behind CDW formation in these compounds is the main focus of this thesis, and an overview of the current understanding for the case of each specific compound will be presented in the introduction section of the relevant chapters.

Typically in all TMDs, the higher temperature transition is the incommensurate phase (ICCDW) for which the formation is governed by the balance between electronic energy gain by opening gaps in the band structure, and the lattice energy cost in order to distort the crystal structure as discussed in Section 1.2. Further lowering of the total energy is then achieved as the electronic order *locks in* to a commensurate geometry with the lattice (CCDW), usually at a lower temperature, by a slight modification of $\mathbf{q}_{\mathrm{CDW}}$. A clear example of this is $2H$-$TaSe_2$ in which a second-order transition occurs at 122 K to a CDW which is first incommensurate with the underlying lattice given by wave vector, $\mathbf{q}_{\mathrm{CDW}} = (1 - \delta)\boldsymbol{a}/3$ followed by first-order lock-in to commensurate CDW at the lower temperature of 90 K where $\delta \rightarrow 0$ [46]. This behaviour is less commonly discussed in the $1T$-TMDs studied in this thesis (see Table 1.1) because the normal-ICCDW or ICCDW-CCDW transitions

are either absent (1 $T$-$TiSe_2$), have limited experimental evidence (1 $T$-$VSe_2$) or occur at high temperatures which are not typically investigated (1 $T$-$TaSe_2$). An intermediate phase which occurs between the ICCDW and CCDW known as nearly-commensurate phase (NCCDW) can also be found in some compounds such as 1 $T$-$TaS_2$ [2].

### 1.4.2 Reciprocal space

Since the crystal structure of 1 $T$-TMDs is defined by the hexagonal unit cell, the reciprocal space Brillouin zone (BZ) shares the same symmetry and is shown in Figure 1.7. The $k_z = 0$ plane has three inequivalent high symmetry points; Γ at the zone centre, M and K which are situated at the centre-edge and corner of the zone respectively. The corresponding symmetry points on the uppermost $k_z$ plane are A, L and H [51]. The electronic structure and vibrational modes of the 1 $T$-TMDs in the following sections will be discussed with reference to this BZ symmetry.

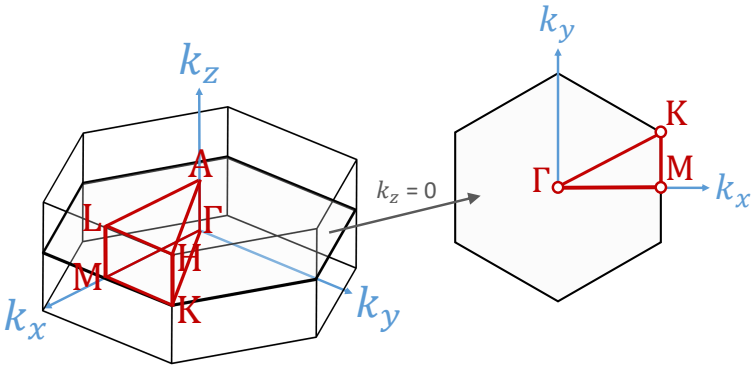


**Figure 1.7:** Three-dimensional hexagonal Brillouin zone (BZ) with high-symmetry points labelled. The grey shaded area is the $k_z = 0$ plane, which is also shown separately.

### 1.4.3 Electronic structure

Shown in Figure 1.8 is a simplified comparison of electronic structure in the 1 $T$-TMDs containing transition metals from groups-IV and -V of the periodic table (see Figure 1.5). In general, compounds from both groups are defined by a hole-like valence band (VB) derived from $p$-orbitals of the chalogen and electron-like conduction band (CB) derived from $d$-orbitals of the metal [16].

The group-IV TMDs (e.g. M = Ti, Zr, Hf) are either small band gap semiconductors (Zr, Hf) or semimetals (Ti) whereby the lowest energy CB of the latter sits close to the Fermi

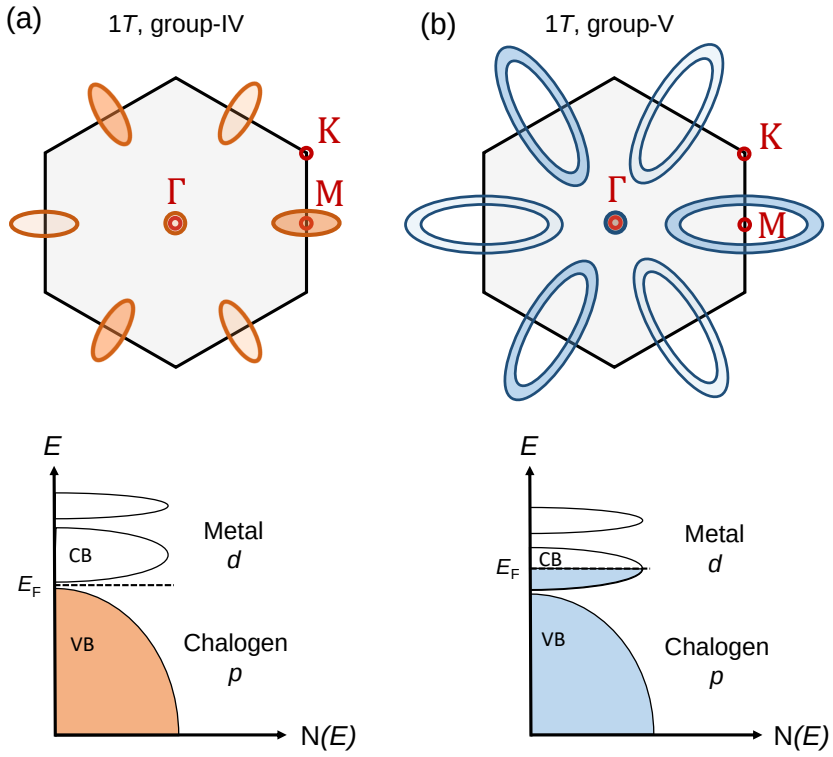


**Figure 1.8:** Electronic structure of 1 $T$-TMDs. Simplified sketch of the Fermi surface and density of states for (a) group-IV and (b) group-V transition metals, with the orbital character of the bands labelled. Here, the binding energy and width of the bands is only to illustrate the main differences between groups -IV and -V.

level and is partially occupied [51]. There is some disagreement between band structure calculations and various experimental results likely due to the subtle deviations from ideal stoichiometry in these compounds, which are usually overall electron doped [42]. In the Zr- and Hf-based compounds, the band gap varies in the range $\sim$ (0.5 - 1) eV. Whereas in the Ti-based compounds, the binding energy difference is typically smaller ($\sim$ 100 meV), and manifests as either a small band gap or overlap. By comparison, the group-V TMDs (e.g. M = V, Nb, Ta) are always metallic; there is no band gap and the lowest energy CB definitively crosses the Fermi level [51]. The Fermi surface (FS) of the 1 $T$-TMDs is characterised by elliptical electron pockets derived from the metal $d$-band at the $M$-point and hole pockets from the chalcogen $p$-band at the Γ-point, as illustrated in the upper panels of Figure 1.8. Depending on the specific compound, the top of the chalcogen $p$-band at Γ will either; just reach $E_F$ and therefore appears as a relatively small hole pocket, or it is located slightly below $E_F$ and is absent from the FS. Regardless, it is shown in the upper panels of Figure 1.8 for completeness. Due to the position of the metal band with

respect to $E_F$ in the group-IV and -V compounds, the electron pocket appears as either a small closed feature or a larger open ellipse respectively [50].

### 1.4.4 Lattice vibrations

Based on the crystal structure of the 1$T$-TMDs in Figure 1.6, there are three atoms per unit cell and the irreducible representations of the zone centre (Γ-point) vibrational modes are given by

$$\Gamma = A_{1g} + E_g(2) + 2A_{2u} + 2E_u(2), \tag{1.19}$$

using standard *Mulliken* notation [54]. $A$ indicates a non-degenerate mode which is symmetric about the principal rotation axis, whereas $E$ indicates a doubly degenerate mode. Subscript $g$ and $u$ indicates that the mode is either symmetric or asymmetric about the centre of inversion respectively, whilst the number indicates the symmetry about the principle axis. In total, there are nine vibrational modes which are summarised in Table 1.2 and the corresponding motion of the atoms within the crystal structure are shown in Figure 1.9.

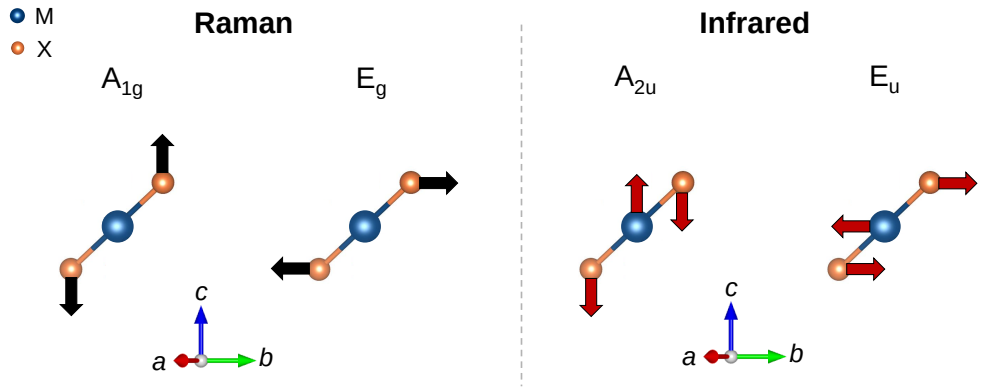


**Figure 1.9:** Lattice vibrations in 1$T$-TMDs. Sketch of the zone centre (Γ-point) Raman- and infrared-active modes with the corresponding motion of the transition metal (M) and chalogen (X) atoms in the crystal lattice as indicated by the arrows. Only atoms along one crystallographic direction are shown for simplicity.

Most importantly for the work in this thesis, there are two types of optical Raman-active phonon modes; namely $A_{1g}$ in which the chalcogen atoms move relative to each other along the z-direction, and $E_g$ in which the chalcogen atoms move in opposite directions either

along the $x$-direction or $y$-direction and hence is doubly-degenerate [55]. The remaining modes are infrared (IR) active.

| Representation | Acoustic | Optical | Activity | Direction |
|---|---|---|---|---|
| $A_{1g}$ | 0 | 1 | Raman | $z$ |
| $E_g$ | 0 | 1(2) | Raman | $x, y$ |
| $A_{2u}$ | 1 | 1 | IR | $z$ |
| $E_u$ | 1(2) | 1(2) | IR | $x, y$ |

**Table 1.2:** Zone centre (Γ-point) vibrational modes for 1 $T$-TMDs. The number of acoustic and optical modes relating to each representation are given with the degeneracy in parentheses.

# Chapter 2

## Experimental details

### 2.1 Theory of photoemission spectroscopy

Photoemission spectroscopy (PES) is a powerful experimental technique which is capable of directly determining the electronic and chemical state of solids by utilising simple energy and momentum conservation laws. Many properties of materials arise from their electronic structure and therefore, this technique has become ubiquitous amongst many research communities for the characterisation of novel materials, and to further advance our understanding of electronic phenomena.

#### 2.1.1 Photoelectric effect

The basic mechanism of photoemission spectroscopy relies on the *photoelectric effect*, a phenomenon which was first documented by Hertz in 1887 [56] and later explained by Einstein in 1905 [57] by famously considering the quantum nature of light. Simply, a photon incident on a sample surface that has greater energy than the work function of that specific material will cause an electron to be excited above the highest available energy level and emitted into the vacuum as illustrated in Figure 2.1.

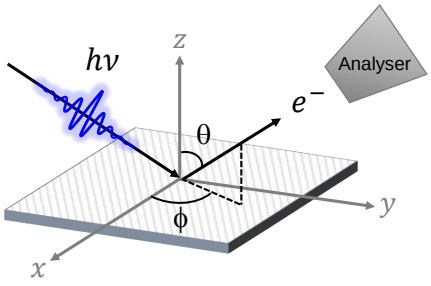


**Figure 2.1:** Sketch of the photoemission process. An incoming photon (E = $h\nu$) causes an electron to be emitted into the vacuum with kinetic energy, $E_{\mathrm{K}}$ at polar ($\theta$) and azimuthal ($\phi$) emission angles with respect to the sample surface normal.

The total energy is conserved in this process and it is possible to express the kinetic energy, $E_{\mathrm{K}}$ of the emitted *photoelectrons* as

$$E_{\mathrm{K}} = h\nu - E_{\mathrm{B}} - \Phi, \tag{2.1}$$

where $h\nu$ is the photon energy and $E_{\mathrm{B}}$ is the electron binding energy. The sample work function, $\Phi$ is the energy required for an electron to pass from the highest occupied level, $E_{\mathrm{F}}$ to the vacuum, $E_{\mathrm{v}}$ i.e. the energy required to overcome the sample-vacuum surface potential (typically 4 - 5 eV for metals) [58]. Hence, the kinetic energy of electrons in the solid prior to emission is simply $E_{\mathrm{K}} = h\nu - E_{\mathrm{B}}$. Equation 2.1 is central to the technique of photoemission spectroscopy as it allows determination of the binding energy of the electron within the solid via the measurable quantity of the outgoing kinetic energy in vacuum. Upon emission, the trajectory of electron can be defined by the polar, $\theta$ and azimuthal $\phi$ angles with respect to the sample surface as shown in Figure 2.1.

By considering the real-space momentum $\mathbf{P} = mv$, the kinetic energy of the emitted photoelectrons with mass, $m$ and velocity, $v$ is then given by

$$E_{\mathrm{K}} = \frac{1}{2}mv^2 = \frac{\mathbf{P}^2}{2m}, \tag{2.2}$$

and hence, the momentum can be written as a function of the kinetic energy:

$$\mathbf{P} = \sqrt{2mE_{\mathrm{K}}}. \tag{2.3}$$

### 2.1.2 Three-step model

Several theories have been proposed to describe the photoemission process, and are continually being refined by the research community. One such theory which has proven to be successful in explaining many of the physical aspects of experimental photoemission in solids is the *three-step model* proposed by Berglund and Spicer [59]. This purely phenomenological model decomposes the photoemission event into three independent steps:

(i) Optical excitation of an electron in the sample

(ii) Transport of the excited electron to the surface

(iii) Escape of the photoelectron into vacuum

and is depicted in Figure 2.2. Here, a complete description of the underlying theory of the three-step model will not be provided. Instead, the most relevant aspects related to each step [(i) - (iii)] of the photoemission process will be discussed in the context of experiment, based on the approach of Hüfner [58] and Damascelli [60]. In particular, there is a focus on the energy and momentum conservation laws which allows the properties of the electron in vacuum to be related to the initial state of the electron in the sample, which is central to the technique of photoemission spectroscopy.

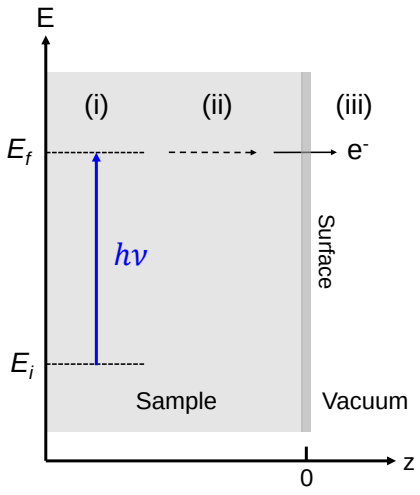


**Figure 2.2:** Sketch of the processes in the *three-step model* of photoemission, based on Ref. [60]. (i) An electron is optically excited from an initial state, $E_i$ to a final state, $E_f$ by a photon with energy $h\nu$. (ii) The electron is transported to the sample surface ($z$-direction) and must avoid inelastic scattering events. (iii) Escape of the photoelectron by traversing the sample-vacuum barrier and obeying energy and momentum conversation laws.

Two additional assumptions are required within the context of the model. The first is that an electron is considered as a *single non-interacting particle* and therefore cannot experience any internal or external perturbation. The second is the *sudden approximation* which assumes that the entire photoemission process [steps (i)-(iii)] occurs faster than the relaxation time of the excited state i.e. the emitted electron carries the final state energy and momentum.

### (i) Optical excitation of an electron in the sample

The first step considers the optical excitation of an electron in reciprocal space from an state initial ($i$) to a final ($f$) state by absorption of a photon. The difference between these states is the energy and momentum imparted by the photon, and hence the following conservation laws apply

$$E_f - E_i = h\nu, \tag{2.4}$$

$$\mathbf{k}_f - \mathbf{k}_i = \mathbf{k}_{h\nu}. \tag{2.5}$$

For typical photon energies used in PES experiments ($h\nu < 100$ eV), the photon carries negligible momentum ($\mathbf{k}_{h\nu} \rightarrow 0$) and hence the final and initial state momentum are the same, $\mathbf{k}_f = \mathbf{k}_i$ [60] according to Equation 2.5. Therefore, the electron undergoes a direct vertical transition in reciprocal space within the first Brillouin zone (BZ) of the *reduced zone scheme* as shown in Figure 2.3 and the final state energy is $E_f = E_i + h\nu$. However, an exactly equivalent energy-momentum transition can be considered in higher-order BZs of the *extended-zone scheme* by considering the momentum equal to the reciprocal lattice vector, $\mathbf{G}$ imparted by the crystal potential. Therefore, the conservation laws in Equations 2.4 and 2.5 can be more conveniently expressed in terms of the electron final state energy and momentum

$$E_f = E_i + h\nu, \tag{2.6}$$

$$\mathbf{k}_f = \mathbf{k}_i + \mathbf{G}, \tag{2.7}$$

whereby the absorption of a photon provides the energy required to reach the final state, and the crystal potential provides the momentum in multiples of the reciprocal lattice vector [61].

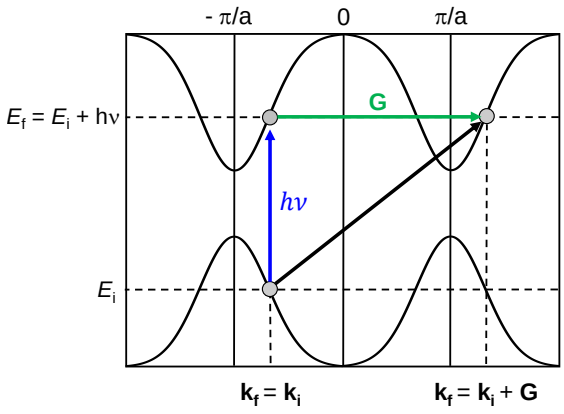


**Figure 2.3:** Initial ($i$) and final ($f$) electron states in reciprocal space, based on Ref. [60]. The photon imparts energy, $h\nu$ but negligible momentum ($\mathbf{k}_{h\nu} \rightarrow 0$) and hence only vertical transitions are allowed within the first Brillouin zone (BZ), or equivalently in higher-order BZs by a displacement of multiples of the reciprocal lattice vector, $\mathbf{G}$ provided by the crystal potential.

### (ii) Transport of the excited electron to the surface

Following photoexcitation, the electron must travel to the sample surface in order to be emitted. During this process, it may be inelastically scattered with sample impurities,

other electrons, or forms of excitation (e.g. phonons) and thus lose kinetic energy. Inelastically scattered electrons will reach the surface with a final state energy and momentum that can no longer be related to the initial state according to the conservation laws of Equations 2.4 and 2.5. Instead, these electrons will contribute to the background photoemission signal due to their broadened energy-momentum distribution.

Therefore, step (ii) of the model is concerned only with photoelectrons which reach the surface without undergoing an inelastic scattering event. The intensity of such photoelectrons is damped exponentially with distance, $d$ within the solid, and can be expressed in terms of the Beer-Lambert law [58]:

$$I(d) = I_0(d)e^{-d/\lambda(E_k)}, \tag{2.8}$$

where $I_0$ is the maximum intensity of the photoelectrons and $\lambda$ is the inelastic mean free path (IMFP), which is defined as the distance travelled by an electron before its intial intensity reaches $(1/e)I_0$. A simple analysis of Equation 2.8 reveals that $\sim$95% of the total photoemission intensity arises from within $3\lambda$ of the surface, and $\sim$65% within $\lambda$. As a result, PES is typically described as a highly surface-sensitive technique since only electrons originating near the surface can propagate towards the sample-vacuum interface in order to be emitted and detected, whilst still maintaining energy and momentum information of the initial state. The surface sensitivity of PES will be discussed further in Section 2.2.2.

**(iii) Escape of the photoelectron into vacuum**

As the electron reaches the surface, it must traverse the sample-vacuum barrier. The de Broglie relation $\mathbf{P} = \hbar\mathbf{K} = mv$ links the real-space momentum of an emitted electron to the total reciprocal space wavevector in the *vacuum*, $\mathbf{K} = (K_x, K_y, K_z)$. According to the geometry in Figure 2.1, the components parallel, $\mathbf{K}_\parallel$ and perpendicular, $\mathbf{K}_\perp$ to the sample surface can be written as

$$\mathbf{K}_\parallel = K_x + K_y, \tag{2.9}$$

$$\mathbf{K}_\perp = K_z, \tag{2.10}$$

and hence, the parallel and perpendicular wavevector components are related to the in-plane $(x, y)$ and out-of-plane $(z)$ momentum respectively.

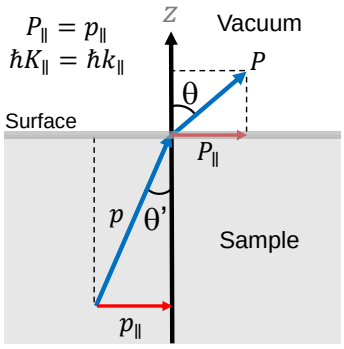


**Figure 2.4:** In-plane momentum conservation ($P_\parallel = p_\parallel$) of electrons at the interface between sample and vacuum based on Ref. [58].

Considering the diagram in Figure 2.4, the sample-vacuum interface does not perturb the in-plane translational symmetry and therefore the momentum parallel to the surface is conserved such that the wavevector of the outgoing photoelectron in the vacuum is the same as the wavevector of an electron propagating in the sample, $\mathbf{P}_\parallel = \mathbf{p}_\parallel$ [58]. The parallel components of the momentum vectors can then be expressed in terms of the angle to the surface normal:

$$\mathbf{P}_\parallel = \mathbf{P}\sin(\theta) = \mathbf{p}_\parallel = \mathbf{p}\sin(\theta'), \tag{2.11a}$$

$$\hbar\mathbf{k}_\parallel = \mathbf{P}\sin(\theta). \tag{2.11b}$$

Based on the momentum of the emitted electrons in Equation 2.3 and the conservation of the parallel components in Equation 2.11b, the momentum of an electron propagating within the sample, $\mathbf{k}_{||}$ can be expressed simply in terms of its kinetic energy after emission, $E_\mathrm{K}$ and the angle of its trajectory with the surface normal, $\theta$ as follows

$$\mathbf{k}_\parallel = \sqrt{\frac{2mE_\mathrm{K}}{\hbar^2}}\sin(\theta). \tag{2.12}$$

The fact that the momentum of electrons in the sample can be related to the measurable quantities $E_\mathrm{K}$ and $\theta$ by a simple conservation law forms the basis for the technique of angle-resolved photoemission spectroscopy (ARPES) as will be discussed in Section 2.2.

By contrast, the perpendicular component of the momentum, $\mathbf{k}_\perp$ is strictly not conserved due to the abrupt change in the potential at the sample-vacuum interface along the surface normal. However, it is possible to estimate the value of $\mathbf{k}_\perp$ by making a crude assumption of a nearly-free electron dispersion (Equation 1.4) for the final states which leads to

$$\mathbf{k}_\perp = \frac{1}{\hbar}\sqrt{2m(E_\mathrm{K}\cos^2(\theta) + V_0)}, \tag{2.13}$$

where $V_0 = E_0 + \Phi$ is the inner potential defined by the energy separation of the bottom of the valence band, $E_0$ to the vacuum level, $E_\mathrm{v}$ according to Figure 2.5. In most cases, an estimate for $V_0$ is made by comparison of experimental results with band structure calculations [60]. For materials with non-trivial Fermi surfaces, the assumption of a nearly-free electron dispersion is rather poor and as a result $\mathbf{k}_\perp$ remains ill-defined. As a result, PES is well suited for the study of quasi two-dimensional solids with an in-plane dispersion related to ($k_x$, $k_y$) determined by $\mathbf{k}_{||}$, but a negligible dispersion along $k_z$ and hence any uncertainty in $\mathbf{k}_\perp$ is less important.

### 2.1.3 Energy considerations

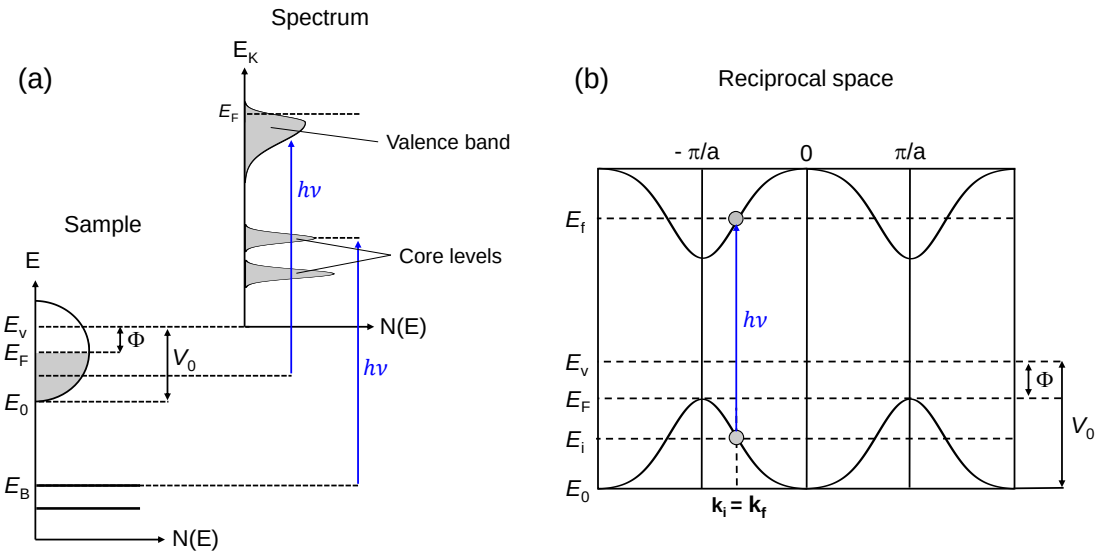


**Figure 2.5:** Energy diagrams based on Ref. [60] for electron states in (a) the sample with corresponding PES spectrum and (b) reciprocal space, where $E_\mathrm{v}$ is the vacuum level, $E_\mathrm{F}$ is the Fermi level, $E_\mathrm{B}$ is the electron binding energy and $E_0$ is the lowest energy of the valence band. h$\nu$ is the photon energy, $\Phi$ is the sample work function and $V_0$ is the inner potential. $E_\mathrm{i}$ and $E_\mathrm{f}$ are the initial and final state energies of the electron respectively.

Shown in Figure 2.5 is a sketch of the various energy levels relevant to PES as discussed throughout Sections 2.1.1 and 2.1.2. Specifically, Figure 2.5(a) shows energy levels within a sample and the corresponding PES spectrum which manifests as a series of bands with

predominantly Gaussian line-shapes at deeper binding energies (core levels) whereas the valence band is convoluted with the F-D distribution near the highest occupied level at $E_{\mathrm{F}}$. Figure 2.5(c) shows the relation of these energy levels to the reciprocal space electronic structure.

### 2.1.4 Spectral function

In the preceding sections, the three-step model was used to describe the energy and momentum of measured photoelectrons in a PES experiment. Here, an extension to this simple theory is presented and explains how the intensity of measured photoelectrons arises mainly from step (i) of the model due to the probability of optical transitions between initial and final states by absorption of a photon [58, 60]. Whilst maintaining the premise of the *sudden approximation*, a single particle in an *interacting many-body system* is now considered.

The optical excitation of an electron from the initial state to the final state is described by wavefunctions $\Psi_i^N$ and $\Psi_f^N$ of the N-electron system respectively. Within the limit of the *sudden approximation*, the optical excitation occurs instantaneously together with the emission of the electron in step (iii) of the three-step model and hence the initial and final states can be expressed in terms of the remaining N-1 electron system

$$\Psi_i^N = \phi_i \, \psi_i^{N-1}, \tag{2.14}$$

$$\Psi_f^N = \phi_f \, \psi_f^{N-1}, \tag{2.15}$$

where $\phi$ is the wavefunction of the single emitted photoelectron and $\psi^{N-1}$ is the wavefunction of the electron system after emission. The probability of a single particle transition is given by Fermi's golden rule

$$w_{f,i} = \frac{2\pi}{\hbar} \left| \left\langle \Psi_f^N \left| \hat{\mathbf{H}} \right| \Psi_i^N \right\rangle \right|^2 \delta\left(E_f^N - E_i^N - h\nu\right), \tag{2.16}$$

where the initial, $E_i^N$ and final state, $E_f^N$ energies are related to the binding energy, $E_{\mathrm{B}}$ of the electron in the sample and its outgoing kinetic energy, $E_{\mathrm{K}}$ after emission

$$E_i^N = E_i^{N-1} - E_B, \tag{2.17}$$

$$E_f^N = E_f^{N-1} + E_{\mathrm{K}}, \tag{2.18}$$

The electron excitation is caused by the interaction with a photon and therefore the perturbation of the system is described by the Hamiltonian

$$\hat{\mathbf{H}} = -\frac{e}{mc}\left(\mathbf{A}\cdot\mathbf{p}\right), \tag{2.19}$$

where $\mathbf{A}$ is the vector potential of the photon field and $\mathbf{p}$ is the electronic momentum operator. It is assumed that $\mathbf{A}$ is constant over atomic distances ($\nabla\cdot\mathbf{A}=0$) according to the electromagnetic dipole approximation. Within Equation 2.16, the transition matrix element is given by $\mathbf{M}_{f,i} = \left\langle \Psi_f^N \left| \hat{\mathbf{H}} \right| \Psi_i^N \right\rangle$ and can be written in terms of the initial and final state wavefunctions in Equations 2.14 and 2.15

$$\left\langle \Psi_f^N \left| \hat{\mathbf{H}} \right| \Psi_i^N \right\rangle = \left\langle \phi_f \left| \hat{\mathbf{H}} \right| \phi_i \right\rangle \left\langle \psi_f^{N-1} | \psi_i^{N-1} \right\rangle. \tag{2.20}$$

The total transition matrix element is then obtained by the sum over all possible final states, $s$ of the N-1 system $\psi_{f,s}^{N-1}$

$$\left\langle \Psi_f^N \left| \hat{\mathbf{H}} \right| \Psi_i^N \right\rangle_s = \left\langle \phi_f \left| \hat{\mathbf{H}} \right| \phi_i \right\rangle \sum_s \left\langle \psi_{f,s}^{N-1} | \psi_i^{N-1} \right\rangle. \tag{2.21}$$

Based on the transition probability for a single particle in Equation 2.16, it follows that the total intensity of emitted photoelectrons is then given by the sum over all transitions; $I = \sum_{f,i} w_{f,i}$ and hence using the total matrix element derived in Equation 2.21 and the final state energy in Equation 2.18, we obtain

$$I \propto \sum_{f,i} \left| \left\langle \phi_f \left| \hat{\mathbf{H}} \right| \phi_i \right\rangle \right|^2 \sum_s \left| \left\langle \psi_{f,s}^{N-1} | \psi_i^{N-1} \right\rangle \right|^2 \delta\left( E_{f,s}^{N-1} + E_{\mathrm{K}} - E_i^N - h\nu \right), \tag{2.22a}$$

$$I \propto \sum_{f,i} |M_{f,i}|^2 \, A(\mathbf{k}, E). \tag{2.22b}$$

Where $M_{f,i} = \left\langle \phi_f \left| \hat{\mathbf{H}} \right| \phi_i \right\rangle$ is the single particle dipole matrix element, and $A(\mathbf{k}, E)$ is the *spectral function* which can be can be linked to the imaginary part of the Green's function, $A(\mathbf{k}, E) = (1/\pi)\mathrm{Im}[G(\mathbf{k}, E)]$ [60]. In a single particle non-interacting system, the spectral function is an infinitely sharp delta function. Instead, in the presence of many-body interactions there is renormalization induced by the complex self-energy, $\Sigma(\mathbf{k}, E) = \Sigma^{'}(\mathbf{k}, E) + i\Sigma^{''}(\mathbf{k}, E)$ which describes all the possible fundamental interactions within the solid. Hence, this leads to corrections of the Green's and spectral function as follows

$$G(\mathbf{k}, E) = \frac{1}{E - E_0 - \Sigma(\mathbf{k}, E)}, \tag{2.23}$$

$$A(\mathbf{k}, E) = -\frac{1}{\pi} \frac{\Sigma''(\mathbf{k}, E)}{[E - E_0 - \Sigma'(\mathbf{k}, E)]^2 + \Sigma''(\mathbf{k}, E)^2}, \tag{2.24}$$

where $E_0$ is the single particle non-interacting energy of the system. The result of the many-body interactions is therefore to induce a Lorentzian broadening of the spectral function via the self energy.

Based on Equation 2.22b, the total measured intensity of photoelectrons in an PES experiment can be expressed simply as

$$I(\mathbf{k}, E) = I_0(\mathbf{k}, E, h\nu) f(E) A(\mathbf{k}, E). \tag{2.25}$$

The initial intensity is proportional to the single particle matrix element, $I_0(\mathbf{k}, E, h\nu) \propto |M_{f,i}|^2$ and therefore depends on the electron momentum, incident photon energy, and polarisation. Inclusion of the Fermi-Dirac distribution, $f(E)$ governs that only occupied states can be measured. Finally, the spectral function, $A(\mathbf{k}, E)$ contains all the energy and momentum information of the measured electrons in the presence of many-body interactions.

## 2.2 Angle-resolved photoemission spectroscopy (ARPES)

ARPES is a variant of photoemission spectroscopy which utilises the angular dependence of emitted photoelectrons in order to map the electronic dispersion in both energy and momentum. It is usually associated with the study of electron states with binding energies within several eV of the Fermi level ($E_\mathrm{B} < 5$ eV) and in particular there is a focus on the valence states closest to $E_\mathrm{F}$ since they are responsible for the electronic and optical properties of solids.

Simply, the technique involves measurement of the emitted electron kinetic energy, $\mathrm{E_K}$ as a function of emission angle, $\theta$. According to Equations 2.1 and 2.12, these quantities allow the electron binding energy, $E_\mathrm{B}$ versus the parallel wavevector $\mathbf{k}_{||}$ to be determined i.e. the electronic dispersion, $E(\mathbf{k}_{||})$ along a specific direction of reciprocal space.

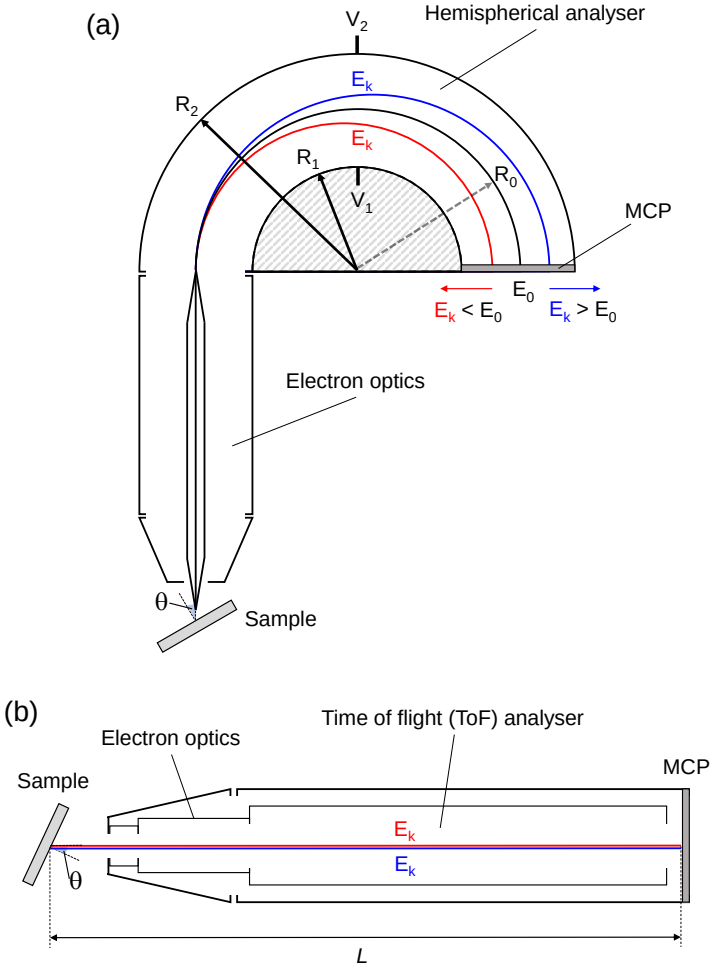


**Figure 2.6:** Kinetic energy analysers. (a) Hemispherical analyser which operates by deflecting electron trajectories according to their energy using an electric field between plates with voltage $V_1$ and $V_2$ (b) Time of flight (ToF) analyser which measures the time, $t$ for electrons to travel a fixed distance, $L$. Detection of electrons is made using a multi-channel plate (MCP).

Detection of photoelectrons in many conventional photoemission experiments is made using a hemispherical analyser as shown in Figure 2.6(a). The kinetic energy is measured by dispersing the radial trajectory of electrons using applied potentials $V_1$ and $V_2$ between two adjacent hemispheres of radii $R_1$ and $R_2$ respectively. The radial dependence of the electric field across the analyser is then

$$E(r) = \frac{(V_2 - V_1)R_1R_2}{(R_1 - R_2)}\frac{1}{r^2}, \tag{2.26}$$

where $r$ is the radius measured from the centre of the analyser, $R_0 = (R_1 + R_2)/2$.

Electrons with kinetic energy, $E_{\mathrm{K}} = E_0$ will follow a circular path with constant radius $R_0$ as illustrated by the black trajectory in Figure 2.6(a). $E_0$ is referred to as the *pass energy* [62] which is controlled by the pass voltage, $V_0$ according to $E_0 = eV_0$ and the radial dependence of the potential is

$$V(r) = \frac{V_0 R_0}{r}. \tag{2.27}$$

It is therefore possible to show [63] that the difference between applied potentials across the hemispheres of the analyser, $V_1$ and $V_2$ is given by

$$V_2 - V_1 = V_0 \left( \frac{R_2}{R_1} - \frac{R_1}{R_2} \right), \tag{2.28}$$

which can be used to select electrons with kinetic energy, $E_{\mathrm{K}} = E_0 = eV_0$ according to

$$e\left(V_2 - V_1\right) = eV_0 \left( \frac{R_2}{R_1} - \frac{R_1}{R_2} \right). \tag{2.29}$$

The sketch in Figure 2.6(a) shows an example of a simple hemispherical analyser which measures only the kinetic energy by dispersing electrons along one dimension of the detector. The emission angle, $\theta$ is then varied by rotating either the sample or analyser with respect to each other. However, more complex hemispherical analysers operate with a two-dimensional (2D) detector whereby the kinetic energy and angular dependence are recorded simultaneously along each axis of the 2D detector. This is achieved by using an entrance slit with finite acceptance angle $\Delta\theta$. Using this method, the complete range of $E_{\mathrm{k}}$ versus $\theta$ is obtained in a single scan without the need for rotation. An alternative type of detector is the time of flight (ToF) energy analyser as shown in Figure 2.6(b). The kinetic energy of electrons with mass, $m_e$ is simply determined by measuring the time taken, $t$ to travel a fixed length, $L$ within the analyser [64] as follows

$$E_{\mathrm{K}} = m_e L^2 / 2t^2. \tag{2.30}$$

### 2.2.1 Experimental setup

The ARPES measurements presented in this thesis were carried out at the Bristol NanoESCA facility (see Figure 2.7) which is situated in the ultra-quiet laboratories of the

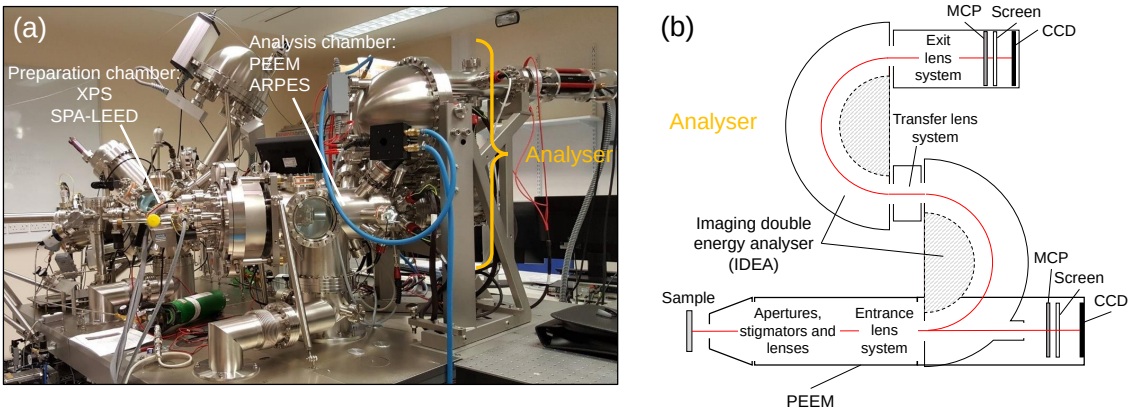


**Figure 2.7:** Experimental setup of the Bristol NanoESCA facility. (a) Image of the Scienta Omicron NanoESCA II system. (b) Schematic of the energy analyser consisting of the PEEM column and imaging double energy analyser (IDEA) which allows switching between real-space (PEEM) and $k$-space (ARPES) imaging mode whilst maintaining the same region of interest on the sample.

Centre for Nanoscience and Quantum Information (NSQI), University of Bristol. The instrument is a Scienta Omicron NanoESCA II equipped with a monochromated He lamp source with He-I$\alpha$ (21.2 eV) and He-II$\alpha$ (40.8 eV) emission. The system is capable of switching between real-space photoemission electron microscopy (PEEM) mode and micron-scale $k$-space imaging ($\mu$-ARPES) whilst maintaining the same region of interest on the sample. This makes it possible to acquire both real-space and $k$-space information from small or complex samples with excellent stability and precision.

The PEEM field of view is (3 - 1100) $\mu$m and has a best possible lateral resolution of $\sim$ 13 nm. This mode allows binding energy or work function mapping of the sample surface in real-space. In addition, it can be used to explore regions of sample which may be suitable for ARPES based on the surface topology, presence of impurities or contamination.

The system allows for measurement of full wavevector ARPES (simultaneous $k_x$, $k_y$) in a single scan at fixed energy. Therefore, the full electron dispersion is constructed by recording an individual ($k_x$, $k_y$) image at each specified binding energy. Collection of photoelectrons is possible over the full solid angle, $\Delta\theta \pm 90°$ according to the geometry in Figure 2.1. For photon energy $h\nu = 21.2$ eV and assuming a typical work function $\Phi = 4.5$ eV, the full solid angle corresponds to a momentum range of ($k_x$, $k_y$) $\approx \pm$ 2.1 Å$^{-1}$ for electrons at the Fermi level ($E_\mathrm{B} = 0$) based on Equations 2.1 and 2.12, which is sufficient to access the entire BZ of many materials. ARPES measurements of micron-

sized regions (min. 3 $\mu$m) is achieved by closing an aperture to the analyser. The region of interest can easily be selected by closing the aperture in real-space PEEM mode before switching to $k$-space imaging mode. Thus, it is possible to study monolayer or few-layer samples of exfoliated 2D materials (often $< 20$ $\mu$m lateral size) such as TMDs [65]. For the measurements presented in this thesis, the $\mu$-ARPES capability is predominantly used to select a clean, flat region of the sample to study. The photoelectron detection operates with an electrostatic PEEM entrance lens followed by two hemispherical energy analysers called the imaging double energy analyser (IDEA) which compensates for spherical aberration [66]. The overall system has a maximum possible energy and momentum resolution of $\sim$ 20 meV and 0.02 Å$^{-1}$ respectively.

For ARPES, the sample is situated in the analysis chamber (see Figure 2.7(a)) with a base pressure of $< 1{\times}10^{-10}$ mbar. It is attached to the cold head of a liquid helium (LHe) flow cryostat which is capable of achieving a minimum temperature of $\sim$ 30 K. Manipulation of the sample orientation is possible with $(x, y, z)$ translation, azimuthal angle and tilt. An adjacent preparation chamber is used for annealing and other sample processing, in addition to spot profile analysis low energy electron diffraction (SPA-LEED). It is equipped with an Al-K$\alpha$ source ($h\nu = 1486.7$ eV) and energy analyser for x-ray photoelectron spectroscopy (XPS).

### 2.2.2 Technical aspects

#### Surface sensitivity

The inelastic mean free path (IMFP), $\lambda$ previously defined in Equation 2.8, depends on the kinetic energy of electrons within the solid and by the measurement of a large number of chemical elements, a so-called *universal curve* has been determined. Shown in Figure 2.8 is a plot of the IMFP as a function of kinetic energy using the *universal curve* formula described in Ref. [67]. Since the kinetic energy of electrons in the solid depends primarily on the incoming photon energy ($E_\mathrm{K} = h\nu - E_B$), the IMFP is commonly used to estimate the surface sensitivity offered by various photon sources. The vertical lines in Figure 2.8 indicate the IMFP corresponding to the expected kinetic energy of electrons within the solid that originated from the Fermi level ($E_B = 0$) after interaction with photons from the specific sources used in this thesis.

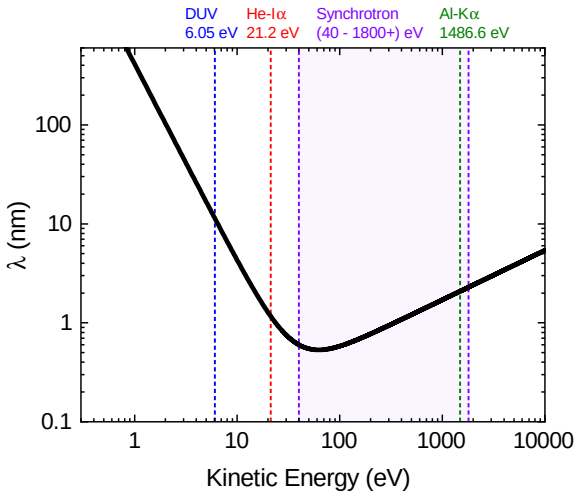


**Figure 2.8:** The *universal curve* of inelastic mean free path (IMFP), $\lambda$ for electrons as a function of kinetic energy in the solid, according to Ref. [67]. The vertical lines show the maximum kinetic energy for electrons at the Fermi level ($E_B = 0$) after interaction with incoming photons of specific energies from sources used this thesis.

### Sample conditions

Rigorous control of the sample conditions are crucial in PES experiments. The surface needs to be extremely clean, flat and free of oxidation.

Firstly, the conservation of parallel momentum in Equation 2.12 within step (iii) of the three-step model depends on in-plane translational symmetry arguments and therefore if the surface is not entirely flat, this equation no longer holds which leads to some uncertainty in the emitted photoelectron momentum.

A high density of defects or impurities in the sample may increase the likelihood of inelastic scattering events during transport of the excited electron to the surface. A similar effect may occur for contamination at the surface or damage induced by oxidation as the sample crosses the sample-surface barrier. Within step (ii) of the three-step model, such events will broaden the energy-momentum distribution of electrons and increase the incoherent photoemission background signal.

In addition, any change to the chemistry of the surface, such as contamination or oxidation, can influence binding energies and lineshapes of electronic states as well as potentially inducing new features (e.g. alternative oxidation states) due to doping effects or a change in the local atomic bonding.

As previously discussed, the majority of detected photoelectrons originate from within several nanometres of the sample surface (see Figure 2.8) hence the extreme surface sensitivity means that the sample conditions described above are of even greater importance. As a result, PES experiments are typically and routinely performed in ultra-high vacuum (UHV) conditions with pressures $\leq 1{\times}10^{-10}$ mbar in order to maintain the sample sur-

face condition, in addition to preventing the scattering of electrons with the atmosphere before reaching the detector. Samples are usually cleaved *in situ* to expose a clean, flat surface. For the case of the layered TMDs, this process is straight forward due to the crystal structure and weak van der Waals bonding between layers.

Finally, samples must be mounted onto electrically conductive substrates or sample holders with suitable adhesive, and connected to electrical ground. The samples should also ideally be reasonable conductors. This is imperative to avoid charging effects which occurs when emitted electrons cannot be replenished via grounding, thus resulting in a net charge on the sample [58]. It is important to note that the sample and energy analyser (spectrometer) will typically be connected to a common electrical ground, meaning they will share the same work function. Hence $\Phi$ in Equation 2.1 is usually taken to be the spectrometer work function.

To achieve the highest energy resolution, the sample is usually cooled to reduce the effect of thermal broadening on the electron states according to Equation 2.25.

## 2.3 X-ray photoelectron spectroscopy (XPS)

X-ray photoelectron spectroscopy (XPS) a variant of photoemission spectroscopy most often associated with the study of electron core levels at deep binding energies, although a range anywhere from the valence states up to the maximum allowed by the photon energy is common ($E_{\mathrm{B}}$ = 0 - 1000 s eV). The technique of XPS depends on the basic photoemission concepts outlined previously in Section 2.1. However, unlike ARPES where the angular-dependence is used to map the electronic dispersion, XPS is often performed at a fixed angle and a spectrum of the intensity of emission as a function of binding energy is determined.

The focus of XPS is to study spectral characteristics of electron core levels such as relative peak intensities, binding energy positions, and linewidth/lineshape. This allows physical or chemical aspects of the sample, including composition, stoichiometry, contamination, impurities and local bonding of atoms, to be determined.

The XPS measurements in this thesis were performed either at the Bristol NanoESCA facility using a Al-K$\alpha$ x-ray source ($h\nu$ = 1486.7 eV) or at the Bending magnet for Emission, Absorption and Reflectivity (BEAR) end-station of the Elettra synchrotron with tunable radiation ($h\nu$ = 40 - 1600 eV) [68, 69]. Detection of photoelectrons in both cases was

performed with a hemispherical energy analyser similar to that sketched in Figure 2.6(a).

## 2.4 X-ray absorption spectroscopy (XAS)

Similar to the other x-ray spectroscopy techniques outlined so far in Sections 2.2 and 2.3, x-ray absorption spectroscopy (XAS) relies fundamentally on the photoelectric effect and is mainly concerned with core level electrons. In the intermediate step before photoemission, a photon is first absorbed by a core electron with particular binding energy and promoted to an unoccupied state, leaving behind a core hole [70, 71]. The excess energy is given to the core electron and it is emitted into the vacuum, whilst the core hole is extremely short-lived ($\sim$ 1 - 2 fs) before it recombines with a higher-energy electron and emits a photon or an Auger electron.

The technique of XAS relies on the absorption step before photoemission. By performing measurements as a function of incident photon energy, a sharp rise in the absorption will occur near the binding energies of each core level. This rise is typically referred to as an absorption *edge* and the nomenclature is based on the principle quantum number, $n$ of the core level where $n = 1$, 2 and 3 correspond to the K-, L- and M-edges respectively. Similar to XPS, these levels are element specific and the characteristic absorption spectrum will depend on the physical or chemical aspects of the sample which may alter the binding energy and lineshape of these features.

The XAS measurements in this thesis (Section 4.3.2) were performed at the BEAR end station, Elettra synchrotron. Absorption spectra were obtained using the total electron yield (TEY) method, whereby the drain current on the sample is monitored as a function of the incident photon energy [72].

## 2.5 Time- and angle-resolved photoemission spectroscopy (TR-ARPES)

Time- and angle-resolved photoemission spectroscopy (TR-ARPES) is a variant of the techniques described in Section 2.2, which utilises ultrashort laser pulses to monitor the electron dynamics in solids in real time. Essentially, TR-ARPES is a form of pump-probe spectroscopy which directly monitors changes to the electron dispersion following perturbation from an intense laser pulse.

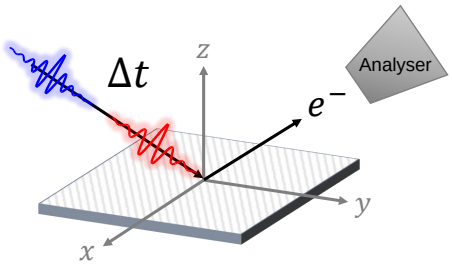


**Figure 2.9:** Sketch of time- and angle-resolved photoemission (TR-ARPES) spectroscopy. Arrival of the pump pulse (red) perturbs the system, which is followed at some later time, $\Delta t$ by the probe pulse (blue) with sufficient energy to cause photoemission.

In order to gain sufficient time-resolution, a source of temporally short light pulses is required. Therefore, ultrafast laser systems are typically used which can provide pulses on the order of tens to hundreds of femtoseconds (1 fs = $10^{-15}$ s). Various probe photon energies can be achieved from ultraviolet in the range (6 - 40) eV using harmonic generation. Each method of pulse generation has various advantages and disadvantages in terms of the ultimate time and energy resolution, sample probing depth and the accessible range of $\mathbf{k}_{||}$. An illustration of the photoemission process in TR-ARPES is shown in Figure 2.9.

First, the arrival of a pump pulse perturbs the electronic system, which is followed at some later time, $\Delta t$ by a probe pulse with an energy larger than the sample work function and therefore sufficient to cause photoemission. The emission angle and kinetic energy of the photoelectrons is monitored by an analyser in the same way as described in Section 2.2. As a result, the probe pulse effectively measures a "snapshot" of the electron dispersion at a time $\Delta t$ after the pump pulse arrival. By varying the time delay, $\Delta t$ between pump and probe pulses, the time evolution of the photoemission spectra can be obtained, as illustrated in Figure 2.10.

The influence of the pump pulse can excite carriers from the occupied to unoccupied states by inducing electronic transitions related to the pump photon energy. This is illustrated in the sketch shown in Figure 2.10(a) where the weak outline of an upward dispersing conduction band (CB) can be seen as it becomes populated shortly after the pump arrival (+ 100 fs). Simultaneously, there is rapid depletion of the normally occupied states highlighted by the downward arrow in the EDCs of Figure 2.10(b). In addition, a significant out-of-equilibrium distribution of electrons is created, which manifests in experiment as a broadening of the states around the Fermi level highlighted by the upward arrow in Figure 2.10(b). The effective electron temperature can often reach $T_{\text{eff}} > 1000$ K based on analysis of the Fermi level width using Equation 1.7. Usually, a slower relaxation of $>$ 1ps occurs back to the initial condition (e.g. - 200 fs in Figure 2.10).

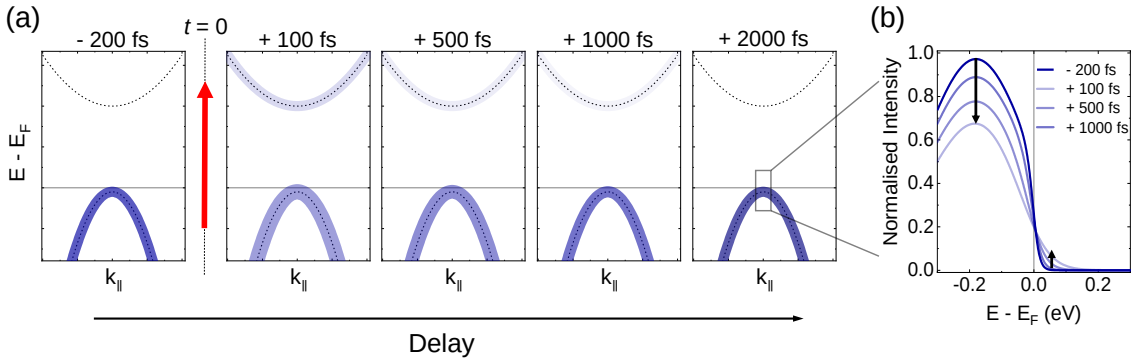


**Figure 2.10:** Time evolution of TR-ARPES spectra. (a) Sketch of the electronic dispersion. The red arrow indicates the arrival of the pump pulse at time $t = 0$. Weak intensity of a band above $E_F$ can be seen as it becomes transiently populated. (b) Sketch of EDCs showing the depletion of occupied states and simultaneous broadening of the Fermi level due to increased effective electron temperature.

### 2.5.1 Experimental setup

The TR-ARPES setup used for the work in this thesis is situated in the Ultrafast Photoemission and Optical Spectroscopy (UPhOS) laboratory at Politecnico di Milano and is described at length in Ref. [73]. To summarise, it is based on a high-repetition rate (100 KHz) Ytterbium (Yb) laser system (*Pharos*, Light Conversion) and utilises nonlinear optical processes in order to generate ultrashort visible pump pulses (1.82 eV, 30 fs), and deep ultraviolet (DUV) probe pulses (6.05 eV, 65 fs) for photoemission. The high repetition rate and excellent stability of the Yb-based laser allows the collection of photoemission data with a large signal-to-noise ratio in relatively short acquisition times whilst also avoiding space-charge effects, a problem which commonly affects low repetition rate systems [74,75]. In addition, the system allows for a great range of tunability of the pump pulse in the range (1.45 – 2) eV, whilst still maintaining an excellent overall temporal and energy resolution of 85 fs and 53 meV respectively, when compared to other setups [76,77].

A schematic of the optical setup for the generation of pump and probe pulses is presented in Figure 2.11(a). The 100 KHz Yb-based laser is used as the source which operates at 6W and outputs a fundamental frequency (FF) of 1028 nm (1.20 eV, 290 fs). Part of the FF is used to supply a non-collinear optical parametric amplifier (NOPA) which relies on generation of a white light super-continuum through a YAG plate, second harmonic generation (SHG) processes via $\beta$-barium-borate (BBO) crystals, and a prism-pair compression system in order to produce pulses centred at 680 nm (1.82 eV) with 23 fs duration. Part

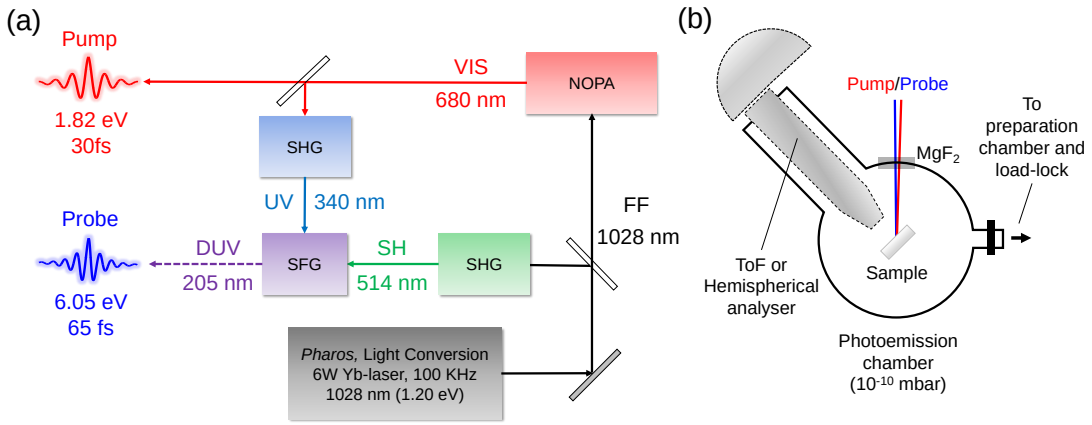


**Figure 2.11:** Setup for time- and angle-resolved photoemission spectroscopy (TR-ARPES) at Politecnico di Milano. (a) Schematic of the optical setup for the generation of pump (1.85 eV, 30 fs) and probe (6.05 eV, 65 fs) pulses based on a 100 KHz Ytterbium (Yb) laser system. (b) The sample is mounted on the cold head of a cryostat inside a UHV chamber. Pump and probe beams enter through a $MgF_2$ window. Photoelectrons are detected using either a time-of-flight (ToF) or hemispherical energy analyser.

of this output is used as the pump pulse for TR-ARPES by passing through a dielectric beam-splitter which broadens the pulse duration slightly to $\sim$ 30 fs. The remainder of the beam is used to generate the second harmonic (SH) at 340 nm (ultraviolet, UV). This is then combined with the 514 nm SH of the original FF via sum frequency generation (SFG) in order to generate the deep ultraviolet (DUV) probe pulses for TR-ARPES at 205 nm (6.05 eV) with 65 fs duration. The time evolution of the photoemission spectrum was measured by varying the time delay between the arrival of pump and probe pulses using a motorised delay stage with a minimum possible step size of 3.33 fs. For sufficient data quality, an average over multiple cycles of a chosen integration time are made at each pump-probe delay. The pump and probe spot sizes are approximately 100 $\mu$m and 50 $\mu$m diameter respectively such that probe measures a homogeneously excited region of the sample.

An illustration of the most relevant features of the experimental apparatus are shown in Figure 2.11(b). Photoemission experiments take place inside a UHV chamber with a base pressure of $\sim 10^{-10}$ mbar and is constructed entirely of $\mu$-metal in order to screen external magnetic fields which may otherwise interfere with the emitted electron trajectories [64]. The sample is mounted on the cold head of a cryostat (10 – 500 K) which can be manipulated with $(x, y, z)$ translation as well as tilt and rotation. Both pump

and probe beams enter through a 2 mm $MgF_2$ window, and the probe beam impinges on the sample at 45° with respect to the analyser axis. Detection of photoelectrons is performed using either a home-built time of flight (ToF) spectrometer (described in Ref. [64]) or a commercial SPECS PHOIBOS 100 2D hemispherical energy analyser for the results presented in Chapters 5 and 7 respectively. The operation of each type of energy analyser is described in Section 2.2. Using the ToF spectrometer, the electronic dispersion is measured by rotating the angle, $\theta$ of the sample with respect to the sample-analyser normal according to Equation 2.12. Instead, the hemispherical analyser is equipped with a 2D CMOS detector which simultaneously measures the kinetic energy and the angular dependence of emitted electrons up to $\pm$ 15° acceptance angle and therefore the total allowed $E(\mathbf{k}_{||})$ window is obtained without sample rotation. The ToF and hemispherical analyser have a minimum possible energy resolution of ~10 meV (for $E_K \approx 2$ eV [64]) and 3 meV respectively. However, the typical experimental energy resolution achieved is (40 - 60) meV, primarily due to the energy broadening associated with temporally short laser pulses [64, 73]. The most significant advantage of the hemispherical analyser is the acquisition of multiple emission angles which drastically reduces experiment times since the total allowed electron dispersion can be obtained in a single scan at each pump-probe delay. By comparison, the ToF records only a single angle at each pump-probe delay and therefore to obtain the temporal evolution of the full electron dispersion would require an order of magnitude greater experiment time. Hence, the ToF is rarely used in this way but instead the pump-probe dynamics are measured at a single fixed angle of relevance. Another advantage of using the hemispherical analyser is that the probe laser beam remains focussed on an identical region of the sample throughout the measurements since no rotation is necessary. Instead, when using the ToF, if the sample is not exactly at the centre of rotation, then the probe beam can move slightly across the sample surface when sweeping the emission angle, $\theta$. This may lead to some asymmetries in the measured electron dispersion if the sample surface is not homogeneous.

The general experimental conditions outlined in this section such as the photon energies and pulse duration were kept constant for all experiments presented in this thesis. However, to study the properties of materials in different phases, the sample temperature was varied using the cryostat. In addition, to investigate the response of materials to varying levels of perturbation induced by the pump pulse, the laser power incident on the sample was controlled using a neutral-density filter and measured with an optometer. It is

usually more meaningful to define the energy deposited per unit area, known as the laser fluence which is calculated using $F = P/RA$, where $P$ is the measured laser power, $R$ is the laser repetition rate and $A = \pi(d/2)^2$ is the area of the laser spot with diameter, $d$ on the sample. The spot size was measured with a beam profiler placed at the pump-probe overlap position, after deflecting the pump and probe beams with a flip mirror located just before the vacuum chamber.

### 2.5.2 Technical aspects

The typical work function of metals are $\sim$ (4 - 5) eV and hence a probe photon energy of 6.05 eV allows access to a theoretical maximum of $\mathbf{k}_{||} \approx \pm$ 0.6 Å$^{-1}$ of the BZ for an electron at the Fermi level ($E_\mathrm{B} = 0$) based on Equations 2.1 and 2.12. This is further reduced to $\mathbf{k}_{||} \approx \pm$ 0.2 Å$^{-1}$ considering the $\pm 15°$ acceptance angle of the energy analyser. The relatively limited range of momentum space means that the TR-ARPES setup presented here is suitable for studies of the electronic structure close to the BZ centre only.

It is also important to note that the 6.05 eV probe photon energy offers a much greater bulk sensitivity when compared to other ARPES techniques which commonly utilise higher photon energies. As shown in Figure 2.8, the IMFP becomes large for electrons with low kinetic energy ($E_\mathrm{K} < 10$ eV) and is particularly energy-dependent in that range. An estimate of the IMFP for electrons close to the Fermi level ($E_\mathrm{B} = 0$) that are emitted by 6.05 eV photons is $\lambda \approx$ (11 - 12) nm, which is an order of magnitude greater than using a He-I$\alpha$ source ($h\nu = 21.2$ eV) of around $\sim$ 1 nm for comparison. This bulk sensitivity increases even further for electrons at deeper (more positive) binding energies, as the emitted kinetic energy will be even lower according to $E_\mathrm{K} = h\nu - E_\mathrm{B}$.

## 2.6 Time-resolved reflectivity (TRR)

Time-resolved optical spectroscopy techniques such as transient absorption and reflectivity are used to study the dynamics of electronic excitations in materials [78]. It is based on a pump-probe scheme whereby an optical pump pulse first perturbs the system followed by an optical probe pulse that measures a property of the system at a later time, $\Delta t$. Experiments on metallic samples are typically performed by measuring the reflected probe intensity, and often represented by the change in reflectivity over the absolute value, $\Delta R/R$

The characteristics of the reflectivity signal will arise due to a combination of processes

related to electronic excitations induced by the pump, and their subsequent relaxation to the initial state via various interactions. Since the energy-momentum distribution of electrons cannot be directly visualised, the technique is less direct than TR-ARPES (see Section 2.5). Therefore, interpretation of the data typically requires a prior knowledge of the electronic band structure of the material, particularly in relation to the pump photon energy which dictates the allowed electronic transitions and if there are any possible resonance effects.

### 2.6.1 Experimental setup

Two different experimental TRR setups were used for the work in this thesis and are described separately in the following.

The work in Chapter 5 relied on a direct comparison between the fluence-dependent dynamics measured in TR-ARPES and TRR. As such, it was imperative that the optical excitation conditions in both experiments were as similar as possible [79]. Therefore, TRR was performed using the same (1.85 eV, 30 fs) pump pulse generated from the NOPA in the TR-ARPES setup described previously in Section 2.5.1. In this case, the (1.85 eV, 30 fs) output was used as both pump and probe, which impinged on the sample at 45° to the surface normal. Crossed polarisation was used in order to avoid interference effects. The reflected probe intensity was measured using a photodiode.

For the work in Chapter 7, TRR measurements were performed using a setup based on a Ti:sapphire laser (Coherent Libra) which outputs pulses (790 nm, 100 fs) at 2 KHz repetition rate. The laser drives two non-collinear parametric amplifiers (NOPA) serving as pump the probe beams. Each NOPA is pumped by the second harmonic of the laser fundamental and seeded by a white light continuum generated in a 1 mm thick sapphire plate which is then amplified in a $\beta$-barium borate (BBO) crystal. The amplified pulse is characterized by a broad spectral range (500 - 700 nm) and is compressed to $\sim$ 20 fs duration using chirp mirrors. The pump beam is modulated at 1 KHz using a mechanical chopper. The time delay between pump and probe is controlled by a mechanical delay stage, and both beams are focused onto the sample by a spherical mirror. The reflected probe beam is detected using a Si photodetector array which operates at the repetition rate of the laser.

As discussed in Section 2.5.1 with reference to the experimental TR-ARPES setup, the pump power in TRR was also controlled with a neutral-density filter, and the laser

fluence was determined in the same way. The spot size in TRR was either measured using the beam profiler as discussed previously, or the *knife-edge* method. The latter utilises a sharp edge mounted on a micrometer stage which is placed at a defined position between the focusing lens and the sample. As the edge cuts the beam, the reflected intensity is measured and the relationship gives the beam diameter [80]. Repeating the procedure at two distances from the sample allows the measured spot size to be extrapolated to the sample.

## 2.7 Raman spectroscopy

The effect of Raman scattering is named after C.V. Raman who made the first experimental observation of the inelastic scattering of light; "*a new radiation*" in 1928 [81] for which he later won the Nobel prize in Physics in 1930. It involves the interaction of a photon with some excitation within a material such that its outgoing energy is different to the incoming energy. Here, the theory will be discussed in the context of vibrational excitations and specifically optical phonons, which is one of the most commonly investigated types of excitation studied by Raman spectroscopy.

Shown in Figure 2.12 is a sketch of energy levels in a material and their relation to light scattering processes. An incoming photon excites the system from its initial state to some virtual state which depends on the photon energy, h$\nu$. This state is extremely short-lived and the system relaxes back to a lower energy by emitting a photon. The majority of light undergoes elastic (Rayleigh) scattering whereby the system relaxes to its original state via the emission of an outgoing photon of identical energy. Instead, a small proportion may experience inelastic (Raman) scattering whereby the system relaxes to a different state due to the interaction with a vibrational excitation. In this instance, the emitted photon will either be red-shifted as it loses energy (Stokes) or blue-shifted as it gains energy (anti-Stokes). Hence, this process allows the determination of the various vibrational state energies in a system by analysis of the change in photon energy after scattering from the material, known as Raman spectroscopy.

The intensity of Raman scattered light is extremely weak compared to the excitation intensity (ratio of $\sim 10^{-7}$ [82]). Therefore, high intensity sources such as lasers operating in the visible range of the spectrum are typically used. Scattering occurs in all directions away from the point of excitation, however many Raman spectroscopy techniques use

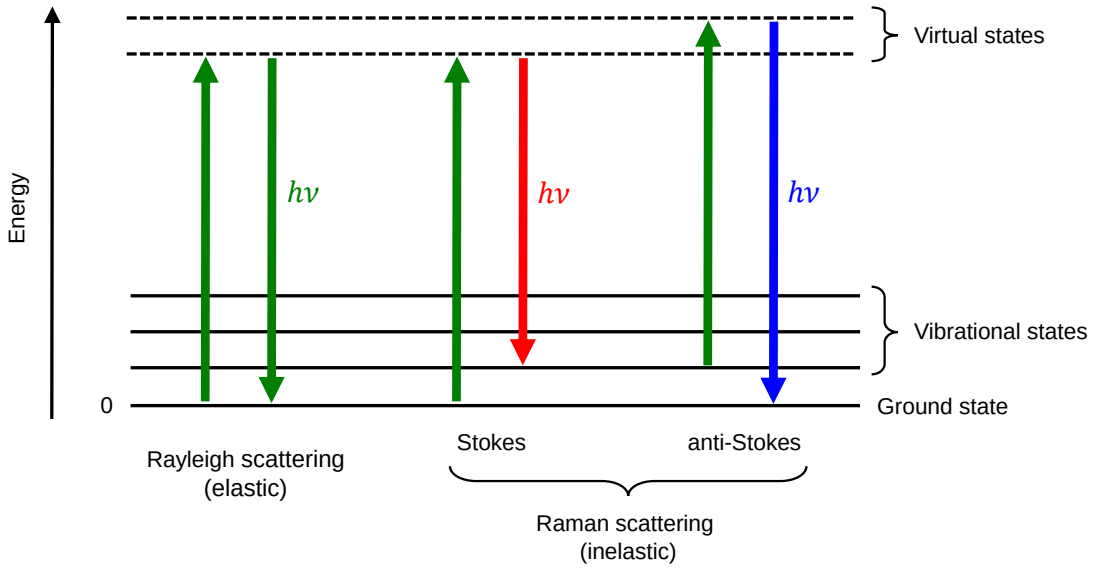


**Figure 2.12:** Sketch of the energy levels associated with light scattering processes. Rayleigh scattering is an elastic process in which the incoming and outgoing photon have the same energy. Raman scattering is an inelastic process in which the photon either loses (Stokes) or gains (anti-Stokes) energy by interaction with a vibrational state in relation to its original state.

*backscattering geometry* such that only the photons travelling directly back towards the source are detected.

### 2.7.1 Theory of light scattering

The mechanism of Raman scattering can be understood with a semi-classical theory that treats light as a wave of oscillating electric field which induces a displacement within a material. The energy-momentum transfer in this process is then described within a quantum mechanical context by considering allowed phonon modes interacting with photons.

The theory is presented here following the approach of Ref. [82]. For a particular phonon mode to be Raman-active there must be a change to the polarisability, $\mathbf{P}$ within a material upon interaction with incoming light with electric field, $\mathbf{E}$

$$\mathbf{P} = \epsilon_0 \chi \mathbf{E}, \tag{2.31}$$

where $\epsilon_0$ is the permittivity of free space and $\chi$ is the dielectric susceptibility of the material. The oscillating electric field of the incident light is given by

$$\mathbf{E}(\mathbf{r},t) = \mathbf{E}(\mathbf{k}_i,\nu_i)\cos\left(\mathbf{k}_i\cdot\mathbf{r} - \frac{\nu_i}{2\pi}t\right), \tag{2.32}$$

where $\nu_i$ is the frequency and $\mathbf{k}_i$ is the wavevector. Similarly, the resulting displacement in the material due to the phonon oscillation

$$\mathbf{u}(\mathbf{r},t) = \mathbf{u}(\mathbf{q},\omega)\cos(\mathbf{q}\cdot\mathbf{r} - \omega t), \tag{2.33}$$

where $\omega$ is the angular frequency ($\omega = 2\pi\nu$) and $\mathbf{q}$ is the wavevector of the phonon. Based on the assumption that the displacement, $\mathbf{u}(\mathbf{r},t)$ is small, it is possible to express the polarisability, $\mathbf{P}$ in terms Equations 2.32 and 2.33 via an expansion of $\chi$. The first-order Raman scattering term of this expression gives

$$\begin{aligned}\mathbf{P}(\mathbf{r},\mathbf{u},t) \propto & f(\mathbf{k}_i,\nu_i,\mathbf{q},\omega) \\ & \times\left\{\cos\left[(\mathbf{k}_i+\mathbf{q})\cdot\mathbf{r} - \left(\frac{\nu_i}{2\pi}+\omega\right)t\right] + \cos\left[(\mathbf{k}_i-\mathbf{q})\cdot\mathbf{r} - \left(\frac{\nu_i}{2\pi}-\omega\right)t\right]\right\},\end{aligned} \tag{2.34}$$

where $f(\mathbf{k}_i,\nu_i,\mathbf{q},\omega)$ is a function containing the Raman tensors which determine the amplitude of the various allowed modes via symmetry-derived selection rules. Most importantly, Equation 2.34 shows that the polarisability contains two oscillatory terms for scattered light given by the sum $\left(\frac{\nu_i}{2\pi}+\omega\right)$ and difference $\left(\frac{\nu_i}{2\pi}-\omega\right)$ of the photon and phonon frequencies. Similarly, there is a corresponding transfer of momentum either; $(\mathbf{k}_i+\mathbf{q})$ or $(\mathbf{k}_i-\mathbf{q})$. This suggests that scattered light will contain two types of outgoing photons which have either gained (+) or lost (-) energy and momentum by interaction with a particular phonon, and hence the following conservation laws can be written

$$h\nu_f = h\nu_i \pm \hbar\omega, \tag{2.35}$$

$$\mathbf{k}_f = \mathbf{k}_i \pm \mathbf{q}. \tag{2.36}$$

Phonon frequencies in most materials are orders of magnitude lower than the frequency of visible light and therefore based on Equation 2.35, the change in the photon frequency is very small i.e. the approximation $\nu_i = \nu_f$ can be made. The photon momenta is directly linked to its frequency and the refractive index, $n$ of the material by $\mathbf{k} = 2\pi n\nu/c$

and therefore based on the previous approximation, $\mathbf{k}_f \approx \mathbf{k}_i = \mathbf{k} = 2\pi n\nu/c$. From Equation 2.36, the phonon momentum is $|\mathbf{q}| = |\mathbf{k}_f - \mathbf{k}_i|$ and in a Raman experiment using *backscattering geometry*, whereby the outgoing photon travels directly back towards the source along the same path as the incoming photon, they have opposite momenta directions $\mathbf{k}_f = -\mathbf{k}$ and $\mathbf{k}_i = \mathbf{k}$ respectively which leads to

$$|\mathbf{q}| \approx |\mathbf{k}_f - \mathbf{k}_i| \approx 2\mathbf{k} \approx \frac{4\pi n\nu}{c}. \tag{2.37}$$

Using an example of excitation with visible light, the corresponding phonon momenta are of the order $\mathbf{q} \approx 10^7 \mathrm{m}^{-1}$ or $\sim 0.001$ Å$^{-1}$, which is very small in comparison to the size of a typical Brillouin zone [83]. Therefore, Raman scattering is usually associated with the study of zone-centre ($\Gamma$-point) phonons with wavevector, $\mathbf{q}/\mathbf{k}_{\mathrm{BZ}} \to 0$.

Using a full quantum mechanical treatment, it is possible to show that anti-Stokes scattering is much less likely to occur than the Stokes process and therefore the detected anti-Stokes intensity in experiments is typically much lower. As discussed previously, the anti-Stokes process requires the system to be initially in a vibrational state i.e. there is an initial population of phonons. The probability of phonon occupation of a particular state is dictated by Bose-Einstein statistics and therefore their total population depends on a thermal distribution. As a result, the ratio of Stokes, $I_{\mathrm{S}}$ to anti-Stokes, $I_{\mathrm{A}}$ intensities for a single mode can be written

$$\frac{I_{\mathrm{as}}}{I_{\mathrm{s}}} = \left(\frac{\frac{\nu_i}{2\pi} + \omega}{\frac{\nu_i}{2\pi} - \omega}\right)^4 \exp\left(-\frac{\hbar\omega}{kT}\right), \tag{2.38}$$

where is $\hbar\omega$ the energy of a particular phonon mode and $T$ is temperature.

Shown in Figure 2.13 is a sketch of a Raman spectrum highlighting the relative intensities between Stokes and anti-Stokes light scattering processes. Rayleigh scattering has orders of magnitude greater intensity than Raman scattering and is usually filtered in experiments to allow detection of the weak Raman signal. The Stokes and anti-Stokes signal will be symmetric about the zero-shift line and energy loss (Stokes) is usually referred to as positive shift. A pair of these Stokes and anti-Stokes lines will occur for each phonon frequency in the material, usually known as *Raman bands*. The implications of Equation 2.38 mean that often only the Stokes bands are analysed due to their greater intensity. The lineshape of Raman bands are well described by a convolution of Gaussian

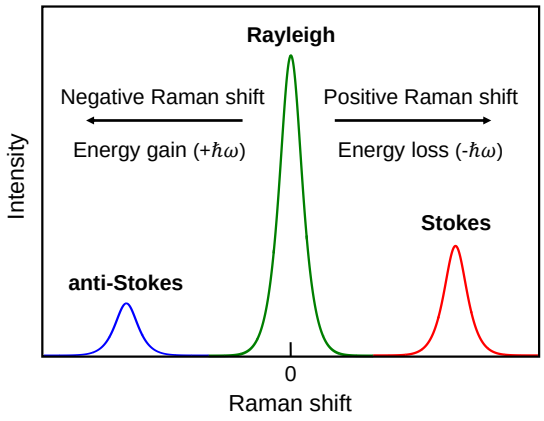


**Figure 2.13:** Sketch of a Raman spectrum showing the relative intensities of different scattering processes. The colours indicate the energy gain (blue-shifted) and energy loss (red-shifted) of the inelastic processes compared to the elastic (zero-energy change, green) process. The width of the modes is described by a Voigt lineshape.

and Lorentzian functions known as a Voigt profile which is depicted in Figure 2.13. This arises due to the combination of phonon energy broadening as a result of thermal effects (Gaussian) and the lifetime of the excited vibrational state (Lorentzian), in addition to more complex processes such as defect scattering and sample inhomogeneities.

### 2.7.2 Experimental setup

Raman spectroscopy measurements were made using a Renishaw InVia Raman spectrometer, situated either at the University of Bath or at the Renishaw Innovation Centre, Wotton-under-Edge, Gorloucestershire, UK. Experiments were performed in backscattering geometry using laser excitation wavelengths of 532 nm or 633 nm and the corresponding gratings were 1800 l/mm or 2400 l/mm respectively. A range of objective lens were used at room temperature in normal conditions, although the temperature-dependent measurements were always performed with a long working distance 50x lens (N.A. = 0.5) to accommodate the optical cryostat or heating stage. The standard spectrometer laser filters usually have a cut-off below (50 - 60) $cm^{-1}$, however for the results presented in Section 5.3, volume Bragg grating notch filters (Renishaw *Eclipse*) were used with a $\pm$ 10 $cm^{-1}$ cut-off. The total spectral resolution of the system was typically better than 1 $cm^{-1}$ in all cases.

For temperature-dependent measurements in the range (77 - 300) K, a Linkam THMS600 stage or an ARS LT3-OM optical flow cryostat with liquid nitrogen was used. For temperatures $>$ 300 K, a home-built resistive heating stage was used with thermocouple mounted close to the sample.

For all experiments, the laser power was kept sufficiently low to avoid any damage to

the sample surface over extended periods. Sample damage is easily visible on the crystal surface under the optical microscope, and is also evidenced in the metallic Se-based TMDs by a broadening of all phonon modes, in addition to a pronounced peak appearing near 250 $cm^{-1}$ related to Se migration at the sample surface [84]. When performing low temperature measurements, the laser power was also kept to a minimum to ensure that any potential laser-heating was reduced such that the cryostat temperature sensor matches the true sample as closely as possible. The laser power at the sample position was measured with a power meter after passing through any optics and cryostat windows, and was typically in the range (50 - 500) $\mu$W.

## 2.8 Electronic transport

Electronic transport concerns the motion of charge carriers through a material. Measurements of the electrical resistance and Hall effect as a function of temperature are sensitive to carrier concentrations, mobilities and scattering mechanisms. Hence, a great deal of information can be extracted simultaneously, and these techniques are particularly suited to studying electronic phase transitions.

### 2.8.1 Resistance

Resistance measurements as a function of temperature, $R(T)$ were obtained using a standard four-point probe technique. The contact configuration is shown in the inset of Figure 2.14 with two outer current leads ($I_{\pm}$) and two inner voltage leads ($V_{\pm}$). A constant excitation current in the range (0.2 - 1) mA was supplied through the outer contacts and the voltage across the inner contacts was recorded with a lock-in amplifier (SR830).

Samples were prepared by cutting pieces from large single crystals using a razor blade into rectangular shapes with typical lateral sizes in the range (0.5 - 1) mm and (2 - 4) mm for the short and long edges respectively. In ideal cases, the cut was aligned approximately with a crystallographic axis as shown Figure 2.14 using the 120° angles as a reference. Contacts were made to the as-grown surfaces by either using only silver conductive paint or by first evaporating pads consisting of 150 nm gold on top of 20 nm chromium, followed by silver paint. Crystals were mounted onto electrically insulating substrates with thermal varnish. Due to the layered structure of TMDs discussed in Section 1.3.2, it is assumed that current will predominantly flow in-plane ($ab$-direction) since the resistance out-of-

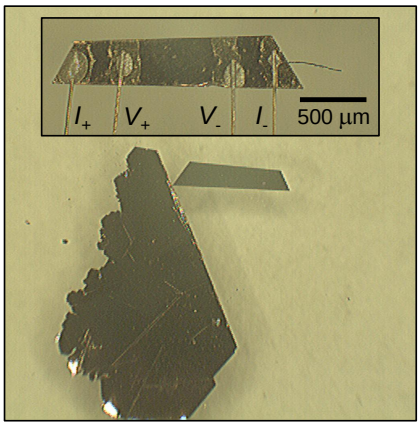


**Figure 2.14:** Contact configuration for four-point resistance measurements. The inset shows a piece of $1T$-$TiSe_2$ cut from a large single crystal. Four gold pads were evaporated on the as-grown surface, to which gold wires were attached with silver conductive paint.

plane ($c$-direction) will likely be orders of magnitude greater. Hence, the chosen contact configuration should be mostly representative of the in-plane resistance, $R_{ab}(T)$. In some cases where the sample dimensions could be determined with reasonable accuracy, the absolute resistivity was estimated according to $\rho = RA/l$ where $l$ is the length between the voltage contacts and $A = wt$ is the cross-sectional area for the current path given by the width, $w$ and thickness, $t$ of the crystal.

Measurements were performed inside either an Oxford Instruments liquid helium cryostat or a JANIS 4K closed-cycle cryocooler. The sample temperature was monitored with a calibrated thermometer mounted directly next to the sample.

### 2.8.2 Hall effect

Under normal conditions, charge carriers within a conductor flow in the direction of the applied current. However, in the presence of a perpendicular magnetic field, charge carriers experience a force known as the *Lorentz force* which causes a curved trajectory towards one side of the conductor. The resulting separation of carriers, produces a voltage difference known as the *Hall voltage* and the effect is known as the *Hall effect*. Here, a simple derivation of the *Hall coefficient*, $R_{\mathrm{H}}$ based on a common experimental geometry is presented, following the approach of Ref. [31].

Shown in Figure 2.15 is a schematic of a typical Hall effect measurement whereby contacts are made to a rectangular sample in the *Hall bar* geometry. A magnetic field $\mathbf{B} = B_z$ is applied perpendicular to a current, $I$ flowing through the sample ($x$-direction in this example). The average current density then depends on the sample dimensions

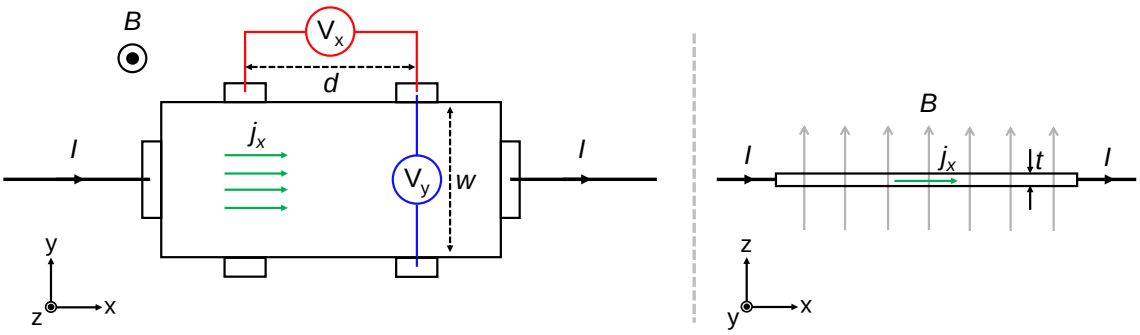


**Figure 2.15:** Schematic of a Hall effect measurement using the *Hall bar* geometry viewed along the $z$- and $y$-directions. A magnetic field, $\mathbf{B}$ is applied perpendicular to the current, $I$ passing through the sample, and orthogonal voltages, $V_x$ and $V_y$ are measured in response.

$$\mathbf{J} = j_x = I/wt. \tag{2.39}$$

where $w$ and $t$ are the width and thickness respectively as shown in Figure 2.15. The applied current generates an in-plane electric field $\mathbf{E} = (E_x, E_y)$. These components are deduced by measuring the orthogonal voltages, $V_x$ and $V_y$ and are are related by

$$E_x = V_x/d, \tag{2.40}$$

$$E_y = V_y/w. \tag{2.41}$$

In the presence of both electric and magnetic fields, there is a resulting Lorentz force on a charge carrier passing through the sample which can be expressed as an equation of motion

$$F = m^* \left( \frac{d\mathbf{v}}{dt} + \frac{\mathbf{v}}{\tau} \right) = q \left( \mathbf{E} + \mathbf{v} \times \mathbf{B} \right), \tag{2.42}$$

where $m^*$ is the effective mass, $\mathbf{v}$ is the drift velocity, $q$ is the charge, and $\tau$ is the scattering time of carriers. Assuming a steady-state condition ($d\mathbf{v}/dt = 0$), Equation 2.42 can be expressed in terms of the in-plane components

$$v_x = \frac{q\tau}{m^*} E_x - \frac{qB\tau}{m^*} v_y, \tag{2.43}$$

$$v_y = \frac{q\tau}{m^*} E_y + \frac{qB\tau}{m^*} v_x. \tag{2.44}$$

Due to the direction of the applied current, the component of the drift velocity in the $y$-direction is negligible ($v_y = 0$) and therefore Equations 2.43 and 2.44 yields

$$E_y = \frac{qB\tau}{m^*} E_x. \tag{2.45}$$

Substituting Equation 2.45 into 2.43 and using a relation for the current density, $j_x = nqv_x$ gives the *Hall coefficient* defined as

$$R_{\mathrm{H}} = \frac{E_y}{j_x B} = \frac{1}{nq}, \tag{2.46}$$

where $n$ is the charge carrier density and $q = -e$ or $+e$ is the elementary charge for electrons and holes respectively. This simple derivation of the Hall coefficient for a metal, shows that its magnitude depends inversely on the carrier density and its sign depends on the type of carrier; either negative for electrons or positive for holes.

# Chapter 3

## Growth of high quality TMD single crystals

### 3.1 Introduction

With the surge of interest in 2D materials in recent years, the high demand for single crystal transition metal dichalcogenides (TMDs) has created a market for their production and sale. As such, a whole range of compounds can now be obtained commercially from companies such as 2D semiconductors [85] or HQ graphene [86]. This makes it possible for researchers to move swiftly into new areas of materials research without the need for a direct collaboration with crystal growers, or attempting to produce the materials themselves, which can take considerable time in order to source the relevant equipment and potentially perform many growth trials before reaching a successful result. Since these materials can be so easily obtained from commercial suppliers, the growth of crystals *in house* by the researcher needs to be justified. The remainder of this section outlines the motivation for the growth of materials used in this thesis.

The first disadvantage of commercial materials is the relatively high cost for only a small number of crystals (typically 1-10 depending on the specific compound). From the point of view of the researcher, this can limit the number of possible experiments and reduces the prospect of sharing samples for wider collaboration, resulting in a more conservative approach to science. Secondly, there is often a lack of transparency from companies in terms of the specific growth conditions, with only limited information provided to the consumers. For the metallic, CDW-bearing TMDs, the growth temperature in particular has a significant impact on the CDW properties [42, 87], as will be discussed in the later chapters of this thesis. This parameter is rarely provided to the consumer. The basic characterisation of these compounds is usually limited to Raman spectroscopy and x-ray

diffraction (XRD) which are rather insensitive techniques for detecting subtle changes in the crystal purity relevant to these compounds which are typically small stoichiometry variations. Arguably one of the most sensitive techniques involves measurements of electronic transport as a function of temperature (e.g. resistivity and Hall effect) as discussed in Section 2.8. This allows information about the CDW transition temperature, carrier concentrations and defect scattering mechanisms, to be simultaneously extracted. Moreover, it is important to perform this type of characterisation for every crystal batch (or even seperate crystals within the same batch) since there can be significant variations (see Chapter 4), even if the conditions are carefully controlled. These type of experiments are currently beyond the capabilities for companies and are not likely to be commercially viable. Instead, only a non-batch specfic XRD or Raman analysis for one of the "typical" samples is provided, which is not sufficient information to assess the quality or characteristic electronic properties of CDW materials.

By growing crystals *in house*, it is possible to produce batches of crystals with a large yield ($\sim$ 10 - 40) for the relatively low cost of the raw materials, glassware, and other basic lab consumables. Therefore, there is no need to be conservative with crystal usage, meaning that the researcher is more likely to explore new ideas, and repeated trial or preliminary experiments are possible. More importantly, there is freedom to share crystals among many collaborators at other institutions to perform a range of complimentary experiments. Clear examples of this approach are displayed throughout this thesis, but considering the work in Chapter 5 as an example; at least four or more separate experimental techniques were employed in order to fully address the scientific question. Another advantage is that it becomes easy to develop an intimate knowledge of the specific properties of the materials in relation to results seen in experiment. For example, often when a surprising or unexpected result arises it may be related to a subtle aspect of the preparation of a particular crystal batch. Aided by a detailed knowledge of the growth conditions, this can easily be traced back to the origin. Instead, with a commercial sample and only a limited knowledge of the sample preparation, it becomes entirely possible to inadvertently assign unexpected behaviour to completely unrelated physical effects. Finally, using the knowledge gained from experiments in relation to the sample preparation, it is possible to repeat the growth process indefinitely to achieve a particular goal. This may simply involve improving crystal purity, or there is freedom to explore other avenues such as; investigating defects (see Chapter 4), and doping using other chalcogens [88] or metals [89].

In the metallic TMDs which exhibit strongly-correlated behaviour, this has the possibility to open up usually inaccessible aspects of physics such as induced superconductivity [10] or investigating the interplay between various CDW commensurability effects in related materials [90, 91].

## 3.2 Chemical vapour transport (CVT)

For the studies conducted in this thesis, single crystal TMDs were grown using chemical vapour transport (CVT). This technique was first described by Schäfer [92] in the 1960s, and has since become a popular method for the growth of TMDs. The basic principle relies on a constant temperature gradient which drives the crystallisation of the elements from a vapour at high temperature. To facilitate this, a halogen transport agent or carrier gas is typically used (e.g. $I_2$, $Br_2$ or $Cl_2$) [93, 94]. The materials are contained within a sealed ampoule which is heated in a tube furnace for a number of days.

### 3.2.1 Outline

TMDs with form $MX_2$ were grown inside an evacuated ampoule by the method of CVT from elemental transition metal (M) and chalcogen (X) using iodine ($I_2$) as the transport agent, driven by a gradient between the reaction ($T_r$) and growth ($T_g$) temperatures. An illustration is shown in Figure 3.1, and the chemical formulae which describe this process are given in Equations 3.1 - 3.3 according to Ref. [88]. Firstly, the reaction of the elements at the hot end of the ampoule is described by

$$M + 2X = MX_2. \tag{3.1}$$

Iodine vapour then combines with the material produced in Equation 3.1 to form gaseous compounds which proceed to the cold end of the ampoule, driven by the temperature gradient. This intermediate transport phase is described by

$$2MX_2 + 2I_2 \rightleftharpoons 2MI_2 + 2X_2. \tag{3.2}$$

The final step describes the crystallisation at the cold end of the ampoule. Solid TMD crystal products ($MX_2$) are formed by the reaction of free transition metal and excess chalcogen left over from the disproportionation of di-iodide to tetra-iodide according to

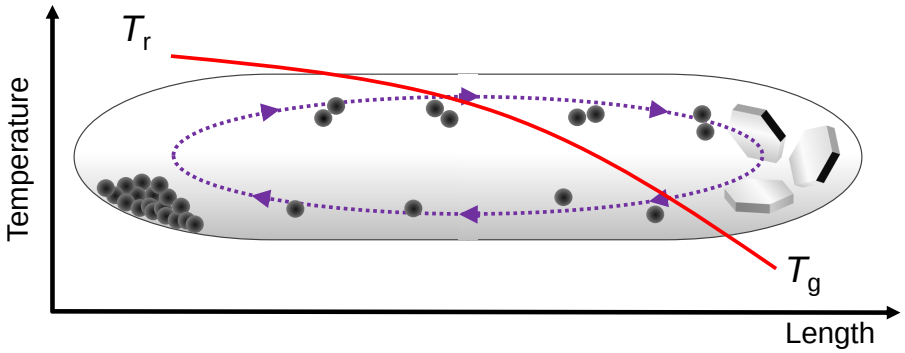


**Figure 3.1:** Illustration of the chemical vapour transport (CVT) process. The starting materials are sealed inside an evacuated ampoule. A vapour is formed at the hot end (reaction temperature, $T_r$) which is then carried by the transport agent due to a temperature gradient across the ampoule length. Single crystals accumulate at the cold end (growth temperature, $T_g$). The solid red line is a sketch of a typical temperature profile.

$$2MI_2 + 2X_2 = MI_4 + MX_2 + X_2. \tag{3.3}$$

This process continues in a cyclic fashion as the starting materials are progressively converted into crystals over time.

### 3.2.2 General methods

This section gives a general description of the experimental apparatus and methods used for the growth of TMD crystals, which is applicable to all of the samples discussed in this thesis. Additional advancements or specific modifications to these conditions, where appropriate, are discussed in Section 3.2.3.

To contain the elements under vacuum, quartz ampoules were used as shown in the inset of Figure 3.2(a). In all cases, the length was 100 mm to achieve the desired temperature gradient. However, several diameters in the range (8 - 25) mm diameter were used which corresponds to a volume of $\sim$ (5 - 49) cm$^{-3}$ by approximating the ampoule as a cylinder. An example of an ampoule with vacuum piece attached is shown in Figure 3.2(a). The relevant features are labelled and include; the KF10 vacuum flange, the *Young's stopcock* and the narrow tapered neck for sealing. The lower (ampoule) portion is made from quartz and is used to contain the material during growth, whereas the upper (vacuum) portion is made from borosilicate glass and is used only to load the material and connect the vacuum pump. These glasses are usually incompatible with each other due to their different soft-

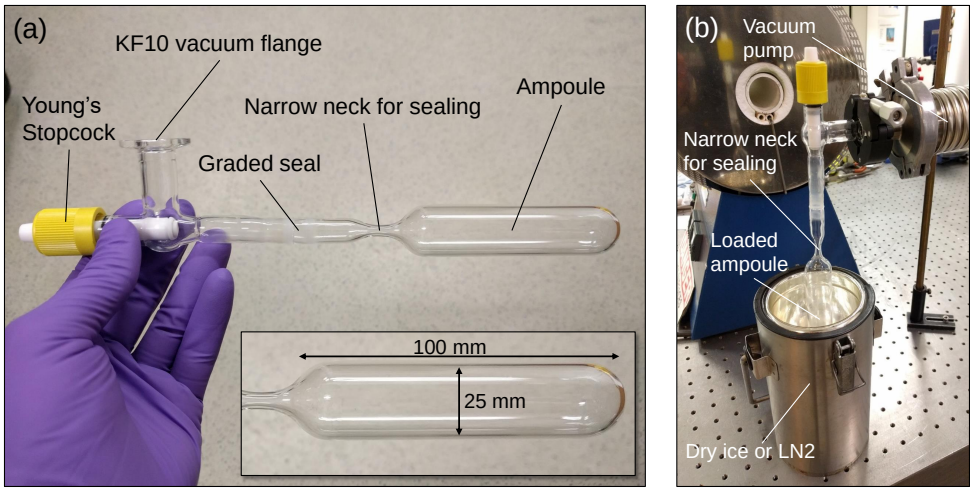


**Figure 3.2:** Quartz ampoule and sealing apparatus. (a) Photograph of a typical quartz ampoule with vacuum piece attached. The inset shows the quartz ampoule with the most commonly used dimensions (100 mm length x 25 mm diameter). (b) Setup for sealing ampoules under vacuum. The lower portion of the loaded ampoule is submerged in dry ice or liquid nitrogen (LN2) to prevent sublimation of iodine during evacuation. The ampoule is sealed by melting the narrow neck with a flame.

ening temperatures and coefficient of expansion. Therefore, a borosilicate-quartz graded seal is used between them. With this design, the vacuum portion can be reused several times by connecting new quartz ampoules.

Prior to loading, the ampoule was cleaned several times with acetone followed by isopropanol in an ultrasonic bath. The ampoule was dried thoroughly before it was annealed at $\sim$ (300 - 400)°C under vacuum for several hours to drive off any remaining residues. Then, under inert atmosphere ($N_2$ glovebox), stoichiometric amounts (1:2 molar ratio) of high purity transition metal ($>$ 99.9%) and chalcogen ($>$ 99.99%) elemental powders ($\sim$ 100 mesh) were weighed and loaded into the ampoule using a glass funnel. A slight excess of chalcogen was also included; typically (2.0 - 3.5 mg) $cm^3$ based on the ampoule volume in an effort to reduce the likelyhood of growing chalogen deficient crystals, which is common for the TMDs [42]. Iodine (99.998% anhydrous) was used as the transport agent and has proven to be effective for the growth of the metallic TMDs in particular [88]. The amount of transport agent is critical in order to produce large, high quality crystals within a reasonable time and depends on the ratio to the transition metal precursor [95]. Typically, an iodine to metal molar ratio of (0.05 : 1) was loaded, which equates to a transport agent concentration of $\sim$ (2.4 - 3.6) mg $cm^{-3}$ based on the ampoule volume,

and falls within the optimum range of $\sim$ (2.0 - 4.0) mg cm$^{-3}$ investigated during the systematic growth of the Ti-based TMDs [88]. Whilst remaining within the optimum range, it is prudent to use the minimum iodine possible, as it has been shown that a small amount may be incorporated into the crystals, which can suppress the CDW transition in TMDs [42]. Another important parameter is the total loaded mass with respect to the ampoule volume as this dictates the overall gas pressure inside the ampoule at elevated temperatures. After several preliminary trials, large high quality crystals were produced using a total mass concentration of $\sim$ (80 - 90) mg cm$^{-3}$ based on the ampoule volume. Successful growths were performed using all ampoule diameters in the range (8 - 25) mm diameter, corresponding to $\sim$ (5 - 49) cm$^3$ volume, by simply scaling the total loaded mass to achieve this concentration.

The setup for ampoule sealing is shown in Figure 3.2(b). The loaded ampoule was evacuated with a vacuum pump which is capable of achieving a base pressure of $\sim 6.5\times10^{-6}$ mbar, whilst the lower portion was cooled by submerging in either dry ice or liquid nitrogen to prevent the sublimation of iodine [88]. The neck of the ampoule was subsequently melted using a torch with a flame produced from a propane/oxygen gas mixture. The result was a sealed quartz tube containing the elemental powders under vacuum. The exact pressure inside the ampoule was not measured.

The ampoule was then placed inside a two-zone tube furnace as shown in 3.3(a). A thermal gradient was created across the ampoule using two independent temperature controllers. The loaded portion of the ampoule was at the hot (reaction) temperature, $T_\mathrm{r}$ and the empty portion was at the cold (growth) temperature, $T_\mathrm{g}$. Under the influence of this gradient, the transport agent carries material from the hot end of the ampoule which then crystallizes at the cold end in a cyclic fashion as discussed in Section 3.2.1 previously. Figure 3.3(b) shows this process in action. Here, an ampoule was removed from the furnace after $\sim$ 24 hours which is still hot, evidenced by the visible iodine gas (violet hue). In the image, most of the untransported material is on the right and some small crystals have begun to form on the left as the material is transported by the iodine gas.

A typical temperature profile is shown in the top panel of Figure 3.3(a). In this example, reaction ($T_\mathrm{r}$ = 683°C) and growth temperatures ($T_\mathrm{g}$ = 613°C) were used (horizontal solid lines) across a 100 mm ampoule, with the respective locations inside the furnace indicated by the vertical dashed lines at 13 cm and 23 cm from right to left according to

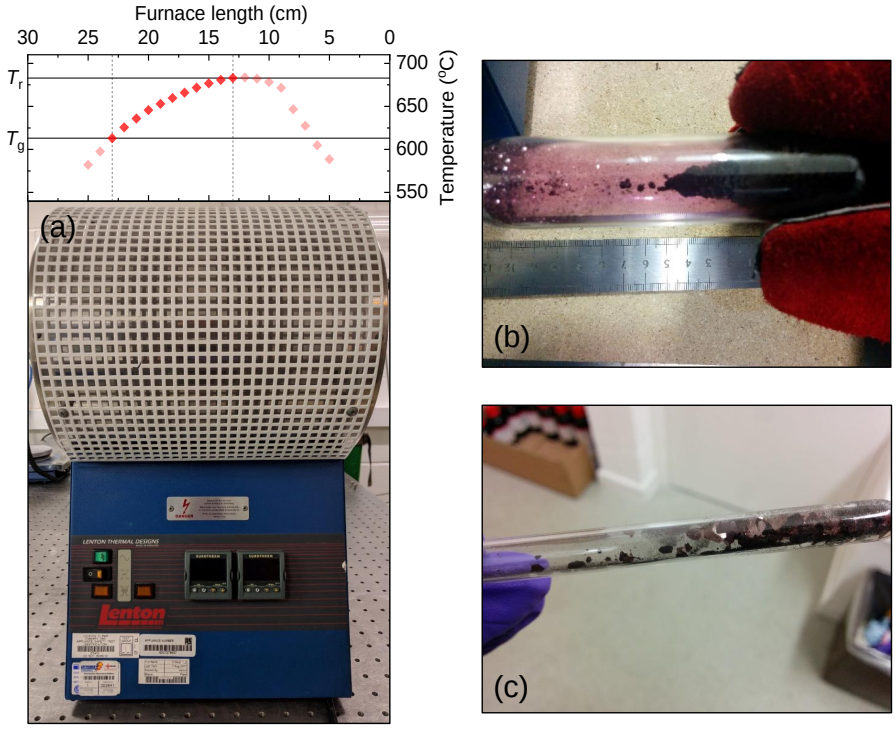


**Figure 3.3:** CVT growth in practice. (a) Two-zone tube furnace from *Lenton Thermal Designs*. The total length is 30 cm. The top panel shows a typical temperature profile across a 100 mm long ampoule. The scale is approximately true to the furnace dimensions in the image. (b) Photograph of a hot ampoule (25 mm diameter) after $\sim$ 24 hours. Small reflective crystals can be seen forming at the cold end on the left and the untransported material is on the right. The violet hue is iodine gas. (c) Single crystals after growth has completed in $\sim$21 days (8 mm diameter ampoule).

the image in the lower panel of Figure 3.3(a). The temperature data was obtained using a rigid, ceramic coated thermocouple probe inserted directly inside the furnace. The furnace was closed at both ends with 5 cm thick insulating caps to ensure a stable heating environment, which was better than $\pm$ 1°C. The choice of $T_g$ was specific to each TMD compound and the desired crystal properties, as will be discussed in the later chapters, however the typical range was $T_g$ = (550 - 700)°C. The temperature gradient across the ampoule was then $\Delta T$ = (50 - 80)°C by adjusting $T_r$ accordingly. The furnace operating temperatures were adjusted gradually over several hours using a ramp rate of 0.5 °C min$^{-1}$. The total growth time was typically $\sim$21 days, after which the furnace was gradually brought to room temperature. The ampoule was opened, and crystals that had collected at the cold end were extracted.

### 3.2.3 Specific method modifications

For the growth of $1T$-$TaSe_2$, it was necessary to quench the ampoule rapidly from high temperature ($T_g \geq 900°C$) in order to retain the metastable $1T$ polytype [49]. This was achieved by plunging the hot ampoule into a water bath at room temperature. If a slow cooling was used like in the methods of Section 3.2.2, the crystals would revert to the stable $2H$ polytype according to Ref. [49].

It should also be noted that occasionally after the CVT process had proceeded for ∼24 hours, the ampoule was brought to room temperature and some of the polycrystalline material was distributed towards the cold end of the ampoule to act as nucleation sites for crystals. The ampoule was then gradually raised back to high temperature and growth proceeded for the remaining scheduled duration. The aim was to encourage the growth of several large crystals as opposed a great number of smaller crystals, where the latter could be expected to occur if the crystals were allowed to self-nucleate at many locations across the ampoule end. It was not conclusive if there were benefits to this method since large crystals of all compounds could be grown irrespective of this step.

## 3.3 Results & Discussion

The crystals produced by CVT were usually thin platelets with hexagonal edges and reflective metallic appearance. The average area was 4 – 5 $mm^2$ and up to a maximum of 8 $mm^2$ as shown in Figure 3.4. The thickness ranged from (10 – 100) $\mu$m, but did not seem to correlate with the specific growth conditions, time, or ampoule dimensions. Each compound has a distinctive colour; either metallic bronze-purple ($1T$-$TiSe_2$), silver ($1T$-$VSe_2$), or gold ($1T$-$TaSe_2$). The colour of $TaSe_2$ allows the particular polytype to be distinguished, where gold is an indication that the metastable $1T$ polytype was successfully retained [96]. Their shape is indicative of their *trigonal* crystal symmetry (hexagonal family) and the well-defined straight edges with 120° angles [e.g. see Figure 3.4(a)] can be used to identify crystallographic axes ($a$- or $b$-axis), which may be useful for roughly aligning the crystal orientation with respect to the experimental lab frame in preparation for measurements.

Under a microscope, it can be seen that the as-grown crystal surfaces usually host some residual material as shown in Figure 3.5(a), which may consist of polycrystalline TMD powder, metal and chalcogen precursors, or iodine. By cleaving the bulk crystals, a

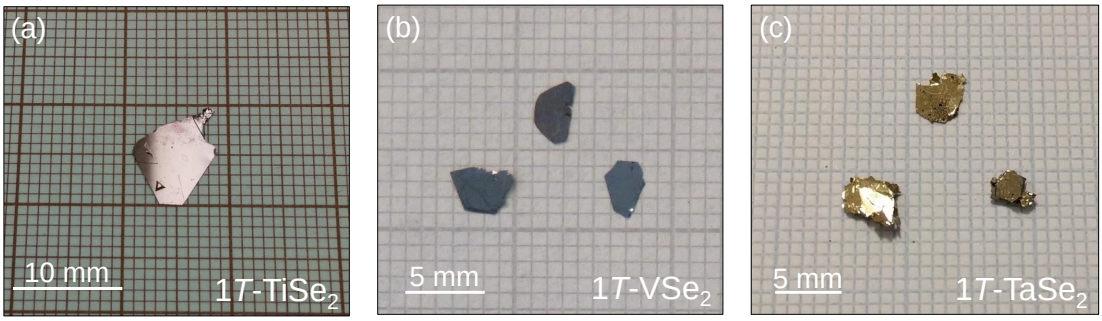


**Figure 3.4:** Typical single crystals of TMDs grown by CVT.

pristine and highly reflective mirror-like surface is revealed such as those in Figure 3.5(b). The surface is typically terraced, consisting of step-edges from various layers with visible hexagonal symmetry. However, it is usually possible to flat regions away from any such structure which are hundreds of microns across. Figure 3.5(c) shows an extreme case of a heavily oxidised surface of 1$T$-$TiSe_2$ after $\sim$ 3 years exposure to air where the significant colour contrast makes the effect obvious. To the eye, the oxidised bulk crystal appears dull and a mixture colours from pale green to deep purple. Despite this, cleaving reveals flat reflective layers as shown in Figure 3.5(d). The visible difference between an oxidised and pristine surface is highlighted in the inset of Figure 3.5(d) where only a partial cleave was made. The inner layers of single crystal TMDs can be considered nominally clean and free of oxidation since they have been protected from the atmosphere by the outer layers. Therefore, the usual methodology is to expose a fresh surface prior to each experiment. This is essential for photoemission experiments as discussed previously in Section 2.2.

The typical growth time ($\sim$21 days) produced many, large crystals suitable for the experiments conducted in this thesis. Using the smallest diameter ampoule (8 mm), this was also sufficient time to convert all of the starting material into crystal form [see Figure 3.3(c)]. For the largest ampoules (25 mm), there was usually some untransported material remaining (i.e. conversion of the raw materials to crystals was incomplete). This varied from an estimated (10 - 50)% of the starting mass, which likely depends on many factors including; the specific compound, total mass concentration, iodine concentration, and furnace temperatures. Crystals were found to grow successfully over shorter durations but usually had a smaller lateral size and the total yield was reduced. For example, small crystals (max. 1 $mm^2$) can be formed in as little as 24 hours [see Fig 3.3(b)].

Smaller diameter ampoules are useful when trialling the growth of new compounds or

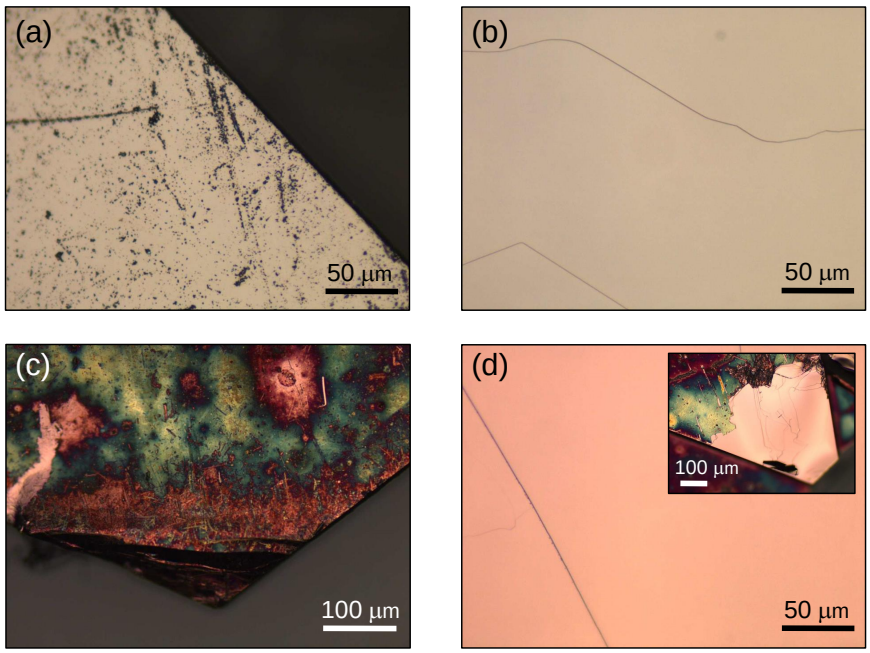


**Figure 3.5:** Microscope images of TMD crystal surfaces. (a) As-grown surface of 1 $T$-$VSe_2$ showing residues. (b) The same crystal in panel (a) after a complete cleave which shows large, clean regions of hundreds of microns across. (c) Heavily oxidised surface of 1 $T$-$TiSe_2$ after $\sim$ 3 years exposure to air. (d) The same crystal in panel (c) after a complete cleave. The inset shows a corner of the crystal after a partial cleave, highlighting the contrast between oxidised and pristine surfaces.

developing methods as the required total loaded mass is less; ~450 mg (8 mm diameter) compared to ~4400 mg (25 mm diameter) to achieve a concentration of ~90 mg $cm^{-3}$. Therefore there is less waste from potentially unsuccessful growths attempts. A disadvantage of smaller diameters is the limited space for crystals meaning that the maximum achievable lateral size is limited by the ampoule diameter. In addition, the crystals have a tendency to fill the space at the cold end of the ampoule and extend across the length of a few centimetres [see Figure 3.3(c)] which likely means that crystals within the batch have varying growth temperatures, considering the profile in Figure 3.3(a). This could lead to greater variations within the batch (see Chapter 4). By contrast, in the trials using large ampoules (25 mm), all of the crystals formed only at the apex of the ampoule and hence had a relatively narrow (almost negligible) range of growth temperatures within the batch. Another advantage of larger ampoules is that the yield is typically larger, although the average crystal size achieved was comparable for all diameters.

Beyond the scope of this thesis, the same methods outlined in Section 3.2.2 were successfully used to grow other pure compounds including; $NbSe_2$ and $ReS_2$. Several doped

compounds were also grown such as $Cr_xTiSe_2$, $Cr_xReS_2$ and $Cr_xReSe_2$, mixed transition metals; $Ti_{1-x}V_xSe_2$ and mixed chalogens; $1\,T$-$TaS_{2-x}Se_x$. In general, no modifications to the general methods were required except in the case of the Re-based compounds where the chosen growth temperatures were typically higher ($T_g \geq 1000$ °C), following the methods of Ref. [97], although lower temperatures were never attempted.

Finally, some possible advancements to the growth methods are discussed. During the early stages of the work in this thesis, liquid nitrogen (77 K) was used to cool the ampoules during evacuation to prevent iodine loss from sublimation [see Figure 3.2(b)]. Later, this was replaced with dry ice (195 K) following the hypothesis that at greater temperatures, the cooling medium will act as a less effective cryopump thus trapping less water, impurities, or organic material, whilst staying sufficiently cool to maintain solid iodine. Using the dry ice method, it was noticed that the maximum achievable crystal purity increased. However, there were several other advances to the method which were implemented at a similar time, and hence it is difficult to attribute this solely to the cooling medium. It is possible to use even greater temperatures, such as melting ice (273 - 275 K) [98], which may further reduce the condensation of organic material. However, the biggest advantage to using either liquid nitrogen or dry ice is that cooling can be maintained for several hours during evacuation, whereas melting ice would likely have to be continuously monitored and replenished to prevent the temperature increasing. If successful growths can be achieved without a halogen transport agent by using only the chalcogen vapour [42], then pumping at room temperature (300 K) or higher is possible, which may drive off further volatile impurities. Another related advancement to the method could be to attach a vacuum gauge to the ampoule sealing apparatus in order to measure the pressure inside the ampoule. It is possible that there may be an influence of the vacuum on the crystal growth process and the quality of resulting crystals.

# Chapter 4

# Influence of crystal growth conditions on the charge density wave properties of 1 $T$-$VSe_2$

## 4.1 Preamble

As outlined in Section 3.1, there exists a continued motivation to grow high-quality single crystals of TMDs, both for fundamental research into their bulk properties in addition to providing a suitable starting material for the preparation of van der Waals heterostructures. With renewed interest in CDW-bearing materials, this is even more relevant due to the sensitivity of strongly-correlated behaviour to disorder and doping effects [15, 42, 91].

In general, 1 $T$-$VSe_2$ has received comparatively less attention than other TMDs until very recent years, with a number of reports focussing on the bulk CDW properties [99–101] and the behaviour in 2D [102–106]. This studies typically rely on preparation of crystals or thin film growth by molecular beam epitaxy, and therefore understanding the influence of growth conditions on the CDW properties is imperative. In addition, there seems to be a number of conflicting reports in the literature with regards to the electronic properties of 1 $T$-$VSe_2$ including; the presence of a second lock-in phase transition to a CDW at $\sim$ (80 - 85) K [48, 107], a possible Kondo-like behaviour at low temperature [108], and varying temperature dependence of the resistance anywhere in the range $T^2 - T^5$ [45, 109–111]. This inconsistency could be explained by the large range of crystal growth conditions used over the past decades. A review of the literature reveals that growth temperatures anywhere in the range (550 - 900)°C have been used, with either $I_2$ or Se vapour transport. These variations could be enhanced further by the fact that 1 $T$-$VSe_2$ can exist with a wide range of stoichiometry [112].

The related compound, $1T$-$TiSe_2$ is particularly sensitive to crystal growth conditions and shows a continuous reduction in the CDW transition temperature from its maximum at $T_{CDW} = (201 \pm 2)$ K to $(140 \pm 5)$ K as the growth temperature is increased from $T_g = 575°C$ to $900°C$ [42]. This effect is generally attributed to an increasing electron doping from excess Ti interstitials between the layers, forming $Ti_{1+x}Se_2$. Doping is relevant in this compound because of the proposed excitonic CDW mechanism, and hence the delicate balance between electron and hole densities is of great importance. The CDW is predicted to be completely suppressed ($T_{CDW} \rightarrow 0$ K) at a doping level of $x = (0.035 \pm 0.005)$. In $1T$-$VSe_2$, samples with $T_g < 600°C$ show the highest transition temperatures [87, 89]. Therefore, a similar effect had been suggested to occur in this compound, whereby layer interstitials of V ions at elevated growth temperatures may result in electron doping. Several recent reports have mentioned the impact of defects in $1T$-$VSe_2$ and related compounds [101, 113–115]. However, a systematic study focusing on the effects of growth temperature on crystal purity and its influence on the CDW properties is lacking, whilst the nature of defects in $1T$-$VSe_2$ remains ultimately unknown.

This chapter concerns the work by Sayers *et al.* entitled "Correlation between crystal purity and the charge density wave in $1T$-$VSe_2$" [116] presented in Section 4.3 which focuses on the electronic transport properties of six different $1T$-$VSe_2$ crystal batches produced with growth temperatures in the range $T_g = (550$ - $700)°C$. Resistance measurements are used to determine the CDW transition temperature, $T_{CDW}$ and to estimate the crystal purity from the residual resistance ratio (RRR). The samples are primarily characterised by both synchrotron and lab-based XPS, and supported by powder x-ray diffraction (PXRD) in order to study the chemical composition and crystal structure in detail. XPS measurements of the electronic core levels are expected to be highly sensitive to changes in the chemical bonding, doping level, and variations in the local environment, making it an ideal technique to study potentially small variations in $1T$-$VSe_2$ crystals. Both the nature and density of defects is discussed in relation to the CDW behaviour and their dependence on the crystal growth temperature.

## 4.2 Introduction

### 4.2.1 Electronic transport properties

Figure 4.1 shows a plot of the electronic transport properties of 1 $T$-$VSe_2$. Results for the sample grown at $T_g$ = 550°C are presented, which has highest crystal purity according to the work in Section 4.3. Resistance as a function of temperature, $R(T)$ is shown in Figure 4.1(a), normalised to the room temperature value. The shape of the curve is qualitatively similar to previous reports [44, 45, 109, 110], with overall metallic behaviour and a slight increase in the resistance near 110 K. The first derivative highlights a sharp CDW transition at $T_{CDW}$= (112.7 ± 0.8) K in this sample which is taken as the point at which $dR/dT$ first crosses zero since this also coincides with the inflexion point where the resistance first increases in the inset of Figure 4.1(a). This corresponds to the well-known normal phase to incommensurate CDW transition which is simply referred to as $T_{CDW}$ for the purpose of this study.

The low temperature resistance of metals is often dominated by defect and impurity scattering. The residual resistance ratio (RRR), $(R/R_{T\to 0K})$ is often used to provide an indication of the crystal purity. In order to compare the different samples in Section 4.3, the ratio $R_{295K}/R_{4K}$ was used. Based on this definition, the sample in Figure 4.1(b) has an RRR of ≈ 49 which exceeds the highest value previously reported in the literature for 1 $T$-$VSe_2$ (∼ 28) [110, 111]. This level of purity was achieved by optimising the growth procedures as discussed in Chapter 3, and then minimising the growth temperature whilst remaining sufficient for crystallisation and the production of large crystals within a reasonable time-frame.

By comparison with Figure 4.1(b), it can be seen that there is a corresponding decrease in the Hall coefficient, $R_H(T)$ below $T_{CDW}$, which suggests a loss of charge carriers from the Fermi surface consistent with the opening of a gap due to the onset of a CDW state. The first derivative, $dR_H(T)/dT$ shows a sharp increase that matches closely with $T_{CDW}$ determined from the resistance. At 300 K, the magnitude of $R_H$ is small and negative with a value of -0.02×$10^{-3}$ $cm^{-3}$ $C^{-1}$ indicating that the dominant carriers are electrons, according to the simple relation in Equation 2.46. Upon cooling, $R_H$ decreases but is only weakly temperature dependent over the range (300 - 112) K. Below $T_{CDW}$, $R_H$ drops markedly until it reaches -1.75×$10^{-3}$ $cm^{-3}$ $C^{-1}$ at 4 K, which is comparable

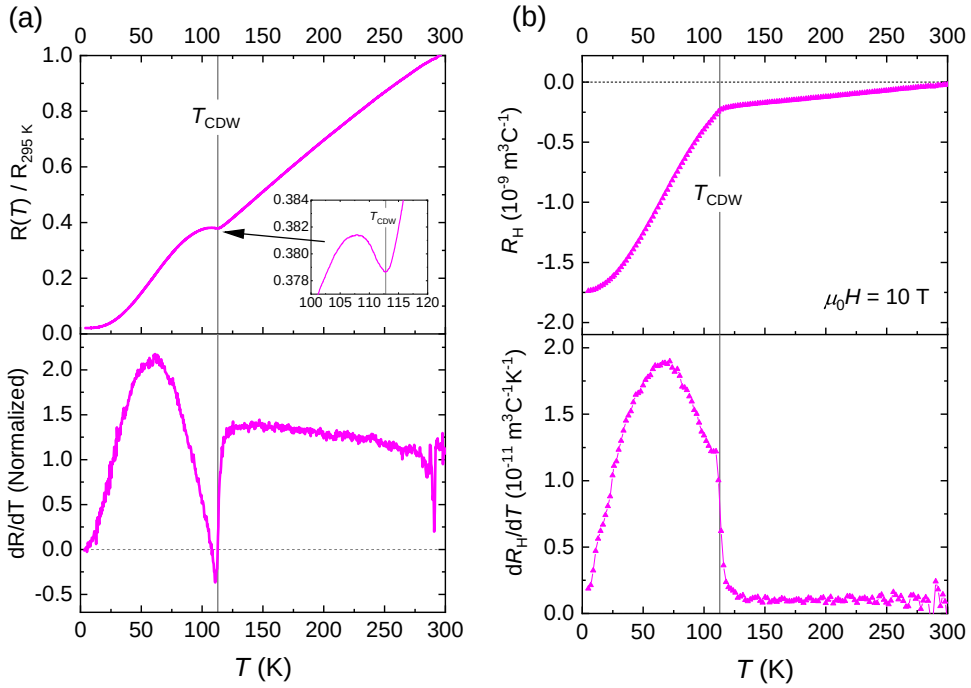


**Figure 4.1:** Electronic transport properties of $1\,T$-$VSe_2$ ($T_g$ = 550°C). (a) Normalised resistance, $R(T)$ (upper) and first derivative of resistance, $dR/dT$ (lower) as a function of temperature. The inset shows the behaviour of $R(T)$ near $T_{CDW}$. (b) Hall coefficient $R_H(T)$ (upper) and first derivative $dR_H(T)/dT$ (lower). The solid vertical line in all panels indicates the CDW transition temperature, $T_{CDW}$ = (112.7 ± 0.8) K as determined from the initial crossing of $dR/dT = 0$.

to previously reported values in the range -$(1-3)\times10^{-3}$ cm$^{-3}$ C$^{-1}$ [44, 45, 109, 110]. The excellent agreement between the independent measurements presented here using different experimental techniques in Figure 4.1(a) and (b), suggests that the determination of $T_{CDW}$ from the crossing point of $dR/dT = 0$ is a valid method.

### 4.2.2 Core level spectroscopy

Shown in Figure 4.2 are measurements of the electronic core levels in $1\,T$-$VSe_2$ ($T_g$ = 550°C) using a non-monochromatic, unpolarized Al-k$\alpha$ ($h\nu$ = 1486.7 eV) x-ray source. A survey scan up to 600 eV binding energy in Figure 4.2(a) shows numerous Se and V core levels (labelled) in addition to some common contaminants which are regularly detected in XPS, such as carbon (C-1s) and oxygen (O-1s). Coincidentally, these features can act as a convenient reference of the absolute binding energy, with O-1s present at 531 eV for example [117].

Se-3$d$ and V-2$p$ levels were selected to study in more detail and some representative

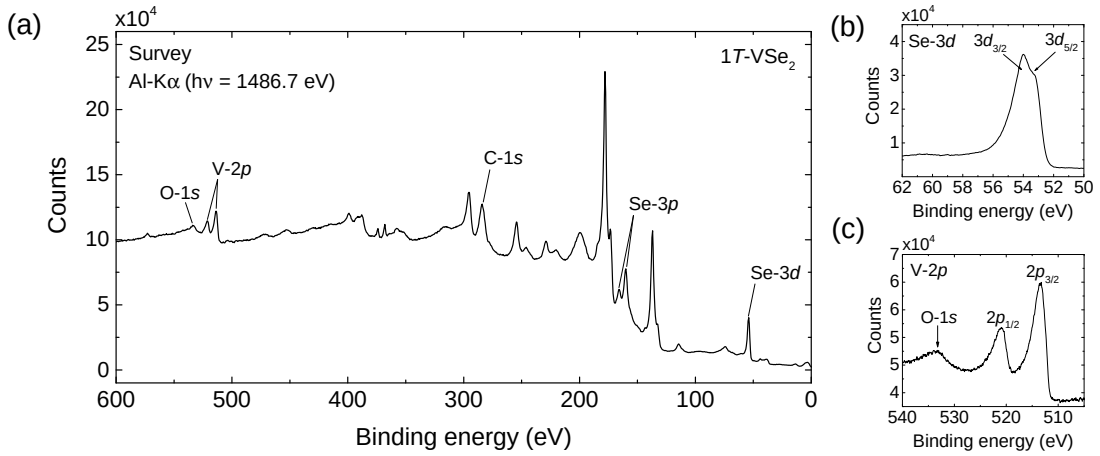


**Figure 4.2:** X-ray photoelectron spectroscopy (XPS) of 1$T$-$VSe_2$ ($T_g$ = 550°C) using an Al-K$\alpha$ source ($h\nu$= 1486.7 eV). (a) Survey spectrum of core levels up to 600 eV binding energy. Panels (b) and (c) show spectra of the Se-3$d$ and V-2$p$ levels respectively, with the relevant features labelled.

spectra are shown in panels (b) and (c) of Figure 4.2 respectively. These particular levels clearly have a large enough intensity to be measured above the background at this photon energy, whilst also being well-separated in energy from other levels. The Se-3$d$ feature should be comprised of the spin-orbit split $3d_{5/2}$ and $3d_{3/2}$ levels (labelled), however the energy resolution for the acquisition of this particular spectrum is not sufficient to resolve them. The centre of the broad Se-3$d$ peak is ∼53.7 eV which is consistent with the two-minus oxidation state of selenium ($Se^{2-}$) for Se bound to V in 1$T$-$VSe_2$ [106]. The close proximity of O-1s to the V-2$p$ levels means that they can be acquired within a single scan.

In order to detect potentially subtle variations between different 1$T$-$VSe_2$ samples, high-resolution measurements are required. The synchrotron XPS measurements in Section 4.3 allowed a binding energy variation of ∼ 100 meV to be clearly observed between the Se core levels of samples with the lowest (550°C) and highest (700°C) growth temperature. In addition, the tunability of the synchrotron radiation allowed selection of the photon energy in order to maximise the spectral intensity of each core level. For example, the photoionisation cross-section of the Se-3$d$ level at $h\nu$ = 150 eV is orders of magnitude greater than using Al-K$\alpha$ ($h\nu$ = 1486.7 eV) as shown in Figure 4.3.

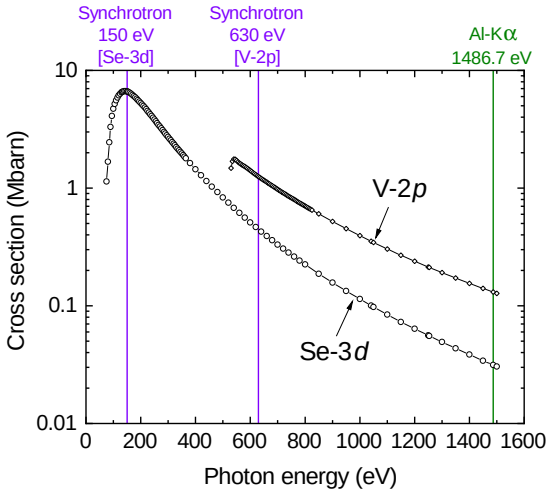


**Figure 4.3:** Photoionisation cross-section for Se-3$d$ and V-2$p$ core levels as a function of incident photon energy, based on theoretical calculations in Ref. [118]. The vertical lines indicate the photon energies used in the work of Section 4.3 compared to Al-k$\alpha$.

## 4.3 Publication entitled: "Correlation between crystal purity and the charge density wave in 1$T$-$VSe_2$"

<table>
<tr><td colspan="5">This declaration concerns the article entitled:<br>Correlation between crystal purity and the charge density wave in 1T-$VSe_2$</td></tr>
<tr><td colspan="5">Publication status (tick one)</td></tr>
<tr><td>Draft manuscript</td><td>Submitted</td><td>In review</td><td>Accepted</td><td>Published</td></tr>
<tr><td></td><td></td><td></td><td>✓</td><td></td></tr>
<tr><td>Reference</td><td colspan="4">C. J. Sayers, L. S. Farrar, S. J. Bending, M. Cattelan, A. J. H. Jones, N. A. Fox, G. Kociok-Köhn, K. Koshmak, J. Laverock, L. Pasquali and E. Da Como. Correlation between crystal purity and the charge density wave in 1$T$-$VSe_2$. Physical Review Materials (2020).</td></tr>
<tr><td>Candidate's contribution to the paper</td><td colspan="4">The candidate produced all of the samples in this work. The candidate obtained the synchrotron x-ray spectroscopy data with the assistance of others. The data analysis and presentation in journal format was solely the work of the candidate.<ul><li>Formulation of ideas: 70%</li><li>Design of methodology: 50%</li><li>Experimental work: 60%</li><li>Presentation of data in journal format: 100%</li></ul></td></tr>
<tr><td>Statement from candidate</td><td colspan="4">This paper reports on original research I conducted during the period of my Higher Degree by Research candidature.</td></tr>
<tr><td colspan="3">Signature:</td><td colspan="2">Date:</td></tr>
</table>

This is the author accepted manuscript of an article published in final form as Sayers, C, Farrar, L, Bending, S, Cattelan, M, Jones, A, Fox, N, Kociok-Kohn, G, Koshmak, K, Laverock, J, Pasquali, L & Da Como, E 2020, 'Correlation between crystal purity and the charge density wave in 1T-VSe2', Physical Review Materials, vol. 4, no. 2, 025002. Available online via: https://doi.org/10.1103/PhysRevMaterials.4.025002

# Correlation between crystal purity and the charge density wave in 1$T$-$VSe_2$

C. J. Sayers,[1,*] L. S. Farrar,[1] S. J. Bending,[1] M. Cattelan,[2] A. J. H. Jones,[3] N. A. Fox,[2,3] G. Kociok-Köhn,[4] K. Koshmak,[5] J. Laverock,[3] L. Pasquali,[5,6,7] and E. Da Como[1]

[1]*Centre for Nanoscience and Nanotechnology, Department of Physics, University of Bath, Bath, BA2 7AY, UK*
[2]*School of Chemistry, University of Bristol, Cantocks Close, Bristol BS8 1TS, UK*
[3]*HH Wills Physics Laboratory, University of Bristol, Tyndall Avenue, Bristol BS8 1TL, UK*
[4]*Material and Chemical Characterisation Facility (MC²), University of Bath, Claverton Down, Bath BA2 7AY, UK*
[5]*IOM-CNR Institute, Area Science Park, SS 14 Km, 163.5, Basovizza, 34149 Trieste, Italy*
[6]*Dipartimento di Ingegneria "Enzo Ferrari", Università di Modena e Reggio Emilia, via P. Vivarelli 10, 41125 Modena, Italy*
[7]*Department of Physics, University of Johannesburg, P.O. Box 524, Auckland Park 2006, South Africa*

We examine the charge density wave (CDW) properties of 1$T$-$VSe_2$ crystals grown by chemical vapour transport (CVT) under varying conditions. Specifically, we find that by lowering the growth temperature ($T_g < 630°C$), there is a significant increase in both the CDW transition temperature and the residual resistance ratio (RRR) obtained from electrical transport measurements. Using x-ray photoelectron spectroscopy (XPS), we correlate the observed CDW properties with stoichiometry and the nature of defects. In addition, we have optimized a method to grow ultra-high purity 1$T$-$VSe_2$ crystals with a CDW transition temperature, $T_{CDW} = (112.7 \pm 0.8)$ K and maximum residual resistance ratio (RRR) $\approx 49$, which is the highest reported thus far. This work highlights the sensitivity of the CDW in 1$T$-$VSe_2$ to defects and overall stoichiometry, and the importance of controlling the crystal growth conditions of strongly-correlated transition metal dichalcogenides.

## I. INTRODUCTION

The metallic transition metal dichalcogenides (TMDs) are well-known to exhibit interesting strongly correlated behaviour such as charge density waves (CDWs) [1, 2] and superconductivity. In 1$T$-$VSe_2$, an incommensurate CDW develops at $T_{CDW} = 110$ K with ($4a$ x $4a$ x $3.18c$) periodic lattice distortion, followed by a further change in the distorted $c$-axis to $3.25c$ below 85 K [3]. Signatures of these phase transitions have been noted in x-ray [3] and electron diffraction [4], magnetic and transport studies [5]. The CDW is likely driven by Fermi surface nesting involving states along the flat portions of the electron pocket centred around the $\overline{M}$-point at the edge of the Brillouin zone [6], which possibly has a three-dimensional character [7]. The common polytype of $VSe_2$ has the trigonal (1$T$) unit cell and belongs to the P$\bar{3}$m1 spacegroup [4]. Fig. 1(a) and (b) shows the layered structure consisting of Se-V-Se planes in the $a$-$b$ direction seperated by a van der Waals (vdW) gap, and octahedral metal coordination when viewed along the $c$-axis.

In addition to the ongoing efforts to understand CDW transitions in bulk TMDs, the recent surge in research of layered 2D materials has reignited interest in this area. So far, it has been shown that 1$T$-$VSe_2$ has a large range of tunability of its CDW properties with dimensionality, as the transition temperature and magnitude of the order parameter are strongly influenced by the sample thickness on a nanometre scale [8, 9]. Control of the distorted lattice periodicity is also possible by strain engineering, and an unconventional ($4a$ x $\sqrt{3}a$) CDW has been observed by STM [19]. At the monolayer limit, there have been reports of possible ferromagnetism [10–12], strongly enhanced CDW order evidenced by a fully-gapped Fermi surface [13], and an increase of the transition temperature up to $T_{CDW} = 220$ K [14].

With increasing interest in studying monolayer or few-layer charge density wave TMDs, the bottom-up approach of growth by molecular beam epitaxy (MBE) [13, 19] or chemical vapour deposition (CVD) [15, 16] techniques has become common. Once optimized, these methods are excellent at producing thin films. However, samples produced this way often suffer from a high number of crystal defects. In particular, the presence of grain boundaries due to coalescing nucleation sites is a common and well-documented problem in 2D materials grown by CVD, such as graphene [17]. Also, there is often an unavoidable interaction with the growth substrate such as doping [18] or strain [19] which can alter the sample properties. Instead, a top-down approach by exfoliation of high-quality crystals as the starting material is still considered the ideal way to obtain pristine monolayers and to provide the basis for construction of van der Waals heterostructures by dry transfer [20].

At present, many researchers either grow their own crystals or obtain them commercially. In both cases, the specific growth conditions are often not reported. However, notably among the TMDs, 1$T$-$VSe_2$ can grow far from ideal stoichiometry in varying conditions [21]. Previous investigations on 1$T$-$VSe_2$ have suggested that the CDW transition temperature is maximum for samples prepared using the lowest growth temperatures ($T_g < 600°C$) where the Se:V ratio is expected to approach 2:1 [22, 23]. Deviations from ideal stoichiometry due to in-

*Corresponding author: c.j.sayers@bath.ac.uk

creasing density of defects can occur at higher growth temperatures, but their nature in this compound remains unknown. Types of defects that are typically found in TMD crystals are labelled in Fig. 1(a) and (b) including vacancies and interstitials [24]. The influence of growth temperature on crystal purity and its relation to CDW properties has been reported in the related compound 1 $T$-$TiSe_2$. Increasing Ti interstitials in the vdW gap between the layers results in electron doping and reduces $T_{CDW}$ by upsetting the delicate balance of electrons to holes which has consequences within the excitonic insulator scenario [25]. In 1 $T$-$VSe_2$, where Fermi surface nesting is suggested to play a role, such a doping effect could have a significant impact on the CDW by altering the topology of the Fermi surface due to the change in chemical potential. Thus far, a detailed study of the growth conditions of 1 $T$-$VSe_2$ in relation to its CDW properties and the role of defects is lacking.

Here, we show that changes in the growth temperature over the range (550 - 700)°C have a significant impact on the physical purity, structure, and intrinsic stoichiometry which subsequently influences the CDW behaviour. Electronic transport measurements show that the CDW transition temperature increases markedly for crystals grown with $T_g < 630$°C. Using x-ray spectroscopy, we are able to identify defects in samples grown at higher temperatures, and correlate this with the observed electronic properties. In addition, we have optimized the conditions for growing ultra-pure 1 $T$-$VSe_2$ at $T_g = 550$°C with a transition temperature of $T_{CDW} = (112.7 \pm 0.8)$ K and a maximum residual resistance ratio (RRR) $\approx 49$ which, to the best of our knowledge, surpasses the highest value reported previously of ∼28 [26, 27].

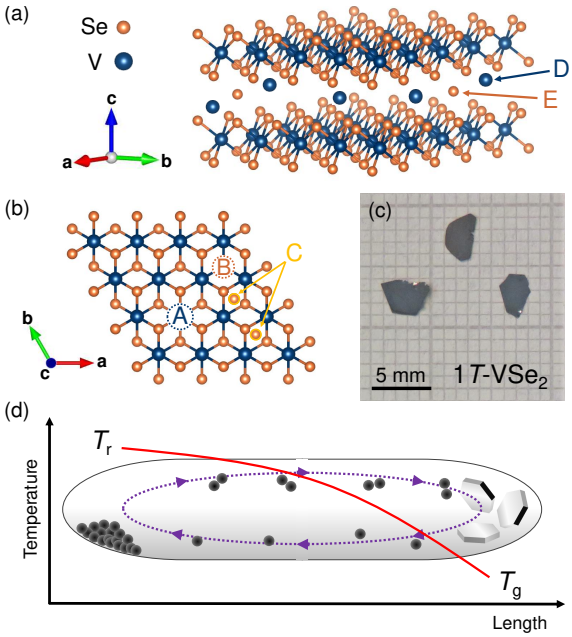


FIG. 1: Growth of 1 $T$-$VSe_2$ crystals. Panels (a) and (b) show the crystal structure of 1 $T$-$VSe_2$ viewed along the layer plane and $c$-axis respectively. Common defect types found in TMDs are labelled. In 1 $T$-$VSe_2$, these correspond to vanadium and selenium vacancies (A and B), selenium aggregates/clusters (C), and interstitials in the van der Waals (vdW) gap between the layer planes (D and E). (c) Image of typical crystals produced by CVT (d) Illustration of the chemical vapour transport (CVT) process. Iodine vapour carries material from the reaction zone at $T_r$ to the growth zone at $T_g$ where crystals form. The solid red line is a sketch of a typical temperature profile.

## II. EXPERIMENTAL METHODS

### A. Crystal growth

1 $T$-$VSe_2$ crystals were grown using a chemical vapour transport (CVT) method [28], whereby a constant temperature gradient drives the crystallisation of the elements from a vapour at high temperature as illustrated in Fig. 1(d). High purity vanadium (99.9%) and selenium (99.99%) powders were sealed inside an evacuated quartz ampoule, together with anhydrous iodine (99.998%) which acts as the transport agent. Under inert atmosphere ($N_2$ glovebox), stoichiometric amounts of the elements (2:1 molar ratio) were loaded plus a slight excess of selenium (2.4 - 3.4 mg $cm^{-3}$), based on the ampoule volume. The amount of iodine (2.10 - 2.25 mg $cm^{-3}$) was chosen to facilitate growth within a reasonable timeframe [29], whilst also minimizing the potential for iodine to be introduced into the crystals which is known to suppress the CDW transition in other TMDs [25]. The ampoule was evacuated using a pump capable of achieving base pressure ($7\times10^{-6}$) mbar and then sealed with a flame. A two-zone tube furnace was used with a temperature gradient between hot (reaction temperature, $T_r$) and cold (growth temperature, $T_g$) zones of $\Delta T$ = (55 - 60)°C which was confirmed with a thermocouple probe. The temperature stability was better than ± 1°C. Growth proceeded for up to 21 days, resulting in many crystals of (5 x 5 x 0.1 mm) forming at the cold end of the ampoule. The crystals were typically thin platelets with hexagonal edges and a highly reflective silver appearance as shown in Fig. 1(c).

With these general conditions, this procedure was carried out several times in order to produce separate sample batches with different growth temperatures, $T_g$ in the range (550 - 700)°C.

### B. Electronic transport

We measured the resistance as a function of temperature, R($T$) for different crystal batches. Samples were cut with a razor blade into rectangular shapes (typical lateral size 4 mm x 1 mm) and mounted on electrically insulating substrates using thermal varnish. Contacts

were made to the as-grown crystal surfaces using silver paste in a standard 4-point configuration. Measurements were performed in a JANIS 4 K closed cycle cryocooler (4 - 300 K) using a lock-in amplifier (SR830) and a typical excitation current of 1 mA.

Multiple crystals were measured from each batch to investigate any possible variations.

### C. X-ray spectroscopy

We used both x-ray photoelectron spectroscopy (XPS) and x-ray absorption spectroscopy (XAS) with synchrotron radiation to study core levels of selenium (Se), vanadium (V) and iodine (I) in 1$T$-$VSe_2$. Measurements were performed at the BEAR end station (Elettra synchrotron, Trieste) [30, 31]. In order to expose a clean surface, the samples were cleaved in a nitrogen glove-bag attached to the fast entry of the preparation chamber.

We found that after prolonged exposure, we were able to induce radiation damage to the sample surface which resulted in noticeable changes in the spectra. Hence, for the results presented in the main text and the Supplemental Material (Ref. [32]), we minimized both the exposure time and photon flux (e.g. $\sim 7{\times}10^{10}$ photons $s^{-1}$ at $h\nu$ =150 eV). Identical experimental conditions were maintained for each sample. As a result of these measures, we did not observe any evolution of the spectra during the measurements which could be related to damage and therefore the properties we report are intrinsic to the samples.

## III. ELECTRONIC PROPERTIES

To investigate the bulk electronic properties of 1$T$-$VSe_2$, we measured the resistance as a function of temperature, R($T$) for different crystal batches as shown in Fig. 2(a). The shape of the curve agrees with previous studies of 1$T$-$VSe_2$ and shows an overall metallic behaviour with a slight increase in the resistance related to the CDW transition at $T_{\mathrm{CDW}} \approx$ (100 - 110) K [5, 33, 34]. At low temperature, the resistivity approaches a finite value related to the amount of impurity scattering [33]. We do not see any indication of an upturn in the resistance of our samples at low temperature (4 K) in contrast to a previous study, which attributed this behaviour to a Kondo effect [35].

The first derivative, d$R$/d$T$ in Fig. 2(b) highlights the CDW transition, $T_{\mathrm{CDW}}$ which we define as the onset temperature where the resistance first starts to increase, and corresponds to the point at which d$R$/d$T$ initially crosses zero [dashed horizontal line in Fig. 2(b)]. Details of obtaining $T_{\mathrm{CDW}}$ in this way are provided in Ref. [32], and we emphasize that by using alternative points in d$R$/d$T$ to define $T_{\mathrm{CDW}}$ does not change the observed trend between samples or the conclusions of

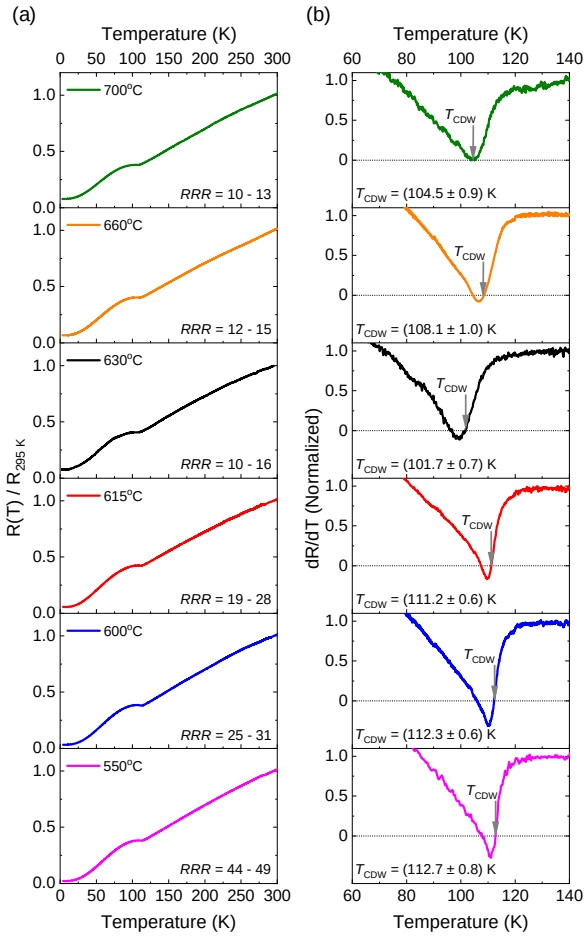


FIG. 2: Resistance of 1$T$-$VSe_2$ samples produced with different growth temperatures as indicated. (a) Normalized resistance, R/$R_{295K}$ for different sample batches. The range of residual resistance ratio (RRR) for each crystal batch is labelled. (b) First derivative of resistance, d$R$/d$T$ highlighting the charge density wave transition, $T_{\mathrm{CDW}}$ which we define as the point at which d$R$/d$T$ initially crosses zero indicated by the arrows.

this work. Fig. 3(a) shows the CDW transition temperatures extracted from d$R$/d$T$ for different sample batches as a function of growth temperature. The overall trend shows that $T_{\mathrm{CDW}}$ is increased at lower growth temperatures, reaching a maximum of $T_{\mathrm{CDW}}$ = (112.7 ± 0.8) K for the 550°C sample. We note that samples with $T_g$ < 630°C show an increase in transition temperature above the typically reported value of $T_{\mathrm{CDW}}$ = 110 K. Based on the trend of our samples produced at the lowest growth temperatures, it seems as if $T_{\mathrm{CDW}}$ is approaching the inherent maximum for 1$T$-$VSe_2$. It is also apparent in Fig. 2(b) that there is an evolution in the width of d$R$/d$T$ feature relating to the CDW transition, where there is a broadening at higher growth temperatures.

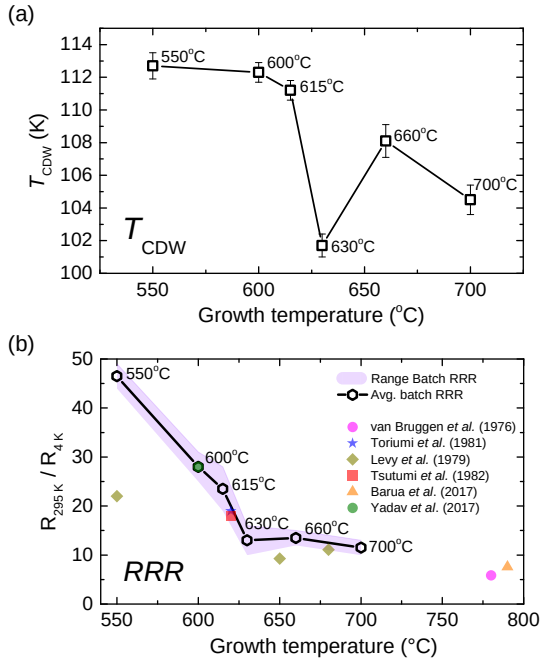


FIG. 3: Electronic properties of 1$T$-$VSe_2$ samples as a function of crystal growth temperature, $T_g$ (a) Charge density wave transition temperature, $T_{CDW}$. (b) Average residual resistance ratio (RRR), $R_{295K}/R_{4K}$. The shaded area corresponds to the RRR range found within each batch of crystals. For comparison, the coloured data points show RRR values taken from the literature as indicated. If the value was not directly quoted in those works, it has been estimated here from the published resistance/resistivity data.

This is seen in both the onset of the transition (gradient of the steep decline near $T_{CDW}$) and width of the minima in $dR/dT$. Such a broadening is often linked to disorder, and the behaviour in our samples is similar to that observed in $NbSe_2$ using electron irradiation dosing to induce atomic defects without doping the system [37]. Additional information can be extracted from the magnitude of the $dR/dT$ minima below zero (dashed horizontal line) which also follows a similar trend, as $dR/dT$ of the sample with highest $T_{CDW}$ becomes the most negative following the CDW transition. We show in Ref. [32] that this corresponds to the magnitude of the resistance increase at $T_{CDW}$ relative to the normal metallic behaviour. Therefore our results are fully consistent with strengthened CDW order where one would expect a more effective gapping of the Fermi surface, as the proportion of charge carriers removed at $T_{CDW}$ is greater.

The residual resistance ratio (RRR) is a well-known parameter often used to estimate the purity of metals. At sufficiently low temperatures, the scattering of carriers is dominated by impurities or crystal defects, which gives rise to a finite (residual) resistance. The magnitude of this residual resistance is thus linked to the density of impurities and/or defects present in the sample. Using the ratio $R_{295K}/R_{4K}$, we are able to compare several samples as shown in Fig. 3(b). Overall, we find that the average RRR within each batch increases for lower growth temperatures, indicating a reduction in impurity/defect scattering. For samples grown at the lowest temperature (550°C), we find a maximum RRR of $\sim$ 49 within the batch. Similar to the behaviour of the CDW transition temperature, there is also a significant increase in the average RRR from $\sim$ 12 to $>$ 22 for samples with $T_g <$ 630°C. This is consistent with the width of the CDW transitions in $dR/dT$ [Fig. 2(b)] for samples $T_g$ = (630 - 700)°C, confirming a defect-induced broadening. By comparing our results to reports of RRR in the literature on 1$T$-$VSe_2$ over a range of growth temperatures, there is a clear agreement with this trend [Fig. 3(b)].

Finally, we discuss the scattering mechanism of charge carriers at low temperature by analyzing the temperature dependence of the resistance. Previously in 1$T$-$VSe_2$ , there have been reports of a strong $T^2$ dependence [5, 34] which could suggest a significant electron-electron scattering. By fitting the low temperature data in the range (5 - 15) K with a power law, $R \propto T^x$ we also find a $T^2$ dependence but only for the sample grown at the highest temperature (700°C). By contrast, the sample grown at the lowest temperature (550°C) shows a $T^3$ behaviour, and there appears to be a progressive shift between these two regimes for intermediate temperatures (see Ref. [32]). In other CDW-bearing TMDs, a temperature dependence in the range $T^3$ - $T^5$ is found for $T \leq$ 25 K, depending on the compound, and is related to electron-phonon scattering [36]. The power then depends on the orbital character of bands involved in either an *intraband* or *interband* scattering, the density of states, and strength of the CDW order (proportion of carriers lost from the Fermi surface). For example, a $T^3$ dependence is found for the ideal resistivity in 2$H$-$NbSe_2$ and can be understood by a simple two-band model which describes an electron-phonon mediated *interband* scattering of *s*-like electrons into the *d*-band. Such a two-band analysis has also been used to successfully describe the temperature dependence of the Hall coefficient in 1$T$-$VSe_2$ [27] and the ideal resistivity was found to be in the range $T^3$ - $T^4$ for the highest purity samples.

We therefore suggest that a similar electron-phonon scattering mechanism is the case for pure 1$T$-$VSe_2$ which is seen here in our sample with largest RRR (550°C). Instead, the low temperature resistance deviates rapidly from this behaviour with increasing disorder and approaches a $T^2$ dependence. Clearly, this behaviour seems to be rather sample dependent and could explain the large variation reported in the literature [5, 26, 27, 34]

In summary, the electronic properties of 1$T$-$VSe_2$ and its CDW behaviour vary quite significantly with crystal growth temperature. The observed trend of $T_{CDW}$ and RRR in Fig. 3 are similar and therefore, the underlying mechanism influencing both of these properties is likely

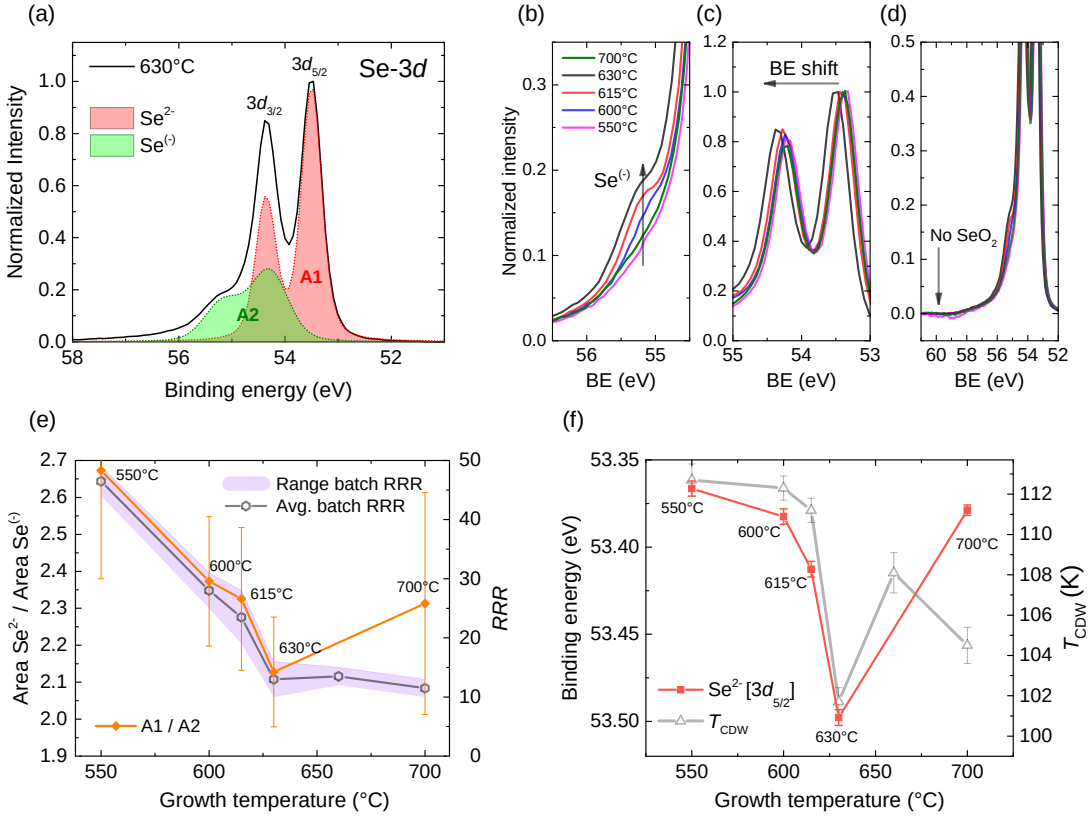


FIG. 4: X-ray photoelectron spectroscopy (XPS) of $1T$-$VSe_2$ samples grown at different temperatures. (a) Se-3$d$ spectra ($h\nu$ = 150 eV). The shaded curves are fits to the data for the $T_g$ = 630°C sample, showing the contribution from $Se^{2-}$ and $Se^{(-)}$ oxidation states. Panels (b) - (d) show the same data as panel (a) and highlight the feature in Se-3$d$ spectra related to the presence of $Se^{(-)}$, the observed shift in binding energy (BE), and the absence of $SeO_2$ (e) The area ratio (A1/A2) as a function of growth temperature, $T_g$ (left axis) obtained from fitting the Se-3$d$ spectra for the $Se^{2-}$ (A1) and $Se^{(-)}$ (A2) oxidation states. A comparison (right axes) is made with the residual resistance ratio (RRR) from electronic transport measurements. (f) Binding energy of the $3d_{5/2}$ peak for $Se^{2-}$ obtained from fitting the data. Error bars in panels (e) and (f) is the standard deviation on the fitting parameters.

to be intrinsically linked. However, at low growth temperatures (550 - 600°C), it appears that the strength of CDW order ($T_{CDW}$) approaches its maximum, whereas the crystal purity (RRR) continues to increase.

## IV. X-RAY SPECTROSCOPY & DISCUSSION

To obtain information about the chemical composition of our samples, we used XPS to study core levels in $1T$-$VSe_2$. Herein, we will mainly discuss the XPS results of the Se-3$d$ core levels for which we find a significant variation between our samples. Instead, the vanadium core levels show no noticeable variation and iodine was either not present in our samples or its concentration was below the detectable limit. These results are included in the Supplemental Material (Ref. [32]). We did not observe any sign of oxidation in the Se-3$d$ spectra which otherwise would be in the form of $SeO_2$ present at $\sim$ 59.9 eV [38] (indicated by the arrow in Fig. 4(d)). Additionally, the XAS results near the O K-edge showed a negligible amount of oxygen and all samples had identical spectra (see Ref. [32]). Therefore, we rule out the presence of oxygen or iodine as an explanation for the observed change in CDW properties.

XPS spectra for the Se-3$d$ core levels of different samples are shown in Fig. 4(a). The main feature is the doublet (labelled) with Se-$3d_{5/2}$ $\approx$ 53.4 eV and spin-orbit splitting $\Delta_{so} \approx 0.86$ eV, which corresponds to the $Se^{2-}$ oxidation state of Se bound to V in $1T$-$VSe_2$ [12]. An additional feature on the high energy side was also found in the region 55 - 56 eV which is highlighted in Fig. 4(b) and shows a clear variation between samples. We find a good fit to the data using two doublets as illustrated in Fig. 4(a) for the $T_g$ = 630°C sample. The binding energy (BE) of the second doublet relating to

the additional feature is Se-3$d_{5/2}$ ≈ 54.2 eV, which we assign to the presence of more positive oxidation states of selenium. Since it appears in our data as a single broad doublet (gaussian width ∼2 larger than $Se^{2-}$), it is likely to arise from a combination of oxidation states. We label this feature $Se^{(-)}$ since its binding energy is slightly lower (i.e. more negative) than pure selenium, $Se^0$ which is expected at ∼ 55.5 eV [38]. Such a feature could indicate the presence of partially bound or unbound Se in the form of vanadium vacancies, in-plane Se aggregates/clusters [12, 39] or Se interstitials [18] (See Fig. 1). From the fitting, the contributions of $Se^{2-}$ and $Se^{(-)}$ states in each sample are given by the shaded areas, A1 and A2 respectively in Fig. 4(a). The ratio A1/A2 gives an indication of the relative amount of $Se^{(-)}$ oxidation states present in our samples, and is shown in Fig. 4(e) as a function of growth temperature. Comparing this ratio with the RRR from electronic measurements [right axis, Fig. 4(e)], there appears to be a correlation with the overall trend which suggests that the presence of these $Se^{(-)}$ states contribute to the impurity/defect scattering in electronic transport.

It can also be seen in Fig. 4(c) that there is a shift in binding energy of the Se-3$d$ spectra between samples. We find that this shift is significant (∼ 120 meV variation), and there is an overall trend of increasing $Se^{2-}$ binding energy for samples grown at higher temperatures as shown in Fig. 4(f). We rule out any energy shift due to local charge effects from increasing concentration of the more positive $Se^{(-)}$ oxidation states discussed previously, since there is negligible broadening of the observed $Se^{2-}$ linewidth between samples. Such a local effect would rather be expected to contribute multiple environments, leading to the inhomogeneous broadening of the observed core level in addition to a binding energy shift. Instead, the rigid shift of the entire Se-3$d$ states is better explained by a doping effect in our samples. Specifically, an overall electron doping raises the Fermi level resulting in an apparent shift of core levels to higher binding energies with respect to our XPS energy analyzer. Therefore, we suggest that samples grown at higher temperatures are either V-rich ($V_{1+x}Se_2$) or Se-deficient ($VSe_{2-x}$). The binding energy shift agrees with the evolution of $T_{CDW}$ [right axis in Fig. 4(f)], and hence we suggest that the suppression of charge density wave order in 1$T$-$VSe_2$ could be related to effective electron doping.

To provide further insight into the composition of our samples and to help elucidate the nature of defects, we obtained the crystal stoichiometry from independent lab-based XPS measurements (non-monochromatic Al-k$\alpha$ source, $h\nu$ = 1486.7 eV) and lattice parameters from powder x-ray diffraction (PXRD) described in Ref. [32]. Shown in Fig. 5 are the results for the $a$- and $c$-axis lattice parameters as a function of growth temperature together with the variation of crystal stoichiometry for comparison (top-axis). Firstly, it can be seen that the stoichiometry (Se/V ratio) of our samples varies from Se/V = 1.98±0.10 to 1.94±0.10 with increasing growth temperature which is consistent with the electron-doping hypothesis (either V-rich or Se-deficient). Considering these two scenarios, it is important to first examine changes in the $c$-axis parameter. Overall we find that it decreases with increasing growth temperature, and therefore it is unlikely that there are significant vanadium interstitials between the layers which may be expected to produce the opposite effect i.e. an *increase* in the $c$-axis by expanding the layer distance [40]. This is supported by our XPS and XAS data (Ref. [32]) that show no additional features which could be linked to extrinsic V species. Hence, we exclude the V-rich ($V_{1+x}Se_2$) scenario which would otherwise manifest as V interstitials in the vdW gap [22, 25]. Instead, we consider what would be the effects of Se-deficiency on the crystal structure. A study of controlled Se loss by annealing in the related compound, 1$T$-$TiSe_2$ [41] previously showed a decrease in the $c$-axis related to the Ti-Se bond length, as $\delta$ increases in $TiSe_{2-\delta}$ and occurs continuously across the range 350 - 950°C. At the same time, a corresponding increase in the a-axis was observed. This trend of the $a$- and $c$-lattice parameters is very similar to what we find for 1$T$-$VSe_2$ in Fig. 5. Therefore, we suggest that our results can be explained by an overall Se-deficiency ($VSe_{2-x}$) at higher growth temperatures due to increasing Se vacancies (defect B in Fig. 1). The desorption of Se at elevated temperatures is in line with previous reports [18, 24] and seems to be of greater significance above 600-700°C [42], which is consistent with our observations. As Se becomes volatile and leaves behind a vacancy, the majority is lost from the crystal. However, a small proportion may become trapped in-plane as aggregates/clusters or between layers as interstitials (defect C and E in Fig. 1 respectively). This may explain the additional $Se^{(-)}$ selenium species seen in XPS [Fig. 4(a)]. It could also be possible that

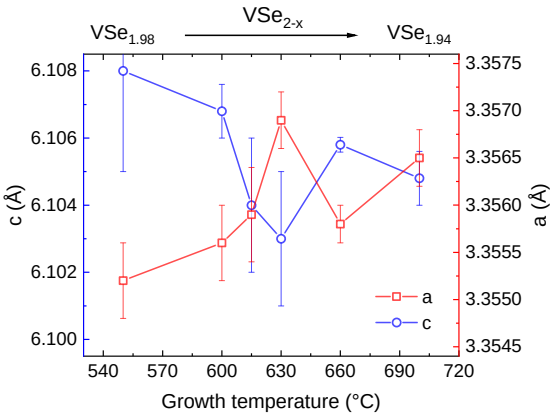


FIG. 5: Lattice parameters of 1$T$-$VSe_2$ samples obtained from powder x-ray diffraction (PXRD). The left and right plot axes show the $c$- and $a$-axis parameters of the P$\bar{3}$m1 unit cell respectively. The top-axis labels shows a comparison with the overall variation of crystal stoichiometry (Se/V ratio) obtained from laboratory XPS measurements.

some additional Se is incorporated into the crystals due to the Se-rich environment during the growth process. This would likely occur at higher growth temperatures considering the greater energy cost to disrupt the lattice by introducing an aggregate or interstitial compared to a vacancy.

Finally, to mimic the effects of growing crystals at high temperatures, we also performed an annealing experiment to investigate the effect on the Se-3$d$ core levels and valence band (VB). Here, we used a $\mu$XPS technique with a focussed beam spot of 100 $\mu$m in order to precisely measure the same region of the sample before and after annealing. Shown in Fig. 6 are the results which compare the pristine sample (cleaved in ultra-high vacuum, UHV), with that following heat treatment (annealing to 520°C for ∼40 mins). Similar to Ref. [41], we expect annealing to result in Se loss from the sample, leading to a binding energy shift as the sample becomes overall electron doped. Indeed, this effect is clearly visible in Fig. 6(a) and the inset shows that the core levels are shifted by approximately 0.5 eV. Although this is much larger than the intrinsic shift in Fig. 4(c), the annealing experiments were performed in UHV ($<1\times10^{-9}$ mbar) as opposed to the Se-rich atmosphere during crystal growth. Given the high vapor pressure of Se (0.07 atm at 520°C), the greater loss of Se in UHV is expected. As discussed previously, the overall electron doping raises the Fermi level meaning that the core levels shift to higher binding energy. This is confirmed by analyzing the VB spectra in Fig. 6(b) where the same 0.5 eV shift is applied to the annealed sample spectrum such that the main features of the VB are overlaid. The up-shifted Fermi level position is indicated by the arrow. These results provide further evidence for the electron-doping scenario, specifically due to an overall Se-deficiency ($VSe_{2-x}$).

In summary, there are likely to be two major types of defects in 1$T$-$VSe_2$ grown by CVT; namely Se vacancies and trapped Se aggregates or interstitials. Both will contribute to the defect scattering of carriers in electronic transport and hence decrease the RRR. However, the effective binding energy shift in XPS suggests that the dominant defect type is Se vacancies as the system becomes overall electron doped. This is further supported by the Se deficiency from measurements of the crystal stoichiometry, lattice parameters and annealing experiments. We suggest that the suppression of the CDW order is caused by a deviation from stoichiometry in the form of electron doping which reduces $T_{CDW}$, similar to 1$T$-$TiSe_2$ [25]. Although the density of defects and doping level are coincidentally linked, we suggest that the CDW is mainly influenced by doping. In fact, a recent STM investigation of the local density of states in the presence of defects showed the CDW gap in 1$T$-$VSe_2$ to be extremely robust to disorder [43]. From our results, this is evidenced by the fact that the $T_{CDW}$ approaches a maximum as the crystal stoichiometry becomes near 2:1 ratio at the lowest growth temperature concomitant with a saturation of the binding energy shift in XPS (doping

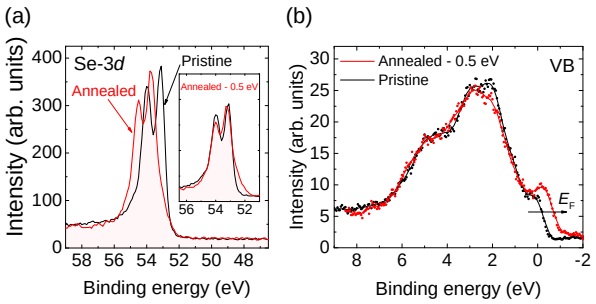


FIG. 6: Effect of annealing on core levels measured by $\mu$XPS ($h\nu$ = 1486.7 eV). (a) Se-3$d$ spectra for the $T_g$ = 630°C sample. A comparison is made between the pristine sample (black) after cleaving in UHV, and the effect of annealing at 520°C for ∼40 minutes (red). The inset shows the same comparison with a shift of -0.5 eV applied to the annealed sample spectrum. (b) Valence band (VB) spectra for the pristine and annealed sample (with -0.5 eV shift applied).

level). Instead, the crystal purity (RRR) is expected to continue to increase below $T_g$ = 550°C without any significant gain in $T_{CDW}$. We note that this is approaching the lower limit of reported growth temperatures for 1$T$-$VSe_2$ and other TMDs using the iodine CVT technique [23]. By decreasing the temperature further, we anticipate that the growth rate will become increasingly slow until the required growth time is impractical or there is insufficient energy for crystallization to occur.

## V. CONCLUSION

From electronic transport measurements, we showed that both the CDW transition temperature, $T_{CDW}$ and the residual resistance ratio (RRR) decreases for 1$T$-$VSe_2$ crystals grown at higher temperatures. This is a result of an increased density of defects, which primarily manifests as Se vacancies as a result of Se desorption from the final crystal products at elevated temperature. Therefore, we suggest 1$T$-$VSe_2$ becomes overall Se deficient which is confirmed by stoichiometry analysis and changes in the unit cell parameters from x-ray diffraction. This deficiency leads to an effective electron doping and a resulting up-shift in the Fermi level, which is evidenced by a rigid shift of Se-3$d$ core levels to higher binding energy in XPS measurements. Although the crystal purity is reduced at higher growth temperatures (lower RRR) due to a larger density of defects, we suggest that the effective electron doping due to overall Se-deficiency is mostly responsible for the reduction in $T_{CDW}$. For samples with $T_g$ < 630°C, we see an increase in the CDW transition temperature above the typically reported value of $T_{CDW}$ ≈110 K. Based on this knowledge, we were able to optimize the chemical vapour transport method in order to produce ultra-high purity 1$T$-$VSe_2$ samples with near ideal stoichiometry at $T_g$ = 550°C with $T_{CDW}$ =

(112.7 ± 0.8) K and maximum RRR ≈ 49.

Our work highlights the importance of carefully controlling the growth conditions of strongly correlated TMDs whose properties are sensitive to defects and deviation from stoichiometry. In addition, the growth of high purity TMD materials is imperative for understanding both the bulk behaviour of these compounds and to provide a suitable source for exfoliation of monolayers and the preparation of van der Waals heterostructures.

**Acknowledgements**

We thank the Elettra synchrotron for access to the BEAR beamline (proposal no. 20180358) and the BEAR staff for assistance during measurements including S. Nannarone and N. Mahne for helpful discussions. Extensive technical support from P. Jones at the University of Bath is gratefully appreciated. We would like to thank S. Cross and S. Friedemann for insightful discussions and sharing preliminary data. We thank G. Balakrishnan for sharing unpublished information with regards to Ref. [35]. The authors acknowledge funding and support from the EPSRC Centre for Doctoral Training in Condensed Matter Physics (CDT-CMP), Grant No. EP/L015544/1. Finally, we acknowledge the Bristol NanoESCA Facility (EPSRC Strategic Equipment Grant No. EP/K035746/1 and EP/M000605/1).

[1] J. A. Wilson, F. J. Di Salvo, and S. Mahajan, Charge-density waves and superlattices in the metallic layered transition metal dichalcogenides, Adv. Phys. **24**, 117 (1975).

[2] K. Rossnagel, On the origin of charge-density waves in select layered transition-metal dichalcogenides, J. Phys. Condes. Mat. **23**, 213001 (2011).

[3] K. Tsutsumi, X-ray-diffraction study of the periodic lattice distortion associated with a charge-density wave in 1$T$-$VSe_2$, Phys. Rev. B **26**, 5756 (1982).

[4] D. J. Eaglesham, R. L. Withers, and D. M. Bird, Charge-density wave transitions in 1$T$-$VSe_2$, J. Phys. C. **19**, 359 (1986).

[5] A. H. Thompson, and B. G. Silbernagel, Correlated magnetic and transport properties in the charge-density-wave states of $VSe_2$, Phys. Rev. B. **19**, 3420 (1979).

[6] K. Terashima, T. Sato, H. Komatsu, and T. Takahashi N. Maeda and K. Hayashi, Charge-density wave transition of 1$T$-$VSe_2$ studied by angle-resolved photoemission spectroscopy, Phys. Rev. B. **68**, 155108 (2003).

[7] V. N. Strocov, M. Shi, M. Kobayashi, C. Monney, X. Wang, J. Krempasky, T. Schmitt, L. Patthey, H. Berger, and P. Blaha, Three-dimensional electron realm in $VSe_2$ by soft-x-ray photoelectron spectroscopy: origin of charge-density waves, Phys. Rev. Lett. **109**, 086401 (2012).

[8] Á. Pásztor, A. Scarfato, C. Barreteau, E. Giannini and C. Renner, Dimensional crossover of the charge density wave transition in thin exfoliated $VSe_2$, 2D. Mat. **4**, 041005 (2017).

[9] J. Yang, W. Wang, Y. Liu, H. Du, W. Ning, G. Zheng, C. Jin, Y. Han, N. Wang, Z. Yang, M. Tian, and Y. Zhang, Thickness dependence of the charge-density-wave transition temperature in $VSe_2$, Appl. Phys. Lett. **105**, 063109 (2014).

[10] Y. Ma, Y. Dai, M. Guo, C. Niu, Y. Zhu, and B. Huang, Evidence of the Existence of Magnetism in Pristine $VX_2$ Monolayers (X = S, Se) and Their Strain-Induced Tunable Magnetic Properties, ACS. Nano. **6**, 1695 (2012).

[11] M. Bonilla, S. Kolekar, Y. Ma, H. C. Diaz, V. Kalappattil, R. Das, T. Eggers, H. R. Gutierrez, M. H. Phan and M. Batzill, Strong room-temperature ferromagnetism in $VSe_2$ monolayers on van der Waals substrates, Nat. Nano. **13**, 289 (2018).

[12] Z.-L. Liu, X. Wu, Y. Shao, J. Qi, Y. Cao, L. Huang, C. Liu, J.-O. Wang, Q. Zheng, Z.-L. Zhu, K. Ibrahim, Y.-L. Wang and H.-J. Gao, Epitaxially grown monolayer $VSe_2$: an air-stable magnetic two-dimensional material with low work function at edges, Sci. Bull. **63**, 419 (2018).

[13] J. Feng, D. Biswas, A. Rajan, M. D. Watson, F. Mazzola, O. J. Clark, K. Underwood, I. Marković, M. McLaren, A. Hunter, D. M. Burn, L. B. Duffy, S. Barua, G. Balakrishnan, F. Bertran, P. Le Fèvre, T. K. Kim, G. van der Laan, T. Hesjedal, P. Wahl, and P. D. C. King, Electronic Structure and Enhanced Charge-Density Wave Order of Monolayer $VSe_2$, Nano. Lett. **18**, 4493 (2018).

[14] P. Chen, W. W. Pai, Y. -H. Chan, V. Madhavan, M. Y. Chou, S. -K. Mo, A. -V Federov, and T. -C. Chiang, Unique Gap Structure and Symmetry of the Charge Density Wave in Single-Layer 1$T$-$VSe_2$, Phys. Rev. Lett. **121**, 196402 (2018).

[15] H. Wang, X. Huang, J. Lin, J. Cui, Y. Chen, C. Zhu, F. Liu, Q. Zeng, J. Zhou, P. Yu, X. Wang, H. He, S. H. Tsang, W. Gao, K. Suenaga, F. Ma, C. Yang, L. Lu, T. Yu, E. H. T. Teo, G. Liu and Z. Liu High-quality monolayer superconductor $NbSe_2$ grown by chemical vapour deposition, Nat. Comms. **8**, 394 (2017).

[16] W. Fu, Y. Chen, J. Lin, X. Wang, Q. Zeng, J. Zhou, L. Zheng, H. Wang, YḢe, H. He, Q. Fu, K. Suenaga, T. Yu, and Z. Liu, Controlled Synthesis of Atomically Thin 1T-$TaS_2$ for Tunable Charge Density Wave Phase Transitions, Chem. Mater. **28**, 7613 (2016).

[17] Q. Yu, L. A. Jauregui, W. Wu, R. Colby, J. Tian, Z. Su, H. Cao, Z. Liu, D. Pandey, D. Wei, T. F. Chung, P. Peng, N. P. Guisinger, E. A. Stach, J. Bao, S. S. Pei and Y. P. Chen, Control and characterization of individual grains and grain boundaries in graphene grown by chemical vapour deposition, Nat. Mat. **10**, 443 (2011).

[18] J. P. Peng, J. Q. Guan, H. M. Zhang, C. Li. Song, L. Wang, K. He, Q. K. Xue, X. C. Ma, Molecular beam epitaxy growth and scanning tunneling microscopy study of $TiSe_2$ ultrathin films, Phys. Rev. B. **91**, 121113(R) (2015).

[19] D. Zhang, J. Ha, H. Baek, Y.-H. Chan, F. D. Natterer, A. F. Myers, J. D. Schumacher, W. G. Cullen, A. V. Davydov, Y. Kuk, M. Y. Chou, N. B. Zhitenev, and J.

A. Stroscio, Strain engineering a $4a \times \sqrt{3}a$ charge-density-wave phase in transition metal dichalcogenide 1T-$VSe_2$, Phys. Rev. Mater. **1**, 024005 (2017).

[20] A. Castellanos-Gomez, M. Buscema, R. Molenaar, V. Singh, L. Janssen, H. S. J. van der Zant, and G. A. Steele, Deterministic transfer of two-dimensional materials by all-dry viscoelastic stamping, 2D. Mater. **1**, 011002 (2014).

[21] K. Hayashi and M. Nakahira, Stability and The Equilibrium Selenium Vapor Pressure of the $1T$-$VSe_2$ Phase, J. Solid. State. Chem. **24**, 153 (1978).

[22] F. J. Di Salvo and J. V. Waszczak, Magnetic studies of $VSe_2$, Phys. Rev. B. **23**, 457 (1981).

[23] F. Levy and Y. Froidevaux, Structural and electrical properties of layered transition metal selenides $V_xTi_{1-x}Se_2$ and $Ta_xTi_{1-x}Se_2$, J. Phys. C: Solid. State. Phys. **12**, 473 (1979).

[24] B. Hildebrand, C. Didiot, A. M. Novello, G. Monney, A. Scarfato, A. Ubaldini, H. Berger, D. R. Bowler, C. Renner, and P. Aebi, Doping nature of native defects in $1T$-$TiSe_2$, Phys. Rev. Lett. **112**, 197001 (2014).

[25] F. J. Di Salvo, D. E. Moncton and J. V. Waszczak, Electronic properties and superlattice formation in the semimetal $TiSe_2$, Phys. Rev. B. **14**, 4321 (1976).

[26] C. S. Yadav, and A. K. Rastogi, Electronic transport and specfici heat of 1T-$VSe_2$, Solid. State. Comms. **150**, 648 (2010).

[27] A. Toriumi and S. Tanaka, Galvanomagnetic properties of 1T-$VSe_2$, Physica. B+C. **105**, 141 (1981).

[28] H. Hedayat, C. J. Sayers, D. Bugini, C. Dallera, D. Wolverson, T. Batten, S. Karbassi, S. Friedemann, G. Cerullo, J. van Wezel, S. R. Clark, E. Carpene, and E. Da Como, Excitonic and lattice contributions to the charge density wave in $1T$-$TiSe_2$ revealed by a phonon bottleneck, Phys. Rev. Research. **1**, 023029 (2019).

[29] H. P. B. Rimmington and A. A. Balchin, The growth by iodine vapour transport techniques and the crystal structures of layer compounds in the series $TiS_xSe_{2-x}$ , $TiS_xTe_{2-x}$, J. Crys. Growth. **21**, 171 (1974).

[30] S. Nannarone, F. Borgatti, A. DeLuisa, B. P. Doyle, G. C. Gazzadi, A. Giglia, P. Finetti, N. Mahne, L. Pasquali, M. Pedio, G. Selvaggi, G. Naletto, M. G. Pelizzo, and G. Tondello, The BEAR Beamline at Elettra, AIP. Conf. Proc. **705**, 450 (2004).

[31] L. Pasquali, A. De Luisa, and S. Nannarone, The UHV Experimental Chamber For Optical Measurements (Reflectivity and Absorption) and Angle Resolved Photoemission of the BEAR Beamline at Elettra, AIP. Conf. Proc. **705**, 1142 (2004).

[32] See Supplemental Material at http://link.aps.org/ for a summary of the $1T$-$VSe_2$ sample properties, details of PXRD measurements, methods of determining the CDW phase transition temperature, $T_{CDW}$ and x-ray spectroscopy (XPS and XAS) of vanadium and iodine core levels.

[33] C. F. van Bruggen, and C. Haas, Magnetic susceptibility and electrical properties of $VSe_2$ single crystals, Solid. State. Comms. **20**, 251 (1976).

[34] M. Bayard and M. J. Sienko, Anomalous electrical and magnetic properties of vanadium diselenide, J. Solid. State. Chem. **19**, 325 (1976).

[35] S. Barua, M. C. Hatnean, M. R. Lees and G. Balakrishnan, Signatures of the Kondo effect in $VSe_2$, Sci. Rep. **7**, 10964 (2017).

[36] M. Naito and S. Tanaka, Electrical Transport Properties in $2H$-$NbS_2$, -$NbSe_2$, -$TaS_2$ and -$TaSe_2$, J. Phys. Soc. Jpn. **51**, 219 (2017).

[37] K. Cho, M. Kończykowski, S. Teknowijoyo, M. A. Tanatar, J. Guss, P. B. Gartin, J. M. Wilde, A. Kreyssig, R. J. McQueeney, A. I. Goldman, V. Mishra, P. J. Hirschfeld and R. Prozorov, Using controlled disorder to probe the interplay between charge order and superconductivity in $NbSe_2$, Nat. Comms. **9**, 2796 (2018).

[38] M. Shenasa, S. Sainkar and D. Lichtman, XPS Study of Some Selected Selenium Compounds, J. Electron. Spec. Rela. Phenom. **40**, 329 (1986).

[39] X. Chia, A. Ambrosi, P. Lazar, Z. Sofer, and M. Pumera, Electrocatalysis of layered Group 5 metallic transition metal dichalcogenides ($MX_2$, M = V, Nb, and Ta; X = S, Se, and Te), J. Mater. Chem. A. **4**, 14241 (2016).

[40] E. Morosan, H. W. Zandbergen, B. S. Dennis, J. W. G. Bos, Y. Onose, T. Klimczuk, A. P. Ramirez, N. P. Ong and R. J. Cava, Superconductivity in $Cu_xTiSe_2$, Nat. Phys. **2**, 544 (2006).

[41] S. H. Huang, G. J. Shu, Woei Wu Pai, H. L. Liu, and F. C. Chou, Tunable Se vacancy defects and the unconventional charge density wave in $1T$-$TiSe_{2-\delta}$, Phys. Rev. B. **95**, 045310 (2017).

[42] L. N. Zelenina, T. P. Chusova and A. N. Titov, Thermodynamic properties of titanium selenides with variable composition $TiSe_2$-$TiSe_{1.80}$, Russ. Chem. Bull. **60**, 581 (2011).

[43] W. Jolie, T. Knispel, N. Ehlen, K. Nikonov, C. Busse, A. Grüneis, and T. Michely, Charge density wave phase of $VSe_2$ revisited, Phys. Rev. B. **99**, 115417 (2019).

# Supplemental material for: "Correlation between crystal purity and the charge density wave in 1$T$-$VSe_2$"

C. J. Sayers,[1,*] L. S. Farrar,[1] S. J. Bending,[1] M. Cattelan,[2] A. J. H. Jones,[3] N. A. Fox,[2,3] G. Kociok-Köhn,[4] K. Koshmak,[5] J. Laverock,[3] L. Pasquali,[5,6,7] and E. Da Como[1]

[1]*Centre for Nanoscience and Nanotechnology, Department of Physics, University of Bath, Bath, BA2 7AY, UK*

[2]*School of Chemistry, University of Bristol, Cantocks Close, Bristol BS8 1TS, UK*

[3]*HH Wills Physics Laboratory, University of Bristol, Tyndall Avenue, Bristol BS8 1TL, UK*

[4]*Material and Chemical Characterisation Facility (MC²), University of Bath, Claverton Down, Bath BA2 7AY, UK*

[5]*IOM-CNR Institute, Area Science Park, SS 14 Km, 163.5, Basovizza, 34149 Trieste, Italy*

[6]*Dipartimento di Ingegneria "Enzo Ferrari", Università di Modena e Reggio Emilia, via P. Vivarelli 10, 41125 Modena, Italy*

[7]*Department of Physics, University of Johannesburg, P.O. Box 524, Auckland Park 2006, South Africa*

*Corresponding author: c.j.sayers@bath.ac.uk

## I. SUMMARY OF SAMPLE PROPERTIES

| $T_g$ (°C) | $T_r$ (°C) | $T_{CDW}$ (K) | RRR range | Comp. | Lattice const. (Å) | |
|---|---|---|---|---|---|---|
| | | | | | $a$ | $c$ |
| 700 | 755 | 104.5 ± 0.9 | 10 - 13 | $VSe_{1.94\pm0.10}$ | 3.3556(3) | 6.1048(8) |
| 660 | 720 | 108.1 ± 1.0 | 12 - 15 | – | 3.3558(2) | 6.1058(2) |
| 630 | 690 | 101.7 ± 0.7 | 10 - 16 | $VSe_{2.25\pm0.10}$ | 3.3569(3) | 6.103(2) |
| 615 | 670 | 111.2 ± 0.6 | 19 - 28 | $VSe_{1.94\pm0.10}$ | 3.3559(5) | 6.104(2) |
| 600 | 655 | 112.3 ± 0.6 | 25 - 31 | $VSe_{1.97\pm0.10}$ | 3.3556(4) | 6.1068(8) |
| 550 | 610 | 112.7 ± 0.8 | 44 - 49 | $VSe_{1.98\pm0.10}$ | 3.3552(4) | 6.108(3) |

TABLE I: Summary of sample properties including; growth temperature ($T_g$), reaction temperature ($T_r$), CDW transition temperature ($T_{CDW}$), range of RRR observed within the batch, chemical composition (Comp.) from XPS measurements, and unit-cell lattice constants from powder x-ray diffraction (PXRD).

Presented in Table. I is a summary of the electronic and physical properties of the sample batches grown at different temperatures. Determination of the electronic properties including RRR and transition temperature, $T_{CDW}$ is discussed in the main text and in supplementary section II.

In order to determine the overall composition of our samples, additional XPS measurements were performed at the Bristol NanoESCA Facility. An unpolarized, non-monochromatic Al-k$\alpha$ ($h\nu = 1486.7$ eV) source was used together with an ARGUS analyser at 45° with respect to the normal of the sample, and the pass energy was 50 eV. The stoichiometry was calculated using the entire area of Se-3$d$ and V-2$p$ photoemission lines, applying a Shirley background subtraction and normalizing the spectra by considering the specific sensitivity factor and inelastic mean-free path. The Se/V ratio of different samples and the composition of $VSe_x$ is shown in Table. I. We believe that the stoichiometry of the 630°C sample is an anomalous result if we compare to trends of the electronic transport and synchrotron XPS in the main text. The crystal available for these measurements was particularly small and it is possible that, despite our best efforts, the surface was only partially cleaved and/or the results are skewed by the overall reduced photoelectron intensity from

the smaller sample.

To determine the crystal lattice constants, powder x-ray diffraction (PXRD) measurements were carried out on a STOE STADI P instrument using Ge-monochromated Cu-K$\alpha$1 radiation ($\lambda$ = 1.54060 Å) operating in transmission mode. The scan range was (20-93)° in $2\theta$. Two Dectris 1K Mythen detectors were used to record data.

The 1$T$-$VSe_2$ crystals were plate-like and even after grinding into a powder, they showed preferred orientation. For peak indexing and refinement of the unit cell, the Werner [1] or Louër [2] algorithms implemented in WINXPOW [3] were used. All samples were successfully indexed to the trigonal ($P\bar{3}m1$) unit cell expected for 1$T$-$VSe_2$ [4]. The resulting lattice parameters are given in Table. I

## II. DETERMINING THE CDW TRANSITION TEMPERATURE

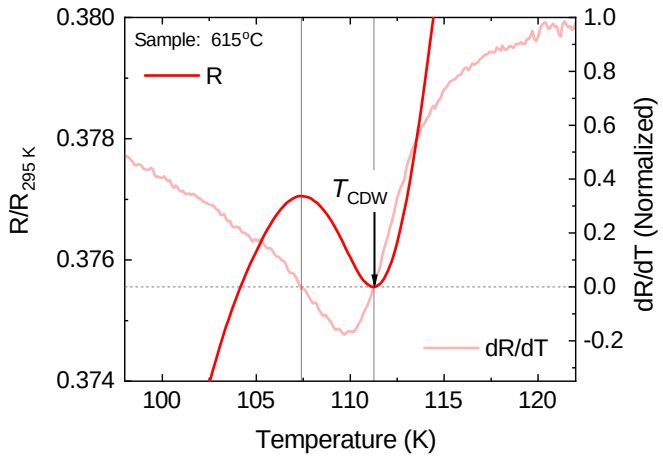


FIG. S1: Determining the CDW transition temperature from resistance measurements. $T_{CDW}$ is the minimum before the inflexion point where the resistance (left axis) starts to increase near ∼110 K, which also corresponds to point at which d$R$/d$T$ (right axis) crosses zero.

As discussed in the main text, the first derivative of resistance, d$R$/d$T$ highlights the CDW transition in 1$T$-$VSe_2$. We define $T_{CDW}$ as the minimum before the inflexion point where the resistance, $R$ begins to increase near ∼110 K as indicated by the arrow in Fig. S1(a). This corresponds to the point at which d$R$/d$T$ initially crosses zero, which is $T_{CDW}$ = (111.2 ± 0.6) K for the 615°C example. The error has been obtained by evaluating the uncertainty

in the $dR/dT = 0$ crossing based on a linear fit to the steep decline before $T_{CDW}$. The same methods were used to define $T_{CDW}$ for all samples in the main text.

Here, we also highlight the two vertical solid lines corresponding to the zero crossing points of $dR/dT$. These points also coincide with the minimum and maximum of the increase in resistance as a result of the CDW transition. In this region, $dR/dT$ becomes negative, and its magnitude below zero therefore provides an indication of the insulating state (resistance increase) that develops near $T_{CDW}$ which is related to the proportion of carriers removed from the Fermi surface at the CDW transition.

## III. TEMPERATURE DEPENDENCE OF THE RESISTANCE

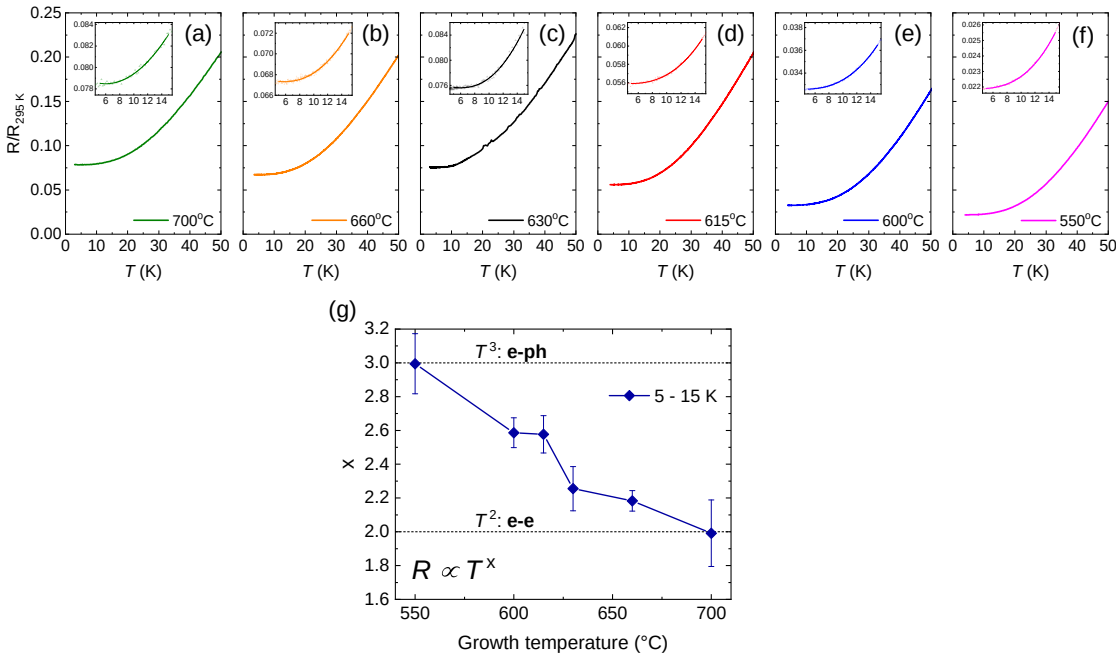


FIG. S2: Temperature dependence of resistance. (a) - (e) Normalized resistance for all samples in the range (4 - 50) K. The inset shows a power law fit, R $\propto T^x$ to the low temperature data (5 - 15 K). (f) x in R $\propto T^x$ as a function of growth temperature. The errors bars are related to the fitting only. The dashed lines indicate the $T^2$ (electron-electron) and $T^3$ (electron-phonon) carrier scattering regimes respectively.

By fitting the low temperature resistance data (5 - 15 K) with a power law it is possible to extract information on the dominant scattering mechanism of electrons. Shown in Fig. S2(a) - (e) is the normalized resistance $< 50$ K for all samples plotted using the same scale. The increasing residual resistance discussed in the main text is obvious here at higher growth temperatures. The insets shows the data ($< 15$ K) with a power law fit. Fig. S2(f) shows the result of the fitting for $x$ in R $\propto T^x$ as a function of growth temperature. The sample grown at 700°C (lowest purity, avg. RRR $\approx$ 11.5) shows a $T^2$ dependence indicating an electron-electron dominated carrier scattering, which has been noted before in this compound [5]. For samples grown at lower temperatures, $x$ progressively increases until it reaches a $T^3$ dependence for the 550 °C sample (highest purity, avg. RRR $\approx$ 46.5) with near ideal stoichiometry ($VSe_{1.98}$). A $T^3$ dependence has been linked to electron-phonon dominated scattering in other TMDs [6]. Interestingly, this evolution seems similar to the trend found for $T_{CDW}$ and RRR in the main text which was linked to the doping level introduced by defects.

## IV. X-RAY SPECTROSCOPY OF VANADIUM CORE LEVELS

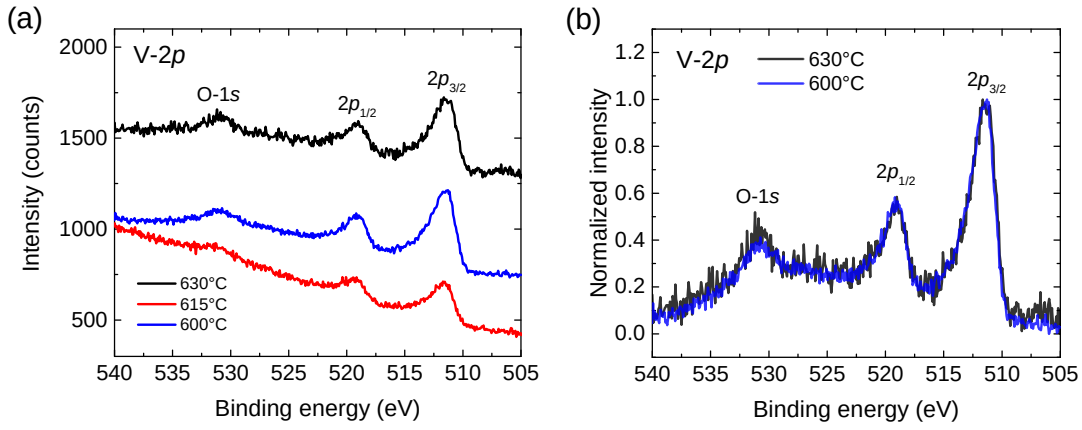


FIG. S3: XPS spectra of V-2$p$ core levels ($h\nu = 630$ eV). (a) Raw data showing the doublet consisting of V-2$p_{1/2}$ and V-2$p_{3/2}$ (b) A direct comparison of the samples with contrasting electronic properties ($T_g = 630$ and 600°C with avg. RRR ~13 and ~28 respectively). The data has been normalized to the V-2$p_{3/2}$ peak, after subtraction of a Shirley background.

In addition to the Se-3$d$ spectra presented in the main text, we obtained additional measurements of the V-2$p$ core levels for 3 samples with a range of growth temperatures over which the electronic properties are changing significantly $T_g$ = (600 - 630)°C. Shown in Fig. S3(a) is the raw V-2$p$ XPS spectra. We find the doublet consisting of V-2$p_{1/2}$ and V-2$p_{3/2}$ at 519.1 eV and 511.3 eV respectively ($\Delta_{so}$ = 7.8 eV). Additionally, there is a small oxygen (*O-1s*) feature at ∼530.7 eV which we believe is not intrinsic to the crystals (see later discussion of XAS data). Our results are qualitatively similar to previous studies of V-2$p$ levels in $1T$-$VSe_2$ [7–10], although there seems to be large variation in the literature. Overall, we find our results are in closest agreement with Ref. [7] if we consider the position of O-1$s$ in that data (531.3 eV) as a reference.

There is no significant variation of the V-2$p$ spectra between our samples as we find the binding energies and lineshape of all features to be nearly identical. This is particularly evident in Fig. S3(b) in which we show the normalized data for the samples with the most contrasting CDW properties ($T_g$ = 630 and 600°C). In addition, we did not observe any features would could be linked to extrinsic vanadium species which has previously been ascribed to interstitials in the van der Waals gap occurring at higher growth temperatures [11]. Therefore, we conclude that there are no significant variations in the vanadium (V-2$p$) states that can explain the observed difference in CDW properties between our samples.

To further examine the vanadium states, we also performed X-ray absorption spectroscopy (XAS) measurements of the V L-edge using the total electron yield (TEY) method of monitoring the drain current on the sample as a function of the incident photon energy. The results are shown in Fig. S4. The main two features at 516.6 eV and 523.6 eV are related to excitations of the V-2$p_{3/2}$ ($L_3$-edge) and V-2$p_{1/2}$ ($L_2$-edge) core levels into unoccupied V-3d states respectively [12].

The XAS spectra for all samples are nearly indistinguishable, both near the V L-edge and O K-edge regions. By examining the O K-edge in these spectra, we suggest that the amount of oxygen throughout our samples is negligible. Instead, the O-1$s$ detected by XPS (Fig. S3) was likely only present on the surface or in the local environment such as the measurement chamber or sample holder, and not intrinsic to the crystals. Therefore, we rule out the presence of oxygen as a possible explanation for the observed difference in CDW properties of our samples.

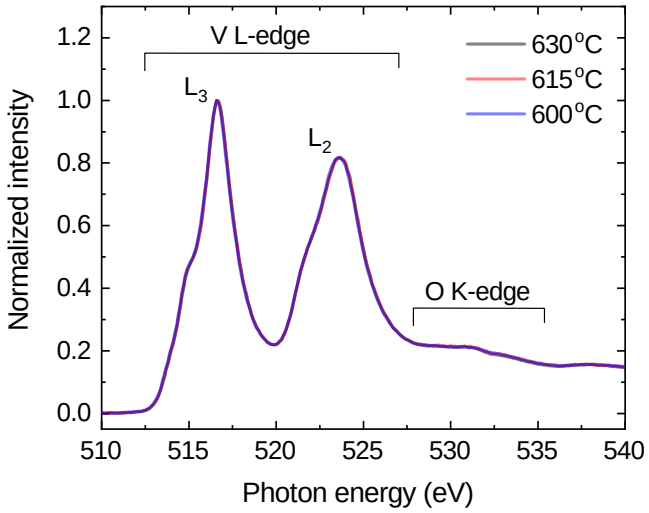


FIG. S4: X-ray absorption spectroscopy (XAS) near the V L-edge and O K-edge. The spectra have been normalized to the maximum of the V $L_3$-edge.

## V. X-RAY SPECTROSCOPY OF IODINE CORE LEVELS

Since iodine is used as the transport agent in the CVT growth process, we looked in the spectral region where we woudl expect I-3$d$ core levels to see if iodine had inadvertently been incorporated into our samples. This effect has been documented in the related compound, 1$T$-$TiSe_2$ in which approx. 0.3 at.% iodine was found regardless of the growth temperature [13] in the range $T_g$ = (600 - 900)°C. In that study, it was found that samples grown using iodine had a slightly reduced CDW transition compared to those grown by direct sublimation in excess Se i.e. without iodine.

Presented in Fig. S5 is the raw XPS data in the spectral region where we expect I-3$d$ core levels. A doublet is expected consisting of I-3$d_{5/2}$ and I-3$d_{3/2}$ at 619.3 and 630.8 eV respectively [vertical dashed lines in Fig. S5]. Based on our data, it is possible to speculate that there is a weak feature in the region (620 - 635) eV but its magnitude is comparable to the noise. At $h\nu$ = 730 eV photon energy, the photoionization cross-section of I-3$d$ should be $\sim$ 2.7 Mbarn, which is more than double the cross-section of V-2$p$ (at $h\nu$ = 630 eV) which was clearly detectable above the noise in our measurements (see Fig. S3). Therefore, we suggest that iodine is either not present in our samples or it is below the detectable limit.

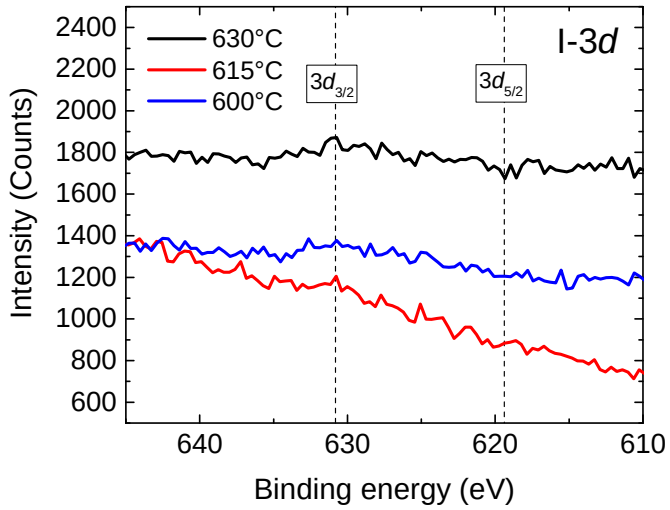


FIG. S5: XPS spectra of I-3$d$ core levels ($h\nu$ = 730 eV). The raw data is shown. The vertical dashed lines indicate the expected peak positions of the I-3$d_{5/2}$ and I-3$d_{3/2}$ doublet.

Moreover, it can be seen that the samples with most contrasting electronic properties ($T_g$ = 630 and 600°C) have nearly identical spectra. Therefore, we can say that if there is iodine present in the crystals, either the concentration does not change significantly with growth temperature and/or it has little effect on the observed CDW properties.

[1] P.E. Werner, L. Eriksson and M. Westdahl, TREOR, a semi-exhaustive trial-and-error powder indexing program for all symmetries, J. Appl. Cryst. **18**, 367 (1985).

[2] A. Boultif and D. Louër, Powder pattern indexing with the dichotomy method, J. Appl. Cryst. **37**, 724 (2004).

[3] WINXPOW: Powder Diffraction Software version, STOE & Cie GmbH, Germany, Software version 3.6.0.1 (Feb 2018).

[4] D. J. Eaglesham, R. L. Withers, and D. M. Bird, Charge-density wave transitions in 1$T$-$VSe_2$, J. Phys. C. **19**, 359 (1986).

[5] A. H. Thompson, and B. G. Silbernagel, Correlated magnetic and transport properties in the charge-density-wave states of $VSe_2$, Phys. Rev. B. **19**, 3420 (1979).

[6] M. Naito and S. Tanaka, Electrical Transport Properties in 2$H$-$NbS_2$, -$NbSe_2$, -$TaS_2$ and -$TaSe_2$, J. Phys. Soc. Jpn. **51**, 219 (2017).

[7] M. Bonilla, S. Kolekar, Y. Ma, H. C. Diaz, V. Kalappattil, R. Das, T. Eggers, H. R. Gutierrez, M.H. Phan and M. Batzill, Strong room-temperature ferromagnetism in $VSe_2$ monolayers on van der Waals substrates, Nat. Nano. **13**, 289 (2018).

[8] Q. Cao, B. Patil, F. F. Yun, F. Xiang,G. Liu, and X. Wang, Defect introduced paramagnetism and weak localization in two-dimensional metal 1$T$-$VSe_2$Nanotechnology. **28**, 475703 (2017).

[9] T. G. U. Ghobadi, B. Patil, F. Karadas, A. K. Okyay, and E. Yilmaz, Catalytic Properties of Vanadium Diselenide: A Comprehensive Study on Its Electrocatalytic Performance in Alkaline, Neutral, and Acidic Media. ACS Omega **2**, 8319 (2017).

[10] Z.-L. Liu, X. Wu, Y. Shao, J. Qi, Y. Cao, L. Huang, C. Liu, J.-O. Wang, Q. Zheng, Z.-L. Zhu, K. Ibrahim, Y.-L. Wang and H.-J. Gao, Epitaxially grown monolayer $VSe_2$: an air-stable magnetic two-dimensional material with low work function at edges, Sci. Bull. **63**, 419 (2018).

[11] F. J. Di Salvo and J. V. Waszczak, Magnetic studies of $VSe_2$, Phys. Rev. B. **23**, 2 (1981).

[12] J. Biener, M. Bäumer, J. Wang, R. J. Madix, Electronic structure and growth of vanadium on $TiO_2$(110), Surf. Sci. **450**, 12 (2000).

[13] F. J. Di Salvo, D. E. Moncton and J. V. Waszczak, Electronic properties and superlattice formation in the semimetal $TiSe_2$, Phys. Rev. B. **14**, 4321 (1976).

## 4.4 Discussion & concluding remarks

The work presented in Section 4.3 provides an important contribution to the understanding of defects in TMD single crystals and in particular, the sensitivity of CDWs to doping. This works represents the first systematic study of the growth temperature on the properties of 1$T$-$VSe_2$ and the nature of defects in this compound. Overall, it was found that increasing the growth temperature reduces both $T_{CDW}$ and the RRR due to a greater density of defects. These general findings are in agreement with previous investigations of 1$T$-$VSe_2$ and related compounds [42, 87, 89] although the presence of metal interstitials, which was previously thought to be the primary form of defect, was not observed. Based on results from a range of experimental techniques, the defects were determined to be predominately Se vacancies. 1$T$-$VSe_2$ becomes overall Se-deficient at elevated growth temperatures which leads to an effective electron doping as the relative amount of V to Se increases. This raises the Fermi level as observed by the rigid shift of Se-3$d$ core levels to deeper binding energies in XPS spectra. This hypothesis was confirmed by annealing experiments which mimic the effects of elevated growth temperatures.

By optimising the crystal growth conditions, samples have been produced with unprecedented purity (RRR $\approx$ 49) which has allowed the determination of the properties of pure 1$T$-$VSe_2$ with a slightly increased transition temperature of $T_{CDW}$ = (112 - 113) K compared to the typically reported value of $\sim$ 110 K. In addition, a $T^3$ dependence of the low temperature resistance was found in the purest samples which was attributed to an electron-phonon scattering mechanism, in contrast to $T^2$ found in doped samples.

With the inclusion of a detailed description of the crystal growth methods, this work will serve as a useful reference for researchers in preparing high-quality single crystal TMDs. A demonstration of the characterisation of such samples and the signatures of crystal defects have been shown using XPS measurements. In the future, a systematic study of 1$T$-$VSe_2$ samples using magnetoresistance and Hall effect measurements could provide additional information about the impact of doping on the carrier densities and mobilities relevant to CDW behaviour [119]. Scanning tunnelling microscopy (STM) experiments similar to Ref. [114] could directly visualise crystal defects in real-space and confirm the presence of Se vacancies in 1$T$-$VSe_2$ suggested by this work. LDOS spectroscopy (i.e. STS) could also investigate the local impact of increasing defect density on the CDW gap structure and long range order.

Since FS nesting is suggested to play an important role in driving the CDW transition in 1$T$-$VSe_2$ [99, 100, 120, 121], knowledge of the electron doping discussed in Section 4.3 may be particularly relevant since any shift in the Fermi level is likely to alter the FS topology and screening effects. In this regard, performing DFT calculations of the band structure and electronic susceptibility [100, 122] with varying position of the Fermi level could provide further insights into the relevance of nesting instabilities and strength of CDW order.

# Chapter 5

# Understanding the role of excitons and phonons in the charge density wave of 1 $T$-$TiSe_2$

## 5.1 Preamble

1 $T$-$TiSe_2$ undergoes a second-order phase transition at $T_{CDW} = 202$ K to a commensurate CDW which can be seen as anomalies in electronic transport such as resistivity [42] and heat capacity measurements [123], amongst others. Diffraction experiments reveal well-resolved superlattice peaks due to a $2a_0 \times 2a_0 \times 2c_0$ periodic lattice distortion (PLD) [42]. Superconductivity can be induced via doping [10] or pressure [124] and emerges upon suppression of the CDW order. As such, 1 $T$-$TiSe_2$ is often used as a model material to investigate the phenomenon of competing CDWs and superconductivity [10, 125]. In fact, continuous control between these strongly-correlated states has been demonstrated by doping the system using electrostatic gating [14]. Further interest in this material was driven by reports of *chiral* ordering of the CDW wavevector which form clockwise and anti-clockwise domains within a single sample [126]. It was later revealed that 1 $T$-$TiSe_2$ may undergo a sequence of two separate phase transitions [127, 128], where the first is related to the well-known CDW transition at $T_{CDW} \approx 200$ K which is followed by the onset of chiral ordering, $T_{chiral}$ at a slightly lower temperature. The chiral charge ordering has been predicted to be optically gyrotropic due to inversion symmetry breaking, and was proposed as a means to observe this unusual state experimentally [129].

In order to fully understand these interesting phenomena, an unambiguous knowledge of the CDW driving mechanism is first required. However, despite decades of research into the properties of 1 $T$-$TiSe_2$, the precise origin of the CDW remains elusive. Various scenar-

ios have been proposed from either a purely electronic origin, such as the excitonic insulator mechanism [28], to an electron-phonon mediated Jahn-Teller type [130]. Generally, it is accepted that neither type of mechanism can solely explain the formation of CDWs in this material and instead, a combination of both excitonic and lattice effects may be important [131–135]. One of the recurring problems in resolving the debate about the origin of the CDW is disentangling the separate electronic and lattice orders. Nearly all theoretical and experimental approaches will have some limitations such that the various physical processes cannot be easily distinguished. Recently, time-resolved optical [132, 136] and photoemission [137–139] pump-probe experiments have allowed the possibility of studying the dynamics of CDW *melting* and *recovery* following perturbation with an intense laser pulse. In these experiments, sufficient energy is supplied to partially suppress the CDW or completely switch from CDW to normal phase. Different types of CDW insulator are expected to respond with characteristic time scales depending on the dominant processes, allowing a classification of these materials in the time-domain [140]. Examples include the build up of electronic screening on the order of (10 - 100) fs, amplitude mode oscillations on the order of (100 - 1000) fs, or the triggering of atomic relaxation (several ps) [140]. Notably, a great advancement in the field was achieved by Porer *et al.* whereby THz radiation was used to observe quenching of the plasmon mode in 1$T$-$TiSe_2$ related to the excitonic component of the CDW, whilst the PLD was found to exist in a metastable non-thermal phase in the absence of exciton correlations [132].

In this chapter, the results of an experimental study will be presented based on complementary techniques of time- and -angle resolved photoemission spectroscopy (TR-ARPES) and time-resolved reflectivity (TRR). Previous TR-ARPES studies have focused on the dynamics of the weak valence band replica intensity at the $\overline{\text{M}}$-point [133, 137]. However, in the work by Hedayat *et al.* entitled "Excitonic and lattice contributions to the charge density wave in 1$T$-$TiSe_2$ revealed by a phonon bottleneck" [79], photo-induced suppression of the CDW gap, $\Delta_{\text{CDW}}$ is tracked directly by measuring the dynamics of the valence band maximum close to the $\bar{\Gamma}$-point, which is made possible by the excellent temporal and energy resolution of the experimental setup [73]. A detailed laser fluence-dependence of these dynamics, together with the observation of coherent phonon oscillations, allows a scenario for the CDW driving mechanism to be proposed. The work is supported by a modified Rothwarf-Taylor (R-T) rate equation model [78, 141] in order to establish the role of excitons and phonons in this complex system.

## 5.2 Introduction

### 5.2.1 On the origin of the CDW

CDW formation in simple 1D metallic systems can be explained by Fermi surface (FS) nesting and has also been applied to the group-V TMDs [2]. However, this scenario has generally been ruled out in the case of 1 $T$-$TiSe_2$ because of the complete absence of parallel portions of FS [21]. As such, several alternative explanations have been developed.

Following early experimental investigations of 1 $T$-$TiSe_2$, it was suggested that CDW formation could naturally be explained by an *excitonic insulator* mechanism, driven by electron-hole coupling, owing to its suitable band structure and low free carrier density [42]. First predicted in 1967 by *Jérome, Rice & Kohn*, an insulating state was said to develop in semiconductors or semimetals with very small band gaps or band overlaps [28]. If the coulomb interaction is weakly screened, it may be sufficient to bind together electrons from the conduction band (CB) and holes from the valence band (VB) to form excitons, as illustrated in Figure 5.1.

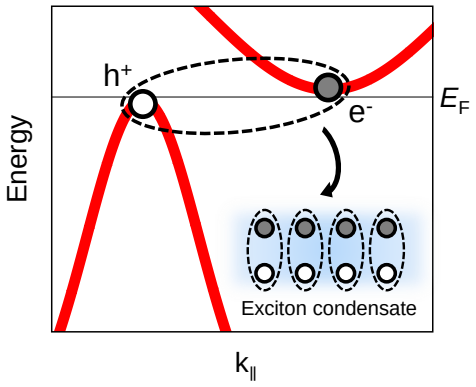


**Figure 5.1:** Excitonic insulator mechanism. Weakly screened electrons ($e^-$) and holes ($h^+$) in the conduction and valence bands of a semiconductor or semimetal with small band gap or overlap couple via the coulomb interaction to form a condensate of excitons at low temperature.

At low temperature this mechanism may become energetically favourable, thus triggering a transition to the excitonic insulator phase, and excitons will spontaneously condense into a macroscopic coherent state, known as *exciton condensation*. In the normal phase, 1 $T$-$TiSe_2$ is either a semiconductor [142,143] or a semimetal [42,144] with a small indirect energy gap (or overlap) between the hole-like VB and electron-like CB on the order of meV, and a reasonably low free carrier density of approximately $n \approx 10^{20}$ cm$^{-3}$ [42, 144, 145]. Hence, there are clear similarities between the properties of 1 $T$-$TiSe_2$ and the criteria outlined in the theory of *Jérome, Rice & Kohn*. Numerous theoretical and experimental

studies have since supported the excitonic insulator scenario and some argue that the CDW is purely of electronic origin [146–148] which can also account for the PLD [149]. Compelling evidence for this scenario was provided by the recent observation of a soft plasmon mode near the expected $\mathbf{q}_{\mathrm{CDW}}$ [27], a purely electronic analogue of the Kohn anomaly described previously in Section 1.2.3.

An entirely different scenario is based on a band-type Jahn-Teller effect [24, 150] and relies on arguments about atomic displacements and the nature of the lowest energy $d$-band [130]. This electron-phonon driven effect is defined by a splitting of the degenerate CB due to the lattice distortion, although it differs from the standard Jahn-Teller effect in that the splitting occurs around the unoccupied states. As the CB splits, the bottom portion cannot overlap with the VB due to electron-hole coupling and therefore, the VB is forced to shift downwards, resulting in a lowering of the electronic energy [142]. The importance of electron-phonon coupling in $1T$-$TiSe_2$ was highlighted by high-resolution inelastic x-ray scattering which found softening of an optical phonon mode near the $L$-point at $T_{\mathrm{CDW}}$ [26].

Thus far, two conflicting scenarios of CDW formation have been discussed; either purely electronic (exciton condensation) or electron-phonon driven (Jahn-Teller type). However, it has been suggested that both mechanisms could in fact contribute partially to the CDW [131], with increasing experimental evidence in support of this hypothesis [132, 133, 142]. Disentangling the separate contributions of excitonic and lattice order in $1T$-$TiSe_2$ is the purpose of the work presented in Section 5.3.

### 5.2.2 Signatures of CDW order in electronic and lattice structure

#### Brillouin zone

In the CDW phase, the PLD is defined by a doubling of the original unit cell ($2a_0 \times 2a_0 \times 2c_0$) and hence the BZ is halved in reciprocal space. As a result, the A-, L- and M-points of the hexagonal BZ (see Figure 1.7) become equivalent to $\Gamma$ in the repeated zone scheme [142]. Figure 5.2 shows an illustration of original normal phase BZ and the reconstructed BZ in two dimensions. This reconstruction has important consequences for the electronic and lattice structure in the CDW phase, as there will be modifications to both the electronic band and phonon dispersions respectively, governed by the new BZ boundaries. The equivalency of $\overline{\mathrm{M}}$ and $\overline{\Gamma}$, highlighted in Figure 5.2, is particularly relevant

to the electronic structure as will be discussed in the following section.

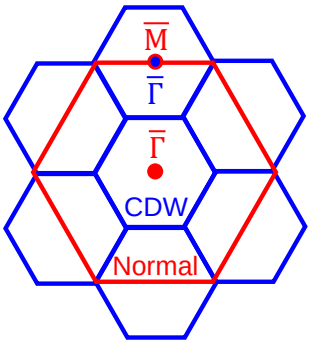


**Figure 5.2:** The BZ of the normal phase (red) is halved as a result of the $2a_0 \times 2a_0 \times 2c_0$ lattice reconstruction in the CDW phase (blue). The $\bar{\Gamma}$ and $\overline{\mathrm{M}}$ points become equivalent.

### Electronic structure

The Fermi surface (FS) of $1T$-$TiSe_2$ consists of a Se-4$p$ derived hole pocket at the BZ centre ($\Gamma$-point) and elliptical Ti-3$d$ derived electron pockets at each of the BZ boundaries (L-point), which are slightly elongated in the L-M direction [145]. A sketch is shown in Figure 5.3(a) and is compared to the experimental FS measured by full-wavevector ARPES in Figure 5.3(b). Here, the overbar notation is used to represent the projection of the high-symmetry points from the $k_z = 0$ plane onto the experimental $k_z$ image plane. In this notation, the hole and electron pockets are located at $\bar{\Gamma}$ and $\overline{\mathrm{M}}$ respectively, following the convention of other photoemission studies [133, 137, 147].

Figure 5.4 shows the results of full-wavevector ARPES measurements of $1T$-$TiSe_2$ in the normal (300 K) and CDW phase (30 K) over the range $E - E_\mathrm{F} = (-0.8 - 0.2)$ eV in steps of 12.5 meV, and an overall energy resolution of $\sim$ 40 meV. A suitable region of cleaved crystal surface was identified using PEEM as shown in Figure 5.4(c). ARPES spectra were then acquired from a $\sim$ 40 $\mu$m$^2$ region of the sample, by closing an aperture to the detection optics as shown by the hexagonal outline in the same panel.

Band dispersions along the directions indicated in Figure 5.4(a) are extracted in order to show the main features of the electronic structure. Figure 5.4(b) shows the normal phase dispersion along the $\overline{\mathrm{M}}$-$\bar{\Gamma}$ direction which consists of a steeply dispersing hole-like Se-4$p$ valence band (VB) at $\bar{\Gamma}$ and a shallower electron-like Ti-3$d$ conduction band (CB) at $\overline{\mathrm{M}}$ that slightly crosses $E_\mathrm{F}$. It is interesting to note the significant spectral intensity of CB states that appear above $E_\mathrm{F}$ which should be normally unoccupied. This effect has been reported previously in $1T$-$TiSe_2$ and was attributed to the narrow band width and flat dispersion within $5k_BT$ of $E_\mathrm{F}$, allowing considerable thermal occupation [21, 151]. It can

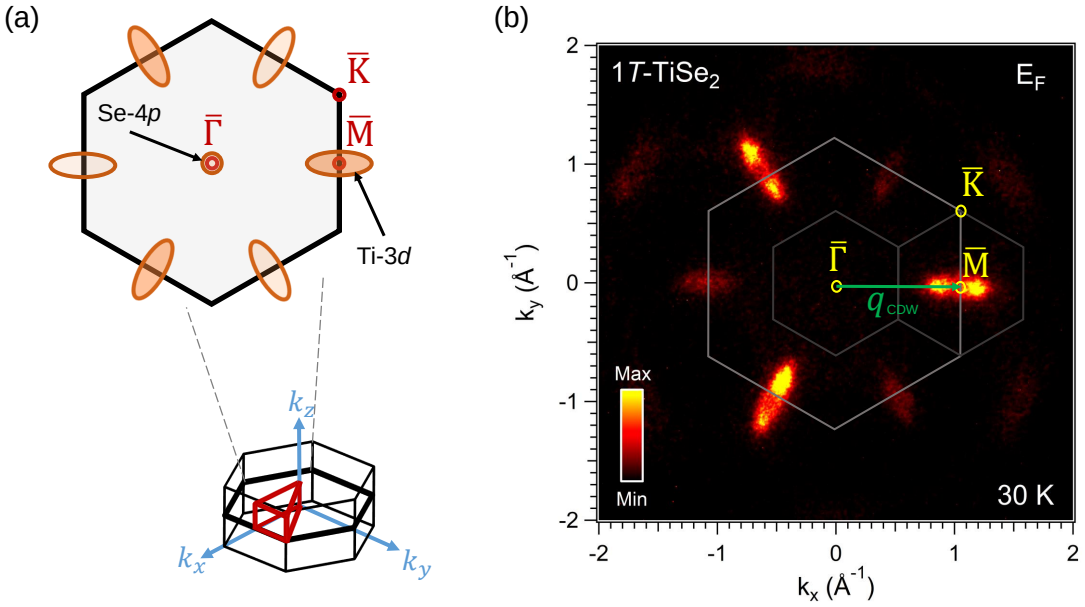


**Figure 5.3:** Fermi surface (FS) of 1$T$-$TiSe_2$. (a) Sketch of the FS showing the hole (Se-4$p$) and electron (Ti-3$d$) pockets at the $\bar{\Gamma}$ and $\bar{\mathrm{M}}$ points of the hexagonal BZ respectively. (b) Full-wavevector ARPES image of the experimental FS in the CDW phase (30 K). The projection of the high-symmetry points onto the experimental $k_z$ image plane are labelled. The large and small hexagons represent the original (normal phase) and reconstructed (CDW phase) BZ. The green arrow indicates the projected CDW wavevector, $\mathbf{q}_{\mathrm{CDW}}$.

also be seen that the VB is comprised of two Se-4$p$ derived subbands [135, 137, 152]. The slight asymmetry in the spectral intensity along the $\bar{\mathrm{M}}$-$\bar{\Gamma}$-$\bar{\mathrm{M}}$ direction likely arises from a matrix element effect. Instead, the dispersion along the $\bar{\mathrm{K}}$-$\bar{\Gamma}$-$\bar{\mathrm{K}}$ direction in Figure 5.4(e) shows the individual subbands clearly where the intensity is uniform and is highlighted further in the MDC overlay extracted from $E - E_{\mathrm{F}} = -0.6$ eV.

Upon entering the CDW phase, there are two main features which develop in the electronic structure which are consistently reported in the literature, and these are discussed in the remainder of this section.

Firstly, as a result of the $2a_0 \times 2a_0 \times 2c_0$ PLD and the equivalent high-symmetry points in the reconstructed BZ (see Figure 5.2), the original VB at $\bar{\Gamma}$ is folded onto the $\bar{\mathrm{M}}$-point and similarly the original CB at $\bar{\mathrm{M}}$ is folded onto the $\bar{\Gamma}$-point. In Figure 5.4(b), a clear replica of the VB at the $\bar{\mathrm{M}}$-point is visible at 30 K. This band folding effect is particularly strong in 1$T$-$TiSe_2$ and there is a significant transfer of spectral weight to the VB replica which has been consistently reported in numerous ARPES studies [135, 151]. By contrast,

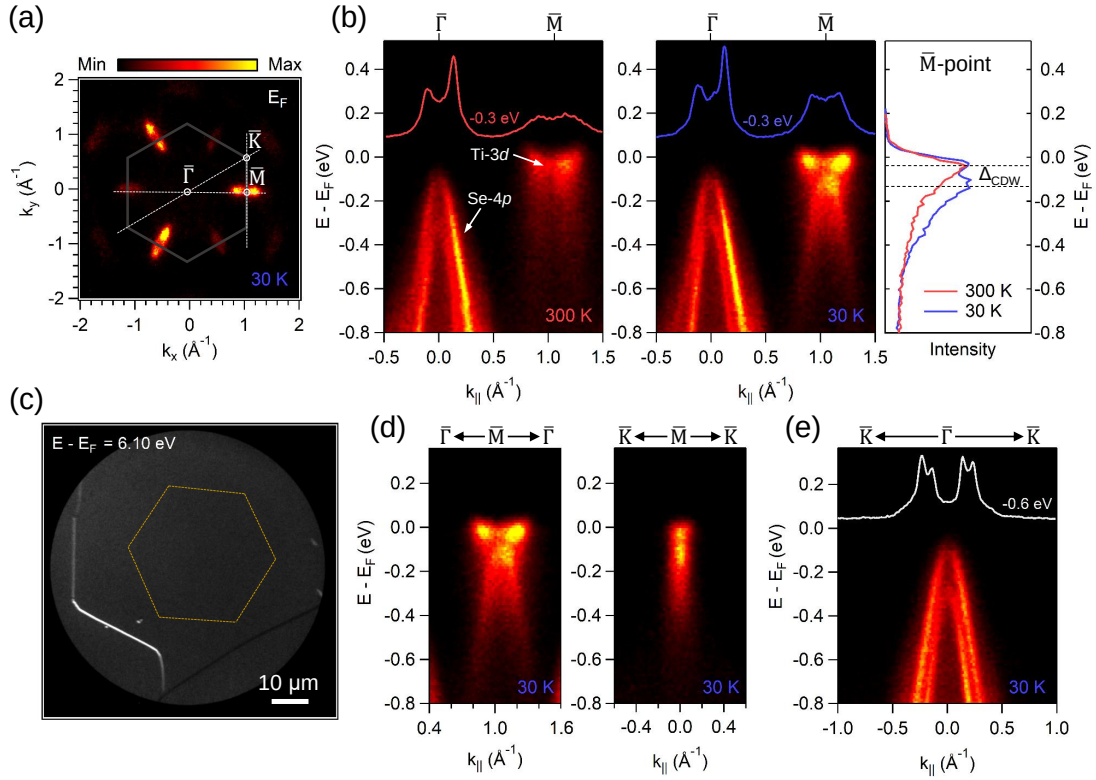


**Figure 5.4:** Full-wavevector ARPES of 1 $T$-$TiSe_2$. (a) Fermi surface with a sketch of the normal phase BZ overlaid. The dashed lines indicate the momentum direction for panels (b) - (e). (b) Comparison of the dispersion along the $\overline{\Gamma}$-$\overline{M}$ direction in the normal (300 K) and CDW (30 K) phase respectively. The top of each panel shows an MDC along $E - E_F = -0.3$ eV. The far right panel shows EDCs from the $\overline{M}$-point. The horizontal dashed lines show the CDW gap, $\Delta_{CDW}$ in the 30 K spectrum. (c) PEEM image of the 1 $T$-$TiSe_2$ surface where the total field of view is 74.5 $\mu$m. The orange hexagon is an outline of the aperture during the ARPES measurements and marks the region of the surface where data was acquired. (d) Comparison of the dispersion at the $\overline{M}$-point along the $\overline{\Gamma}$-$\overline{M}$-$\overline{\Gamma}$ and $\overline{K}$-$\overline{M}$-$\overline{K}$ directions. (e) Dispersion along the $\overline{K}$-$\overline{\Gamma}$-$\overline{K}$ direction highlighting the two valence subbands. The white trace is an MDC along $E - E_F = -0.6$ eV.

the CB replica intensity is either extremely weak [135] or entirely not visible [146, 149], as is the case in Figure 5.4(b). Interestingly, a broad outline of the VB replica can already be seen at 300 K as there is spectral intensity that extends far below the CB minimum at the $\overline{M}$-point, although there is no obvious parabolic dispersion. Comparison of the un-normalised MDCs at $E-E_F$ = –0.3 eV reveals that approximately 50% of the 30 K VB replica intensity is already present at 300 K. These observations have previously been related to significant fluctuations of CDW order far above $T_{CDW}$ [146, 152]. Finally, it is interesting to note the contrast between the clear dispersion of the folded VB along

the $\bar{\Gamma}$-$\bar{M}$-$\bar{\Gamma}$ direction which follows the long-axis of the elliptical electron pocket and the apparent lack of dispersion along the $\bar{K}$-$\bar{M}$-$\bar{K}$ direction in Figure 5.4(d). Since the original VB at $\bar{\Gamma}$ is entirely symmetric in all directions, this suggests that only the portion of the dispersion along the same direction as $\mathbf{q}_{CDW}$ is folded to the $\bar{M}$-point.

The second feature of the CDW phase is the opening of a gap, $\Delta_{CDW}$ near $E_F$. This is predominantly seen as a downshift in the VB at $\bar{\Gamma}$ [142, 152] and results in an overall reduction in the electronic energy as the occupied states are lowered. EDCs extracted along the $\bar{M}$-point in Figure 5.4(b) show a gap between the CB and VB replica of $\Delta_{CDW} = (90 \pm 5)$ meV at 30 K in reasonable agreement with previous studies [135, 142, 152]. Referring back to the experimental FS in Figure 5.3(b), lowering of the VB due to the opening of a gap, results in the loss of the Se-4$p$ hole pocket from the FS in addition to an obvious loss of intensity at the centres of the elliptical Ti-3$d$ electron pockets. The latter is reflected in the band dispersion of Figure 5.4(b) whereby the original shallow parabolic CB in normal phase assumes a *mexican hat* shape with double-minima in the CDW phase [147, 149], a feature commonly associated with an excitonic insulator [153].

### Lattice structure

According to Section 1.4.4, there are two Raman-active modes for the lattice structure of 1$T$-$TiSe_2$ with $E_g$ and $A_{1g}$ symmetry which correspond to the in-plane and out-of-plane vibrations of Se atoms around a central Ti atom, respectively.

Figure 5.5 shows Raman spectroscopy measurements of 1$T$-$TiSe_2$. In the normal phase (300 K), the two expected Raman modes; $E_g$ and $A_{1g}$ are found at 136 cm$^{-1}$ ($\sim$ 4.1 THz) and 201 cm$^{-1}$ ($\sim$ 6.0 THz) respectively, in good agreement with previous studies [55, 154]. In the CDW phase (80 K), reconstruction of the BZ due to the $2a_0 \times 2a_0 \times 2c_0$ PLD discussed previously, means that several branches of the phonon dispersion (see Section 5.3.3) will be folded to the $\Gamma$-point and therefore become detectable in Raman spectroscopy as mentioned in Section 2.7. As a result, two new modes are visible; $E_g^*$ and $A_{1g}^*$ which are found at 73 cm$^{-1}$ ($\sim$ 2.2 THz) and 112 cm$^{-1}$ ($\sim$ 3.4 THz) respectively, and the latter is the well-known CDW amplitude mode which is commonly observed as coherent oscillations in time-resolved studies [132, 133, 136]. The emergence of these modes with reducing temperature below $T_{CDW}$ is second-order and is discussed further in Section 5.3.3.

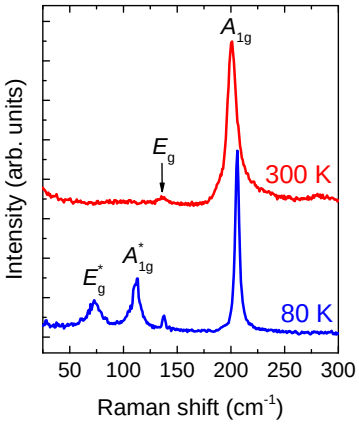


**Figure 5.5:** Raman spectroscopy of $1T$-$TiSe_2$. There are two Raman-active modes in the normal phase (300 K); $E_g$ and $A_{1g}$ which correspond to the in-plane and out-of-plane vibrations of Se atoms around a central Ti atom, respectively. In the CDW phase (80 K), two additional modes become visible due to the PLD; labelled $E_g^*$ and $A_{1g}^*$, where the latter is commonly referred to as the CDW amplitude mode. Spectra are offset for clarity.

## 5.3 Publication entitled: "Excitonic and lattice contributions to the charge density wave in $1T$-$TiSe_2$ revealed by a phonon bottleneck"

<table>
<tr><td colspan="5">This declaration concerns the article entitled:<br>Excitonic and lattice contributions to the charge density wave in $1T$-$TiSe_2$ revealed by a phonon bottleneck</td></tr>
<tr><td colspan="5">Publication status (tick one)</td></tr>
<tr><td>Draft manuscript</td><td>Submitted</td><td>In review</td><td>Accepted</td><td>Published</td></tr>
<tr><td></td><td></td><td></td><td></td><td>✓</td></tr>
<tr><td>Reference</td><td colspan="4">H. Hedayat, C. J. Sayers, D. Bugini, C. Dallera, D. Wolverson, T. Batten, S. Karbassi, S. Friedemann, G. Cerullo, J. van Wezel, S. R. Clark, E. Carpene and E. Da Como. Excitonic and lattice contributions to the charge density wave in $1T$-$TiSe_2$ revealed by a phonon bottleneck. Physical Review Research 1 023029 (2019).</td></tr>
<tr><td>Candidate's contribution to the paper</td><td colspan="4">The candidate produced the samples and performed several supporting experiments. The simulations were carried out solely by the candidate. The candidate was involved signficantly in the interpretation of results and performed a large portion of the data analysis. All figures in the main manuscript and supplementary information were produced by the candidate. The candidate wrote the supplementary information and sections of the main manuscript.<ul><li>Formulation of ideas: 40%</li><li>Design of methodology: 25%</li><li>Experimental work: 25%</li><li>Computational work: 100%</li><li>Presentation of data in journal format: 60%</li></ul></td></tr>
<tr><td>Statement from candidate</td><td colspan="4">This paper reports on original research I conducted during the period of my Higher Degree by Research candidature.</td></tr>
<tr><td colspan="3">Signature:</td><td colspan="2">Date:</td></tr>
</table>

PHYSICAL REVIEW RESEARCH **1**, 023029 (2019)

# Excitonic and lattice contributions to the charge density wave in $1T$-$TiSe_2$ revealed by a phonon bottleneck

H. Hedayat,[1] C. J. Sayers,[2] D. Bugini,[1] C. Dallera,[1] D. Wolverson,[2] T. Batten,[3] S. Karbassi,[4] S. Friedemann,[4] G. Cerullo,[1] J. van Wezel,[5] S. R. Clark,[4,6] E. Carpene,[7] and E. Da Como[2,*]

[1]*Dipartimento di Fisica, Politecnico di Milano, 20133 Milano, Italy*

[2]*Department of Physics, Centre for Nanoscience and Nanotechnology (CNAN) and Centre for Photonics and Photonic Materials (CPPM), University of Bath, Bath BA2 7AY, United Kingdom*

[3]*Renishaw PLC, Wotton-under-Edge GL12 7DW, United Kingdom*

[4]*HH Wills Physics Laboratory, University of Bristol, Bristol BS8 1TL, United Kingdom*

[5]*Institute for Theoretical Physics, Institute of Physics, University of Amsterdam, 1090 GL Amsterdam, Netherlands*

[6]*Max Planck Institute for the Structure and Dynamics of Matter, CFEL, Hamburg, Germany*

[7]*IFN-CNR, Dipartimento di Fisica, Politecnico di Milano, 20133 Milano, Italy*

(Received 12 April 2019; published 26 September 2019)

Understanding collective electronic states such as superconductivity and charge density waves is pivotal for fundamental science and applications. The layered transition metal dichalcogenide $1T$-$TiSe_2$ hosts a unique charge density wave (CDW) phase transition whose origins are still not fully understood. Here, we present ultrafast time- and angle-resolved photoemission spectroscopy (TR-ARPES) measurements complemented by time-resolved reflectivity (TRR) which allows us to establish the contribution of excitonic and electron-phonon interactions to the CDW. We monitor the energy shift of the valence band (VB) and coupling to coherent phonons as a function of laser fluence. The VB shift, directly related to the CDW gap closure, exhibits a markedly slower recovery dynamics at fluences above $F_{th} = 60\,\mu J\,cm^{-2}$. This observation coincides with a shift in the relative weight of coherently coupled phonons to higher-frequency modes in TRR, suggesting a phonon bottleneck. Using a rate equation model, the emergence of a high-fluence bottleneck is attributed to an abrupt reduction in coupled phonon damping and an increase in exciton dissociation rate linked to the loss of CDW superlattice phonons. Thus, our work establishes the important role of both excitonic and phononic interactions in the CDW phase transition and the advantage of combining complementary femtosecond techniques to understand the complex interactions in quantum materials.

DOI: 10.1103/PhysRevResearch.1.023029

## I. INTRODUCTION

Charge density waves (CDWs) are an important component in phase diagrams of many correlated electron systems [1,2]. Typically observed in low-dimensional materials, the signatures of a CDW phase have been reported in two-dimensional transition metal dichalcogenides (TMDs) [3], cuprate superconductors [4], $\pi$-conjugated polymers [5], and metal oxides [6]. The central importance of CDW states arises from the relationship between fluctuations in their order parameter and superconductivity, Mott insulating states, and spin density waves [1,7]. In the TMD $1T$-$TiSe_2$ superconductivity appears in proximity to CDW incommensurability [8], which can be achieved by pressure [9], copper doping [10], or electrostatic gating [11]. Thus, understanding of the CDW transition mechanism for this material has attracted considerable scientific interest, especially concerning its driving mechanism [12–14].

The CDW phase in $1T$-$TiSe_2$ is achieved upon cooling below $T_{CDW} = 202$ K, where the hexagonal lattice of the *normal phase* found at room temperature undergoes a reconstruction forming a $2a \times 2a \times 2c$ superlattice. This structural fingerprint, denoted here as *periodic lattice distortion* (PLD), occurs together with the opening of an electronic gap ($\Delta = 130$ meV at 80 K), which is large compared to other TMDs exhibiting a CDW [2,15]. Following early experiments on $TiSe_2$, it was suggested that the CDW state is in fact an excitonic insulator stabilized by Coulomb interactions [16,17], owing to the semimetallic character of the band structure, featuring holes in the Se-4$p$ valence band (VB) at the $\bar{\Gamma}$ point and electrons in the Ti-3$d$ conduction band (CB) at the $\bar{M}$ point of the first Brillouin zone (BZ) [Fig. 1(a)]. Thus, the presence of a PLD and excitons motivated several experimental and theoretical studies aimed at identifying the role of phonons compared to Coulomb interactions [12,15,18,19]. These efforts have highlighted $1T$-$TiSe_2$ as a model system for studying many-body electron and phonon interactions in condensed matter physics and recently culminated with the report of Bose-Einstein condensation of excitons in this material [20].

When compared to other CDW materials of the TMD family, $1T$-$TiSe_2$ has small atomic displacements in going from the normal phase structure to the PLD, only ~0.02 Å [21], in

*edc25@bath.ac.uk

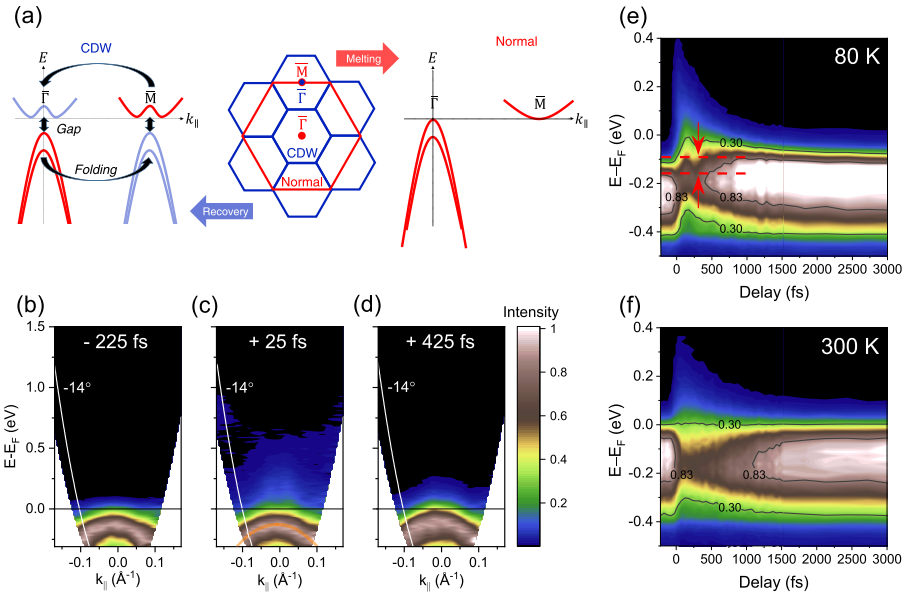


FIG. 1. Valence band dynamics in the CDW and normal phase of $1T$-$TiSe_2$. (a) Sketch of the $TiSe_2$ band structure when switching between the CDW phase (blue) and normal phase (red), together with the projection of the first Brillouin zone (BZ) similar to the one reported in Ref. [53]. Band folding arising from the $2a \times 2a \times 2c$ PLD is indicated by the curved arrows as $\bar{\Gamma}$ and $\bar{M}$ become equivalent. Vertical arrows show the lowering of the VB maximum due to the formation of a CDW gap, $\Delta$, near the Fermi level. (b)–(d) Time evolution of the ARPES maps in the CDW phase along the $\bar{K}$-$\bar{\Gamma}$-$\bar{K}$ direction at select pump-probe delays for 125 $\mu$J cm$^{-2}$ fluence. The orange line in (c) is a guide to the eye for the VB dispersion. It corresponds to an effective mass of $-0.35m_e$ which is comparable to previous reports [23,54]. The $-14°$ angle for the analysis of the VB dynamics is shown as the white solid line. (e), (f) VB dynamics at 80 and 300 K, respectively, for a pump fluence of 250 $\mu$J cm$^{-2}$. The red dashed lines in the 80 K plot indicate the maximum VB shift after pump excitation. The black curves indicate contours at different ARPES intensity. Close inspection of the VB spectra [panels (e), (f)] reveal two subbands which are analyzed separately in the Supplemental Material for completeness [34].

stark contrast to changes of up to 0.1 Å observed in $1T$-$TaS_2$, for example [18]. The small PLD has been argued to indicate the limited importance of electron-phonon coupling in driving the CDW, thus favoring a purely excitonic mechanism [2,22]. The typical and consistently reported signatures of the CDW transition in $1T$-$TiSe_2$ are a downwards shift of the VB energy [23], as a consequence of the CDW gap ($\Delta$) opening, and the presence of backfolded VB appearing in momentum space at $\bar{M}$, consistent with the superlattice structure as sketched in Fig. 1(a) (the in-plane $2a \times 2a$ reconstruction results in $\bar{M}$ being at the center of the reconstructed BZ) [24,25]. However, these important observations, reported by steady-state angle-resolved photoemission spectroscopy (ARPES), have failed to conclusively identify the excitonic or lattice contribution to the CDW.

Ultrafast spectroscopy is the experimental tool of choice to probe out-of-equilibrium phenomena in correlated electron systems [26–29]. One of the central themes in this research field is *bottleneck* dynamics, where out-of-equilibrium phonons impede excited carriers from rejoining the CDW or superconducting condensate [26,29,30]. Previous ultrafast studies on $TiSe_2$ have not reported such bottleneck effects or used them to disentangle the excitonic and electron-phonon contributions to the CDW [31–33]. Nevertheless, recent experimental evidence based on optical pump–THz probe has shown how excitonic order can be transiently suppressed at any sample temperature below $T_{CDW}$, but with the PLD remaining robust only up to 150 K [13]. Also, signatures of phonon driven oscillations in the CDW recovery have been seen by time- and angle-resolved photoemission spectroscopy (TR-ARPES) clearly suggesting a role for phonons [33]. While such reports cast doubts on a purely excitonic picture, they also open several critical questions: Are phonons and excitons only weakly coupled? How and on what timescale does the lattice dynamics contribute to the CDW recovery? More generally, to what extent is the electron-phonon coupling involved in the CDW formation? To address some of these questions which are also relevant for other CDW materials, a combination of complementary ultrafast spectroscopies is required. While most previous studies used only a single technique, a holistic understanding of the phenomena can be obtained when perturbations to the CDW induced by pump pulses are monitored both in the electronic band structure, for example, using ARPES, and in the PLD, by a complementary phonon sensitive spectroscopic probe.

Here, we use TR-ARPES and TRR to clarify how phonon dynamics in $1T$-$TiSe_2$ influences the CDW *recovery* following transient perturbation by 30-fs, 1.82-eV light pulses. In TR-ARPES, thanks to a purposely designed combination of time resolution (<70 fs), energy resolution (∼53 meV), and sensitivity at low laser fluence (enabled by the 80-kHz laser repetition rate), we are able to probe the VB dynamics. We

find three distinct *out-of-equilibrium regimes* as a function of excitation fluence. At fluences below $F_{\rm th} = 60\,\mu{\rm J\,cm^{-2}}$ the weakly perturbed CDW recovers within a short timescale of 2 ps. Above this fluence the CDW is still partially present, but its recovery exhibits a bottleneck concomitant with a change in the coherently coupled phonons seen in TRR. With the help of a rate equation model we describe how phonons contribute to the recovery dynamics. Finally, for a fluence above $F_{\rm CDW} = 200\,\mu{\rm J\,cm^{-2}}$, we enter a third regime with a transient complete suppression of the CDW.

## II. METHODS

High-quality $1T$-$TiSe_2$ single crystals were grown using the chemical vapor transport method. Titanium (99.9%) and selenium (>99.9%) powders were sealed inside an evacuated quartz ampoule, together with iodine (>99.9%) which acts as the transport agent. To ensure the correct stoichiometry, a slight selenium excess was included. Single crystals with a typical size of $4 \times 4 \times 0.1\,{\rm mm^3}$ were selected for TR-ARPES measurements. The Supplemental Material [34] shows resistivity as a function of temperature, where the salient features of the CDW transition appear below 202 K and confirms the high quality of our samples as discussed in Ref. [16].

TR-ARPES experiments were performed using a custom setup [35] based on a high-repetition-rate amplified Yb laser (Pharos, Light Conversion) operated at 80 kHz. The pulses from this laser, 290 fs in duration and at 1030 nm, are used to pump a noncollinear optical parametric amplifier (NOPA) which outputs 30-fs pulses at 680 nm (1.82 eV). The NOPA output is used both as the pump beam in our TR-ARPES experiment and also to generate the 205-nm (6.05 eV) probe beam for photoemission, through a series of nonlinear optical processes [35]. The time resolution (cross correlation between pump and probe pulses) is 65 fs, while energy resolution is ∼53 meV. In order to measure angle-resolved photoemission we used a time-of-flight detector and spectra for different angles were recorded by rotating the crystal with respect to the analyzer [34]. Our photon energy allows us to probe up to $\pm 0.2\,{\rm \AA^{-1}}$ within the BZ, which is sufficient to clearly observe the dynamics of charge carriers in the vicinity of the $\bar{\Gamma}$ point. Before TR-ARPES measurements, the $1T$-$TiSe_2$ single crystals were cleaved *in situ* to expose a clean surface, and oriented using low-energy electron diffraction (LEED). Degenerate time-resolved reflectivity (TRR) experiments were performed with the 30-fs pulses at 680 nm as pump and probe beams. They impinged on the sample surface at about 45° with crossed polarizations in order to avoid interference artifacts. All the experiments were performed at a sample temperature ranging from 80 to 300 K as specified in the figures.

## III. EXPERIMENTAL RESULTS

In TR-ARPES, the pump pulse first promotes electrons from the occupied to the unoccupied states with the same momenta, while the subsequent UV probe pulse is used to photoemit electrons and the transient energy dispersion is mapped in momentum space. Figures 1(b)–1(d) show the evolution of the TR-ARPES maps at three different time delays between the pump pulse and the probe for a $TiSe_2$ single crystal at 80 K. The sample temperature is ideal since it is below $T_{\rm CDW} = 202\,{\rm K}$, but sufficiently high to allow perturbations to the PLD as we show below. Figure 1(b) shows the TR-ARPES map at −225 fs delay (i.e., before the pump photoexcitation), which reflects the VB dispersion in the vicinity of the $\bar{\Gamma}$ point ($\boldsymbol{k}_\parallel = 0$) in the CDW phase along the $\bar{\rm K}$-$\bar{\Gamma}$-$\bar{\rm K}$ direction. The effect of the pump is apparent in Fig. 1(c) at time delay +25 fs where electrons from the VB have been promoted into a high-energy CB for $\boldsymbol{k}$ states at the edges of our detection window. As a high-energy CB becomes transiently populated, a photoelectron signal is observed above the Fermi level, $E_{\rm F}$. The effect of the pump and the TR-ARPES maps exhibit features similar to what has been reported in other TR-ARPES studies [32,36,37]. Like in other semimetals [38,39], carrier relaxation from high-energy states occurs within a few hundred femtoseconds (see Appendix A).

The key signature of the CDW is the gap, Δ: Figure 1(d) shows that the VB is shifted upwards in energy, i.e., Δ is reduced, even at +425 fs delay. This VB shift lasting longer than the pump laser duration (30 fs) is a signature of laser-induced perturbation of Δ. Changes in the VB binding energy are extensively documented in *steady-state* ARPES, when heating the $1T$-$TiSe_2$ lattice from $T < T_{\rm CDW}$ to the normal phase [15,23]. In order to accurately study the VB energy shift, we have performed an analysis at the fixed detection angle −14° ($k_\parallel \approx -0.1\,{\rm \AA^{-1}}$ for the VB) [solid white line in Figs. 1(b)–1(d)] as a function of pump-probe time delay. This angle allows better separation between the Fermi level and the VB, thus avoiding effects due to smearing of the Fermi-Dirac distribution.

As confirmation that the energy shift is indeed a dynamic perturbation of the CDW, and not just heating of the VB electron distribution, we show in Figs. 1(e) and 1(f) the VB dynamics at 80 and 300 K, respectively. While the data at 80 K exhibit a clear upshift in the VB energy lasting for the whole measurement window of 3 ps, the 300 K trace shows no energy shift and only a loss of intensity due to the transient depletion of electrons in the VB. A closer examination of the VB photoemission spectrum (PES) allows us to identify an energy position that shows no dynamics upon pumping at 300 K, i.e., a nodal point in the energy distribution curves that occurs at about 30% of the maximum intensity; see Appendix B. This intensity value is used hereafter to monitor the VB dynamics.

The possibility to tune the pump fluence gives additional important insights. Figure 2 illustrates how the VB shift and spectral weight are influenced. A crucial finding of our study is the measurement of the fluence, $F$, necessary for a transient closure of the CDW gap, reported to be $\Delta = 0.13\,{\rm eV}$ [23]. For the analysis, it is important to note that the dominant contribution to the opening of Δ comes from a VB downshift of 0.11 eV at $\bar{\Gamma}$, observed upon cooling from room temperature to 80 K [23]. Figure 2(a) shows the time dependence of the VB shift for selected pump fluences. The *maximum* VB shift occurs after about 200 fs in all traces, and for $250\,\mu{\rm J\,cm^{-2}}$ reaches ∼0.1 eV. The rise time in the VB shift occurs on timescales almost identical to the folded VB ARPES intensity suppression at $\bar{\rm M}$, recently measured in a comparable fluence range by Buss *et al.* [40]. Figure 2(b) reports the VB shift as a function of fluence at specific

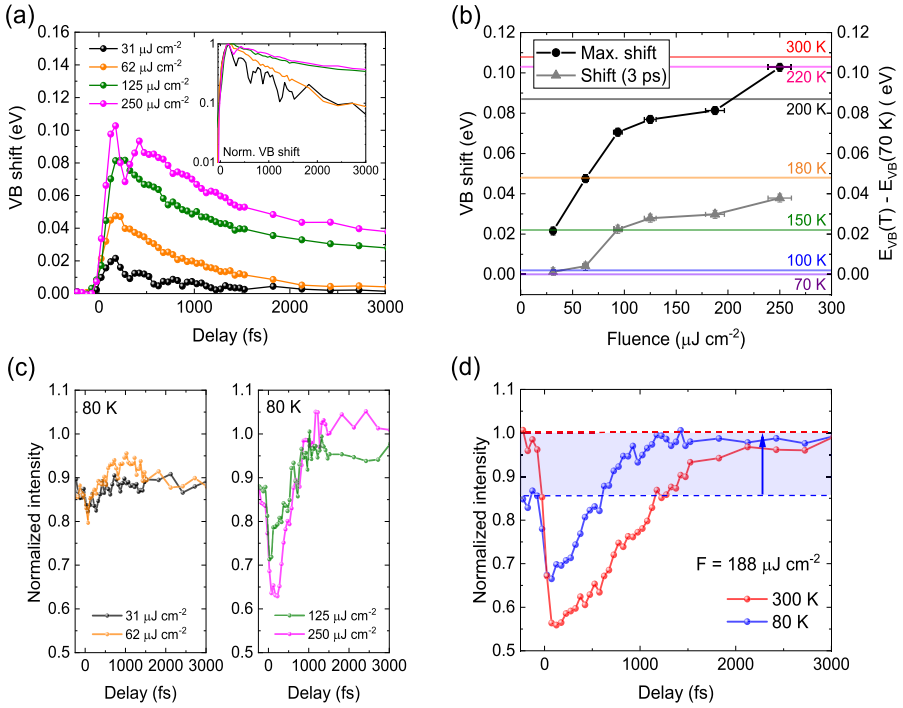


FIG. 2. Fluence dependence of the VB dynamics and spectral intensity. (a) VB energy shift, referred to the unperturbed position, as a function of pump-probe time delay at different pump laser fluences as indicated in the main panel. VB position has been extracted from the contour at 0.3 of the maximum ARPES intensity [example in Fig 1(e)]. The inset shows the same data normalized to the maximum VB energy shift on a logarithmic scale. (b) Maximum VB shift (dots) and shift at 3 ps (triangles) extracted from panel (a) as a function of fluence. The horizontal lines are linked to the right $y$ axis and are the shift in VB energy determined by high-resolution steady-state ARPES as the sample temperature is increased from 70 K, adapted from Ref. [23]. The VB position at 70 K from steady-state ARPES has been set to coincide with the VB energy at negative delays in our experiments. Energy error bars on VB shift data points are <2 meV. (c) Intensity of the VB at 80 K and for different laser fluences as indicated, normalized to ARPES intensity at negative delays and at room temperature [shown in (d)]. (d) Comparison between the normalized VB intensity in the CDW phase (80 K) and normal phase (300 K). A gain in intensity is observed in the 80 K data indicated by the blue shaded region.

time delays corresponding to the maximum shift (dots) and at $t = 3$ ps (triangles), the latter will be discussed below. To gauge the VB maximum shift with respect to the level of CDW perturbation, we have also plotted the shift in the equilibrium VB binding energy as horizontal lines in Fig. 2(b), taken from high-resolution steady-state ARPES [23] in going from 70 to 300 K. Two key observations are apparent from the trend of the VB maximum. First, the maximum shift is initially linear for low fluence before reaching a plateau for $F > 93\,\mu\mathrm{J\,cm^{-2}}$ equivalent to a shift in the equilibrium VB binding energy observed at temperatures between 180 and 200 K. Second, this plateau persists until a critical fluence of $F_{\mathrm{CDW}} = 200\,\mu\mathrm{J\,cm^{-2}}$, beyond which the VB transiently shifts above the 200 K line of equilibrium data and is consistent with complete suppression of $\Delta$ and disappearance of CDW order. These nonlinear trends are not due to saturation of absorption from $TiSe_2$ (Appendix A) or average laser heating [34], but are instead an intrinsic characteristic of the CDW dynamics.

Returning to the VB dynamics in Fig. 2(a) for the low fluences of 31 and 62 $\mu\mathrm{J\,cm^{-2}}$ we find a fast recovery, described by a monoexponential decay with equal time constants of ~770 fs. This leads to a complete VB recovery, i.e., 0 eV shift, at time delays >2 ps. For higher fluences, multiexponential decays with lifetimes longer than 1100 fs are found. The inset in Fig. 2(a) gives a clearer comparison of the same data, plotted on a logarithmic normalized intensity scale. The dynamics can be grouped into two well-defined categories and points to a threshold fluence, $F_{\mathrm{th}}$, between these regimes of fast and slow VB recovery. The residual VB shift at 3 ps (triangles), shown in Fig. 2(b), clearly identifies $F_{\mathrm{th}} > 62\,\mu\mathrm{J\,cm^{-2}}$. Note that $F_{\mathrm{th}} \simeq F_{\mathrm{CDW}}/3.3$, and so does not coincide with the complete suppression of $\Delta$ occurring at $F_{\mathrm{CDW}}$.

Following these observations, we look at the spectral *intensity* dynamics from the TR-ARPES. The left panel in Fig. 2(c) shows the spectral weight obtained by integrating the PES up to the Fermi level for $F < F_{\mathrm{th}}$, normalized as described in the caption. For both fluences the spectral weight is depleted upon photoexcitation and reestablished within 500 fs. However, for the $62\,\mu\mathrm{J\,cm^{-2}}$ data (orange curve) at a delay >500 fs the spectral weight shows a small and short-lived intensity *gain*. Similar behavior, but more pronounced and longer lasting, is observed for the two higher fluences reported in the right panel of Fig. 2(c). Photoexcitation with $F \geqslant F_{\mathrm{th}}$ therefore increases spectral weight in the VB. To confirm the origin of

this gain we compare the traces at 80 and 300 K in Fig. 2(d). At negative delay, the total intensity measures electrons in the VB up to the Fermi level. This is diminished when going from 300 to 80 K because CDW formation transfers spectral weight from $\bar{\Gamma}$ to the VB folded at $\bar{\mathrm{M}}$; cf. Fig. 1(a). Crucially, the 300 K data in the normal phase do not show any increase in intensity above the initial value. Thus, the observed gain (blue arrow) is caused by the photoinduced unfolding of the VB from $\bar{\mathrm{M}}$ to the $\Gamma$ point and indicates breaking of exciton pairs in the CDW condensate [36], and/or a disturbance of the PLD.

The results of Fig. 2 report the $1T$-$TiSe_2$ VB dynamics in a fluence regime rarely studied by TR-ARPES [40]. It is important to point out that previous time-resolved all-optical experiments in the low-fluence regime $F < F_{\mathrm{th}}$ have clarified how the initial perturbation of the CDW by femtosecond laser pulses is nonthermal, i.e., it concerns mainly the electronic order in the system represented by the exciton condensate and to a negligible extent the lattice degrees of freedom [13,14]. This is consistent with electron-electron and electron-exciton scattering times on the order of hundreds of femtoseconds [13]. When discussing possible scenarios for the CDW in $TiSe_2$, we consider that the CDW formation is due to both excitonic *and* lattice interactions, where the relative contributions and relationship are currently unknown. For fluences below $F_{\mathrm{th}}$, the rapid VB recovery is consistent with electronic dynamics and suggests that mainly the excitonic part of the CDW is perturbed. Above $F_{\mathrm{th}}$ there is an additional contribution with a longer recovery time, indicating a bottleneck in reestablishing the CDW ground state.

Interestingly, $F_{\mathrm{th}}$ identified from the 3 ps data in Fig. 2(b) corresponds to a VB position at 150 K from steady-state measurements. This is the sample temperature at which recent femtosecond THz experiments reported the disappearance of the phonon fingerprint of the PLD [13]. All together this suggests that the $<$200 fs nonthermal shift of $\sim$0.05 eV at $F_{\mathrm{th}}$ can be interpreted as a lower limit for the initial excitonic contribution to the CDW. Above $F_{\mathrm{th}}$, a second weakening process for $\Delta$ plays a role. Notice that a simple picture in which excitonic and phononic contributions can be obtained separately from the VB dynamics alone, and summed to obtain the full $\Delta$, does not apply. Rather, we now look at how phonons influence the dynamics of $\Delta$.

Understanding of the CDW bottleneck dynamics benefits from monitoring lattice degrees of freedom. While steady-state ARPES experiments can provide indirect information on lattice structure from changes in the electronic band structure, time-resolved experiments allow the dynamics of a subset of phonons to be probed in real time [41]. In TR-ARPES, we observe that below $F_{\mathrm{th}}$ the VB dynamics are modulated by periodic oscillations, very likely connected to coherent phonons, whereas above $F_{\mathrm{th}}$ their amplitude weakens or is undetectable [34]. Oscillations of the VB in TR-ARPES signify the presence of phonons connected with the order parameter. Thus, it is conceivable that such oscillations will weaken as the CDW is perturbed above $F_{\mathrm{th}}$. Further information on phonon dynamics can be obtained from optical TRR experiments which offer a slightly higher time resolution and probe the change in refractive index of our crystal modulated by phonons. Figure 3(a) shows clear oscillations in TRR for all fluences. It is important to note that below $F_{\mathrm{th}}$, both the period and damping time are similar to those seen in TR-ARPES. Figure 3(b) illustrates the oscillatory component of the signal at different fluences after subtraction of an exponential decay. A Fourier transform (FT) of the data from Fig. 3(b) allows us to identify two well-separated oscillation frequencies: a low-frequency mode at 3.36 THz (112 $\mathrm{cm}^{-1}$) and a high-frequency mode at 6.03 THz (201 $\mathrm{cm}^{-1}$). The lower frequency is that of the Raman active $A_{1g}^{*}$ phonon of $1T$-$TiSe_2$ [34,42]. At $F \leqslant F_{\mathrm{th}}$ the $A_{1g}^{*}$ is the most intense coherently coupled phonon with the largest amplitude. This mode is a consequence of the PLD and is not present in the normal phase of $1T$-$TiSe_2$ [42]. We show in Ref. [34] that the $A_{1g}^{*}$ mode is selectively coupled to the CDW and recent experiments by Monney *et al.* have shown how it modulates the CDW recovery after quasiresonant excitation at $\Delta$ [33]. At $F \geqslant 132\,\mu\mathrm{J\,cm}^{-2}$ the oscillations are instead dominated by the higher-frequency mode, similar in frequency to the $A_{1g}$ phonon of the normal phase [34,42], or two zone-edge modes triggered by a second-order process [43,44]. Both assignments for the high-frequency 6.03 THz oscillations are consistent with a perturbed PLD and excitation of phonon modes of the normal phase structure [34].

The progressive change of amplitude between the selectively coupled phonons (SCPs) as the laser intensity increases can be interpreted with two hypotheses: (i) $A_{1g}^{*}$ phonons that do not couple coherently in the CDW recovery; (ii) a loss of PLD (disappearance of $A_{1g}^{*}$) and thus rearrangement of the lattice towards the normal phase, as also supported by the unfolding results, cf. Fig. 2(c). Information on phonons is relevant for the bottleneck, since a substantial population of excited vibrational modes (hot phonons) can transfer energy back into the already perturbed exciton condensate and suppress its reestablishment. Most important is the observation that phonons linked to the normal phase structure modulate the dynamics when the bottleneck in the recovery appears, as clearly shown by the comparison of FT amplitudes and VB shift in Fig. 3(d).

## IV. MODEL AND DISCUSSION

We have performed a series of simulations capable of describing the VB dynamics as a function of laser fluence. These are inspired by the Rothwarf-Taylor (R-T) model which was initially used to describe the equilibration of Cooper pairs in superconductors with hot electrons and phonons [26,45] and has also been applied to CDW materials [46]. Photoexcitation dynamics in $1T$-$TiSe_2$ is tracked via three populations: hot carriers (electrons and holes) $n_e$ created by the pump; low-energy unbound quasiparticles (QPs), $n_q$, originating from breaking excitons into electrons and holes [a process consistent with Fig. 2(c)]; and a population of SCPs, $N_p$. Following the pump pulse, carriers rapidly relax via electron-electron and electron-phonon scattering, breaking excitons into unbound QPs and exciting SCPs and other phonons in the process. Figure 4(a) outlines the main processes resulting in the relaxation bottleneck. A scheme of all the physical processes accounted for in the model is in Fig. S10 of the Supplemental Material [34]. QPs can recombine into the exciton condensate with a rate $R$ by exciting the SCPs further, while absorption of SCPs by the exciton

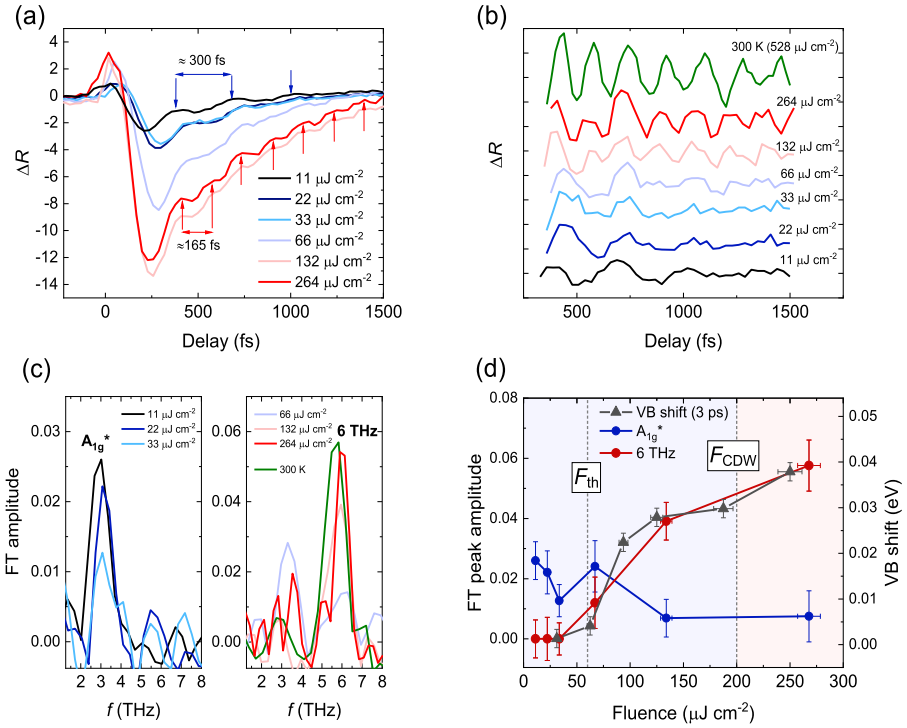


FIG. 3. Coherent coupling to phonons in TRR. (a) Coherent phonon oscillations observed by time-resolved reflectivity (TRR) in the CDW phase (80 K) at different laser fluences. (b) Oscillations after subtraction of an exponential decay in the TRR data in panel (a) and offset for clarity. (c) Fourier transform (FT) amplitude for the oscillations in panel (b) at 80 K together with the normal phase (300 K) for comparison. (d) FT amplitude of the $A_{1g}^{*}$ and 6-THz modes, as a function of fluence. The VB shift at 3 ps (black triangles) from Fig. 2(b) is superimposed (right $y$ axis).

condensate can dissociate excitons to create QPs with a rate $\eta$. The SCPs also equilibrate with the bath through anharmonic decay at a rate $\gamma$. The complete model is discussed in the Supplemental Material [34].

Figure 4(b) shows that the VB dynamics can be accurately modeled approximating the VB shift as $\Delta(t) - \Delta_{80\,\mathrm{K}}$ via [26]

$$\Delta(t) = \Delta_{80\,\mathrm{K}}\sqrt{1 - n_q(t)/n_c}, \tag{1}$$

where $\Delta_{80\,\mathrm{K}} = 130\,\mathrm{meV}$ is the CDW gap at 80 K [23] and $n_c$ is the critical QP density, which we have estimated based on our Hall effect measurements [34] and reports from literature [19]. In the model $n_e$ has been determined from the measured laser pulse fluences. The fluence dependence of the two main fitting parameters $\gamma$ and $\eta$, reported in Fig. 4(c), shows a correspondence with the VB shift behavior and to the FT amplitudes of the different coherent phonons in Fig. 3(d). The bottleneck effect emerges in the model due to the SCPs becoming simultaneously less damped (smaller $\gamma$) and scattering more frequently with excitons (larger $\eta$). The model does not distinguish between $A_{1g}^{*}$ and $A_{1g}$ phonons. Thus the substantial change in $\eta$ at $F_{\mathrm{th}}$ implicitly accounts for the switch between these modes seen in TRR experiments, and for the likely change in exciton-phonon scattering rates in the weakened PLD. A correlation between the values of $\gamma^{-1}$ and the damping time of coherent oscillations $\tau_{\mathrm{damp}}$ extracted from TRR experiments appears from Fig. 4(c). This quantitative correspondence for the same physical observable, inferred from the modeled VB dynamics and independently extracted from TRR data, lends weight to the credibility of our model. Future work with structural probes such as time-resolved x-ray diffraction will help to probe the anharmonic decay of SCP in momentum space [43,47] and thus further verify such correlation. The ratio $\gamma/\eta$ reported in Fig. 4(d) is an important metric for which the strong bottleneck regime occurs when $\gamma/\eta < 1$ [26]. In contrast to superconductors, where the bottleneck regime arises directly from the nonlinearity of the R-T equations without changing $\eta$ and $\gamma$ as a function of fluence, in CDW materials the electronic order is coupled to the PLD. Weakening of the PLD results in dramatic changes to the interactions at play in the recovery of excitons as illustrated by Fig. 4(d).

A comparison with previous femtosecond experiments performed at lower sample temperatures supports our conclusions that the anharmonic decay of SCP plays a role in the CDW bottleneck dynamics [13,33]. Monney *et al.* observed coherent $A_{1g}^{*}$ phonon oscillations in the recovery of the folded band intensity at the $\bar{\mathrm{M}}$ point upon excitation with pulses at 400-meV photon energy and a fluence of $400\,\mu\mathrm{J\,cm^{-2}}$ [33]. While this laser fluence is almost an order of magnitude larger

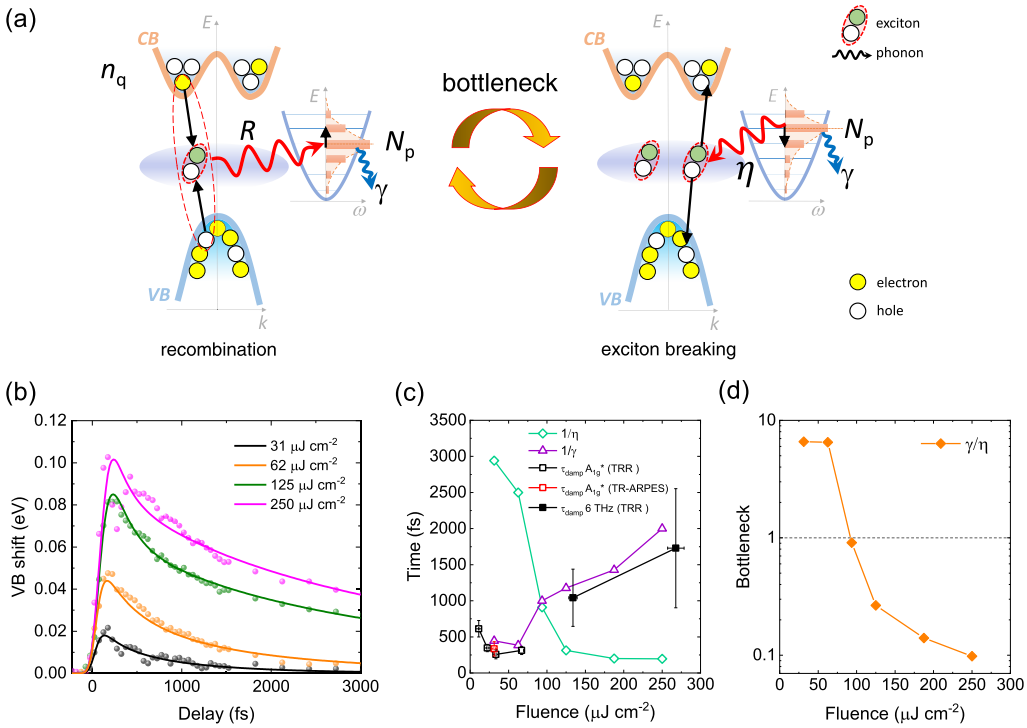


FIG. 4. Modeling of VB dynamics and phonon bottleneck in the CDW recovery. (a) Bottleneck involving the quasiparticle population, $n_q$, and the out-of-equilibrium SCPs, $N_p$. The straight black arrows indicate the transition from electron and hole quasiparticles to the exciton condensate in both directions. Red curved arrows indicate the scattering of two quasiparticles with an SCP in the recombination process (left panel) or the scattering of an exciton with an SCP generating two quasiparticles (right). $\gamma$ is used to indicate the anharmonic phonon-phonon scattering with the thermal bath. The orange arrows illustrate the iterative dynamics between recombination and reexcitation influenced by $\gamma$. The Supplemental Material (Fig. S9) includes a further diagram illustrating the fast photoexcitation process preceding this bottleneck dynamics [34]. (b) VB dynamics extracted from the model (solid curves) overlaid with the TR-ARPES data (dots) from Fig. 2(a). (c) Fluence dependence of the fitting parameters $1/\eta$ (green diamonds) and $1/\gamma$ (purple triangles) together with damping times, $\tau_{\text{damp}}$, from experiments as indicated in the legend. (d) Ratio $\gamma/\eta$ (log scale) as a function of pump laser fluence extracted from the model simulations.

than our $F_{\text{th}}$, we note that the sample temperature was 30 K and the photon energy is comparable to the CDW gap, thus directly generating quasiparticles with the pump pulse instead of hot free carriers. A pump photon energy of 1.55 eV, i.e., similar to this work was employed in the broadband THz spectroscopy experiments of Porer *et al.* [13], where a delayed recovery of the excitonic order was seen at fluences above 40 $\mu$J cm$^{-2}$, i.e., comparable to our $F_{\text{th}}$, and with an additional suppression for higher fluences. From our data, the additional suppression can be related to phononic effects. Moreover, in agreement with our arguments that the anharmonic decay influences the CDW recovery, Porer *et al.* observed that the sample temperature had to be increased to 150 K in order to show a photoinduced melting of the PLD. Combining these results, it is evident that the sample temperature is an important factor. The temperature of the heat bath can control $\gamma$, leading to much longer damping times as temperature is decreased below ∼60 K as confirmed in the TRR data of Ref. [14].

We conclude that below $F_{\text{th}}$ only a limited number of QPs are excited out of the excitonic condensate and relax by coupling to $A_{1g}^*$ phonons characteristic of the PLD. Above $F_{\text{th}}$ the excitonic part of the CDW gap is perturbed to an extent where the coupling to the $A_{1g}^*$ phonons is weakened and the QP population is substantial. Thus, recovery of the CDW experiences a bottleneck controlled by the anharmonic decay of hot phonons and the modified phonon dispersion of the weakened PLD. Our results therefore provide evidence that in the out-of-equilibrium regimes probed in our experiments, the reformation of the CDW in $1T$-$TiSe_2$ upon electronic cooling is always influenced by lattice degrees of freedom. In addressing the introductory questions on exciton-phonon coupling, we come to the following conclusions: (i) we exclude that $1T$-$TiSe_2$ should be classified as typical Peierls CDW material, since the initial perturbation of $\Delta$ occurs on a short timescale ∼200 fs consistent with electronic screening of Coulomb interactions [Fig. 2(a)], in agreement with similar conclusions made by others [31,32,40]; (ii) for the quasiparticles, i.e., electron and holes at the band edge, the selective coupling to $A_{1g}^*$ phonons of the PLD is involved in the exciton condensation and thus a selective coupling with specific modes should be considered strong; (iii) ultimately, if PLD phonons are out of thermal equilibrium with the lattice bath, or not present at all (due to a loss of PLD), $\Delta$ is recovered only to its corresponding steady-state value of ∼150 K.

We argue that the low-fluence regime explored in this work contributes to the discussion on the mechanism of CDW formation in $1T$-$TiSe_2$ in the absence of light excitation, i.e., in the ground state. Focusing on the recovery dynamics allows us to extract relevant parameters in understanding how SCPs of the PLD structure and of the normal structure interact with charge carriers and excitons. Most importantly our work highlights the role of anharmonic coupling between SCPs and the thermal bath, which in our simplified model is the lattice temperature set by other low-energy phonon modes. As shown by Weber *et al.* optical phonon modes interacting with an acoustic branch experience a softening as temperature is lowered close to $T_{CDW}$ [48]. Our work probes how phonons are directly influencing $\Delta$ and provides estimates for the scattering rates between excitons and SCPs.

To generalize the discussion and extend it to other TMD materials exhibiting a CDW transition, it is interesting to compare our results with the very recent work of Shi *et al.* on $1T$-$TaSe_2$ [49]. The CDW transition temperature in $1T$-$TaSe_2$, 473 K, is more than twice that of $TiSe_2$ and the system is known to exhibit laser-induced perturbation of the electronic order at much higher fluences than those we report here [31,50]. Interestingly, Shi *et al.* show a transient energy shift of CDW-related tantalum bands as a function of fluence by TR-ARPES. This is consistent with what we show in Fig. 2(b), although on a completely different scale of fluences. In $1T$-$TaSe_2$, even after the pump-induced band shift has reached a plateau, the coherent phonon oscillations related to the PLD are seen, uncovering a metastable state mediated by selective electron-phonon coupling [49]. What is remarkable is that the damping time of those oscillations shows similarities to our observations of Fig. 3(c); i.e., the damping time is faster as the electronic gap is closing. Such behavior could signal the fact that a phonon bottleneck is involved in the formation of the metastable state in $1T$-$TaSe_2$ as well. As Shi *et al.* commented, this could be explained as a modulation of the electron-phonon coupling, a scenario in line with the Peierls-Mott nature of the CDW in $1T$-$TaSe_2$ [50]. The different nature of the CDW in $TiSe_2$, where the excitonic and phononic contributions cooperate to generate a gap, is seen in the switching of the coupled phonon modes as the CDW gap closes. Our combined TRR and TR-ARPES approach could be used to determine at which fluence the PLD of $1T$-$TaSe_2$ is perturbed to an extent where phonons of the normal phase play a role. It may also be applied to other CDW TMDs, since many of them exhibit detectable changes in PLD through Raman resonances across the respective $T_{CDW}$ [51].

## V. CONCLUSIONS

In summary, the CDW dynamics of $1T$-$TiSe_2$ following ultrafast photoexcitation shows different out-of-equilibrium regimes accessed by changing pump laser fluence. There exists two distinct regimes below the complete melting of the CDW, one in which the PLD structural order appears robust and a weak perturbation of the excitonic condensate results in a fast recovery time of $<2$ ps. For fluences above 60 $\mu J\,cm^{-2}$ the CDW is still present in a metastable state controlled by the lattice degrees of freedom, i.e., hot phonons and partial loss of PLD. Our study conclusively shows that the dynamics of the CDW gap can be modeled as the increase of QPs excited out of the exciton condensate, which in turn depends on SCPs. In the absence of full thermalization of this subset of phonons with the bath, the full recovery of the CDW is impeded. Future work aiming at controlling the CDW by targeted excitation of phonons with intense THz pulses could represent a new avenue to connect the incommensurate CDW in $1T$-$TiSe_2$ to the superconductivity [11] as well as three pulse experiments to investigate the symmetry of the weakened PLD [52]. The combination of ultrafast spectroscopy methods presented here, TRR and TR-ARPES, has proven decisive in giving insights into the complex nature of the CDW in $1T$-$TiSe_2$. This experimental approach can be applied to many other correlated electron materials such as superconductors and topological insulators in order to disentangle the complex many-body interactions that dominate their unique properties.

## ACKNOWLEDGMENTS

We thank P. Jones, P. Reddish, and W. Lambson for technical support. C.J.S. and S.K. acknowledge funding and support from the Engineering and Physical Sciences Research Council (EPSRC) Centre for Doctoral Training in Condensed Matter Physics (CDT-CMP), Grant No. EP/L015544/1. S.R.C. and D.W. acknowledge support from EPSRC under Grants No. EP/P025110/1 and No. EP/M022188/1, respectively. J.v.W. acknowledges support from a VIDI grant financed by the Netherlands Organization for Scientific Research (NWO). H.H. acknowledges financial support through the Postdoctoral International Fellowship program of Politecnico Milano. S.F. acknowledges support from EPSRC under Grant No. EP/N026691/1. E.D.C. and J.v.W. wish to thank the Royal Society for a Research Grant and an International Exchange Program. E.D.C. acknowledges support from Horizon 2020 (Grant No. 654148, Laserlab-Europe). G.C. acknowledges support by the European Union's Horizon 2020 Research and Innovation Programme under Grant Agreement No. 785219 (GrapheneCore2). C.D., E.C., and G.C. acknowledge financial support from Politecnico di Milano through the "UPhOS" Interdepartmental Laboratory project.

## APPENDIX A: TIME DEPENDENCE OF FREE CARRIER POPULATION AND LINEARITY WITH PUMP FLUENCE

In order to check the linearity of the laser pumping effect in our TR-ARPES experiment, we have analyzed the total intensity above the $E_F$, for all spectra, which provides an indication of the transient free carrier population induced by the pump pulse. For this, we used the normalized spectra in Fig. 6 at each pump-probe delay and integrated across the high-energy tail to intensity $\leqslant 0.25$ (just below the nodal point of all spectra in the normal phase) as shown by the example in the inset of Fig. 5(a). The main panel of Fig. 5(a) shows the result of the integration as a function of pump-probe delay for each fluence in the CDW phase (solid lines) and in the normal phase (dashed line) for comparison. All curves have a maximum near +50 fs and recover to their values before pump excitation (at −225 fs) within 1500 fs. Figure 5(b) shows the integrated signal at negative (−175 fs) and at positive (+50 fs) time delays for different fluences. Importantly, the (−175 fs)

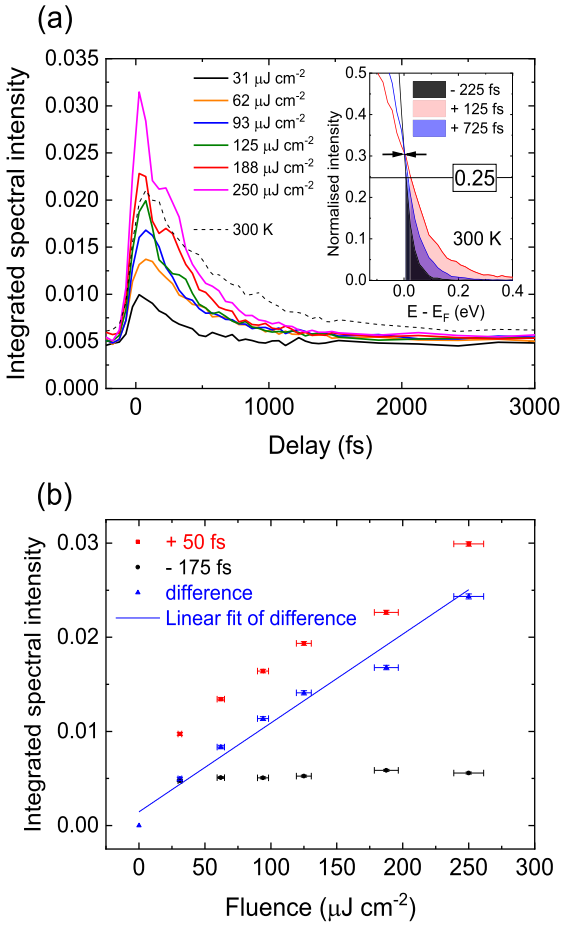


FIG. 5. Linearity of free carrier population above the Fermi level with pump fluence. (a) Integrated spectral intensity above the Fermi level, $E_F$, as a function of pump-probe delay for each pump fluence in the CDW phase (80 K). The dashed line shows the normal phase (300 K) for comparison. The inset shows representative PES at 300 K and the criterion used to calculate the free-carrier population. (b) Fluence dependence of the integrated spectral intensity of the Fermi tail at −175 fs time delay (black dots), at +50 fs time delay (red squares) and their difference (blue triangles). The linear fit gives $R^2 = 0.97377$.

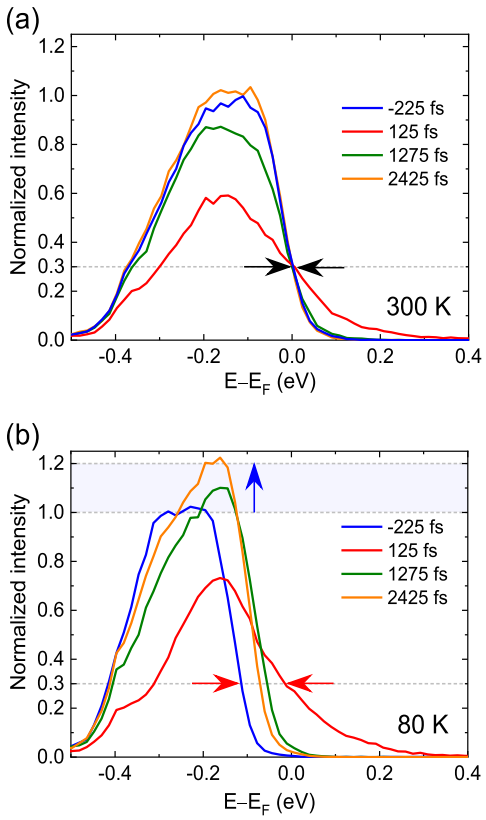


FIG. 6. Photoemission spectra (PES) for various pump-probe delays. (a) Normal phase, 300 K and (b) CDW phase, 80 K for fluence, $F = 250\,\mu\mathrm{J\,cm^{-2}}$ obtained along the −14° emission angle. Curves in both panels are normalized to the intensity at −225 fs delay. The black arrows [panel (a)] indicate the nodal point for all spectra in the normal phase. At this same point in the CDW phase (b), there is a clear shift in energy at positive time delay due to the VB shift (red arrows). The blue shaded region in (b) highlights increased intensity at positive delay attributed to replica band unfolding as discussed in the main text relating to Fig. 2(d).

tail contribution, black dots in Fig. 5(b), is found to be the same at all fluences within the experimental error. This is consistent with the tail being an equilibrium effect. If we subtract the tail at negative times, represented by the black dots, then all data points scale down, giving an intercept passing through the origin for the line of best fit. The $y$-axis error of the integrated spectral intensity is related to the statistical error ($\sqrt{N}$) in the number of counts, $N$, and the $x$-axis error is the fluctuation of laser fluence estimated with an optometer and by analyzing the fluctuation of the VB peak intensity measured at positive delays multiple times under the same conditions with high statistics. Further aspects on the linearity of photoexcited carrier population can be found in Ref. [34].

## APPENDIX B: KEY SIGNATURES OF CDW SUPPRESION IN TR-ARPES

In order to highlight all the spectroscopic features of CDW suppression seen in our experiment, the photoemission spectra (PES) for various pump-probe delays are shown in Fig. 6; which are extracted from the data in Figs. 1(e) and 1(f). In the normal phase at 300 K, Fig. 6(a), shortly after the pump pulse (+125 fs), there is a clear reduction of the VB intensity and a significant broadening of the photoemission peak across the Fermi level. We do not observe any shift in the VB energy (horizontal black arrows) and the intensity at long delay (+2425 fs) returns to the initial value (at −225 fs). At sample temperatures below $T_{CDW}$ the same initial reduction in intensity and broadening of states occurs [+125 fs, Fig. 6(b)]. However, in contrast to the normal phase data, there is a clear upshift of the VB

energy (horizontal red arrows). This upshift is a signature of the photoinduced CDW gap closing. In addition, at long delay ($\geqslant$1 ps) there is an *increase* in the VB intensity (blue shaded region) which we attribute to the unfolding of the VB replica from $\bar{M}$ to $\bar{\Gamma}$ as the CDW order is suppressed as discussed with reference to Figs. 2(c) and 2(d).

[1] C. W. Chen, J. Choe, and E. Morosan, Charge density waves in strongly correlated electron systems, Rep. Prog. Phys. **79**, 084505 (2016).

[2] K. Rossnagel, On the origin of charge-density waves in select layered transition-metal dichalcogenides, J. Phys.: Condens. Matter **23**, 213001 (2011).

[3] J. A. Wilson, F. J. Di Salvo, and S. Mahajan, Charge-density waves and superlattices in metallic layered transition-metal dichlacogenides, Adv. Phys. **24**, 117 (1975).

[4] S. Gerber *et al.*, Three-dimensional charge density wave order in $YBa_2Cu_3O_{6.67}$ at high magnetic fields, Science **350**, 949 (2015).

[5] R. Osterbacka, X. M. Jiang, C. P. An, B. Horovitz, and Z. V. Vardeny, Photoinduced Quantum Interference Antiresonances in $\pi$-Conjugated Polymers, Phys. Rev. Lett. **88**, 226401 (2002).

[6] M. Sato, H. Fujishita, S. Sato, and S. Hoshino, Neutron inelastic scatterning and x-ray structural study of the charge density wave state in $K_{0.3}MoO_3$, J. Phys. C: Solid State Phys. **18**, 2603 (1985).

[7] P. Monceau, Electronic crystals: An experimental overview, Adv. Phys. **61**, 325 (2012).

[8] Y. I. Joe *et al.*, Emergence of charge density wave domain walls above the superconducting dome in $1T$-$TiSe_2$, Nat. Phys. **10**, 421 (2014).

[9] A. F. Kusmartseva, B. Sipos, H. Berger, L. Forro, and E. Tutis, Pressure Induced Superconductivity in Pristine $1T$-$TiSe_2$, Phys. Rev. Lett. **103**, 236401 (2009).

[10] E. Morosan, H. W. Zandbergen, B. S. Dennis, J. W. G. Bos, Y. Onose, T. Klimczuk, A. P. Ramirez, N. P. Ong, and R. J. Cava, Superconductivity in $Cu_xTiSe_2$, Nat. Phys. **2**, 544 (2006).

[11] L. J. Li, E. C. T. O'Farrell, K. P. Loh, G. Eda, B. Ozyilmaz, and A. H. C. Neto, Controlling many-body states by the electric-field effect in a two-dimensional material, Nature **529**, 185 (2016).

[12] J. van Wezel, P. Nahai-Williamson, and S. S. Saxena, Exciton-phonon-driven charge density wave in $TiSe_2$, Phys. Rev. B **81**, 165109 (2010).

[13] M. Porer, U. Leierseder, J.-M. Ménard, H. Dachraoui, L. Mouchliadis, I. E. Perakis, U. Heinzmann, J. Demsar, K. Rossnagel, and R. Huber, Non-thermal separation of electronic and structural orders in a persisting charge density wave, Nat. Mater. **13**, 857 (2014).

[14] E. Mohr-Vorobeva, S. L. Johnson, P. Beaud, U. Staub, R. De Souza, C. Milne, G. Ingold, J. Demsar, H. Schaefer, and A. Titov, Nonthermal Melting of a Charge Density Wave in $TiSe_2$, Phys. Rev. Lett. **107**, 036403 (2011).

[15] K. Rossnagel, L. Kipp, and M. Skibowski, Charge-density-wave phase transition in $1T$-$TiSe_2$: Excitonic insulator versus band-type Jahn-Teller mechanism, Phys. Rev. B **65**, 235101 (2002).

[16] F. J. Di Salvo, D. E. Moncton, and J. V. Waszczak, Electronic properties and superlattice formation in semimetal $TiSe_2$, Phys. Rev. B **14**, 4321 (1976).

[17] D. Jerome, T. M. Rice, and W. Kohn, Excitonic insulator, Phys. Rev. **158**, 462 (1967).

[18] H. Cercellier, C. Monney, F. Clerc, C. Battaglia, L. Despont, M. G. Garnier, H. Beck, P. Aebi, L. Patthey, H. Berger, and L. Forró, Evidence for an Excitonic Insulator Phase in $1T$-$TiSe_2$, Phys. Rev. Lett. **99**, 146403 (2007).

[19] G. Li, W. Z. Hu, D. Qian, D. Hsieh, M. Z. Hasan, E. Morosan, R. J. Cava, and N. L. Wang, Semimetal-to-Semimetal Charge Density Wave Transition in $1T$-$TiSe_2$, Phys. Rev. Lett. **99**, 027404 (2007).

[20] A. Kogar *et al.*, Signatures of exciton condensation in a transition metal dichalcogenide, Science **358**, 1314 (2017).

[21] R. Bianco, M. Calandra, and F. Mauri, Electronic and vibrational properties of $TiSe_2$ in the charge-density-wave phase from first principles, Phys. Rev. B **92**, 094107 (2015).

[22] Y. Yoshida and K. Motizuki, Electron lattice interaction and lattice instability of $1T$-$TiSe_2$, J. Phys. Soc. Jpn. **49**, 898 (1980).

[23] P. Chen, Y. H. Chan, X. Y. Fang, S. K. Mo, Z. Hussain, A. V. Fedorov, M. Y. Chou, and T. C. Chiang, Hidden order and dimensional crossover of the charge density waves in $TiSe_2$, Sci. Rep. **6**, 37910 (2016).

[24] T. Pillo, J. Hayoz, H. Berger, F. Levy, L. Schlapbach, and P. Aebi, Photoemission of bands above the Fermi level: The excitonic insulator phase transition in $1T$-$TiSe_2$, Phys. Rev. B **61**, 16213 (2000).

[25] M. D. Watson, O. J. Clark, F. Mazzola, I. Marković, V. Sunko, T. K. Kim, K. Rossnagel, and P. D. C. King, Orbital- and $k_z$-Selective Hybridization of Se 4$p$ and Ti 3$d$ States in the Charge Density Wave Phase of $TiSe_2$, Phys. Rev. Lett. **122**, 076404 (2019).

[26] C. Giannetti, M. Capone, D. Fausti, M. Fabrizio, F. Parmigiani, and D. Mihailovic, Ultrafast optical spectroscopy of strongly correlated materials and high-temperature superconductors: A non-equilibrium approach, Adv. Phys. **65**, 58 (2016).

[27] S. Vogelgesang, G. Storeck, J. G. Horstmann, T. Diekmann, M. Sivis, S. Schramm, K. Rossnagel, S. Schafer, and C. Ropers, Phase ordering of charge density waves traced by ultrafast low-energy electron diffraction, Nat. Phys. **14**, 184 (2018).

[28] F. Boschini *et al.*, Collapse of superconductivity in cuprates via ultrafast quenching of phase coherence, Nat. Mater. **17**, 416 (2018).

[29] J. Orenstein, Ultrafast spectroscopy of quantum materials, Phys. Today **65**(9), 44 (2012).

[30] S. G. Han, Z. V. Vardeny, K. S. Wong, O. G. Symko, and G. Koren, Femtosecond Optical-Detection of Quasiparticle Dynamics in High-$T_c$ $YBa_2Cu_3O_{7-\delta}$ Superconducting Thin Films, Phys. Rev. Lett. **65**, 2708 (1990).

[31] S. Hellmann *et al.*, Time-domain classification of charge-density-wave insulators, Nat. Commun. **3**, 1069 (2012).

[32] T. Rohwer *et al.*, Collapse of long-range charge order tracked by time-resolved photoemission at high momenta, Nature **471**, 490 (2011).

[33] C. Monney *et al.*, Revealing the role of electrons and phonons in the ultrafast recovery of charge density wave correlations in $1T$-$TiSe_2$, Phys. Rev. B **94**, 165165 (2016).

[34] See Supplemental Material at http://link.aps.org/supplemental/10.1103/PhysRevResearch.1.023029 for electronic transport measurements, laser heating considerations, details of the R-T simulations, and temperature-dependent Raman spectroscopy.

[35] F. Boschini, H. Hedayat, C. Dallera, P. Farinello, C. Manzoni, A. Magrez, H. Berger, G. Cerullo, and E. Carpene, An innovative Yb-based ultrafast deep ultraviolet source for time-resolved photoemission experiments, Rev. Sci. Instrum. **85**, 123903 (2014).

[36] S. Mathias *et al.*, Self-amplified photo-induced gap quenching in a correlated electron material, Nat. Commun. **7**, 12902 (2016).

[37] G. Rohde *et al.*, Tracking the relaxation pathway of photo-excited electrons in $1T$-$TiSe_2$, Eur. Phys. J.: Spec. Top. **222**, 997 (2013).

[38] T. Limmer, J. Feldmann, and E. Da Como, Carrier Lifetime in Exfoliated Few-Layer Graphene Determined from Intersubband Optical Transitions, Phys. Rev. Lett. **110**, 217406 (2013).

[39] D. Bugini, F. Boschini, H. Hedayat, H. Yi, C. Chen, X. Zhou, C. Manzoni, C. Dallera, G. Cerullo, and E. Carpene, Ultrafast spin-polarized electron dynamics in the unoccupied topological surface state of $Bi_2Se_3$, J. Phys.: Condens. Matter **29**, 30LT01 (2017).

[40] J. H. Buss *et al.*, A setup for extreme-ultraviolet ultrafast angle-resolved photoelectron spectroscopy at 50-kHz repetition rate, Rev. Sci. Instrum. **90**, 023105 (2019).

[41] L. Perfetti, P. A. Loukakos, M. Lisowski, U. Bovensiepen, H. Berger, S. Biermann, P. S. Cornaglia, A. Georges, and M. Wolf, Time Evolution of the Electronic Structure of $1T$-$TaS_2$ through the Insulator-Metal Transition, Phys. Rev. Lett. **97**, 067402 (2006).

[42] J. A. Holy, K. C. Woo, M. V. Klein, and F. C. Brown, Raman and infrared studies of superlattice formation in $TiSe_2$, Phys. Rev. B **16**, 3628 (1977).

[43] T. Huber, S. O. Mariager, A. Ferrer, H. Schafer, J. A. Johnson, S. Grubel, A. Lubcke, L. Huber, T. Kubacka, C. Dornes, C. Laulhe, S. Ravy, G. Ingold, P. Beaud, J. Demsar, and S. L. Johnson, Coherent Structural Dynamics of a Prototypical Charge-Density-Wave-to-Metal Transition, Phys. Rev. Lett. **113**, 026401 (2014).

[44] L. Rettig, R. Cortés, J.-H. Chu, I. R. Fisher, F. Schmitt, R. G. Moore, Z.-X. Shen, P. S. Kirchmann, M. Wolf, and U. Bovensiepen, Persistent order due to transiently enhanced nesting in an electronically excited charge density wave, Nat. Commun. **7**, 10459 (2016).

[45] A. Rothwarf and B. N. Taylor, Measurement of Recombination Lifetimes in Superconductors, Phys. Rev. Lett. **19**, 27 (1967).

[46] V. V. Kabanov, J. Demsar, and D. Mihailovic, Carrier-relaxation dynamics in intragap states: The case of the superconductor $YBa_2Cu_3O_{7-\delta}$ and the charge-density-wave semiconductor $K_{0.3}MoO_3$, Phys. Rev. B **61**, 1477 (2000).

[47] P. Beaud *et al.*, A time-dependent order parameter for ultrafast photoinduced phase transitions, Nat. Mater. **13**, 923 (2014).

[48] F. Weber, S. Rosenkranz, J. P. Castellan, R. Osborn, G. Karapetrov, R. Hott, R. Heid, K. P. Bohnen, and A. Alatas, Electron-Phonon Coupling and the Soft Phonon Mode in $TiSe_2$, Phys. Rev. Lett. **107**, 266401 (2011).

[49] X. Shi *et al.*, Ultrafast electron calorimetry uncovers a new long-lived metastable state in $1T$-$TaSe_2$ mediated by mode-selective electron-phonon coupling, Sci. Adv. **5**, eaav4449 (2019).

[50] C. Sohrt, A. Stange, M. Bauer, and K. Rossnagel, How fast can a Peierls–Mott insulator be melted? Faraday Discuss. **171**, 243 (2014).

[51] S. Sugai, Lattice-vibrations in the charge density-wave states of layered transition-metal dichalcogenides, Phys. Status Solidi B **129**, 13 (1985).

[52] S. Wall, D. Wegkamp, L. Foglia, K. Appavoo, J. Nag, R. F. Haglund, J. Stahler, and M. Wolf, Ultrafast changes in lattice symmetry probed by coherent phonons, Nat. Commun. **3**, 721 (2012).

[53] C. Monney, E. F. Schwier, M. G. Garnier, N. Mariotti, C. Didiot, H. Cercellier, J. Marcus, H. Berger, A. N. Titov, H. Beck, and P. Aebi, Probing the exciton condensate phase in $1T$-$TiSe_2$ with photoemission, New J. Phys. **12**, 125019 (2010).

[54] T. E. Kidd, T. Miller, M. Y. Chou, and T. C. Chiang, Electron-Hole Coupling and the Charge Density Wave Transition in $TiSe_2$, Phys. Rev. Lett. **88**, 226402 (2002).

*Supplementary information for:*

# Excitonic and lattice contributions to the charge density wave in 1$T$-$TiSe_2$ revealed by a phonon bottleneck

**H. Hedayat[1], C. J. Sayers[2], D. Bugini[1], C. Dallera[1], D. Wolverson[2], T. Batten[3], S. Karbassi[4], S. Friedemann[4], G. Cerullo[1], J. van Wezel[5], S. R. Clark[4,6], E. Carpene[7], E. Da Como[2]**

*1 Dipartimento di Fisica, Politecnico di Milano, 20133 Milano, Italy*

*2 Department of Physics, Centre for Nanoscience and Nanotechnology (CNAN) and Centre for Photonics and Photonic Materials (CPPM), University of Bath, BA2 7AY Bath, UK*

*3 Renishaw plc, Wotton-under-Edge, GL12 7DW, UK*

*4 HH Wills Physics Laboratory, University of Bristol, BS8 1TL Bristol UK*

*5 Institute for Theoretical Physics, Institute of Physics, University of Amsterdam, 1090 GL Amsterdam, The Netherlands*

*6 Max Planck Institute for the Structure and Dynamics of Matter, CFEL, Hamburg, Germany*

*7 IFN-CNR, Dipartimento di Fisica, Politecnico di Milano, 20133 Milano, Italy*

## 1. Characterisation of the CDW transition by electronic transport measurements

In order to confirm the sample quality of 1$T$-$TiSe_2$ single crystals used in TR-ARPES, we have performed electronic transport measurements including the temperature dependence of the in-plane resistivity and Hall effect. From this, we determine the CDW transition temperature and estimate the density of carriers involved in the phase transition. The in-plane resistivity, $\rho_{ab}$ as a function of temperature for a single crystal 1$T$-$TiSe_2$ sample is shown in Fig. S1(a). The behaviour is typical of this material, and the expected CDW transition ($T_{CDW}$ = 202 K) for near-stoichiometric samples is observed as a kink in the first derivative [1] (Fig. S1(b)). Hall effect measurements are presented in Fig. S1c. Above the CDW transition, at 205 K, the Hall coefficient,$R_H$ is positive and the associated charge carrier density is $n$= 6.78 × $10^{20}$ $cm^{-3}$ using the simple relation; $R_H = 1/n \cdot q$, where $q$ is the elementary charge. As the temperature is reduced below the CDW transition, $R_H$ becomes negative indicating that the dominant conduction switches from holes to electrons. In addition, the charge carrier density is rapidly decreasing and reaches a value of $n$= 3.09 × $10^{19}$ $cm^{-3}$ at 80 K. The difference above and below the transition is $\Delta n$=6.47 × $10^{20}$ $cm^{-3}$ which provides an estimate of the density of carriers

removed by the CDW (formation of bound exciton states), and is in excellent agreement with previous studies [2,3].

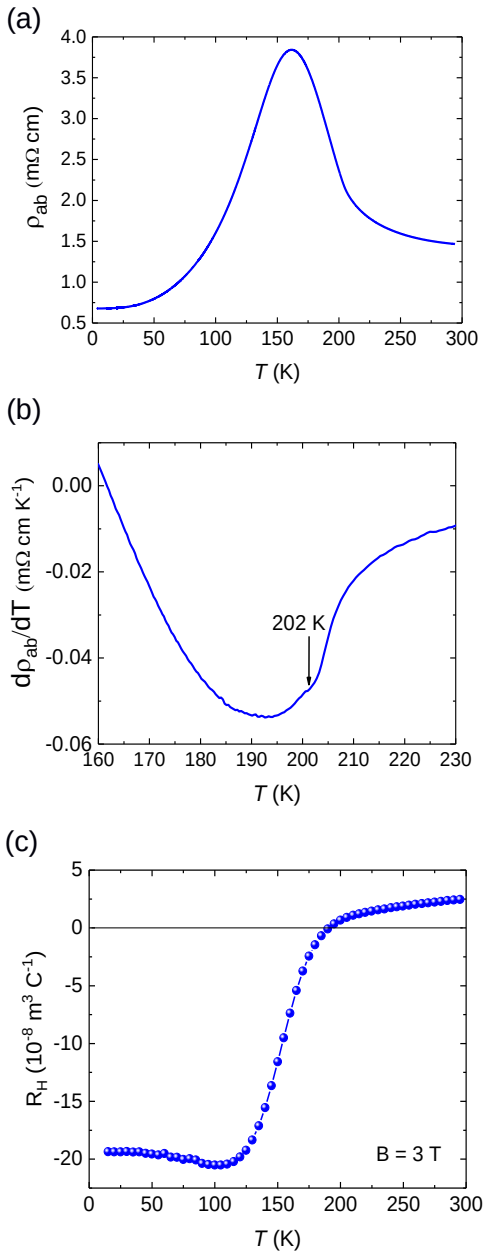


**Fig. S1.** Electronic transport measurements of 1$T$-$TiSe_2$. (a) In-plane resistivity, $\rho_{ab}$ as a function of temperature in the range (4.2 – 295) K. (b) First derivative of the resistivity (panel a.), highlighting the transition to CDW phase at approximately 202 K. (c) Hall coefficient, $R_H$ as a function of temperature with an applied magnetic field of 3 T.

**2. Details of TR-ARPES and TRR experiments.**

In order to measure angle-resolved photoemission maps (Fig. 1(b-d) of the main text) we used a time-of-flight (TOF) detector. Spectra for different angles were recorded by rotating the crystal with respect to the analyser. The angular dependence of emission was converted into $k_{\parallel}$, momentum parallel to the crystal surface, according to $k_{\parallel} = \sqrt{2m\,E_{kin}/\hbar^2}\,sin\theta$, where $m$ is the electron mass, $E_{kin}$ is the photoelectron kinetic energy and $\theta$ is the emission angle. The angular acceptance of the TOF detector is ± 1.5° which corresponds to a momentum resolution of approximately ± 0.013 $Å^{-1}$ at 1 eV kinetic energy. ARPES maps of energy versus momentum are therefore acquired by taking spectra at different pump-probe delays and different angles between the crystal surface and the detector. The analysis of VB shift dynamics presented in the main text, however has been performed on data acquired at a single fixed angle (-14°) with high statistics. We have used crossed polarisation of pump (p-pol) and probe (s-pol) beams. In order to construct Fig.1(b-d) in the main text, (i) each Photo Emission Spectrum (PES) (i.e. the spectrum at each angle) has been normalised to its respective maximum intensity (the VB peak) (ii) the energy-vs-angle map has been converted to energy-vs-momentum. In order to make the comparison between TR-ARPES and TRR experiments as close as possible we have used the pump beam from the same laser system, and determined the laser fluence accurately as follows. For both TR-ARPES and TRR experiments, the pump power has been measured with the same optometer. For TR-ARPES, the pump spot size has been measured with a beam profiler, deflecting pump and probe beams with a flip mirror (just before entering the vacuum chamber) and placing the beam profiler at the pump-probe overlap position. Corrections due to the incidence angle "θ" (with respect to the sample normal), which makes the pump beam slightly elliptical on the sample surface, have been included. For TRR measurements we have used the "knife-edge" method: a sharp edge mounted on a micrometer stage is placed at a defined position between the focusing lens and sample: as the edge cuts the beam, the reflected intensity is measured. Intensity versus edge position provides the beam size. Repeating the procedure at two known distances from the sample allows us to extrapolate the pump spot size (100 μm) on the specimen. The probe is approximately half of the pump spot size to ensure sampling of a uniformly excited area.

### 3. Coherent phonon oscillations

An interesting aspect of our experiment is the observation of coherent oscillations of the valence band (VB). Previously, TR-ARPES experiments have seen coherent oscillations only by focussing on the intensity of the weak folded replica of the VB at the $\bar{M}$-point [4,5]. Here instead, we report oscillations in the VB binding energy at $\bar{\Gamma}$, which is directly related to the CDW gap, Δ. Fig. S2a shows TR-ARPES data for 31 μJ cm$^{-2}$ fluence where oscillations are clearly seen at different signal intensity contours (black lines) indicating the coherent coupling between phonons and the VB binding energy. Subtraction of an exponential decay allows the oscillatory component to be extracted as shown in Fig. S2b. At this fluence, a damped oscillation of magnitude ± 5 meV occurs with period 290 – 300 fs ($f \approx 3.4$ THz) which corresponds to the $A_{1g}$* amplitude mode. Such assignment is consistent with previous optical [6,7] and TR-ARPES experiments [5]. For fluences above $F_{th}$ (62 μJ cm$^{-2}$), we could not confidently extract the frequency of the oscillations because of the low amplitude and strong damping, making them hardly distinguishable above the level of the noise.

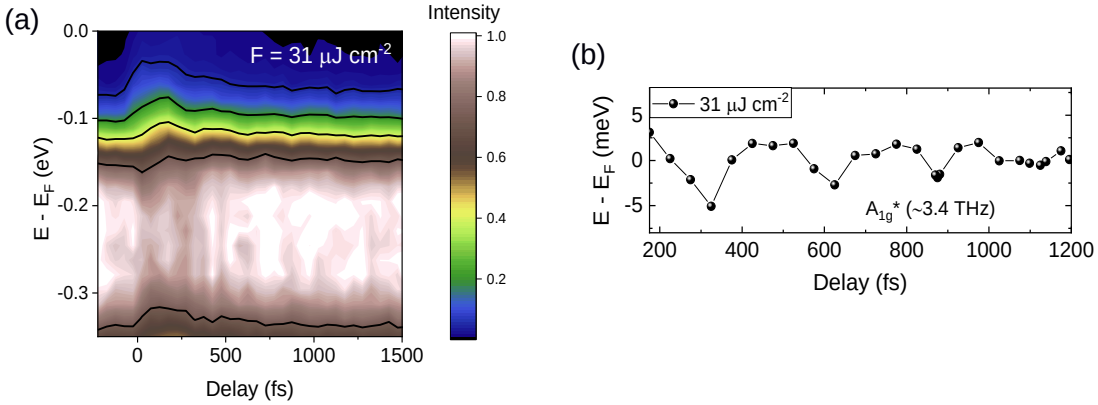


**Fig. S2.** VB oscillations**.** (a) Coherent oscillations in the VB dynamics for $F$ = 31 μJ cm$^{-2}$. The black lines indicate different intensity levels. (b) VB dynamics after subtraction of the exponential intensity decay (black dots), the frequency of oscillations is ~ 3.4 THz, consistent with the A1g* amplitude mode.

Together with the TR-ARPES experiments, we have also performed complementary time-resolved optical reflectivity (TRR) using similar experimental conditions as TR-ARPES (same pump photon energy and comparable fluences). First we show TRR data performed at very low fluence, $F$ = 8 μJ cm$^{-2}$ . Fig. S3 illustrates a crossover between the dominant phonon oscillation

of $A_{1g}$* (3.19 THz) below $T_{CDW}$ to $A_{1g}$ (5.95 THz) when the sample temperature is increased above $T_{CDW}$.

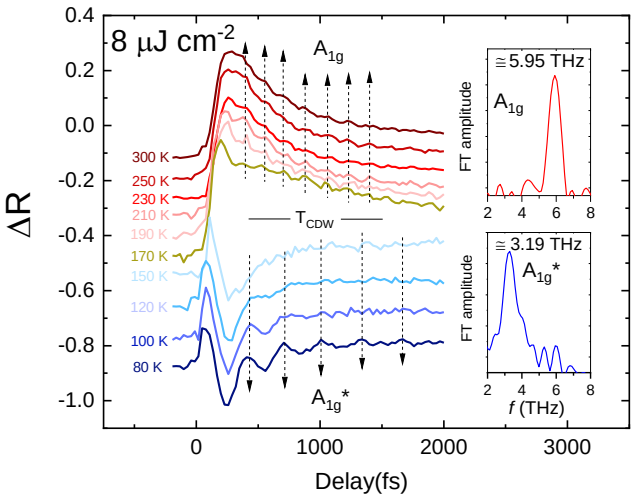


**Fig. S3.** Temperature dependent TRR in the normal and CDW phase. Data was collected using a pump laser fluence of 8 μJ $cm^{-2}$ for sample temperatures indicated on the figure. The data have been offset for the sake of clarity. The insets show the Fourier transform of the oscillatory part in the TRR data at 300 K (top) and 80 K (bottom).

Fig. 3 in the main text shows a similar behaviour but with the sample held at a constant temperature of 80 K and laser fluence increased in a similar way to TR-ARPES experiments. For the experiments performed at different fluence, we should point out that since high frequency oscillations appear at higher fluence there is the possibility of seeing the unfolded $A_{1g}$* mode (or another phonon of similar frequency) of the high symmetry structure, that gives rise to a pair of coherent zone-edge modes (that is second-order Raman active). We have approached the possibility of coherent zone-edge modes with a calculation of the phonon dispersion in $TiSe_2$ using density functional theory (DFT). Phonon dispersions were calculated for the normal phase of $TiSe_2$ via DFT as implemented in the plane-wave Quantum Espresso code closely following the approach of Doung *et al* [8]. LDA (PZ) and GGA (PBE) pseudopotentials were used in the projector

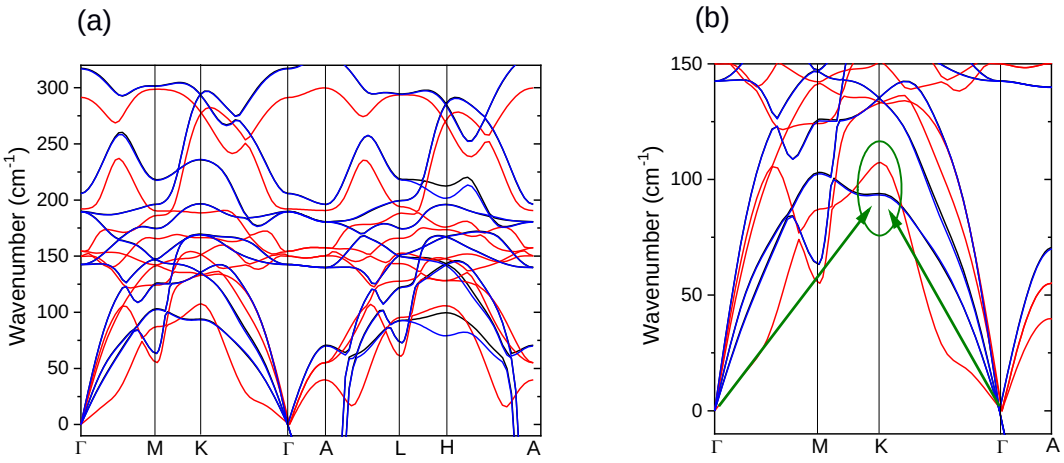


**Fig. S4.** DFT calculations of the phonon dispersion in 1$T$-$TiSe_2$. (a) Phonon dispersion calculated in the normal phase by DFT LDA (blue) and GGA (red) approximations. (b) Phonon dispersion along the high symmetry points Γ, M and K of the BZ. The green arrows indicate the excitation of two zone edge modes in a momentum and energy range (green circle) close to 100 $cm^{-1}$ (3 THz), i.e. corresponding to 200 $cm^{-1}$ (6 THz) when involving two of them.

augmented wave method with kinetic energy and charge density cutoff energies of 85 and 850 Ry respectively and a Monkhorst-Pack mesh of 24 x 24 x 12 k-points. Similar to Doung *et al* [8], a Fermi-Dirac smearing of electron occupations at the Fermi level of 0.005 Ry (equivalent to a temperature of 789 K) was used. The phonon dispersion calculations used a 4 x 4 x 2 grid of q-points for evaluation of the dynamical matrix. Fig. S4 shows the phonon dispersion for $TiSe_2$ in the *normal phase*. Panel (b) sketches a possible second order process involving two phonons with opposite momentum, thus total change in momentum Δk = 0, at frequencies ranging between 92 $cm^{-1}$ (2.76 THz) and 108 $cm^{-1}$ (3.24 THz) depending on the pseudopotentials. A similar sketch in the Γ-M boundary would give similar frequencies.

A second order Raman process would result in oscillations at frequency close to 200 $cm^{-1}$ (6 THz), as observed in our TRR[1*]. Coherent phonon frequency doubling has already been observed in femtosecond x-ray experiments other CDW materials [9,10], but it typically

[1] * Assessing the probability of such second order process would require the calculation of matrix elements including electronic states and their dispersion. The computational restriction linked to the difficulty in calculating the polarizability, thus the Raman tensors, for a metal or semimetal (Mills et al. Annals of Physics, 56, 504 (1970)) relegates this aspect to future work.

requires high pump fluence. Such behaviour is consistent with the notion that a second order process may become more likely as laser fluence is increased.

We argue here that coherent oscillations at 200 $cm^{-1}$ (6 THz) are *not* necessarily a phenomenon triggered by the high laser fluence. Fig. S3 demonstrates that in proximity of $T_{CDW}$ oscillations switch from the $A_{1g}$* phonon of the PLD to the $A_{1g}$ phonon of the normal phase. Remarkably the frequency of the oscillations at 300 K is similar to the one dominating TRR at fluences between 132 μJ $cm^{-2}$ and 264 μJ $cm^{-2}$ when the sample is held at 80 K (as reported in Fig. 3(c) of main text) with a frequency of 6.01 THz. The data of Fig. S3 clearly show that the oscillations of frequency 5.95 THz, occur in a low fluence regime as soon as the PLD is lost and changes into the structure of the normal phase. While we cannot completely exclude second order Raman processes, and these may be probed with future investigations, our DFT calculations suggest that such phenomena are energetically consistent with the normal phase structure. Thus, independent of the precise assignment of the high frequency oscillations, we can affirm that above $F_{th}$ the PLD is perturbed and phonons of a structure similar to the normal phase modulate the TRR signal.

The link between the CDW dynamics and the oscillations of frequency corresponding to the $A_{1g}$* mode has been extensively discussed in the literature [5,6,7]. In order to show further evidence for this selective coupling between the CDW and this particular phonon mode, we look at how the frequency and amplitude of the oscillations evolve as a function of temperature. Fig. S5 shows data extracted from TRR experiments with the sample at different temperatures and at constant low fluence of $F$ = 3 μJ $cm^{-2}$.

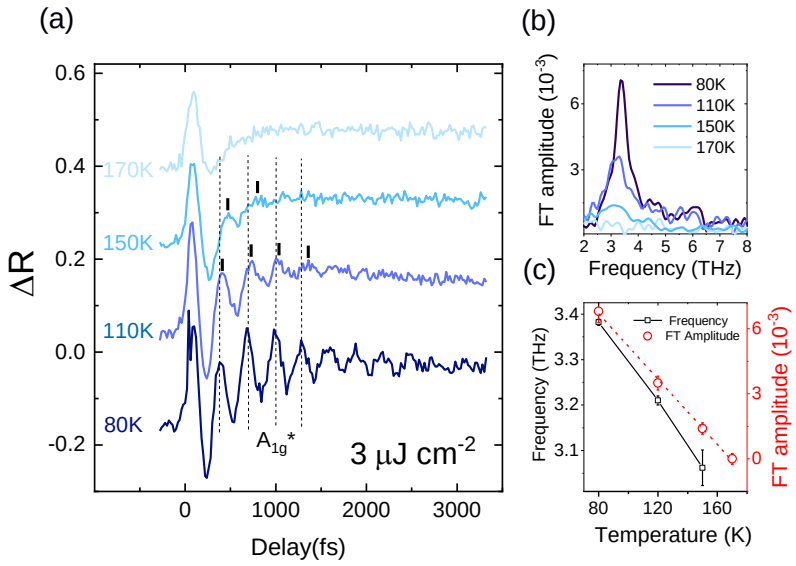


**Fig. S5**. Temperature dependent TRR in the CDW phase. (a) TRR at different sample temperatures as indicated on the figure with a pump laser fluence of 3 μJ $cm^{-2}$. The data have been offset for the sake of clarity. (b) Fourier transform of the oscillatory part in the TRR data at different temperatures. (c) Frequency and amplitude of the oscillations as a function of temperature.

The amplitude of the $A_{1g}$* oscillations shown in Fig. S5(b) displays a steep increase below T = 170 K. This trend is consistent with a BCS type of behaviour, i.e. similar to the gap dependence on temperature measured by ARPES [11] and confirms TRR experiments on 1$T$-$TiSe_2$ [6]. The assignment of the oscillations shown in Fig. S5 to the $A_{1g}$* is further confirmed by the similar frequency shift with temperature seen in Raman experiments reported in Fig. S14 of this Supplementary. Thus, we can affirm a *selective coupling* of the $A_{1g}$* mode to the CDW as also discussed in steady-state Raman and IR spectroscopy experiments on 1$T$-$TiSe_2$ [3,12].

The oscillations observed by TRR experiments and reported in Fig. 3(a-b) of the main text, have also been used to extract the damping time, $\tau_{damp}$ by fitting the data with a damped sinusoidal function (Fig. S6) with either 3.4 THz or 6 THz frequency (for fluence less than or greater than 100 μJ $cm^{-2}$, respectively). Note that the only fluence at which both oscillatory components can be clearly distinguished is 66 μJ $cm^{-2}$ where the FT of Fig. 3(c) in the main text shows two peaks of comparable width, thus comparable damping time.

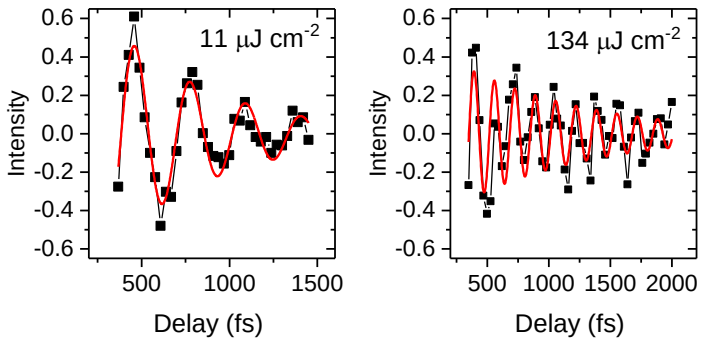


**Fig. S6**. Coherent oscillations from TRR. Damped sinusoidal fits allowed the damping time $\tau_{damp}$ to be extracted from data at different fluence.

The damping time and phase of oscillations for the $A_{1g}$* in TRR and TR-ARPES are very similar, highlighting the correspondence of the two techniques in looking at the phonon dynamics.

**4. Linearity of free carrier population with pump fluence**

In addition to the data presented in Appendix A of the main text, a second piece of experimental evidence for the linearity of optical pumping effect is shown in Fig. S7(a) which has been obtained by integrating the TR-ARPES intensity of the conduction band (CB) around 0 fs delay, see integration box in Fig. S7(b-c) for different pump laser fluences. This signal is proportional to the number of electrons promoted from the VB to a high energy CB by the pump pulse. The error bars are calculated in the same manner as discussed above for Fig. 5 in main text. The integrated CB intensity in Fig. S7(a) is fitted well by a linear relationship with an intercept that passes through the origin. Altogether, this and Appendix A provide compelling evidence that our experiments were performed well within the linear regime of optical pumping.

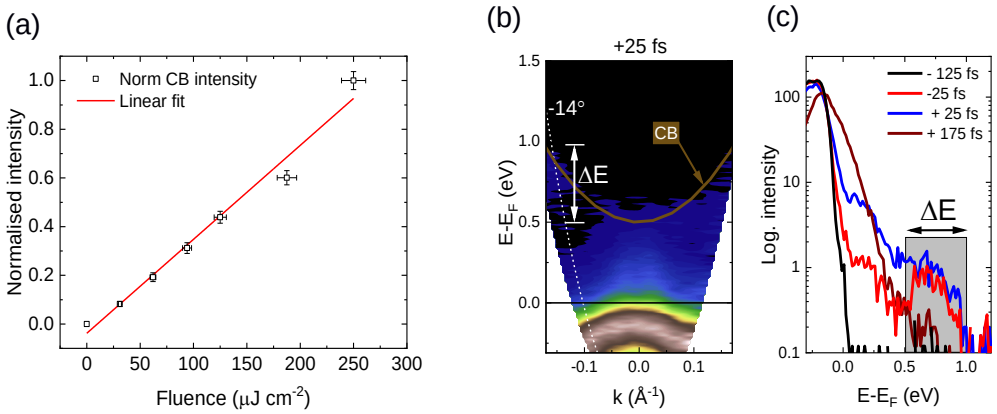


**Fig. S7.** Linearity of CB population with pump fluence. (a) Integrated spectral intensity of the CB obtained from the energy region ΔE (0.5 - 1 eV above $E_F$) shown in panel b and c. (b) TR-ARPES map recorded at +25 fs time delay showing transient population of the CB. The dark yellow parabola is a guide to the eye for a high energy CB populated with the pump pulse. An assignment of this CB can be found in Rohde et al. Eur. Phys. J. Special Topics 222, 997–1004 (2013). (c) Time evolution of the spectral intensity at -14° and highlighting the integration energy window, ΔE centred on the CB.

## 5. Laser heating dissipation

The experimental results shown in Fig. S8 reports the VB dynamics for different pump laser fluence discussed in the main manuscript in addition to data measured at room temperature (300 K) with $F$ = 250 μJ cm$^{-2}$.

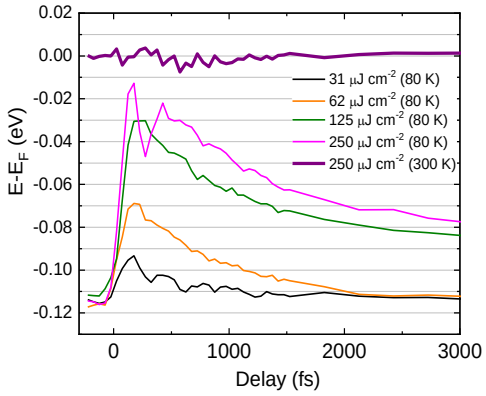


**Fig. S8.** VB dynamics probed by TR-ARPES for different pump laser fluence. The data up to $F$ = 250 μJ cm$^{-2}$ (pink curve) are the same as in main manuscript but plotted with y-axis as binding energy E-$E_F$ instead of VB shift. At negative delay, comparison of the 80 K traces with the additional trace recorded at 300 K and $F$ = 250 μJ cm$^{-2}$ shows that there is no significant change in the VB binding energy which could be attributed to laser-induced heating between pulse cycles.

It is clear that for all data measured at 80 K the VB binding energy before the pump pulse, i.e. at negative delays, is below -0.11 eV, which is a value consistent with the VB in the CDW phase [11]. Data at room temperature do not show a fluence dependence of the VB binding energy (as expected) and we report here only the maximum fluence investigated, 250 μJ $cm^{-2}$. In case of incomplete heat dissipation in between the laser pulses, i.e. average heating, the VB binding energy at negative times for the curves at 80 K would have a value in between -0.11 eV and 0 eV, which is not the case. This result signifies that the CDW gap re-equilibrates to its 80 K value within the 12.5 μs time interval between pulses for 80 kHz repetition rate of the laser system.

**6. Dynamics of individual valence sub-bands**

In the main text, the analysis and discussion of the TR-ARPES spectra has considered the overall VB dynamics. e.g. the total spectral feature $E - E_F$ = (-0.1 to -0.2) eV in Fig. 6. However, from high-resolution ARPES and band structure calculations, it is known that two Se-4p valence sub-bands are found at $\Gamma$ [11,13,14]. We have been able to extract the dynamics of the individual high and low-energy sub-bands (VB1 and VB2 respectively) by fitting the spectra at each pump-probe delay with a two Gaussian model (G1 and G2) as shown by the example in Fig. S9(a). We have imposed some reasonable constraints on the peak positions (x1 – x2 > 0.11 eV) and FWHM (w1 > 0.1 eV, w2 > 0.2 eV) as deduced from the static spectra before pump arrival (negative delay). The results are plotted in Fig. S9(b) for the individual sub-band positions (x1 and x2) and display surprisingly similar dynamics despite the number of free parameters.

The sub-band nearest the Fermi level (VB1) shows similar dynamics to the total VB discussed in the main text. As the laser fluence is increased above 60 μJ $cm^{-2}$, a plateau is reached around 2000 fs (bottleneck) and the VB does not recover to its CDW energy position within our experimental time window.

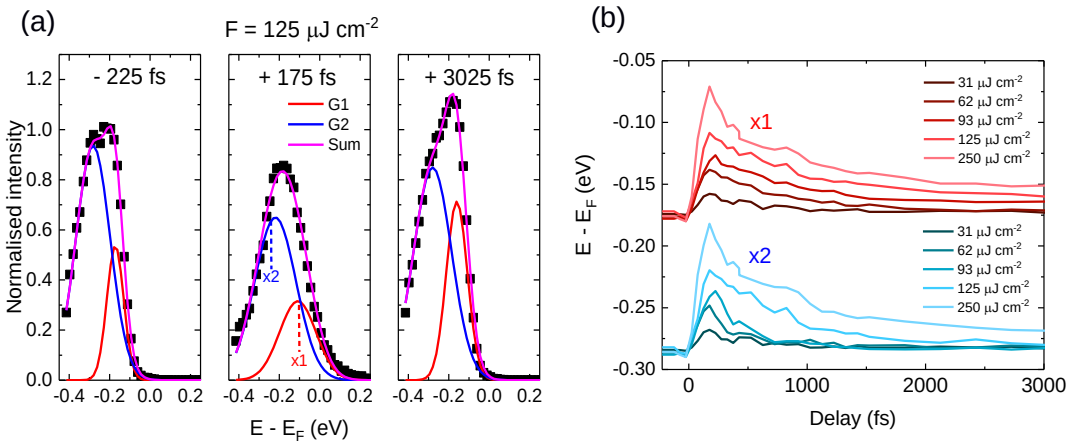


**Fig. S9.** Fitting individual valence sub-bands. (a) Example of fitting TR-ARPES spectra ($F$ = 125 μJ cm$^{-2}$) using a two Gaussian model (G1 and G2). This allows the position of individual valence sub-bands at each pump-probe delay to be extracted. (b) Results of the fitting for the peak positions (x1 and x2) as a function of pump-probe delay for each laser fluence.

## 7. Simulation of VB dynamics using a modified R-T population model

Exposing a material to an intense laser pulse momentarily creates a significant out-of-equilibrium distribution of charge carriers. The subsequent relaxation of carriers typically occurs by electron-electron and electron-phonon scattering on timescales ranging from hundreds of femtoseconds (fs) up to several picoseconds (ps) [15]. For simple metals, these relaxation processes have been successfully described using the well-known two temperature model (TTM) by considering the effective temperature of electron and lattice subsystems and their exchange of thermal energy following excitation [16,17,18]. For strongly-correlated materials such as superconductors and CDW systems, the relaxation dynamics are often more complicated due to the presence of a gap in the electronic spectrum and bound electron-electron (Cooper pair) or electron-hole (exciton) states. It was recognized by Rothwarf & Taylor (R-T) [19] that quasiparticles (QPs) in gapped systems may experience a bottleneck in the relaxation dynamics as their lifetime is not simply governed by their intrinsic recombination rate, but must also account for re-absorption of selectively coupled phonons (SCPs) that can break pairs. The application of the R-T model for the population dynamics in a host of strongly-correlated materials has been discussed in detail [20]. Here, we use a modified version of the R-T model to simulate the relaxation processes in 1$T$-$TiSe_2$ in the CDW phase, under the premise of an excitonic insulator scenario. We model the photo-excited dynamics via a set of coupled differential equations describing the populations above equilibrium of hot free carriers $n_e$, QPs

$n_q$, and SCPs $N_p$, respectively. Although the model does not consider the details of electronic band structure, we distinguish between $n_e$ and $n_q$. The latter being either relaxed electrons and holes at the band edge ready to form excitons in the condensate or electrons and holes generated from exciton breaking. Equations (1) – (3) give a complete description of the processes sketched in Fig. 4(a) of the main text, and are also presented more explicitly in Fig. S10,

$$\frac{dn_e}{dt} = S(t) - \frac{n_e}{\tau_e} - \frac{n_e}{\tau_{ep}} - \frac{n_e}{\tau_{th}}, \quad (1)$$

$$\frac{dn_q}{dt} = \frac{n_e}{\tau_e} + \eta N_p - 2Rn_T n_q - R{n_q}^2, \quad (2)$$

$$\frac{dN_p}{dt} = \frac{n_e}{\tau_{ep}} - \frac{\eta N_p}{2} + Rn_T n_q + \frac{R{n_q}^2}{2} - \gamma N_p. \quad (3)$$

Equation (1) describes the injection of hot free carriers by the pump pulse via the rate $S(t)$. We assume photo-induced electron/hole symmetry $n_e = n_h$ and therefore treat these free carriers collectively with a single density $n_e$. Following the pump pulse, hot carriers will rapidly relax via several pathways including electron-electron or electron-phonon scattering with timescales $\tau_e$ and $\tau_{ep}$ respectively or via the thermal bath with timescale $\tau_{th}$. Implicit in our model is the condensate of excitons (formed by bound quasiparticle pairs). The hot free carriers are expected to contribute additional screening of the Coulomb interaction binding excitons, so relaxation via electron-electron scattering is modelled as breaking exciton pairs. This creates an excess QP population (above thermal equilibrium), described by the source term in equation (2). Again, we have assumed quasi-electron-hole symmetry and so consider a single density $n_q$ describing both. Importantly, another source of QPs comes from the absorption of SCPs with rate $\eta$ which will also break excitons. The remaining terms describe the recombination of QPs into excitons given by the rate $R$, accounting also for the presence of thermally excited QPs with density $n_T$. Both the relaxation of hot free carriers via electron-phonon scattering and QP recombination excite the SCPs (above thermal equilibrium), as captured in equation (3). The factor of 2 in equations (2) and (3) arises because two QPs are created for one absorbed phonon during an exciton pair breaking event and vice versa during recombination. The first term in equation (3) assumes a 1:1 ratio of free carriers scattering with SCPs for simplicity and we find that the model is rather insensitive to this factor. Finally, the anharmonic decay rate of SCPs to the thermal bath is given by $\gamma$ in equation (3).

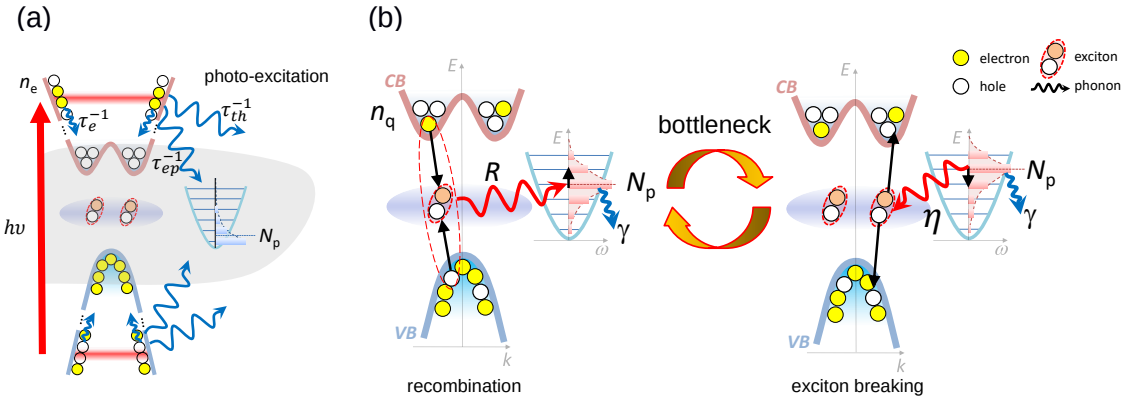


**Fig. S10.** Sketch of processes considered by the modified R-T model. (a) Photoexcitation illustrating the main scattering processes for hot electrons and hot holes with other carriers, $\tau_e^{-1}$, selectively coupled phonons, $\tau_{ep}^{-1}$, and the thermal bath, $\tau_{th}^{-1}$. These processes appear in equation (1) of the model. (b) Bottleneck involving the quasiparticle population, $n_q$, and the out of equilibrium SCPs $N_p$. The straight black arrows indicate the transition from electron and hole quasiparticles to the exciton condensate in both directions. Red curved arrows indicate the recombination of two quasiparticles, generating an SCP (left panel) or the breaking of an exciton with an SCP, generating two quasiparticles (right). $\gamma$ is the anharmonic phonon-phonon scattering rate with the thermal bath. The orange arrows (bottleneck) are used to illustrate the iterative processes between recombination and exciton breaking limited by the $\eta/\gamma$ and appear in equations (2) and (3) of the modified R-T model.

The free carrier population generated by the pump pulses assumes that each photon generates a single photocarrier. Therefore, the total number of photocarriers, $n_0$depends on the laser fluence, $F$ and sample characteristics,

$$n_0 = \frac{(1-r)\alpha F}{h\upsilon}, \tag{4}$$

where $r$ = 0.60 is the reflectivity of 1$T$-TiSe$_2$ at pump wavelength 682 nm ($h\upsilon$ = 1.82 eV) and $\delta = 1/\alpha$ = 15 nm is the penetration depth based on the dielectric constant $\varepsilon$ = -8 + i15 (ref. [21]). The number of total photocarriers for the laser fluence range used in our experiment (31–250 µJ cm$^{-2}$) corresponds to (0.28 – 2.3) × 10$^{20}$ cm$^{-3}$. The photocarrier generation rate, $S(t)$ is then simply given by the product of the total carriers, $n_0$ and a Gaussian pulse profile, $P$ as

$$S(t) = n_0 P = n_0 \frac{2}{\tau_p\sqrt{2\pi}} e^{-2\left(\frac{t}{\tau_p}\right)^2}, \tag{5}$$

where $\sqrt{2}ln(2)\tau_p$ is the pulse FWHM.

Solving equations (1) – (3), with the equilibrium initial conditions $n_e = n_q = N_p = 0$ for each laser fluence gives the time evolution of the populations with the scattering and recombination rates as fit parameters in the model. Most importantly, any variation in the QP population, $n_q(t)$ over time can be related to a dynamic change in the CDW gap, Δusing a simple mean-field equation [20]

$$\Delta(t) = \Delta_{80K}\sqrt{1 - n_q\,(t)/n_c}, \tag{6}$$

where $\Delta_{80K}$ = 130 meV is the gap at 80 K (ref. [10]). Here, $n_c$ is the critical QP density based on the carriers involved in forming the CDW. Since an increase in the QP population indicates the breaking of excitons, complete suppression of the CDW occurs when $n_q \geq n_c$. For the case of 1$T$-$TiSe_2$, any variation in the magnitude of the CDW gap Δ can be approximated as a VB shift since it has been shown that the CDW has little or no effect on the CB energy [22,11]. With this assumption, the simulated VB shift dynamics is simply $\Delta(t) - \Delta_{80K}$. The fluence dependence of the free parameters used in the model are shown in Fig. S11: $\tau_e$ (panel a) influences the dynamics at short times,$R$(panel b) mainly affects the overall QP density and therefore the magnitude of the VB shift, but with little change to the dynamics. The central finding of our experiments, i.e. the recovery dynamics, are crucially dominated by $\eta$ and $\gamma$ (panel c). The ratio $\eta/\gamma$ is an important metric for which the strong bottleneck regime occurs when $\eta/\gamma < 1$ as shown in the inset of Fig. S11(c).

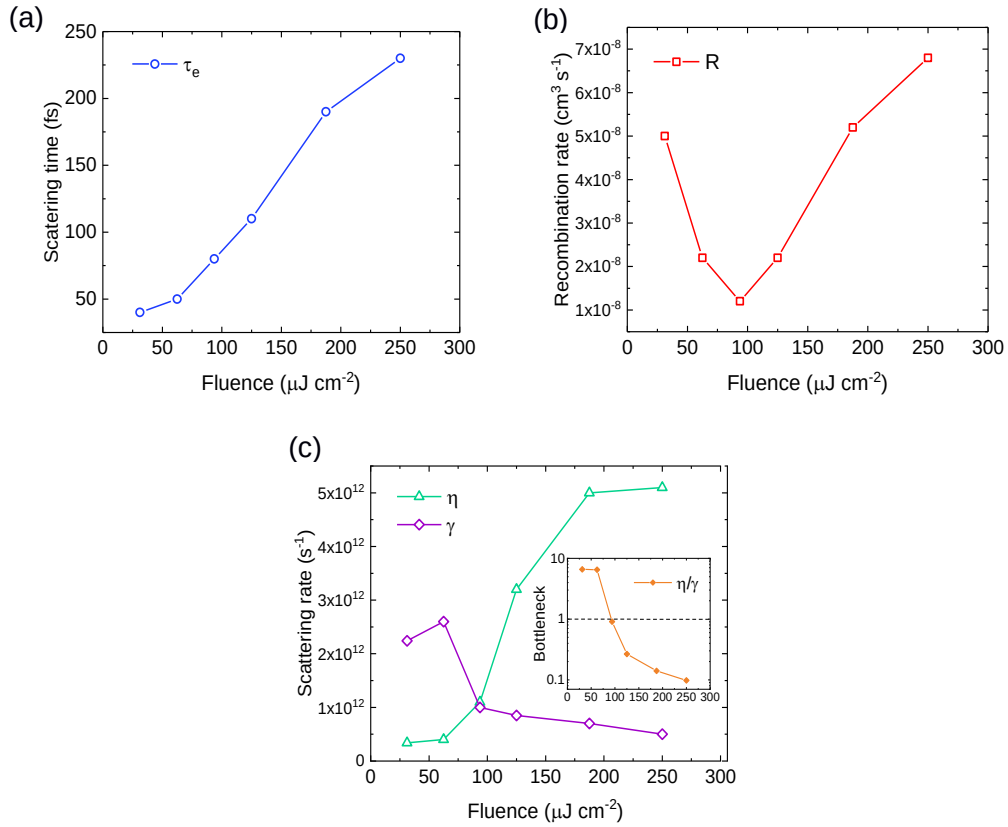


**Fig. S11.** Fluence dependence of parameters used in the modified R-T model**.** (a) Electron-electron scattering time, $\tau_e$. (b) Exciton recombination rate, $R$. (c) Scattering rates of collisions between excitons and SCPs, $\eta$ and the anharmonic decay rate, $\gamma$ with the thermal bath. The inset shows the bottleneck ratio, $\eta/\gamma$ on a logarithmic scale and the dashed line indicates the strong bottleneck regime for $\eta/\gamma < 1$.

All other parameters remained fixed including the scattering time for free carriers with phonons and the thermal bath for which we used $\tau_{ep}$= $\tau_{th}$= 1 ps. Best agreement with the data was found using a thermal QP density, $n_T$ = 0.1 × $10^{20}$ $cm^{-3}$ and a critical quasiparticle density,$n_c$ = 0.8 ×$10^{20}$ $cm^{-3}$, comparable to our Hall effect measurements and previous estimates [2,3] in the range (0.6 – 6) ×$10^{20}$ $cm^{-3}$. Examples are shown in Fig. S12 of the VB dynamics simulations for two cases corresponding to below ($F$ = 31 μJ $cm^{-2}$) and above ($F$ = 125 μJ $cm^{-2}$) the pump fluence required for the onset of the bottleneck seen in TR-ARPES with $\eta/\gamma$ = 6.6 and 0.26, respectively.

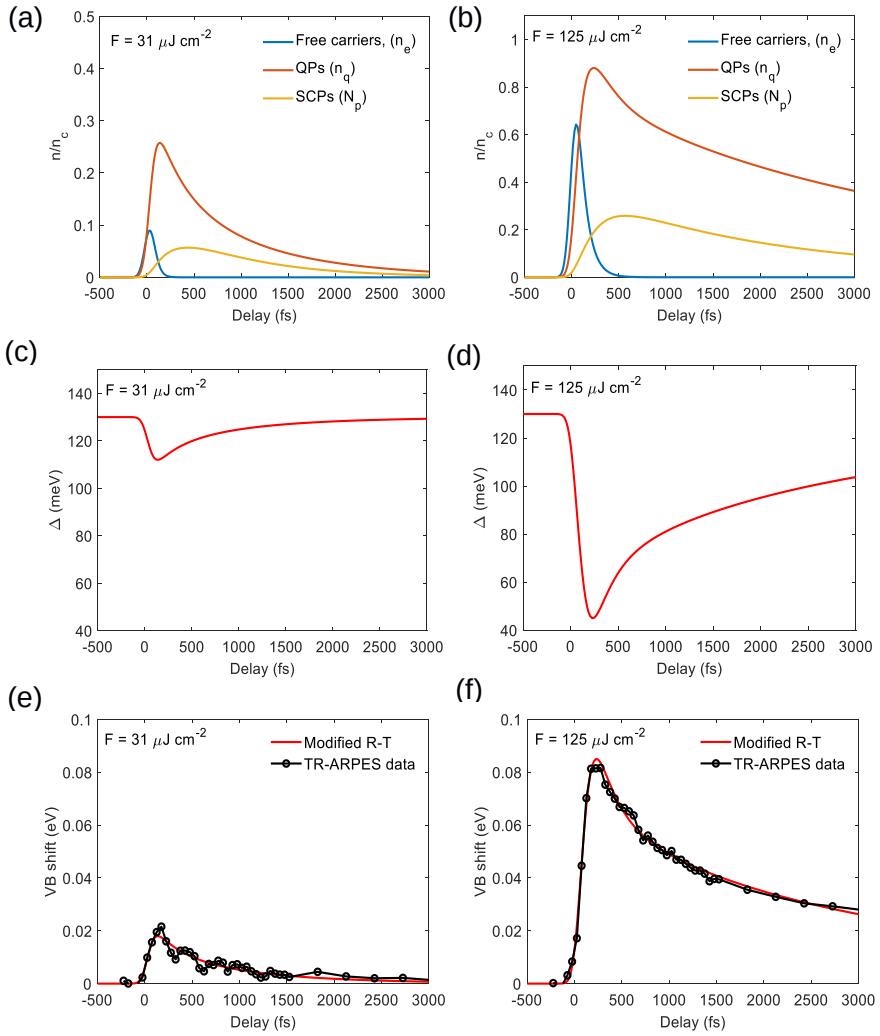


**Fig. S12.** Example of VB dynamics modelling using a modified R-T population model. Examples are shown below ($F$ = 31 μJ cm$^{-2}$) and above ($F$ = 125 μJ cm$^{-2}$) the pump fluence required for the onset of the bottleneck seen in TR-ARPES. (a) - (b) Solutions to Equations (1) – (3) showing the time evolution of particle populations. The results are normalised by the critical QP density, $n_c$. (c) – (d) Dynamics of the CDW gap, Δ based on the QP density, $n_q$ using equation 6. (e) – (f) Comparison between experimental (circles) and modelled VB shift.

It can be seen in Fig. S12(b) ($F$ = 125 μJ cm$^{-2}$) that the QP density (orange curve) does not recover to the initial value, but instead experiences a bottleneck. This translates as a plateau in the VB shift at 3 ps in agreement with the experimental data (see panel d and f).

**8. Temperature dependence of phonon modes determined by Raman spectroscopy**

In order to further understand the origin of the coherent oscillations seen in our TR-ARPES experiment, we have used Raman spectroscopy to investigate the temperature dependence of phonon modes in single crystal 1$T$-$TiSe_2$ in the range (80 – 300 K). By this method, we are able to identify the Raman-active modes at the BZ centre ($\Gamma$-point). The experiments were performed on single crystals from the same batch as those used in TR-ARPES. A Renishaw InVia Raman spectrometer was used in the backscattering geometry, equipped with a 633 nm laser excitation wavelength, 2400 l/mm grating and long working distance 50x lens (N.A. = 0.5). The spectral resolution of this configuration was better than 1 $cm^{-1}$. Volume Bragg grating notch filters (Eclipse) with a cut-off of ± 10 $cm^{-1}$were used to access the low-frequency tails of the CDW related modes. The laser power was kept sufficiently low to avoid heating effects and was measured on the sample to be (230 ± 5) µW.

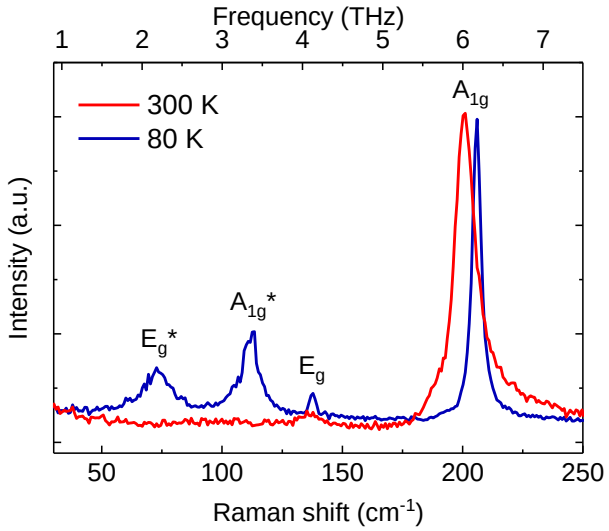


**Fig. S13.** Raman active phonons in 1$T$-$TiSe_2$. Raman spectra in the normal (300 K) and CDW (80 K) phase with the relevant modes labelled. Two additional modes are found in the CDW phase, including the $A_{1g}^*$ mode selectively coupled to the CDW.

Fig. S13 highlights the key differences in the Raman spectrum of 1$T$-$TiSe_2$ above and below the CDW transition. In the normal phase (T = 300 K), there are two clear phonon modes; $E_g$ = 136 $cm^{-1}$ (4.08 THz) and $A_{1g}$ = 201 $cm^{-1}$ (6.03 THz) in good agreement with previous studies [12,23] and correspond to the in-plane and out-of-plane vibrations of Se atoms around a central Ti atom, respectively. In the CDW phase (80 K), the formation of the (2a x 2a x 2c) superlattice means that the BZ boundary ($\bar{A}$, $\bar{L}$ and $\bar{M}$-point) is folded to the zone centre ($\bar{\Gamma}$-point) [22]. As a result, two new modes become visible at $\bar{\Gamma}$ which include; $E_g^*$ = 73 $cm^{-1}$ (2.19 THz) and $A_{1g}^*$

= 112 $cm^{-1}$ (3.36 THz), in addition to the original normal phase modes. $A_{1g}^{*}$ is commonly referred to as the CDW amplitude mode and can been seen as coherent oscillations with frequency 3.4 THz in our TR-ARPES (Fig. 7 in main text) and TRR data (Fig. 3 main text and Fig. S3 and S5).

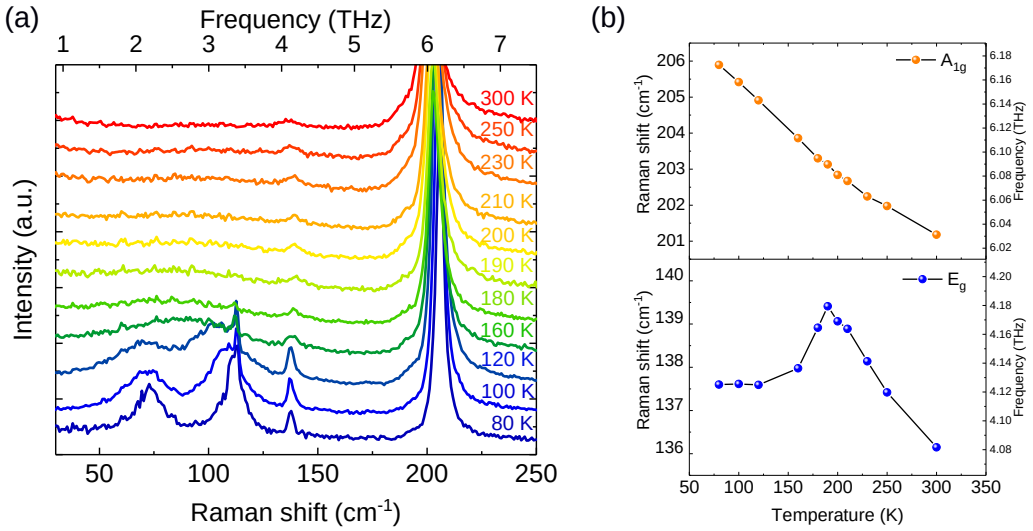


**Fig. S14.** Temperature-dependence of Raman active phonon modes in 1*T*-$TiSe_2$**.** (a) Raman spectra in the range (300 – 80 K). (b) Evolution of the $A_{1g}$ and $E_g$ mode frequencies with temperature.

The temperature dependence of Raman modes is shown in Fig. S14(a). As the temperature is reduced, the rise in the modes ($E_g^{*}$ and $A_{1g}^{*}$) related to the PLD is apparent. These modes first appear as a single broad feature at 160 K and only become clearly distinguishable at 120 K, far below the CDW transition temperature of 202 K. This extreme broadening of CDW modes at intermediate temperatures is different to other TMDs (e.g. 2H-$TaSe_2$) and has been previously suggested to be a signature of large fluctuations in the order parameter [24]. The frequency of the normal phase modes ($E_g$ and $A_{1g}$) are shown in Fig. S14(b) as a function of temperature. Initially, both modes show typical phonon hardening behaviour with decreasing temperature but experience a change near the CDW transition. Clearly evident is the softening of the $E_g$ below 190 K, which is particularly sensitive to the CDW formation due to the significant in-plane lattice distortion as reported previously [25]. In contrast, the $A_{1g}$ mode, which is associated with out-of-plane vibrations, only displays a slight change in gradient near 200 K.

**References**


1. Di Salvo, F. J., Moncton, D. E. and Waszczak, J. V., Electronic properties and superlattice formation in the semimetal $TiSe_2$. *Phys. Rev. B.*,**14**, 4321 (1976).

2. Li, G., Hu, W. Z., Qian, D., Hsieh, D., Hasan, M. Z., Morosan, E., Cava, R. J., and Wang, N. L., Semimetal-to-Semimetal Charge Density Wave Transition in 1T-$TiSe_2$. *Phys. Rev. Lett.* **99**(2):027404, (2007).

3. Wilson, J. A., Barker, A. S., Di Salvo, F. J., & Ditzenberger, J. A., Infrared properties of the semimetal $TiSe_2$. *Phys. Rev. B*, ***18***(6) (1978).

4. Hellmann, S., Rohwer, T., Kalläne, M., Hanff, K., Sohrt, C., Stange, A., Murnane, M. M., Kapteyn, H. C., Kipp, L., Bauer, M., and Rossnagel, K. Time-domain classification of charge-density-wave insulators. *Nat. Comms*. **3**, 1069 (2012).

5. Monney, C., Puppin, M., Nicholson, C. W., Hoesch, M., Chapman, R. T., Springate, E., Berger, H., Magrez, A., Cacho, C., Ernstorfer, R., and Wolf, M., Revealing the role of electrons and phonons in the ultrafast recovery of charge density wave correlations in 1*T*-$TiSe_2$. *Phys. Rev. B*, **94**, 165165 (2016).

6. Möhr-Vorobeva, E., Johnson, S.L., Beaud, P., Staub, U., De Souza, R., Milne, C., Ingold, G., Demsar, J., Schaefer, H. and Titov, A., Nonthermal Melting of a Charge Density Wave in $TiSe_2$. *Phys. Rev. Lett.* **107**(3)**:** 4 (2011).

7. Porer, M., Leierseder, U., Menard, J.M., Dachraoui, H., Mouchliadis, L., Perakis, I.E., *et al.* Non-thermal separation of electronic and structural orders in a persisting charge density wave, *Nature Materials*,**13**(9)**:** 857-861 (2014).

8. Duong, D. L., Burghard, M. and Schön J. C., Ab initio computation of the transition temperature of the charge density wave transition in $TiSe_2$. *Phys. Rev. B* **92**, 245131 (2015).

9. Huber, T., Mariager, S. O., Ferrer, A., Schäfer, H., Johnson, J. A., Grübel, S., Lübcke, A., Huber, L., Kubacka, T., Dornes, C., Laulhe, C., Ravy, S., Ingold, G., Beaud, P., Demsar, J. and Johnson, S. L., Coherent Structural Dynamics of a Prototypical Charge-Density-Wave-to-Metal Transition. *Phys. Rev. Lett.* **113**, 026401 (2014).

10. Rettig, L., Cortes, R., Chu, J. H., Fisher, I. R., Schmitt, F., Moore, R. G., Shen, Z. –X., Kirchmann, P. S., Wolf, M., and Bovensiepen, U., Persistent order due to transiently enhanced nesting in an electronically excited change density wave. *Nature Communications* **7**, 10459 (2015).

11. Chen, P., Chan, Y.-H., Fang, X.-Y., Mo, S.-K., Hussain, Z., Fedorov, A.-V., Chou, M.-Y. and Chiang, T.-C., Hidden Order and Dimensional Crossover of the Charge Density Waves in $TiSe_2$. *Scientific Reports* **6**:37910 (2016).

12. Holy, J. A., Woo, K. C., Klein, M. V., and Brown, F. C., Raman and infrared studies of superlattice formation in $TiSe_2$. *Phys. Rev. B* **16**(8), 3628–3637 (1977).

13. Zunger, A. and Freeman, A. J., Band structure and lattice instability of $TiSe_2$. *Phys. Rev. B*, **17**, 1839 (1978).

14. Rohwer, T., Hellmann, S., Wiesenmayer, M., Sohrt, C., Stange, A., Slomski, B., Carr, A., Liu, Y., Avila, L. M., Kallane, M., Mathias, S., Kipp, L., Rossnagel, K. and Bauer, M., Collapse of long-range charge order tracked by time-resolved photoemission at high momenta, *Nature* **471**, 490–494 (2011).

15. Shah, J., Ultrafast Spectroscopy of Semiconductors and Semiconductor Nanostructures. *Springer* (1999).

16. Anisimov, S. I., Kapeliovich, B. L., and Perel'man, T. L., Electron emission from metal surfaces exposed to ultrashort laser pulses, *Sov. Phys. JETP* **39**, 375 (1974).

17. Allen, P. B., Theory of thermal relaxation of electrons in metals. *Phys. Rev. Lett.* **59**(13):1460-1463 (1987).

18. Baranov, V. V. and Kabanov,V. V., Theory of electronic relaxation in a metal excited by an ultrashort optical pump. *Phys. Rev. B.* **89**(12):125102 (2014).

19. Rothwarf, A., and Taylor, B. N., Measurement of Recombination Lifetimes in Superconductors, *Phys. Rev. Lett.***19**, 27 (1967).

20. Giannetti, C., Capone, M., Fausti, D., Fabrizio, M., Parmigiani, F., and Mihailovic, D., Ultrafast optical spectroscopy of strongly correlated materials and high-temperature superconductors: a non-equilibrium approach, *Advances in Physics* **65**:2, 58-238 (2016).

21. Reshak, A. H. and Auluck, S. Electronic and optical properties of the 1T phases of $TiS_2$, $TiSe_2$, and $TiTe_2$, *Phys. Rev. B.* **68**, 245113 (2003).

22. Kidd, T. E., Miller, T., Chou, M. Y. and Chiang, T. C., Electron-Hole Coupling and the Charge Density Wave Transition in $TiSe_2$, *Phys. Rev. Lett.* **88**, 226402 (2002).

23. Sugai, S., Murase, K., Uchida, S., and Tanaka, S., Raman studies of lattice dynamics in 1T-$TiSe_2$, *Solid State Comms*. **35**(5), 433–436 (1980).

24. Uchida, S., and Sugai, S., Infrared and Raman studies on commensurate CDW states in transition metal dichalcogenides. *Physica B+C*, **105**(1–3), 393–399 (1981).

25. Duong, D. L., Ryu, G., Hoyer, A., Lin, C., Burghard, M., and Kern, K. Raman Characterization of the Charge Density Wave Phase of 1T-$TiSe_2$: From Bulk to Atomically Thin Layers. *ACS Nano* **11**(1), 1034–1040 (2017).

## 5.4 Discussion & concluding remarks

The work in Section 5.3 demonstrates a unique experimental approach of complimentary time- and angle-resolved photoemission spectroscopy (TR-ARPES) and time-resolved reflectivity (TRR) measurements in order to disentangle the contributions of excitonic and lattice-driven CDW order in 1*T*-$TiSe_2$. TR-ARPES allowed direct visualisation of changes to the electronic structure related to CDW order such as the gap, $\Delta_{CDW}$ following perturbation with an intense laser pulse. In particular, the experimental setup [73] allowed valence band dynamics near $\bar{\Gamma}$ to be tracked over a relatively unexplored range of low-moderate laser fluence (31 - 250 $\mu$J cm$^{-2}$) with high-stability. TRR allowed fingerprints of the lattice distortion in the form of coherent phonon oscillations to be studied. Using the same pump laser in both TR-ARPES and TRR allowed confidence in the validity of comparing the fluence-dependent behaviour between experiments.

The main results demonstrated that dynamics of CDW suppression such as gap closing and band-replica unfolding occur on relatively short timescales ($\leq$ 200 fs) and significant suppression occurs at low fluence (e.g. $\sim$50 meV max. VB shift at 62 $\mu$J cm$^{-2}$). These two aspects suggest a primarily exciton-driven CDW mechanism since the exciton binding energy is reduced significantly due to screening of the coloumb interaction between electron-hole pairs via free carriers promoted by the pump pulse which reduces the CDW gap directly [28], and the process occurs on a timescale which is consistent with the build up of this screening potential [140].

A detailed pump fluence dependence of the dynamics reveals several regimes. At low fluence (31 - 62 $\mu$J cm$^{-2}$), the CDW gap was found to recover fully within $\sim$2 ps. However in the high fluence regime (93 - 250 $\mu$J cm$^{-2}$), the recovery is impeded and the VB remains up-shifted within the experimental time window of 3 ps. A threshold fluence, $F_{\text{th}} = 60$ $\mu$J cm$^{-2}$ was established to trigger the onset of this recovery bottleneck. In addition, coherent oscillations of the CDW gap were observed in TR-ARPES at low fluence, with a frequency characteristic of the $A_{1g}^{*}$ CDW amplitude mode ($\sim$ 3.4 THz) [132, 133, 136]. Using the same pump pulse in TRR, these oscillations were studied in detail over a similar fluence range. A progressive switching of the dominant oscillation frequency from the $A_{1g}^{*}$ mode (3.4 THz) to the $A_{1g}$ (6 THz) mode of the normal phase structure was found, which coincided precisely with the threshold fluence, $F_{\text{th}}$ required for the onset of the VB up-shift.

The experimental results were compared with simulations of the quasiparticle dynamics based on a modified Rothwarf-Taylor (R-T) model [78, 141]. A set of coupled differential rate equations described the population of free carriers generated by the pump pulse, $n_e$, quasiparticles from the dissociation of electron-hole pairs (excitons), $n_q$, and selectively-coupled phonons (SCPs), $N_p$. Excellent agreement with experiments were found across the entire fluence range and a crossover to the *bottleneck* regime ($\gamma/\eta < 1$) [78] was found beyond $F_{\text{th}} = 60$ $\mu$J cm$^{-2}$, related to the exciton dissociation rate, $\eta$ and the anharmonic decay of SCPs to the thermal bath, $\gamma$.

In summary, the results presented in this chapter are consistent primarily with an excitonic mechanism, [28, 146, 147] based on the rapid photo-induced CDW suppression dynamics and required pump fluence. In the low fluence regime, sufficient screening of the exciton binding energy reduces $\Delta_{\text{CDW}}$, whilst the lattice order remains and complete CDW recovery is possible. In the high fluence regime however, the lattice order is also suppressed. The eventual loss of PLD phonons and emergence of the normal phase lattice structure is concomitant with the impeded recovery of the CDW. These results are supported by simulations of the quasiparticle dynamics which reveals a bottleneck in the recovery above critical fluence, by considering the dissociation and recombination of excitons and their interaction with phonons. Thus, this work highlights the importance of both excitonic and lattice order and their contributions to the CDW phase in 1$T$-$TiSe_2$ [131, 132, 142]. The detailed fluence-dependence demonstrates the regimes in which these forms of order can exist under out-of-equilibrium conditions, and their contributions to the CDW order parameter, related to $\Delta_{\text{CDW}}$.

The complementary techniques of TR-ARPES and TRR used in this work allowed direct probing of the electronic structure combined with structural information in form of coherent phonon oscillations. This experimental approach could be applied to disentangle possible competing or co-operating many-body interactions in other complex strongly-correlated systems. Since each experiment utilises the same pump pulse, fluence-dependent behaviour can be compared with great confidence, and may become particularly important in the very low fluence regime often used to study cuprate superconductors [155], for example.

# Chapter 6

## Fermi surface nesting in 1$T$-$VSe_2$

### 6.1 Preamble

1$T$-$VSe_2$ exhibits a CDW that is consistently reported in the literature as a single transition at $T_{CDW} \approx 110$ K and evidenced by clear signatures in electronic transport measurements including; resistivity, Hall coefficient and magnetic susceptibility [44, 45, 109]. However, structural probes such as x-ray diffraction measurements have previously revealed signatures of two separate CDW transitions in this compound [48]. At $T_{c1} = 110$ K, there is a second-order transition to an incommensurate CDW with $(4a_0 \times 4a_0 \times 3.18c_0)$ PLD, which is followed by a first-order lock-in transition around $T_{c2} \approx$ (80 - 85) K via a small change in the distorted $c$-axis to $3.25c$ [48]. The corresponding CDW wavevectors are then represented by; $\mathbf{q_1} = (1/4a_0, 0.314c_0)$ and $\mathbf{q_2} = (1/4a_0, 0.307c_0)$ for the separate states respectively. These findings were later supported by electron diffraction measurements which also observed two phase transitions and suggested that $T_{c2}$ may be associated with an unusual $3q$-$2q$ transition [107]. It was shown that a $3q$ CDW state first forms at 110 K which then transforms into an irregular pattern of $2q$ domains below 80 K whereby only two of the possible three $\mathbf{q}$-vectors are present [107, 156]. The $2q$ phase is mostly overlooked in the recent literature either because the signatures of the $3q$-$2q$ transition are comparatively weak to the normal-$3q$ transition or there are conflicting reports due to discrepancies in sample purity as will be discussed further in Chapter 4.

Because of two-dimensional nature of the layered TMDs, Fermi surface (FS) nesting has been proposed as a likely scenario for CDW formation because of the suitable FS topology [2] as discussed in Section 1.2.3. However, in some 2D materials such as 2$H$-$NbSe_2$, evaluation of the electronic susceptibility suggests that FS nesting may be entirely

negligible, despite exhibiting a distinct Kohn anomaly near the expected CDW **q**-vector characteristic of a nesting instability [23, 157]. Such observations have brought into question the relevance of FS nesting in these materials and whether this scenario is applicable to anything other than a purely 1D Peierls-like system [23]. 1$T$-$VSe_2$ is an ideal candidate to investigate the possibility of nesting-driven CDW formation in TMDs due to the presence of large parallel portions of FS, which could be prone to nesting similar to other group-V 1$T$-TMDs [2]. This hypothesis has been investigated both theoretically [50] and experimentally by ARPES [99, 120, 121], with considerable importance placed on 3D ($k_z$-dependent) nesting. As discussed in Section 1.2.3, to investigate the role of FS nesting, it is possible to calculate the electronic susceptibility, $\chi^0(\mathbf{q}, k)$ (Equation 1.17) and compare it to experimental measurements of the FS. A divergence in both the real and imaginary parts of $\chi^0(\mathbf{q}, k)$ near the expected $\mathbf{q}_{\mathrm{CDW}}$ [22, 23, 33], will be highly suggestive of a nesting-like instability. This approach was has been used to investigate CDW formation in other TMDs such as 2$H$-$TaSe_2$ [122].

This chapter reports on detailed measurements of the FS and band dispersions of 1$T$-$VSe_2$ using full-wavevector ARPES in order to investigate FS nesting driven CDW formation in this compound. The stability offered by single-shot $(k_x, k_y)$ acquisition across the entire BZ, combined with excellent momentum resolution ($\sim$0.02 Å$^{-1}$), is ideal to study the subtle impact of FS topology. In the work by Jones *et al.* entitled "Charge density wave gap in 1$T$-$VSe_2$: Momentum and temperature dependence" [100], ARPES images at $E_{\mathrm{F}}$ are measured as a function of temperature in order to search for gaps, $\Delta_{\mathrm{CDW}}$ and to determine their location on the FS in momentum space. The experimental results are compared to DFT calculations of the electronic susceptibility, $\chi^0(\mathbf{q}, k)$ to investigate the role of nesting and the possibility of separate 3$q$ and 2$q$ CDW states in this material.

## 6.2 Introduction

### 6.2.1 Topology of the Fermi surface

Shown in Figure 6.1(a) is a sketch of the FS of 1$T$-$VSe_2$ which shows the small Se-4$p$ hole pocket at $\bar{\Gamma}$ and large elliptical V-3$d$ electron pockets at the $\overline{\mathrm{M}}$-points of the BZ. The experimental FS of 1$T$-$VSe_2$ measured by full-wavevector ARPES in the CDW phase (30 K) is shown in Figure 6.1(b) for comparison. The electron pockets exhibit large parallel portions across the $\overline{\mathrm{M}}$-point, and their shape is remarkably similar to the example of a

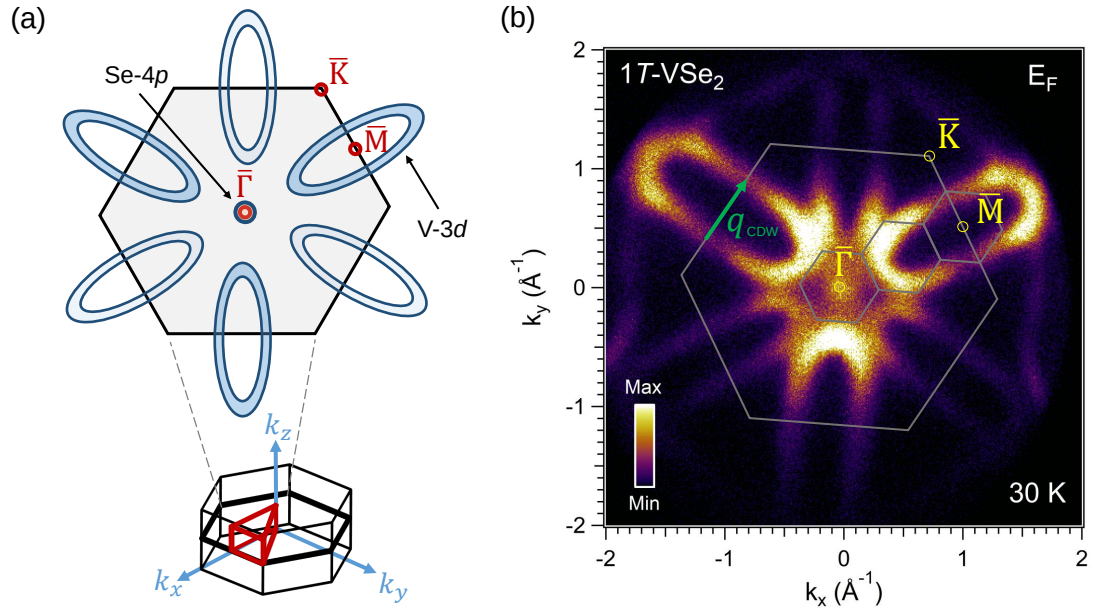


**Figure 6.1:** Fermi surface (FS) of 1 $T$-$VSe_2$. (a) Sketch of the FS showing the hole (Se-4$p$) and electron (V-3$d$) pockets at the $\bar{\Gamma}$ and $\overline{\mathrm{M}}$ points of the hexagonal BZ. (b) Full-wavevector ARPES image of the experimental FS in the CDW phase (30 K). The large and small hexagons represent the original (normal phase) and reconstructed (CDW phase) BZ. The projection of the high-symmetry points onto the experimental $k_z$ image plane are labelled. The green arrow indicates the projected CDW wavevector, $\mathbf{q}_{\mathrm{CDW}}$.

quasi-2D FS sketched in Figure 1.3. This type of FS topology is expected to be prone to electronic instabilities due to the potential energy gain by gapping a high proportion of states via a single $\mathbf{q}$-vector [2]. The green arrow in Figure 6.1(b) represents the expected in-plane CDW wavevector, $\mathbf{q}_{\mathrm{CDW}} = 1/4a_0$ and based purely on symmetry arguments, the length of this wavevector effectively links the parallel portions of FS that cross the BZ boundary. Indeed, there is a noticeable loss of spectral intensity along these portions of FS which strongly suggests that states here are lowered away from $E_{\mathrm{F}}$ due to the opening of gaps, $\Delta_{\mathrm{CDW}}$. The intensity is minimum precisely on the BZ boundary across the $\overline{\mathrm{M}}$-point, suggesting that these central portions are most effectively nested by $\mathbf{q}_{\mathrm{CDW}}$. Moving away from $\overline{\mathrm{M}}$ towards the ends of the pocket, the separation of parallel portions becomes $<$ $\mathbf{q}_{\mathrm{CDW}}$ due to their slightly elliptical shape (see Figure 6.1), and therefore are likely less effectively nested. Section 6.3 provides a more detailed analysis of the FS, band dispersions and the influence of the CDW transition on the electronic structure.

### 6.2.2 Signatures of multiple CDW phase transitions

As discussed in Section 4.2.1, electronic transport measurements of 1$T$-$VSe_2$ as a function of temperature show an overall metallic behaviour with a slight increase in the resistance near the well-known CDW transition at $T_{\mathrm{CDW}} = 110$ K. The first derivative of resistance, $dR/dT$ highlights the CDW transitions in more detail as shown in Figure 6.2(a). Here, the main feature is the well-known transition with an onset $\sim 110$ K and a minimum at $\sim 100$ K, which is labelled $T_{\mathrm{c1}}$. In addition, there is a second feature which appears as a small dip in $dR/dT$ near $\sim 80$ K and is labelled $T_{\mathrm{c2}}$. Signatures of this same feature can be seen in previous resistance data [158, 159] but have been typically overlooked. Since the feature in Figure 6.2(a) is rather weak and obscured by the tail of $T_{\mathrm{c1}}$, a subtraction of a fit to the sloping background over the range (65 - 95) K is made and shown in the inset. $T_{\mathrm{c2}}$ is then defined as the minimum of this dip feature and the associated error is half of its full width which gives $T_{\mathrm{c2}} = (82.0 \pm 5.0)$ K. Both the shape and location of this feature is found to be reproducible for measurements of several 1$T$-$VSe_2$ crystals from the same batch. Hence, based on the resistance measurements presented here, there are two distinct CDW critical temperatures $T_{\mathrm{c1}}$ and $T_{\mathrm{c2}}$ which agree closely with those found in previous studies [48, 107] as discussed in Section 6.1.

Another interesting aspect of the electronic transport measurements is the observation of a hysteresis in the resistance with temperature. Shown in Figure 6.2(b) is the raw resistance data for cooling and warming sweeps which are nearly identical across the entire temperature range except for the region (110 - 75) K where they deviate slightly. This effect is highlighted further in the inset of Figure 6.2(b), where the grey curve shows a positive difference between warming and cooling sweeps. The upper and lower limits of the hysteric temperature range is remarkably similar to the CDW transitions $T_{\mathrm{c1}}$ and $T_{\mathrm{c2}}$, respectively [48, 107]. Such behaviour has been observed in previous transport studies of 1$T$-$VSe_2$ over a similar temperature range [87, 111, 160]. Although the origin of the hysteresis has never been fully explained, it has been discussed in the context of a structural lock-in at $T_{\mathrm{c2}}$ [160]. Assuming $T_{\mathrm{c2}}$ is the $3q$-$2q$ transition [107], then upon cooling the reduction seen in $dR/dT$ in Figure 6.2(a) indicates that the resistance increases slightly i.e. the $2q$ is mores resistive than the $3q$ phase. Therefore, it is plausible that upon heating, the system remains locked in the $2q$ phase and follows a more resistive path as seen in Figure 6.2(b), before eventually transforming directly from the $2q$ phase to the

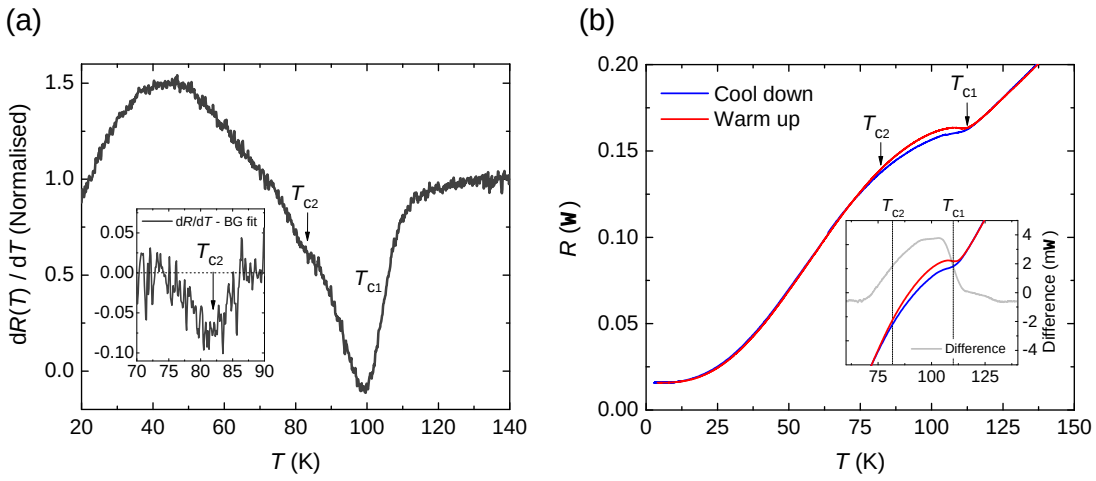


**Figure 6.2:** Electronic transport measurements of $1\,T$-$VSe_2$. (a) Normalised first derivative of resistance, $dR/dT$ highlighting the separate CDW transitions, $T_{c1}$ and $T_{c2}$. The inset shows the feature around $T_{c2}$ after subtraction of a fit to the sloping background over the range (65 - 95) K. (b) Raw resistance data. The inset highlights the region of hysteresis between the cooling and warming temperature sweeps, whilst the grey line is the difference. Vertical dashed lines indicate the CDW transition temperatures, $T_{c1} = 110$ K and $T_{c2} = 83$ K determined in Ref. [48].

normal phase at $T_{c1}$. It is known that the cooling and heating rates can have a profound influence on the resistance behaviour of the Ta-based TMDs and their alloys [91,161,162]. Therefore, it could be that the behaviour in $1\,T$-$VSe_2$ is linked to a kinetic effect and the increasing establishment of long-range $2q$ order at low temperatures, thus making the difference in resistive states more dramatic between cooling and heating sweeps across the entire (300 - 4) K range compared to the weak anomalies seen in $dR/dT$ when passing directly through the phase transition temperatures.

To investigate the possibility of separate CDW transitions in $1\,T$-$VSe_2$ further, Raman spectroscopy measurements were performed to look for signatures in the lattice structure. The results are presented in Figure 5.5(a). Two modes can clearly be seen corresponding to the $E_g$ (in-plane) and $A_{1g}$ (out-of-plane) vibrations expected for $1\,T$-TMDs (see Section 1.4.4) and are found at $\sim$ 138 $cm^{-1}$ and 208 $cm^{-1}$ respectively at 300 K, in reasonable agreement with previous studies [163,164]. In addition, there is a prominent broad feature around 340 $cm^{-1}$ which could be linked to a two-phonon process, similar to that observed in $1\,T$-$TiSe_2$ [55]. There is no dramatic difference between the normal phase (300 K) and CDW phase (77 K) spectra presented here, apart from a narrowing

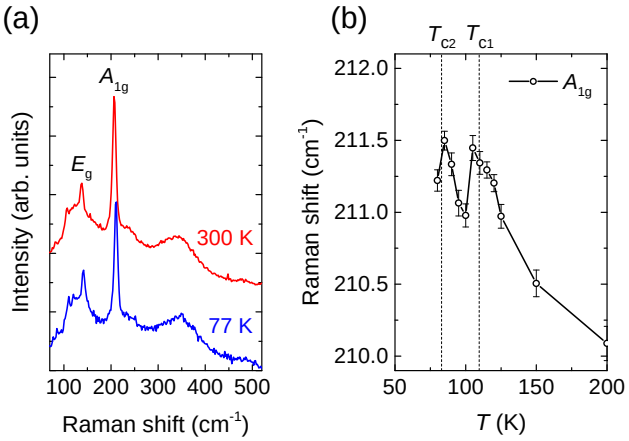


**Figure 6.3:** Raman spectroscopy of 1$T$-$VSe_2$. (a) Comparison of the normal (300 K) and CDW (77 K) phase. Spectra are offset for clarity. (b) Frequency of the $A_{1g}$ mode as a function of temperature. Vertical dashed lines indicate the CDW transition temperatures, $T_{c1} = 110$ K and $T_{c2} = 83$ K determined in Ref. [48].

of the Raman linewidth and a shift to higher frequencies as expected at low temperature. Because of the reconstruction of the BZ related to the $4a_0 \times 4a_0 \times 3.18c_0$ PLD, it is expected that several phonon branches will be folded to Γ as the high-symmetry points become equivalent. However, similar to 1$T$-$TiSe_2$ [79, 165], the evolution of these modes with temperature is significantly second-order, and they cannot be well-resolved until at least 20 K in 1$T$-$VSe_2$ [163].

Despite this, a detailed temperature-dependence of the Raman spectra reveals that signatures of the CDW transitions in 1$T$-$VSe_2$ can still be observed. In particular, the out-of-plane $A_{1g}$ mode would be expected to be sensitive to small changes in the $c$-axis related to the transition at $T_{c2}$, similar to previous structural studies [48]. Figure 5.5(b) shows the frequency of the $A_{1g}$ mode as a function of temperature. In the range (300 - 110) K, there is an almost linear increase in the frequency from $\sim$ 208 cm$^{-1}$ to 211 cm$^{-1}$ as expected for a stiffening of the V-Se bond with reducing temperature. However, below $T_{c1}$ there is a rapid softening of the $A_{1g}$ frequency which partially recovers before it appears to exhibit a second softening below $T_{c2}$. It should be noted that due to the base temperature of the liquid nitrogen cryostat (77 K) used to perform the measurements in Figure 5.5(b), there are insufficient data points below $T_{c2}$ to be conclusive of this second mode softening. However, the analysis presented here provides further possible evidence of two separate CDW transitions in 1$T$-$VSe_2$ which are also consistent with the electronic measurements in Figure 6.2.

## 6.3 Publication entitled: "Charge Density Wave Gap in 1 $T$-$VSe_2$: Momentum and Temperature Dependence"

<table>
<tr><td colspan="5">This declaration concerns the article entitled:<br>Charge Density Wave Gap in 1 T-VSe<sub>2</sub>: Momentum and Temperature Dependence</td></tr>
<tr><td colspan="5">Publication status (tick one)</td></tr>
<tr><td>Draft manuscript</td><td>Submitted</td><td>In review</td><td>Accepted</td><td>Published</td></tr>
<tr><td>✓</td><td></td><td></td><td></td><td></td></tr>
<tr><td>Reference</td><td colspan="4">A. J. H. Jones, C. J. Sayers, M. Cattelan, L.S. Farrar, S. J. Bending, N. A. Fox, E. Da Como, and J. Laverock. Charge Density Wave Gap in 1 $T$-$VSe_2$: Momentum and Temperature Dependence. In preparation (2020).</td></tr>
<tr><td>Candidate's contribution to the paper</td><td colspan="4">The candidate produced the sample for this work and performed preliminary photoemission measurements. The candidate contributed to the interpretation of the results and provided suggestions for the presentation in journal format.<ul><li>Formulation of ideas: 20%</li><li>Design of methodology: 10%</li><li>Experimental work: 25%</li><li>Presentation of data in journal format: 10%</li></ul></td></tr>
<tr><td>Statement from candidate</td><td colspan="4">This paper reports on original research I conducted during the period of my Higher Degree by Research candidature.</td></tr>
<tr><td colspan="3">Signature:</td><td colspan="2">Date:</td></tr>
</table>

## Charge Density Wave Gap in 1 $T$-$VSe_2$: Momentum and Temperature Dependence

A. J. H. Jones,[1] C. J. Sayers,[2] M. Cattelan,[3] L. S. Farrar,[2] S. J. Bending,[2] N. A. Fox,[1,3] E. Da Como,[2] and J. Laverock[1]

[1] *H. H. Wills Physics Laboratory, University of Bristol, Tyndall Avenue, Bristol BS8 1TL, UK*
[2] *Centre for Nanoscience and Nanotechnology, Department of Physics, University of Bath, Bath, BA2 7AY, UK*
[3] *School of Chemistry, University of Bristol, Cantocks Close, Bristol BS8 1TS, UK*

Using μARPES (micro angle resolved photoemission spectroscopy), we reveal the momentum and temperature dependent spectral signatures of charge density wave (CDW) order in 1 $T$-$VSe_2$. We find the ARPES CDW gap ($\Delta_{30K} = 10$ meV) opens at 83 K, corresponding to the $3q$-$2q$ transition, rather than at the conventional ($3q$) CDW transition of 110 K. We interpret the results in the context of the electronic susceptibility function, suggesting that the CDW gap is centered above the Fermi level in the $3q$ phase, and that the availability of states at the Fermi surface assists the $3q$-$2q$ transition. Our results emphasize the importance of this often overlooked phase.

Transition metal dichalcogenides (TMDs) are well-known charge density wave (CDW) materials,[1] and the family as a whole are attracting immense interest as two-dimensional (2D) layered heterostructures for future electronic applications.[2,3] In addition to CDW order, several members also host superconductivity,[4,5] which competes with the CDW, or novel magnetic order with potential for spintronics applications.[6,7] However, despite the surge of recent interest in TMDs, metallic $VSe_2$ has received rather less attention. 1 $T$-$VSe_2$ is iso-structural to other 1 $T$ polymorph 2D-TMDs, however its electronic structure exhibites a substantial 3D component that has previously been directly observed by angle-resolved photoemission spectroscopy (ARPES).[8,9] Correspondingly, the CDW that develops below 110 K is 3D, and its link with the Fermi surface (FS), through nesting, has been suggested both theoretically[10] and experimentally.[8,9,11] In its few-layer form, $VSe_2$ has recently been associated with a range of fascinating and potentially useful pheneomena; for example, the CDW transition exhibits a strong sensitivity to thickness at the nanoscale,[12,13] ferromagnetism has recently been predicted[14] and observed[15,16] in $VSe_2$ monolayers, which have been proposed to host ferrovalley physics,[17] and a metal-insulator transition is expected at a few layers.[18] Nevertheless, the CDW in bulk 1 $T$-$VSe_2$ is not well understood, for example doubts remain over the magnitude of the CDW gap, and its connection with the FS is yet to be established. Detailed knowledge of such electronic behavior is much needed in order to fully exploit the material properties in future devices.

At $T_{c1} = 110$ K, an incommensurate CDW of wave vector $\mathbf{q_1} = (1/4\mathbf{a}^*, 0, 0.314\mathbf{c}^*)$ develops, subsequently followed by a second transition at $T_{c2} = 82$ K, which is accompanied by a small change in $q_z$ to $\mathbf{q_2} = (1/4\mathbf{a}^*, 0, 0.307\mathbf{c}^*)$.[19] Pronounced phonon softening is predicted over a broad range of $\mathbf{q}$ near both $q$-vectors.[20] $T_{c2}$ has been shown to represent a transition from a $3q$ to $2q$ CDW state, whereby only two of the three symmetry-related $\mathbf{q}$ vectors are simultaneously present in a single domain.[22] The $3q$-$2q$ transition involves a sudden increase in the CDW amplitude, larger than anticipated from analysis of the Landau free energy.[22] Both CDW phases have appreciable correlation lengths, up to 40 nm along $\mathbf{c}$.[19] Despite being the low temperature phase in $VSe_2$, the $2q$ state has largely been overlooked in previous studies, although weak anomalies are visible in prior transport data.[12,13,21] Spectroscopic studies have so far been limited to indirect measurements of the amplitude of the CDW gap, e.g. 80 meV and 100 meV have been reported by scanning tunneling spectroscopy (STS)[23] and ARPES,[11] respectively. Such large gaps (corresponding to $2\Delta/k_BT_c \sim 17$) are well beyond that expected from mean-field weak coupling (where $2\Delta/k_BT_c \approx 3.5$),[24] and has led to speculation of strong fluctuations in the CDW order parameter.[23] However, the suppression of the mean-field $T_c$ by fluctuations is at odds[25] with the long CDW coherence length in $VSe_2$.

Here, we use μARPES to study the signatures of CDW order in bulk $VSe_2$, directly revealing the gap in the spectral function that develops below the transition temperature and its momentum dependence. Our observation of a gap $\Delta \sim 10$ meV, opening at the $2q$ transition, is in good general agreement with mean-field weak coupling expectations.

Single crystal samples of 1 $T$-$VSe_2$ were grown by chemical vapor transport with iodine as the transport agent. The starting materials consisted of high-purity vanadium (99.9%) and selenium (99.99%) powders. A slight excess of selenium was included to encourage stoichiometry. Resistivity measurements confirm the bulk CDW transitions at $T_{c1} = 109$ K and $T_{c2} = 83$ K.[26] Samples were cleaved under ultra-high vacuum in situ by mechanical exfoliation, and ARPES measurements were performed at the Bristol NanoESCA Facility using a He I ultraviolet (21.2 eV) source with energy resolution of 40 meV. Bulk single crystals were found to cleave rather inhomogeneously, yielding individual terraces tens of microns in size. We therefore employ μARPES of a selected area (50 μm) from single domains, thereby circumventing problems associated with surface uniformity.

The experimental FS and electronic structure of 1 $T$-$VSe_2$ are shown in Fig. 1 at 30 K, well below both CDW transitions, and are in good agreement with previous ARPES measurements.[8,9,11] Also shown are FLAPW (full-potential linear augmented plane wave) electronic structure calculations using the all-electron

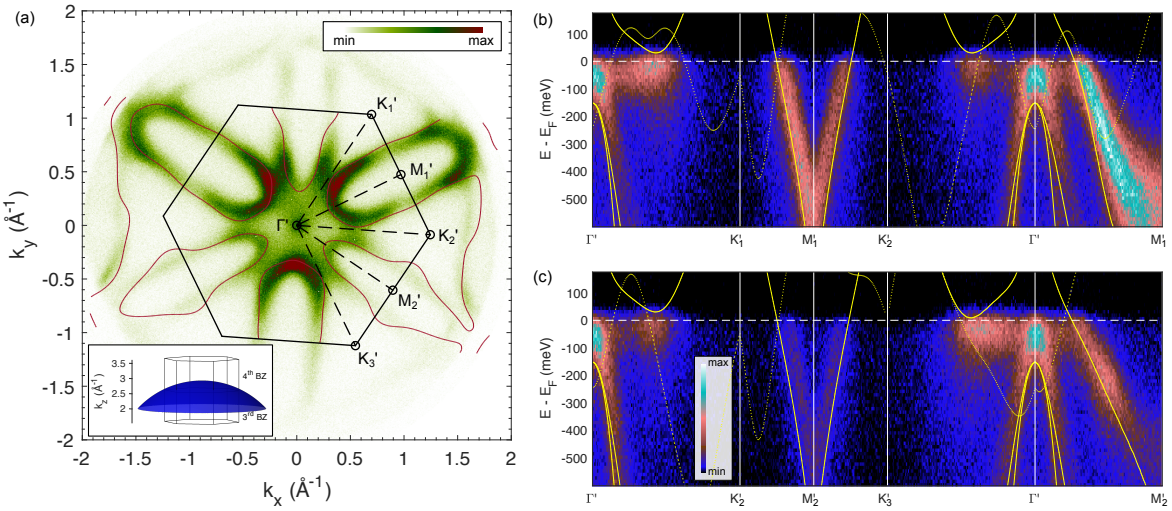


FIG. 1: μARPES of $VSe_2$ in the CDW phase at 30 K, recorded on a 50 μm × 50 μm region of the sample. (a) Fermi surface, with the FLAPW band structure shown overlaid. High symmetry points are labeled, projected onto the experimental $k_z$ surface. The inset shows the $k_z$ coverage of the image plane ($V_0 = 10.7$ eV). (b) and (c) Energy dispersive cuts through the bright and faint Fermi surface sheets, respectively. Solid lines show the unrenormalized FLAPW band structure evaluated over the experimental $k_z$ surface; dotted lines are the FLAPW bands displaced by the CDW wave vector, $\mathbf{q}^* = (1/4\mathbf{a}^*, 0, 0.319\mathbf{c}^*)$.

Elk package.[27,28] The FS [Fig. 1(a)] exhibits three mirror planes, and the three bright pockets are slightly larger than the three fainter ones, originating from bands with character predominantly from the topmost V ions. In Figs. 1(b) and (c), ARPES spectra are shown along a path through each of these pockets. The experimental $k_z$ momenta accessed by our ARPES measurements are determined by the photon energy and inner potential, $V_0$, assuming free electron-like final states. Through comparison with our FLAPW band structure calculations, we find optimum agreement between experiment and theory assuming $V_0 = 10.7$ eV, larger than a previous study at soft x-ray energies.[8] The experimental $k_z$ parabola is shown in the inset to Fig. 1(a), and illustrates that we are predominantly sampling close to the Brillouin zone (BZ) boundary in $k_z$. Overall, very good agreement is observed between experiment and theory, although there are discrepancies in the energy of the Se band at $\Gamma'$ (which we attribute to inaccuracies in the estimation of V $3d$ and Se $4p$ hybridisation),[8] and the degree of warping of the FS pockets (which we attribute to the extreme surface sensitivity at ultraviolet photon energies; the warping has been well-resolved in 3D at soft x-ray energies).[8]

In Figs. 1(b) and (c), we also show the FLAPW band structure displaced by the CDW wave vector. The CDW bands overlap the original bands at the FS (e.g. between $K_1'$ and $M_1'$), implying the CDW bands will interact with the original band structure and open a CDW gap at $E_F$. Indeed, in Fig. 1(a), a weak loss of intensity along the arms of the FS pockets (along $K_1'$-$M_1'$) is visible at 30 K.

In order to examine the gapping of the FS in more detail, spectra are shown at four points around the FS in Fig. 2(a-b) in the normal (120 K) and CDW phase (30 K), corresponding to the inner and outer edges of the $M'$ pocket (0° and 180°) and midway along its arms [90° and 270°, locations are labeled in Fig. 2(c)]. The inner and outer edges remain ungapped and metallic at low temperature, however, a small gap of 5 – 10 meV develops along the arms of the pocket. This represents our first central result, providing direct spectroscopic evidence of CDW order. We note that this behavior is replicated on both $M'$ pockets, i.e. the top-left pocket [Fig. 2(a)] and top-right pocket [Fig. 2(b)]. The full momentum dependence of the CDW gap is shown in Fig. 2(c), where the magnitude of the gap averaged over both FS pockets is plotted as a function of angle around the pocket. The pockets remain metallic (ungapped) along $\Gamma'$-$M'$, opening a maximum gap (which is related to the CDW interaction strength) of 10 meV on their arms. Although the momentum dependence of the gap has been inferred by early ARPES measurements, the proposed amplitudes were an order of magnitude larger.[11] Recent STS measurements of strained ultrathin $VSe_2$, in which a different CDW wave vector to the bulk is observed, have suggested a momentum-averaged gap of $\Delta = 4.5$ meV, roughly centered about $E_F$.[20]

Further evidence for associating the gapping of the FS with the CDW comes from the temperature dependence of the gap, shown in Fig. 3. The intensity of the ungapped part of the FS gradually increases with decreasing temperature, reflecting the sharpening of the bands in

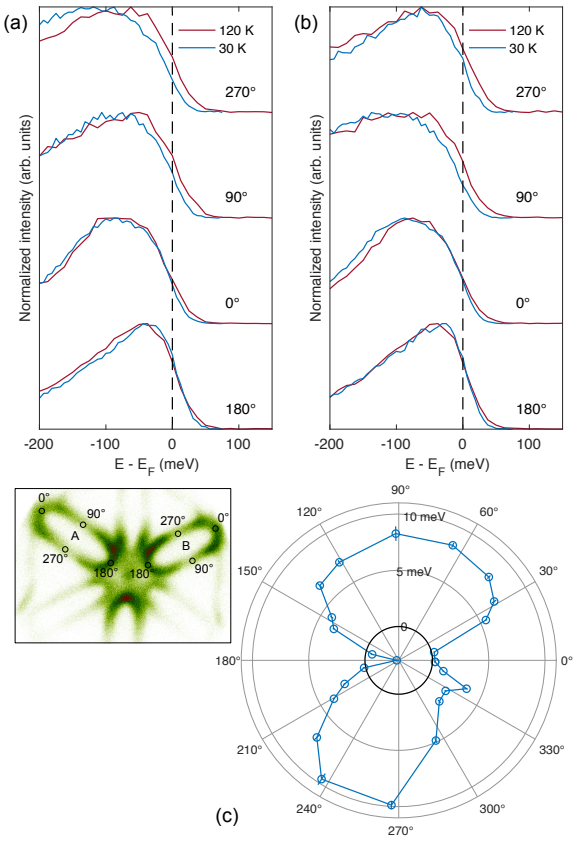


FIG. 2: Momentum dependence of the FS gap at 30 K. Spectra are shown around (a) the top left and (b) top right $M'$ pockets in the normal state (120 K) and CDW phase (30 K), and labeled by their angle around the $M'$ points (see inset). (c) Angular dependence of the magnitude of the gap around the FS, averaged over both FS sheets. Errors in (c) represent statistical errors in estimating the gap magnitude only.

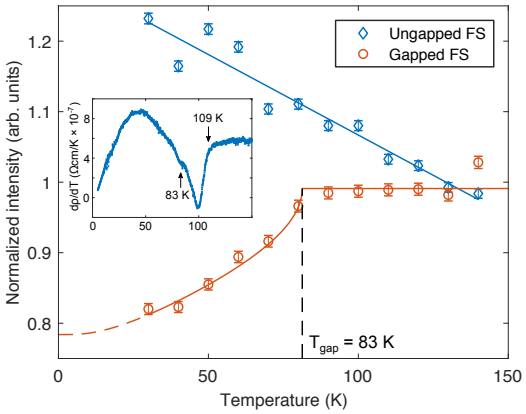


FIG. 3: Temperature dependence of the CDW gap, measured as the intensity at the FS of the gapped regions of the FS (90° and 270°) compared with the ungapped regions (0° and 180°). Errorbars indicate statistical errors in the measurement. The fit to the gapped regions represents BCS-like behavior[26] with a $T_{\rm gap} = 83$ K. The inset displays the derivative of the resistivity in the same temperature range.[26]

energy over our momentum window. In contrast, the intensity of the gapped portion of the FS remains roughly flat until it drops sharply in intensity at $T_{\rm gap} = 83$ K, closely following the Bardeen-Cooper-Schrieffer (BCS) expression,[26] as anticipated for a CDW within weak coupling mean-field theory.[24,30,31] This represents our second central result: the temperature at which the CDW gap in ARPES opens occurs at the transition to the $2q$ state, $T_{c2}$, and not at the familiar $T_{c1}$ temperature. We estimate that a gap at $E_{\rm F}$ of larger than 2 meV ought to be detectable in our data, placing an approximate upper limit on the ARPES gap above $T_{c2}$. Our experimental values of $\Delta_{\rm max}$ and $T_{\rm gap}$ lead to $2\Delta/k_{\rm B}T_c \sim 2.8$, assuming a gap that opens symmetrically about $E_{\rm F}$, which are fully consistent with the mean-field value and the large CDW coherence length.

The inset to Fig. 3 shows the anomalies in the resistivity due to the CDW transitions. The anomaly at $T_{c2}$ is much weaker than, and is obscured, by the tails of $T_{c1}$, and it is pertinent to ask why our ARPES results are apparently so insensitive to the CDW order at $T_{c1}$. In order to gain insight into the CDW behavior, we show the Lindhard susceptibility function from our FLAPWW calculations in Fig. 4 along a path in the 3D BZ. Re $\chi_0(\mathbf{q})$, which corresponds to the response function of the electronic subsystem (within the constant matrix element approximation), is found to peak at $\mathbf{q}^* = (1/4\mathbf{a}^*, 0, 0.319\mathbf{c}^*)$, very close to the experimental CDW wave vectors. This peak is sharp in the $(q_x, q_y)$ plane, at least as sharp as other related CDW systems.[32] However, it is somewhat softer in $\mathbf{c}^*$ [inset to Fig. 3(a)], consistent with the multiple $q_z$ found experimentally. For CDW order to be associated with FS nesting, this peak must also be reflected in Im $\chi_0(\mathbf{q})$, which corresponds to the low energy transitions at $E_{\rm F}$.[32] Indeed, Im $\chi_0(\mathbf{q})$ does peak near $\mathbf{q}^*$, but slightly larger instabilities, by $\sim 15\%$, are found at slightly modified $\mathbf{q}$. Therefore, although FS nesting does not select the wave vector of the electronic instability, it contributes substantially to the peak in Re $\chi_0(\mathbf{q})$ that does, particularly along $\mathbf{c}^*$. This is in contrast to $2H$-$NbSe_2$[32] and $TaSe_2$,[32,33] for example, in which FS nesting plays little role in the peaks in Re $\chi_0(\mathbf{q})$ or CDW wave vector.

We now focus on which electronic states are responsible for the electronic instability at $\mathbf{q}^*$ via the k-resolved susceptibility, $\chi_0(\mathbf{q}^*, \mathbf{k})$, see Figs. 4(b-e).[33] This function, analyzed at $\mathbf{q}^*$, reveals the contribution of individual states to $\chi_0(\mathbf{q})$ at this wavevector: Bright regions highlight states that either nest with other states at $\mathbf{q}^*$, or contribute significant finite energy transitions, and therefore in the case of FS nesting $\chi_0(\mathbf{q}^*, \mathbf{k})$ should essentially contour the FS. The results are shown in Fig. 4(b) at

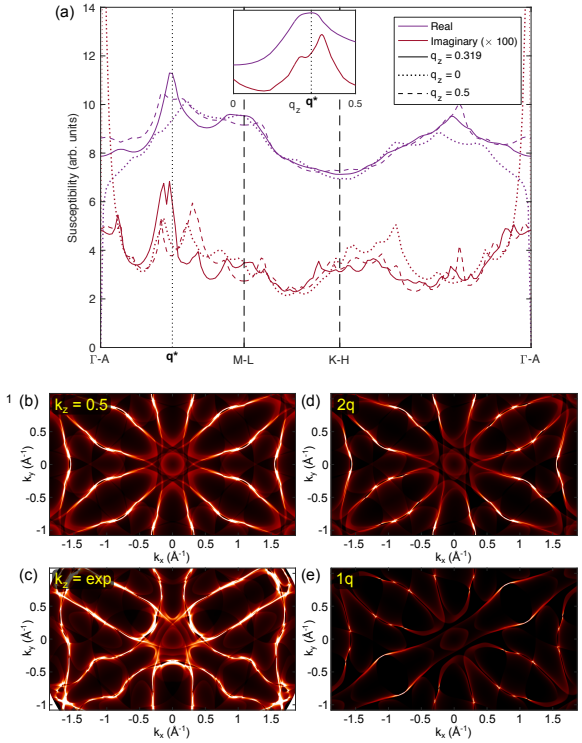


FIG. 4: (a) Noninteracting susceptibility, $\chi_0(\mathbf{q})$, of 1 $T$-$VSe_2$ based on the FLAPW electronic structure, shown along a path through the BZ. The peak in Re $\chi_0(\mathbf{q})$ is shown by the dotted line, $\mathbf{q}^* = (1/4\mathbf{a}^*, 0, 0.319\mathbf{c}^*)$. The inset shows the susceptibility along $\mathbf{q} = (1/4\mathbf{a}^*, 0, q_z\mathbf{c}^*)$. (b-e) $\mathbf{k}$-resolved susceptibility function, Re $\chi_0(\mathbf{q}^*, \mathbf{k})$, of the $3q$ CDW structures shown (b) on a constant $k_z = 0.5\mathbf{c}^*$ slice and (c) through the experimental $k_z$ parabola. (d) and (e) illustrate the susceptibility due to $2q$ and $1q$ CDW structures, respectively.

the top of the BZ ($k_z = 0.5\mathbf{c}^*$), and closely resemble the FS, consistent with the strong role played by FS nesting. The noticeable contribution from states near $k_x = k_y = 0$ represent finite energy transitions. It is also clear that states along the arms of the FS pockets, which correspond to the gapped regions in the experiment, contribute strongly at this $k_z$ momentum and wavevector, in contrast to the weak intensity from states at the inner and outer edges of the FS pockets. This provides a natural explanation for the momentum dependence of the FS gap, whereby gapped states are strongly nested, and ungapped states nest only weakly. Fig. 4(c) shows Re $\chi_0(\mathbf{q}^*, \mathbf{k})$ evaluated over the experimental $k_z$ parabola, for direct comparison with the μARPES FS shown in Fig. 1(a). Although the intensity from the FS near $\Gamma'$ is bright here, we emphasize that small discrepancies between experimental and theoretical band structures, the empirical inner potential, or a departure of the final states in ARPES from the free electron parabola can significantly change this picture.

Finally, in Figs. 4(d-e) we show Re $\chi_0(\mathbf{q}^*, \mathbf{k})$ resulting from both $2q$ and $1q$ CDW order, respectively, evaluated at $k_z = 0.5\mathbf{c}^*$. These are compared directly with panel (b), which represents $3q$ CDW structure (equivalent to the sum of $2q$ and $1q$), and are all shown with the same color intensity scaling. Both $2q$ and $3q$ images show similar brightness near the gapped portions of the FS, indicating that a $2q$ CDW already gaps most of the available states compared with the $3q$ CDW. The additional $1q$ CDW competes for the same parts of the FS as the $2q$ CDW. This represents our third main result: The $2q$ CDW structure already gaps most of the available states and therefore the additional gain in electronic energy in forming the $3q$ structure is comparatively small.

Returning to the question of why the $3q$ CDW is so weak in our μARPES measurements, we suggest that in this structure the CDW band crossings occur above $E_F$, and are therefore hidden from probes of the occupied states, such as ARPES, a mechanism that has recently been proposed for 2$H$-$NbSe_2$.[34] We note that applying a shift of $\Delta q_z = -0.006\mathbf{c}^*$ to the theoretical $\mathbf{q}^*$ wave vector leads to an energy shift of $\approx +10$ meV in the band crossings in the $\Gamma$-$K$ direction, sufficient to place the bottom of the gap above $E_F$. This model is fully consistent with our data, though requires a probe of unoccupied states, e.g. STS, to test this unambiguously.

If the above hypothesis is true, the origin of the CDW in $VSe_2$ is delicately poised. The $3q$ state appears to favor the lattice energy (e.g. phonon softening) at the expense of the electronic energy, whereas the $2q$ state maximizes the available electronic energy gain by slightly adjusting $q_z$. This may have important implications for which CDW structure is chosen in few layer systems, as the three dimensionality of the system is gradually removed. For example, there appears to be a crossover in CDW behavior as a function of layer thickness at a critical thickness comparable with the $c$-axis CDW correlation length.[12,13]

In summary, μARPES reveals the magnitude, momentum and temperature dependence of the CDW gap in bulk 1 $T$-$VSe_2$, establishing low-temperature CDW properties in good agreement with mean-field weak-coupling expectations. The maximum CDW gap in μARPES reaches 10 meV along the arms of the FS pocket, and surprisingly is found to develop at the $3q$-$2q$ transition (83 K). We therefore suggest that the $3q$ CDW between 83 K and 110 K has a gap that is centered above $E_F$, and encourage further investigations using experimental probes of the unoccupied states, e.g. STS. More generally, our results also shed light on systems with competing CDW instabilities.

**Acknowledgements**

Authors acknowledge the Bristol NanoESCA Facility funded by the Engineering and Physical Sciences Research Council (EPSRC) Strategic Equipment Grant No.

EP/M000605/1, and funding and support from the EPSRC Centre for Doctoral Training in Condensed Matter Physics (CDT-CMP), Grant No. EP/L015544/1. Calculations were performed using the computational facilities of the Advanced Computing Research Centre, University of Bristol (http://www.bris.ac.uk/acrc/).

[1] J. A. Wilson, F. J. Di Salvo, and S. Mahajan, Charge-density waves and superlattices in the metallic layered transition metal dichalcogenides, Adv. Phys. **24**, 117 (1975).

[2] Q. H. Wang, K. Kalantar-Zadeh, A. Kis, J. N. Coleman, and M. S. Strano, Electronics and optoelectronics of two-dimensional transition metal dichalcogenides, Nature Commun. **7**, 699 (2012).

[3] D. Jariwala, V. K. Sangwan, L. J. Lauhon, T. J. Marks, and M. C. Hersam, Emerging Device Applications for Semiconducting Two-Dimensional Transition Metal Dichalcogenides, ACS Nano **8**, 1102 (2014).

[4] R. F. Frindt, Superconductivity in Ultrathin $NbSe_2$ Layers, Phys. Rev. Lett. **28**, 299 (1972).

[5] A. F. Kusmartseva, B. Sipos, H. Berger, L. Forró, and E. Tutiš, Pressure Induced Superconductivity in Pristine 1$T$-$TiSe_2$, Phys. Rev. Lett. **103**, 236401 (2009).

[6] X. Xu, W. Yao, D. Xiao, and T. F. Heinz, Spin and pseudospins in layered transition metal dichalcogenides, Nature Phys. **10**, 343 (2014).

[7] L. Bawden, S. P. Cooil, F. Mazzola, J. M. Riley, L. J. Collins-McIntyre, V. Sunko, K. W. B. Hunvik, M. Leandersson, C. M. Polley, T. Balasubramanian, T. K. Kim, M. Hoesch, J. W. Wells, G. Balakrishnan, M. S. Bahramy, and P. D. C. King, Spinvalley locking in the normal state of a transition-metal dichalcogenide superconductor, Nature Commun. **7**, 11711 (2016).

[8] V. N. Strocov, M. Shi, M. Kobayashi, C. Monney, X. Wang, J. Krempasky, T. Schmitt, L. Patthey, H. Berger, and P. Blaha, Three-dimensional electron realm in $VSe_2$ by soft-x-ray photoelectron spectroscopy: origin of charge-density waves, Phys. Rev. Lett. **109**, 086401 (2012).

[9] T. Sato, K. Terashima, S. Souma, H. Matsui, T. Takahashi, H. Yang, S. Wang, H. Ding, N. Maeda, and K. Hayashi, Three-Dimensional Fermi-Surface Nesting in 1$T$-$VSe_2$ Studied by Angle-Resolved Photoemission Spectroscopy, J. Phys. Soc. Jpn. **73**, 3331 (2004).

[10] A. M. Woolley and G. Wexler, Band structures and Fermi surfaces for 1$T$-$TaS_2$, 1$T$-$TaSe_2$ and 1$T$-$VSe_2$, J. Phys. C: Solid State Phys. **10**, 2601 (1977).

[11] K. Terashima, T. Sato, H. Komatus, T. Takahashi, N. Maeda, and K. Hayashi, Charge-density wave transition in 1$T$-$VSe_2$ studied by angle-resolved photoemission spectroscopy, Phys. Rev. B **68**, 155108 (2003).

[12] J. Yang, W. Wang, Y. Liu, H. Du, W. Ning, G. Zheng, C. Jin, Y. Han, N. Wang, Z. Yang, M. Tian, and Y. Zhang, Thickness dependence of the charge-density-wave transition temperature in $VSe_2$, Appl. Phys. Lett. **105**, 063109 (2014).

[13] Á. Pásztor, A. Scarfato, C. Barreteau, E. Giannini, and C. Renner, Dimensional crossover of the charge density wave transition in thin exfoliated $VSe_2$, 2D Mater. **4**, 041005 (2017).

[14] Y. Ma, Y. Dai, M. Guo, C. Niu, Y. Zhu, and B. Huang, Evidence of the Existence of Magnetism in Pristine $VX_2$ Monolayers (X = S, Se) and Their Strain-Induced Tunable Magnetic Properties, ACS Nano **6**, 1695 (2012).

[15] M. Bonilla, S. Kolekar, Y. Ma, H. Coy Diaz, V. Kalappattil, R. Das, T. Eggers, H. R. Gutierrez, M.-H. Phan, and M. Batzill, Strong room-temperature ferromagnetism in $VSe_2$ monolayers on van der Waals substrates, Nature Nanotechnol. **13**, 289 (2018).

[16] Z.-L. Liu, X. Wu, Y. Shao, J. Qi, Y. Cao, L. Huang, C. Liu, J.-O. Wang, Q. Zheng, Z.-L. Zhu, K. Ibrahim, Y.-L. Wang, and H.-J. Gao, Epitaxially grown monolayer $VSe_2$: an air-stable magnetic two-dimensional material with low work function at edges, Sci. Bull. **63**, 419 (2018).

[17] W.-Y. Tong, S.-J. Gong, X. Wan, and C.-G. Duan, Concepts of ferrovalley material and anomalous valley Hall effect, Nature Commun. **7**, 13612 (2016).

[18] Quantum size effects in layered $VX_2$ (X=S, Se) materials: Manifestation of metal to semimetal or semiconductor transition, A. H. M. Abdul Wasey, S. Chakrabarty, and G. P. Das, J. Appl. Phys. **117**, 064313 (2015).

[19] K. Tsutsumi, X-ray-diffraction study of the periodic lattice distortion associated with a charge-density wave in 1$T$-$VSe_2$, Phys. Rev. B **26**, 5756 (1982).

[20] D. Zhang, J. Ha, H. Baek, Y.-H. Chan, F. D. Natterer, A. F. Myers, J. D. Schumacher, W. G. Cullen, A. V. Davydov, Y. Kuk, M. Y. Chou, N. B. Zhitenev, and J. A. Stroscio, Strain engineering a $4a \times \sqrt{3}a$ charge-density-wave phase in transition metal dichalcogenide 1T-$VSe_2$, Phys. Rev. Mater. **1**, 024005 (2017).

[21] R. H. Friend, D. Jérome, D. M. Schleich, and P. Molinié, Pressure enhancement of charge density-wave formation in $VSe_2$: The role of Coulomb correlations, Solid State Commun. **27**, 169 (1978).

[22] D. J. Eaglesham, R. L. Withers, and D. M. Bird, Charge-density wave transitions in 1T-$VSe_2$, J. Phys. C **19**, 359 (1986).

[23] I. Ekvall, H. E. Brauer, E. Wahlström, and H. Olin, Locally modified charge-density waves in Na intercalated $VSe_2$ studied by scanning tunneling microscopy and spectroscopy, Phys. Rev. B **59**, 7751 (1999).

[24] G. Grüner, *Density Waves in Solids* (Addison-Wesley, 1994).

[25] W. L. McMillan, Microscopic model of charge-density waves in 2$H$-$TaSe_2$, Phys. Rev. B **16**, 643 (1975).

[26] See Supplementary Materials for details.

[27] J. K. Dewhurst, S. Sharma, L. Nordstöm, F. Cricchio, O. Grånäs, and E. K. U. Gross, The Elk FP-LAPW code, `http://elk.sourceforge.net` (2017).

[28] The FLAPW calculations were performed within the local density approximation using experimental[29] lattice parameters. The details of the band structure were found to be robust agains both relaxation of structural parameters and exchange-correlation functional.

[29] C. S. Yadav and A. K. Rostogi, Electronic transport and specific heat of 1$T$-$VSe_2$, Solid State Commun. **150**, 648 (2010).

[30] N. Ru, C. L. Condron, G. Y. Margulis, K. Y. Shin, J. Laverock, S. B. Dugdale, M. F. Toney, and I. R. Fisher, Effect

of chemical pressure on the charge density wave transition in rare-earth tritellurides $R\mathrm{Te}_3$, Phys. Rev. B **77**, 035114 (2008).

[31] V. Brouet, W. L. Yang, X. J. Zhou, Z. Hussain, R. G. Moore, R. He, D. H. Lu, Z. X. Shen, J. Laverock, S. B. Dugdale, N. Ru, and I. R. Fisher, Angle-resolved photoemission study of the evolution of band structure and charge density wave properties in $R\mathrm{Te}_3$ ($R$ = Y, La, Ce, Sm, Gd, Tb, and Dy), Phys. Rev. B **77**, 235104 (2008).

[32] M. D. Johannes and I. I. Mazin, Fermi surface nesting and the origin of charge density waves in metals, Phys. Rev. B **77**, 165135 (2008).

[33] J. Laverock, D. Newby, Jr., E. Abreu, R. Averitt, K. E. Smith, R. P. Singh, G. Balakrishnan, J. Adell, and T. Balasubramanian, $k$-resolved susceptibility function of 2$H$-$TaSe_2$ from angle-resolved photoemission, Phys. Rev. B **88**, 035108 (2013).

[34] A. Soumyanarayanan, M. M. Yee, Y. Hea, J. van Wezel, D. J. Rahn, K. Rossnagel, E. W. Hudson, M. R. Norman, and J. E. Hoffman, Quantum phase transition from triangular to stripe charge order in $NbSe_2$, Proc. Natl. Acad. Sci. **110**, 1623 (2013).

## Supplementary Information for "*Charge Density Wave Gap in 1T-$VSe_2$: Momentum and Temperature Dependence*"

A. J. H. Jones,[1] C. J. Sayers,[2] M. Cattelan,[3] L. S. Farrar,[2] S. J. Bending,[2] N. A. Fox,[1,3] E. Da Como,[2] and J. Laverock[1]

[1]*H. H. Wills Physics Laboratory, University of Bristol, Tyndall Avenue, Bristol BS8 1TL, UK*
[2]*Centre for Nanoscience and Nanotechnology, Department of Physics, University of Bath, Bath, BA2 7AY, UK*
[3]*School of Chemistry, University of Bristol, Cantocks Close, Bristol BS8 1TS, UK*

### Resistivity

Four-point resistivity measurements were performed on crystals from the same batch as that used in the main manuscript. Example curves are shown in Fig. S1 between 4 K and room temperature. All crystals had residual resistivity ratios ($\rho_{294K}/\rho_{4K}$) of between 13 and 14, indicating high quality samples, and were in good agreement with previous measurements.[1,2] All crystals exhibited anomalies in the resistivity at $T_{c1}$ and $T_{c2}$ (seen in the first derivative of the resistivity in the main manuscript), although the anomaly in $T_{c2}$ is much weaker than in $T_{c1}$. The charge-density wave (CDW) transition temperatures were determined as $T_{c1} = 109$ K and $T_{c2} = 82 - 87$ K using linear fits above and below the onset of $T_{c1}$ and the width of the anomalous region around $T_{c2}$, respectively.

### BCS model of the temperature dependent Fermi surface

The temperature-dependent Fermi surface (FS) measurements were performed with an instrumental resolution of 40 meV. To perform the integration, images were first normalized to the total number of counts in the image. The increase in signal under the ungapped portions of FS with decreasing temperature is accounted for by the sharpening of the bands at lower temperatures (specifically, the sharpening in thermal energy broadening leads to a sharpening in momentum in our integration area). The temperature-dependence of the gapped portions of FS show a BCS-like behavior, with a different pre-factor. Here, we explain the origin of this different pre-factor, and show that it is consistent with the BCS gap equation.

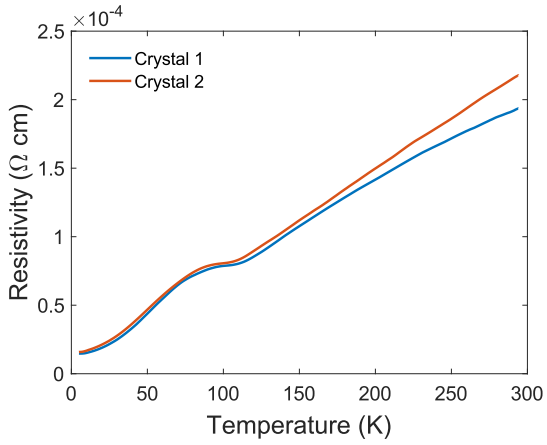


FIG. S1: Resistivity of two of the 1$T$-$VSe_2$ crystals from the same batch as that presented in the main manuscript.

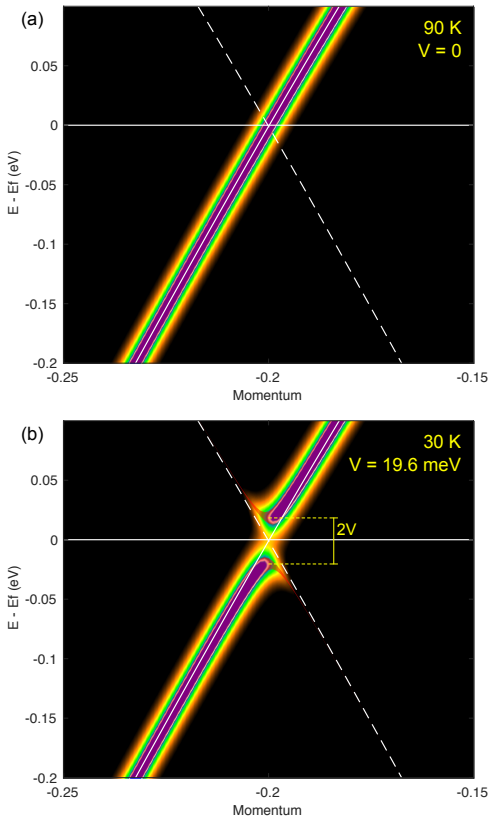


FIG. S2: Model spectral function for (a) noninteracting and (b) interacting CDW bands. The solid line is the noninteracting dispersion, and the dashed line is the CDW shadow band. The spectral function is shown as the color map, and the semi-transparent red line shows the eigenvalues of the interacting model, with a width given by $|u_k|^2$. The magnitude of the gap $\Delta = 2V$, is given by Equation 2 with $T_c = 81.3$ K and $V_0 = 20$ meV.

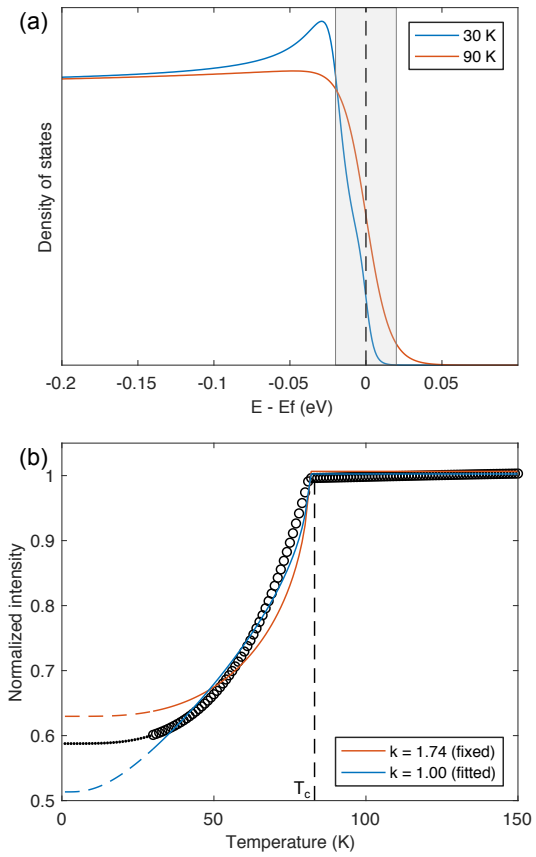


FIG. S3: (a) Densities of states of the model CDW bands, shown above and below $T_{\mathrm{CDW}}$. The shaded region indicates the energy window of the experimental FS measurement, corresponding to the integration window in the model. (b) Results of the temperature-dependent model (symbols) and their fits to Equation 1, with $k$ both fixed to the BCS value of 1.74, and allowed to vary (leading to $k = 1.00$).

The pre-factor extracted from a fit to the temperature-dependence of the FS intensity is $k \approx 1$, following the form,

$$I_{\mathrm{EF}} = 1 - a \tanh\left(k\sqrt{\frac{T_c}{T} - 1}\right), \qquad (1)$$

where $a$ represents the normalized intensity loss at $E_{\mathrm{F}}$ with $\Delta = \Delta_0$, i.e. maximally gapped at $T = 0$. To account for the finite instrumental resolution, Equation 1 is evaluated within an energy window of 40 meV about $E_{\mathrm{F}}$.

We begin with a simple 1D model for interacting CDW bands,[3] interacting via the parameter $V_0 = 20$ meV. In the normal state above $T_{\mathrm{CDW}}$, $V = 0$ and the spectral function follows that of the noninteracting bands, see Fig. S2(a). Below $T_{\mathrm{CDW}}$, however, the original band interacts with the shadow CDW band, turning away from the crossings between the two and opening a gap of $\Delta = 2V$, shown in Fig. S2(b).

In order to compare our model with the experimentally measured quantity, we now compute the densities of states of the model, shown in Fig. S3(a), and integrate them within the energy window of the experimental FS measurement. The effects of the gap on the measured FS intensity is clear in Fig. S3(a), leading to a substantially weakened integral in the CDW state.

We now extend the model to other temperatures, using the interpolation formula of the BCS gap equation,

$$\Delta(T) = \Delta_0 \tanh\left(1.74\sqrt{\frac{T_c}{T} - 1}\right), \qquad (2)$$

which describes the temperature dependence of the superconducting gap in weak coupling theory, and is also appropriate for describing CDW gaps.[4] The pre-factor 1.74 comes from interpolating the exact numerical results of the self-consistent BCS weak coupling gap equation.

The results of applying this are shown in Fig. S3(b), alongside fits to Equation 1 within the experimental temperature range (30 K $\leq T \leq$ 150 K). Constraining the prefactor $k$ in the fit to the BCS value of 1.74 yields a poor fit, failing to capture the shape of the results. On the other hand, allowing $k$ to vary yields a good fit to the model in the experimental range, corresponding to $k = 1.00$, which is very close to the experimentally-determined prefactor. This agreement supports our argument that the experimental temperature dependence is representative of weak coupling BCS-like CDW.

[1] R. H. Friend, D. Jérome, D. M. Schleich, and P. Molinié, Pressure enhancement of charge density-wave formation in $VSe_2$: The role of Coulomb correlations, Solid State Commun. **27**, 169 (1978).

[2] Á. Pásztor, A. Scarfato, C. Barreteau, E. Giannini, and C. Renner, Dimensional crossover of the charge density wave transition in thin exfoliated $VSe_2$, 2D Mater. **4**, 041005 (2017).

[3] V. Brouet, W. L. Yang, X. J. Zhou, Z. Hussain, R. G. Moore, R. He, D. H. Lu, Z. X. Shen, J. Laverock, S. B. Dugdale, N. Ru, and I. R. Fisher, Angle-resolved photoemission study of the evolution of band structure and charge density wave properties in $RTe_3$ ($R$ = Y, La, Ce, Sm, Gd, Tb, and Dy), Phys. Rev. B **77**, 235104 (2008).

[4] G. Grüner, *Density Waves in Solids* (Addison-Wesley, 1994).

## 6.4 Discussion & concluding remarks

The work in Section 6.3 presented a detailed study of the Fermi surface (FS) of 1$T$-$VSe_2$ utilising full-wavevector ARPES with single-shot ($k_x$, $k_y$) acquisition in order to visualize the FS topology and the effects of the CDW transition on the electronic structure. The importance of FS nesting was evaluated by comparing the experimental results with DFT calculations of the momentum-resolved electronic susceptibility, $\chi^0(\mathbf{q}, k)$.

Full-wavevector ARPES images reveal a quasi-2D FS with notably large parallel portions along the arms of the V-3$d$ electron pockets centred at the $\overline{\text{M}}$-point. Such a FS topology should be prone to nesting-like instabilities according to Section 1.2.3. Indeed, in the CDW phase (30 K) there is a noticeable loss of intensity along the centre portions of the electron pockets which should be well nested by $\mathbf{q}_{\text{CDW}}$, suggesting these states are removed from the FS due to the opening of a gap. Comparing the EDCs between the normal (120 K) and CDW (30 K) phase, shows that a gap opens along the parallel arms of the electron pockets, evidenced by a lowering of the Fermi edge, with a maximum of $\Delta_{\text{CDW}}(30\text{ K}) = 10$ meV at their centre across the BZ boundary ($\overline{\text{K}}$-$\overline{\text{M}}$-$\overline{\text{K}}$). Instead, the curved portions of FS on the inner and outer edges of the electron pocket remain ungapped. This provides direct evidence for CDW order in 1$T$-$VSe_2$ and is highly suggestive of a FS nesting type scenario. In addition, the momentum-dependence of $\Delta_{\text{CDW}}$ shows that a large proportion of the electron pocket is partially gapped and its magnitude varies continuously ($\Delta_{\text{CDW}} = 10 \rightarrow 0$ meV) from the $\overline{\text{K}}$-$\overline{\text{M}}$-$\overline{\text{K}}$ cross-section (max.) to the edges (min.) of the pocket.

Surprisingly, temperature-dependence of the FS intensity reveals that the CDW gap opens at $\sim$ 83 K rather than the well-known transition temperature at $\sim$ 110 K. This is very close to the value of $T_{\text{c2}} \approx$ (80 - 85) K found by Tsutsumi *et al.* [48], and later explained as a 3$q$-2$q$ transition by Eaglesham *et al.* [107]. Therefore in Section 6.3, it was suggested that the gap observed by ARPES occurs at the transition to the 2$q$ CDW state ($T_{\text{c2}}$) and not at the familiar 3$q$ CDW state ($T_{\text{c1}}$). The temperature-dependence of the gap closely follows the BCS relation and the experimental values of $\Delta_{\text{CDW}}$ and $T_{\text{CDW}}$ leads to $2\Delta k_B T_c \sim 2.8$, which is consistent with a weak coupling CDW within mean-field theory. Electrical transport measurements show anomalies near $T_{\text{c1}}$ and $T_{\text{c2}}$ which is clearly visible in $dR/dT$. The latter was determined to be $T_{\text{c2}} = (82 \pm 5)$ K which is in good agreement with a fit to the photoemission data using a simple BCS expression.

DFT calculations of the electronic susceptibility showed a divergence in $\mathrm{Re}\,\chi^0(\mathbf{q})$ near $\mathbf{q}_{\mathrm{CDW}} = (1/4a_0, 0.314c_0)$ which is close to the previously determined experimental value [48]. Peaks were found in both the real and imaginary parts of $\chi^0(\mathbf{q}, k)$ at similar $q$-vectors, an important criteria in the assignment of CDWs to FS nesting instabilities [22]. The susceptibility was evaluated over the entire BZ and showed that states along the arms of the electron pockets contribute the most to $\mathrm{Re}\,\chi^0(\mathbf{q})$ in agreement with the gapped regions of FS found in experiment. It was found that the $2q$ CDW gaps most of the available electronic states and the $3q$ CDW competes for the same parts of the FS, which could explain the apparent sensitivity of the ARPES measurements to the gap opening at $2q$ ($T_{\mathrm{c2}}$) compared to the $3q$ ($T_{\mathrm{c1}}$), despite the latter being the most obvious phase transition in electronic transport measurements. Band crossings responsible for the $3q$ gap may occur above $E_{\mathrm{F}}$ and therefore are hidden to ARPES, similar to $2H$-$NbSe_2$ [166].

Future investigations of the possible $3q$-$2q$ CDW transition in $1\,T$-$VSe_2$ could utilize spectroscopic probes of the unoccupied states (i.e. STS) in order to unambiguously test the hypothesis of a $3q$ CDW gap situated above $E_{\mathrm{F}}$. Similar to the work of Tsutsumi *et al.* [48], a structural probe such as high-resolution x-ray diffraction measurements could be used to look for small changes in the $c$-axis parameter related to the potential structural lock-in near $T_{\mathrm{c2}} = (80 - 85)$ K.

In summary, the combination of experimental and theoretical results presented in Section 6.3 strongly suggests a FS nesting driven CDW instability in $1\,T$-$VSe_2$, and reiterates the importance of nesting in the group-V TMDs [2]. More generally, it highlights $1\,T$-$VSe_2$ as a suitable system to study the effects of electronic CDW instabilities because of its specific FS topology and reduced complexity in the absence of other strongly-correlated phases. The importance of 3D nesting discussed previously [50, 99, 120, 121] together with the apparent interplay between $3q$ and $2q$ CDWs in $1\,T$-$VSe_2$ via a modification of $q_z$, suggests there may be important implications of reduced dimensionality in future investigations of few-layer samples and vdW heterostructures. Recent results have thus far demonstrated a 3D-2D crossover at a thickness comparable to the $c$-axis CDW correlation length [158, 159] and in the monolayer limit, a dramatic enhancement of charge order [102, 103] and possible emergent ferromagnetism [104–106] has been observed.

# Chapter 7

# Interplay between the charge density wave and metal-insulator transition in 1$T$-$TaSe_2$

## 7.1 Preamble

Within the TMD family, the tantalum-based compounds, $MX_2$ (M = Ta, X = S/Se) of both the 1$T$ and 2$H$ polytypes are amongst the most extensively studied because of their rich phase diagrams consisting of a whole range of strongly-correlated behaviour including CDWs and an unusual metal-insulator transition (MIT). Understanding the potential competition or co-operation between various phases of matter is an ongoing goal of fundamental research. In particular, there has been a focus on the relationship between CDWs and superconductivity in the cuprates [9] and TMDs [10,15,125] which are generally thought to be competing. By contrast, the interplay between CDWs and the MIT in the Ta-based TMDs is less clear.

1$T$-$TaSe_2$ exhibits a first-order ICCDW-CCDW transition at 473 K [49] involving portions of the elliptical Ta-5$d$ electron pockets centred at the $\overline{\text{M}}$-point, similar to other group-V TMDs [2]. Interestingly, surface-sensitive probes of the electronic structure such as ARPES [167] and STM [168] have also observed a large gap opening across the entire FS below $\sim$ 260 K, reminiscent of a metal-insulator transition (MIT). Despite this, 1$T$-$TaSe_2$ seems to remain metallic in the bulk at all temperatures [169]. As a result, the MIT has been explained as a Mott insulating phase that develops only at the surface [167] for which the CDW acts as a precursor by modifying the band structure and enhancing the likelyhood of electron localisation [170]. Recent alternative explanations for the MIT in the sulphide (1$T$-$TaS_2$) involve the effect of three-dimensional CDW stacking order and

hybridization of atomic orbitals [171–173].

In general, questions surrounding the origin of the MIT in the Ta-based compounds, and its relationship with CDW order remain. Although 1$T$-$TaSe_2$ has received less attention than the sulphide (1$T$-$TaS_2$), it has recently been suggested to be more a suitable system in which to investigate these questions because of its simpler phase diagram, strong experimental signatures of electronic order, and well-separated onset temperatures between the CDW and MIT [174]. One approach is to utilise ultrafast spectroscopy techniques to investigate characteristic electron dynamics during the *melting* and *recovery* of strongly correlated phases following perturbation with an intense laser pulse [140], as has been demonstrated already in 1$T$-$TaS_2$ [175–180]. In particular, TR-ARPES allows direct visualisation of the electronic structure and can track photo-induced suppression of the order parameter in real time [79,181]. Previous TR-ARPES studies of 1$T$-$TaSe_2$ have either focused on suppression dynamics of the MIT phase on short timescales ($\leq$ 500 fs) [174] or the CCDW phase at room temperature only [182].

This chapter reports on a detailed investigation of coherent phonon oscillations in the low-temperature MIT phase (77 K) of 1$T$-$TaSe_2$ using TR-ARPES and TRR up to several picoseconds. In the work by Sayers *et al.* entitled "Selective electron-phonon coupling in the insulating phase of 1$T$-$TaSe_2$" [183], the valence band dynamics related to the MIT gap, $\Delta_{\mathrm{MIT}}$ at the $\bar{\Gamma}$-point is tracked using photon energy, $h\nu = 6$ eV with unprecedented time and energy resolution [73] compared to previous studies [174, 182]. The MIT phase was found to be extremely robust and did not show any significant collapse even at the highest pump laser fluence. However, the pump triggers extremely strong and long-lived coherent oscillations of the band edge with a single frequency component belonging to the CDW amplitude mode. By contrast, the transient reflectivity $\Delta R/R$ signal is clearly modulated by multiple frequencies belonging to phonons of the distorted lattice. Since the TR-ARPES and TRR experiments utilise similar optical pump pulses, it is likely that multiple phonons are also triggered in TR-ARPES. However, the direct visualisation of the band structure offered TR-ARPES shows that the VB binding energy, related to the order parameter, $\Delta_{\mathrm{MIT}}$ is in fact selectively coupled only to the CDW amplitude mode evidenced by its single frequency component. In addition, TRR measurements above room temperature showed that the CDW amplitude mode can be suppressed by the optical pump, whilst the distorted lattice structure remains robust up to $T_{\mathrm{CDW}}$ in a metastable state.

## 7.2 Introduction

### 7.2.1 Strongly-correlated behaviour in the tantalum based TMDs

The tantalum-based TMDs are perhaps most well-known for exhibiting numerous charge density wave (CDW) phases including; incommensurate (ICCDW), nearly-commensurate (NCCDW) and commensurate (CCDW), with transition temperatures over a wide range of $T_{\mathrm{CDW}}$ = (75 - 473) K [2]. Signatures of metal-insulator transitions (MITs) are observed in both $1T$ polytypes, although only $1T$-$TaS_2$ appears to become insulating in the bulk [6, 169]. Superconductivity is naturally found only in the $2H$ polytypes [184, 185], although it can be induced in the $1T$ polytypes using pressure [186] or doping [187]. Many of these different phases are found within a single compound, making them an ideal platform to study co-operating or competing states of matter.

A summary of the various phases found in the tantalum-based TMDs are listed in Table 7.1. In general, the $2H$ polytypes have less diverse and comparatively weaker CDW order i.e. typically fewer CDW transitions that occur at lower temperatures ($\leq$ 122 K), however they are naturally superconducting. This is in contrast to the $1T$ polytypes which have multiple high-temperature CDW transitions in the range (180 - 473) K, but no natural superconductivity. This simple observation is suggestive of competing CDW and superconducting order in the tantalum-based TMDs, whereby if CDW order is weak then superconductivity emerges and vice versa. This hypothesis is supported by studies of induced superconductivity in the $1T$ polytypes [186, 187] where the critical temperature, $T_{\mathrm{c}}$ is found to be maximum when the CDW transition, $T_{\mathrm{CDW}}$ is suppressed.

In addition to the *intrapolytypic* transitions outlined so far, many *interpolytypic* transformations can also occur, which is dictated by the stability of particular crystal structures and not related to any strongly-correlated effects. For example, $1T$ and $2H$ polytypes may transform to 4Hb, 3R and 6R at high temperature which can either be reversible or irreversible [188]. The $2H$ and $3R$ polytypes are the most stable forms evidenced by their natural formation at the lowest growth temperatures, whereas the other polytypes are metastable and can only be obtained by quenching from high temperature during crystal growth or via the interpolytypic transformations [2].

| Compound | ICCDW | NCCDW | CCDW | MIT | Superconductivity |
|---|---|---|---|---|---|
| $2H$-$TaS_2$ | - | - | 75 K [2] | No | Yes, 1.5 K [184] |
| $2H$-$TaSe_2$ | 122 K [46] | - | 90 K [46] | No | Yes, 0.13 K [185] |
| $1T$-$TaS_2$ | 550 K [2] | 350 K [2] | 180 K [2] | Yes [6] | No$^{\dagger}$ |
| $1T$-$TaSe_2$ | 600 K$^{*}$ [49] | - | 473 K [49] | Yes [167] | No$^{\ddagger}$ |

**Table 7.1:** Summary of strongly-correlated behaviour in the tantalum-based TMDs including incommensurate (ICCDW), nearly-commensurate (ICCDW) and commensurate (CCDW) charge density waves, metal-insulator transitions (MIT) and superconductivity. $^{*}$Predicted normal state to ICCDW transition temperature since an interpolytypic transformation ($1T \rightarrow 3R$) at 530 K makes it experimentally inaccessible. Induced superconductivity using $^{\dagger}$pressure ($T_c$ = 5 K at 2.5 GPa) [186] or $^{\ddagger}$doping ($T_c$ = 2.5 K for $x = 0.6$ in $1T$-$TaSe_{2-x}Te_x$) [187].

### 7.2.2 Characteristics of the CDW

As discussed previously, the metastable $1T$ phase of $TaSe_2$ is retained by rapidly quenching to room temperature from $T_g \geq 900°C$ [49]. The $1T$ structure will then remain stable until heating above 530 K where an irreversible interpolytypic $1T \rightarrow 3R$ transformation occurs [188]. The normal state to ICCDW transition is predicted at higher temperatures ($\geq$ 600 K) and is therefore not accessible experimentally. At $T_{CDW}$ = 473 K, $1T$-$TaSe_2$ exhibits a first-order ICCDW to CCDW transition [49]. Hence, the room temperature phase of $1T$-$TaSe_2$ is the commensurate CDW and this is the most discussed feature of this material in the literature. For the remainder of this chapter, when referring generically to the *CDW phase* and the *CDW transition temperature*, it relates to the commensurate CDW phase and the ICCDW to CCDW transition respectively.

Figure 7.1(a) shows a sketch of the Fermi surface of $1T$-$TaSe_2$. The CDW is associated with opening of gaps along the arms of the elliptical (Ta-5$d$) electron pockets centred around the $\overline{\text{M}}$-point [174] where the expected CDW vector, $\mathbf{q}_{CDW}$ links parallel portions of the FS approximately along the $\overline{\text{K}}$-$\overline{\text{M}}$-$\overline{\text{K}}$ direction with a small rotation. The origin of CDW formation has been discussed in terms of FS nesting based on geometrical arguments [2] and susceptibility calculations [189], although experimental evidence does not conclusively support such a scenario [21,53]. A possible alternative explanation involves a $\mathbf{q}$-dependent electron-phonon coupling [25].

The CDW is accompanied by an in-plane $\sqrt{13}a_0 \times \sqrt{13}a_0$ periodic lattice distortion

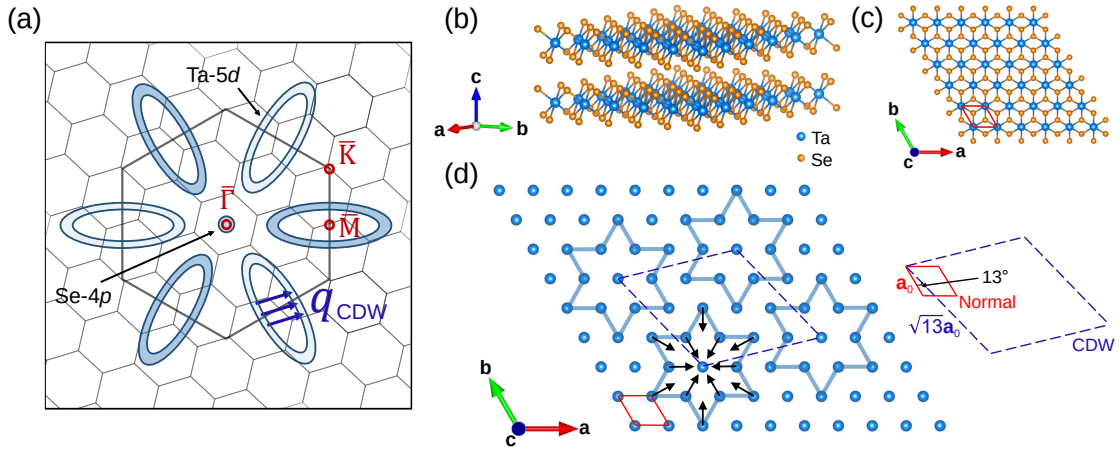


**Figure 7.1:** Characteristics of the CDW in $1T$-$TaSe_2$. (a) Sketch of the Fermi surface in the CDW phase with hexagonal Brillouin zone (BZ) and projected high-symmetry points labelled. The small hexagons represent the reconstructed BZ due to the PLD. The expected CDW vector, $\mathbf{q}_{\mathrm{CDW}}$ is indicated. Panels (b) and (c) show the crystal structure along the layer plane and $c$-axis respectively. (d) View of an inner Ta-plane. In the CDW phase, the displacement of the 12 nearest neighbours surrounding a central Ta atom is indicated by the black arrows and results in the "star-of-David" configuration. The PLD is defined by a $\sqrt{13}a_0 \times \sqrt{13}a_0$ unit cell (blue dashed lines) with 13° rotation relative to the normal phase cell (red solid lines).

(PLD) which is rotated by 13° with respect to the original cell. Figure 7.1(d) shows the inward displacement of the 12 nearest neighbours surrounding a central Ta atom which results in a superlattice comprised of Ta clusters in the so-called "star-of-David" configuration [2]. It is interesting to note that the magnitude of the in-plane PLD is rather large compared to other TMDs ($\sim$ 7% of the normal phase lattice parameters [190]).

The ICCDW-CCCDW transition is strongly first-order and therefore results in sudden and dramatic changes to the electronic [49] and structural properties [191] over a narrow temperature range. The most commonly reported feature is the large increase in electrical resistivity at 473 K when passing from the ICCDW to the CCDW phase as illustrated in Figure 7.2(a). The distorted CCDW lattice has a total of 114 optical modes and at least 57 are Raman-active with $A_g$ symmetry [191]. Many of these modes are visible in Raman spectroscopy measurements and remain well-defined up to 472 K i.e. just below $T_{\mathrm{CDW}}$ as shown in Figure 7.2(b). However, upon entering the ICCDW phase by heating to 478 K, there is a sudden loss of definition of all modes, particularity in the range (50 - 100) $\mathrm{cm}^{-1}$. This behaviour has been noted in other compounds such as $2H$-$TaSe_2$ and $1T$-$TaS_2$ when the commensurate CDW order is lost [192].

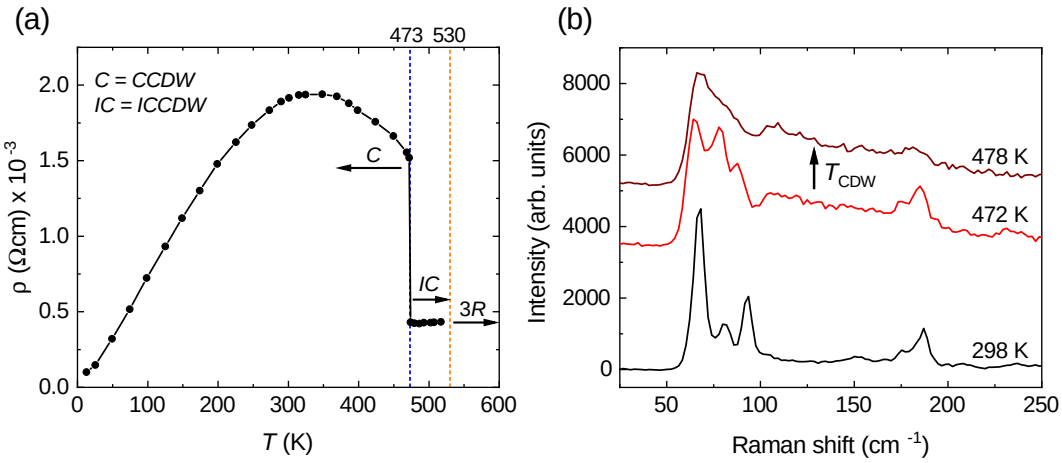


**Figure 7.2:** Experimental signatures of CDW order in $1T$-$TaSe_2$. (a) In-plane resistivity as function of temperature reproduced from Ref. [49]. The ICCDW-CCDW transition ($T_{CDW}$ = 473 K) is highlighted as well the interpolytypic $1T \rightarrow 3R$ transformation (530 K). (b) Raman spectra showing the evolution of the Raman-active zone centre phonons through the ICCDW-CCDW transition.

### 7.2.3 On the origin of the MIT

As mentioned previously, a MIT is observed in $1T$-$TaSe_2$ using surface-sensitive probes such as ARPES [167] and STM [168], evidenced by a large gap of $\Delta_{MIT} \approx$ (200 - 300 meV) below $E_F$ which develops below $\sim$ 260 K, and displays a hysteric behaviour with temperature [167]. The gap occurs across all $k$-space and hence there is a complete loss of FS. Despite this, $1T$-$TaSe_2$ appears to remain metallic at all temperatures based on bulk-sensitive electrical transport measurements [49], in stark contrast to the MIT in $1T$-$TaS_2$ which clearly displays insulating behaviour [6]. Consequently, the MIT in $1T$-$TaSe_2$ has been explained as a Mott transition which occurs only at the surface [167, 168].

In a simple description, metals with a suitable band structure may become insulators if there are significant electron-electron interactions. A theory was proposed by Neville Mott [193] to explain anomalous experimental results of some $d$-electron metals that depends on the strength of the coulomb repulsion, $U$ between electrons and the hopping integral between neighbouring sites, $t$ which can be linked to the band width [194, 195]. Consider a metal with a partially-filled band that crosses $E_F$, if electron-electron repulsion is strong or the band is narrow, the electrons may become localised and unable to hop between neighbouring sites, thus becoming insulating. Mott showed that this effect

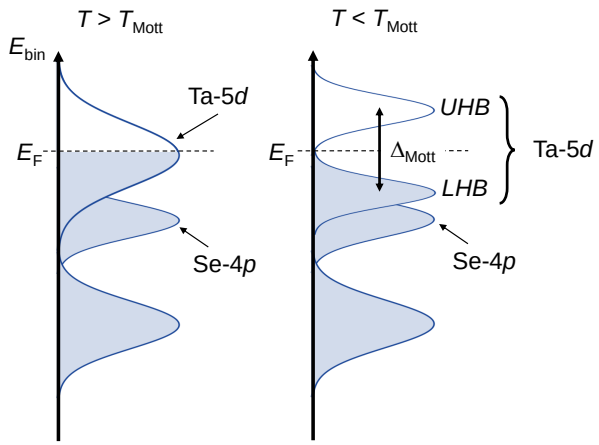


**Figure 7.3:** Mott insulating phase in $1T$-$TaSe_2$. (a) Sketch of the electronic structure close to the Fermi level, $E_F$. The relevant feature is the half filled electron-like Ta-5$d$ band which crosses $E_F$. Upon entering the Mott phase, the Ta-5$d$ band splits into two narrow subbands, labelled as the lower (LHB) and upper (UHB) Hubbard bands, and separated by a gap, $\Delta_{Mott}$.

naturally opens a gap by splitting the partially filled band into two subbands, resulting in the *Mott insulator* and the transition is dictated by the critical ratio $U/t$.

In the case of $1T$-$TaSe_2$, it is believed that the CDW is a precursor to the Mott transition by modifying the band structure, resulting in a half-filled Ta-5$d$ band at $E_F$. Upon cooling, the increasing CDW amplitude causes in a reduction of the conduction band width until the critical value for Mott localisation is reached [170]. The result is a splitting of the Ta-5$d$ band into lower (LHB) and upper (UHB) Hubbard bands [167, 196] at $E_F$ separated by a gap, $\Delta_{Mott}$ as illustrated in Figure 7.3. Since ARPES only probes the occupied states, this transition appears first as a narrowing of the Ta-5$d$ band and then eventually a considerable lowering of the band edge below $E_F$.

An alternative explanation for the MIT in the sulphide ($1T$-$TaS_2$) has recently emerged based on a three-dimensional CDW stacking effect and hybridization of atomic orbitals [171–173]. As discussed already, there are numerous similarities between the $1T$ Ta-based compounds and therefore such a scenario should also be considered a possibility in $1T$-$TaSe_2$.

## 7.3 Publication entitled: "Selective electron-phonon coupling in the insulating phase of $1T$-$TaSe_2$"

<table>
<tr><td colspan="5">This declaration concerns the article entitled:<br>Selective electron-phonon coupling in the insulating phase of $1T$-$TaSe_2$</td></tr>
<tr><td colspan="5">Publication status (tick one)</td></tr>
<tr><td>Draft manuscript</td><td>Submitted</td><td>In review</td><td>Accepted</td><td>Published</td></tr>
<tr><td>✓</td><td></td><td></td><td></td><td></td></tr>
<tr><td>Reference</td><td colspan="4">C. J. Sayers, H. Hedayat, A. Ceraso, F. Museur, M. Cattelan, L. S. Hart, D. Wolverson, L. S. Farrar, S. Dal Conte, G. Cerullo, C. Dallera, E. Carpene and E. Da Como. Selective electron-phonon coupling in the insulating phase of $1T$-$TaSe_2$. In preparation (2020).</td></tr>
<tr><td>Candidate's contribution to the paper</td><td colspan="4">The candidate provided the samples and performed the time-resolved photoemission and reflectivity measurements, with the assistance of others. The candidate performed the supporting experiments of full-wavevector ARPES and temperature-dependent Raman spectroscopy. The candidate performed the data analysis and contributed significantly to the interpretation of the results. The presentation of data in journal format is solely the work of the candidate.<ul><li>Formulation of ideas: 50%</li><li>Design of methodology: 50%</li><li>Experimental work: 75%</li><li>Presentation of data in journal format: 100%</li></ul></td></tr>
<tr><td>Statement from candidate</td><td colspan="4">This paper reports on original research I conducted during the period of my Higher Degree by Research candidature.</td></tr>
<tr><td colspan="3">Signature:</td><td colspan="2">Date:</td></tr>
</table>

## Selective electron-phonon coupling in the insulating phase of 1$T$-$TaSe_2$

C. J. Sayers,[1,*] H. Hedayat,[2] A. Ceraso,[2] F. Museur,[3] M. Cattelan,[4] L. S. Hart,[1] D. Wolverson,[1] L. S. Farrar,[1] S. Dal Conte,[2] G. Cerullo,[2] C. Dallera,[2] E. Carpene,[5] and E. Da Como[1]

[1] *Centre for Nanoscience and Nanotechnology, Department of Physics, University of Bath, Bath, BA2 7AY, UK*
[2] *Dipartimento di Fisica, Politecnico di Milano, 20133 Milano, Italy*
[3] *Laboratoire de Physique, Ecole Normale Supérieure de Lyon, CNRS 69364 Lyon Cedex 07, France*
[4] *School of Chemistry, University of Bristol, Cantocks Close, Bristol BS8 1TS, UK*
[5] *IFN-CNR, Dipartimento di Fisica, Politecnico di Milano, 20133 Milano, Italy*

1$T$-$TaSe_2$ is host to co-existing strongly-correlated phases including charge density waves (CDWs) and an unusual metal-insulator transition (MIT) at low temperature. Here, we investigate coherent phonon oscillations in the low-temperature phase of 1$T$-$TaSe_2$ using a combination of time- and angle-resolved photoemission spectroscopy (TR-ARPES) and time-resolved reflectivity (TRR). Perturbation by an intense femtosecond laser pulse triggers a modulation of the valence band edge at the $\bar{\Gamma}$-point related to the MIT gap, which is comprised of a single frequency consistent with the CDW amplitude mode. By contrast, a similar pulse used in transient reflectivity measurements instead triggers a modulation of $\Delta R/R$ comprised of multiple frequencies. Thus, our work reveals a selective-electron phonon coupling between the CDW amplitude mode and the electron dynamics related to the MIT. In addition, we were able to access a metastable regime such that the CDW amplitude mode is suppressed by the optical pump below $T_{\mathrm{CDW}}$ whereas the lattice-order remains robust.

### INTRODUCTION

Understanding the delicate interplay between various co-operating or competing phases of matter in quantum materials is an ongoing goal of fundamental research [1–3]. Driving these systems out of equilibrium using an intense femtosecond laser pulse offers the possibility to transiently suppress forms of electronic and lattice order then subsequently monitor their recovery in real-time [4]. The characteristic dynamics of these processes allows a classification of these materials in the time-domain [5], and has been used to disentangle the underlying mechanisms of complex materials such as cuprate superconductors [6] and exciton-lattice driven CDW systems [7] or unlocking normally hidden states of matter [8].

An ideal platform to investigate these phenomena are the trigonal (1$T$) tantalum-based transition metal dichalcogenides (TMDs), $MX_2$ (M = Ta, X = S/Se) which are host to whole range of strongly-correlated behaviour including; charge density waves (CDWs) [9], metal-insulator transitions (MITs) [10], quantum spin liquid states [11], and superconductivity [12, 13].

The sulphide (1$T$-$TaS_2$) has been studied extensively using time-resolved techniques [14–19], motivated mostly due to its rich phase diagram. It exhibits multiple CDW transitions including; an incommensurate (550 K), nearly-commensurate (350 K), and commensurate (180 K) phase [9] which occurs concomitantly with a metal-insulator transition (MIT), and has historically been associated with a Mott phase [20]. However, an alternative explanation has recently been proposed based on the three-dimensional stacking order of the CDW and hybridization of atomic orbitals [21–23]. Thus, important questions surrounding the nature of the MIT and its relationship with CDW order remain.

The selenide (1$T$-$TaSe_2$) has received comparatively far less attention, although it was recently suggested to be the more suitable compound in which to investigate the relationship between the CDW and MIT phases because of the well-separated transition temperatures, larger electronic gap, and reduced complexity due to the absence of the nearly-commensurate phase (NCCDW) [19].

1$T$-$TaSe_2$ undergoes a first-order transition from an incommensurate (ICCDW) to commensurate (CCDW) charge density wave at $T_{\mathrm{CDW}} = 473$ K [24]. It is accompanied by an in-plane $\sqrt{13}a_0$ x $\sqrt{13}a_0$ periodic lattice distortion (PLD) which is rotated by 13° with respect to the original unit cell, and forms a 13-atom superlattice comprised of Ta clusters in the so-called "star-of-David" configuration [9]. The CCDW phase is associated with gaps in the electronic structure near the $\bar{M}$-point along the arms of the elliptical (Ta-5$d$) electron pockets [19]. Fig. 1(a) shows a sketch of the Fermi surface (FS) with the CDW vector, $\mathbf{q}_{\mathrm{CDW}}$ linking parallel portions of the electron pockets approximately along the $\bar{K}$-$\bar{M}$-$\bar{K}$ direction which could be prone to FS nesting [9], although the importance of electronic instabilities in these compounds is not entirely clear [25, 26].

An MIT occurs at $\sim$ 260 K which is evidenced by a large gap opening of (200 - 300) meV below the Fermi level, $E_{\mathrm{F}}$ from surface-sensitive measurements such as ARPES [10] and STM [27]. Despite significant gaps found in the MIT phase of both the 1$T$ Ta-based compounds, only 1$T$-$TaS_2$ becomes insulating at low temperature whereas 1$T$-$TaSe_2$ appears to remains metallic to bulk-sensitive probes such as electrical transport [24]. Consequently, the MIT in 1$T$-$TaSe_2$ has been explained

as a Mott insulating phase that occurs only at the surface [10, 27]. In this scenario, the CDW is a precursor to the Mott transition, since it modifies the band structure to create a narrow half-filled conduction band (CB), which becomes prone to localization when the band width is decreased below a critical value as the temperature is reduced [28]. Although the CDW gap is located near the $\bar{M}$-point and the majority of the FS remains unaffected by the transition, the low-temperature MIT results in a gap, $\Delta_{MIT}$ which lowers the energy of states across all $k$-space [10] as illustrated in Fig. 1(b).

Time- and angle-resolved photoemission spectroscopy (TR-ARPES) is a powerful tool which allows direct visualization of the electronic band structure following perturbation with an intense laser pulse. In strongly-correlated systems, it can be used monitor the collapse and recovery of electronic order in real-time by probing energy gaps, $\Delta$ related to the order parameter [5–7]. Recent TR-ARPES studies of 1$T$-$TaSe_2$ using high-harmonics ($h\nu \approx 22$ eV) have focused predominantly on the gap suppression dynamics on short timescales [19] or the room temperature (CCDW) phase only [29].

Here, we study the dynamics of 1$T$-$TaSe_2$ in the low-temperature phase (77 K) at the $\bar{\Gamma}$-point using 6 eV photon energy with unprecedented time- and energy-resolution. We track the valence band edge related to the magnitude of $\Delta_{MIT}$ over picoseconds and find that it exhibits very strong, long-lasting oscillations with a single frequency related to the $A_{1g}$-symmetry CDW amplitude mode ($\sim$ 2.2 THz at 77 K). Using complimentary time-resolved reflectivity (TRR) and temperature-dependent Raman spectroscopy measurements, we compare the coherent oscillations triggered by the optical pump pulse to vibrational modes of the CCDW lattice. Our results confirm a selective electron-phonon coupling which links the MIT gap, $\Delta_{MIT}$ to the amplitude mode of the CDW, and sheds light on the interplay between these strongly-correlated phases.

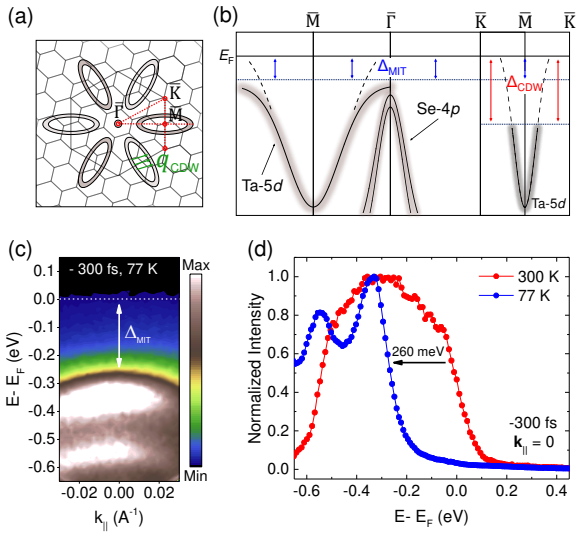


FIG. 1: Electronic order in 1$T$-$TaSe_2$. (a) Sketch of the Fermi surface (FS) in the charge density wave (CDW) phase at room temperature. The projected high-symmetry points of the hexagonal Brillouin zone (BZ) are labelled. The small hexagons represent the reduced BZ due to the $\sqrt{13}a_0$ x $\sqrt{13}a_0$ PLD with 13° rotation. The green arrows indicate the possible CDW vector, $\mathbf{q}_{CDW}$. (b) Sketch showing the location of gaps in the electronic band structure due to the CDW and MIT. The dashed red lines in panel (a) mark the chosen path through the BZ. (c) TR-ARPES spectrum (-300 fs) in the low-temperature phase at 77 K. (d) Comparison of EDCs extracted from the $\bar{\Gamma}$-point ($\mathbf{k}_{||}$= 0) at 300 K and 77 K. The black arrow shows the band edge shift as a result of a gap, $\Delta_{MIT}$ opening at low-temperature.

## METHODS

TR-ARPES experiments were performed using visible (1.82 eV, 30 fs) pump and deep-ultraviolet (6.05 eV, 80 fs) probe pulses produced by a series of nonlinear optical processes using the output of an Yb-based laser (Pharos, Light Conversion) operating at 80 KHz repetition rate, as described in Ref. [30]. Photoemission spectra were acquired using a SPECS PHOIBOS 100 2D hemispherical energy analyser. The overall time- and energy-resolution of this configuration were approximately 50 fs and 35 meV, respectively.

TRR was performed using a setup based on a Ti:sapphire laser (Coherent Libra) which outputs (790 nm, 100 fs) pulses at 2 kHz repetition rate. The laser drives two non-collinear parametric amplifiers (NOPAs) serving as pump and probe beams. The amplified pulse is characterized by a broad spectral range (500 - 700 nm) and is compressed to $\sim$ 20 fs duration using chirp mirrors. The pump beam is modulated at 1 kHz using a mechanical chopper. Pump and probe beams were incident on the sample using crossed polarizations, and the reflected signal was detected using a Si photodetector array.

Temperature-dependent Raman spectroscopy was performed using a Renishaw InVia Raman spectrometer with 532 nm excitation wavelength. The laser power was minimized to avoid heating effects and was measured to be (65 $\pm$ 1) $\mu$W on the sample. Further details are provided in the Supplemental Material (Ref. [31]).

## RESULTS & DISCUSSION

The electronic band structure of 1$T$-$TaSe_2$ consists of a broad Ta-5$d$ band and two steeply dispersing Se-4$p$ subbands [32] as illustrated in Fig. 1(b), which extend up to $E_F$ at room temperature [10]. Shown in Fig. 1(c) are

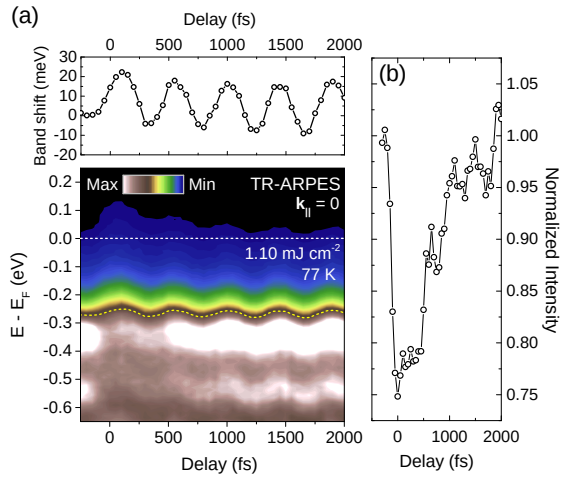


FIG. 2: Valence band dynamics in the low temperature phase. (a) TR-ARPES spectra (77 K) at the $\bar{\Gamma}$-point with 1.10 mJ cm$^{-2}$ pump fluence. The upper panel shows the shift of the VB edge extracted from the yellow dashed line in the lower panel. (b) Normalised maximum VB intensity.

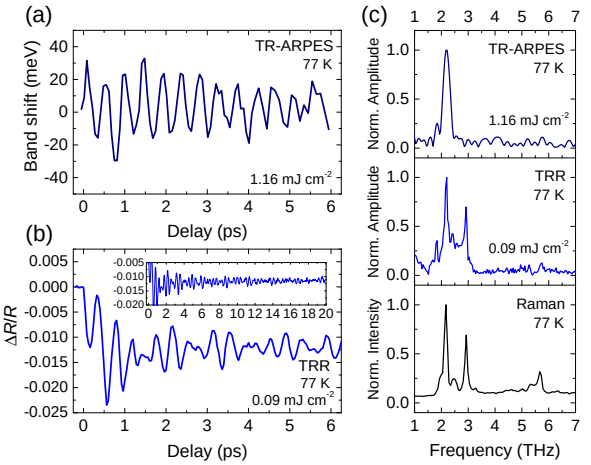


FIG. 3: Selective-electron phonon coupling. (a) VB shift from TR-ARPES (1.16 mJ cm$^{-2}$). (b) Transient reflectivity signal, $\Delta R/R$ measured by TRR (0.09 mJ cm$^{-2}$). The inset shows the same data up to 20 ps delay. (c) Normalised Fourier transform (FT) amplitude of the TR-ARPES and TRR oscillatory components in panels (a) and (b) together with a Raman spectrum for comparison.

TR-ARPES spectra of $1T$-$TaSe_2$ in the low temperature phase (77 K) at the $\bar{\Gamma}$-point before pump arrival (- 300 fs) with dispersion approximately along the $\bar{M}$-$\bar{\Gamma}$-$\bar{M}$ direction based on low energy electron diffraction (LEED) [31]. Here, there is an obvious loss in photoemission intensity below $E_F$ as the band edge is lowered in energy due to the opening of a gap, $\Delta_{MIT}$. A comparison of EDCs in Fig. 1(d) extracted along $\bar{\Gamma}$ ($\mathbf{k}_{||} = 0$) shows a lowering of the band edge by $\sim$ 260 meV between 300 K and 77 K, which is in very close agreement with previous reports [10]. ARPES measurements at higher momenta using $h\nu = 21.2$ eV shows that $\Delta_{MIT}$ extends across all $k$-space and the entire FS is removed at 40 K, indicative of an insulating state [31]. These results are in contrast to bulk sensitive electrical transport measurements which show that $1T$-$TaSe_2$ remains metallic to 4 K [24, 31]. Thus, it seems plausible that the MIT occurs only at the surface as suggested previously [10, 27, 28].

The lower panel of Fig. 2(a) shows the valence band dynamics at the $\bar{\Gamma}$-point after perturbation with 1.16 mJ cm$^{-2}$ pump fluence. At $t = 0$, there is an instantaneous loss of valence band intensity and a transfer of spectral weight above $E_F$, indicative of the out-of-equilibrium electron distribution generated by the pump arrival. This is highlighted further in Fig. 2(b) and shows the recovery of the valence band intensity occurs within $\sim$ 2 ps.

The upper panel in Fig. 2(a) shows the band edge position extracted from a constant intensity contour in the lower panel indicated by the dashed line. Considering the moderate pump fluence, the MIT gap is only weakly perturbed since there is no significant upshift of the band related to the collapse of electronic order, suggesting the state is relatively robust compared to other strongly-correlated phases. For example, complete CDW gap suppression ($\sim$ 100 meV shift) can be achieved in the related compound, $1T$-$TiSe_2$ with $\sim$ 4-5 times lower pump fluence [7].

Most notably, the pump triggers strong coherent oscillations of the band edge of approximately $\pm$ 25 meV around the equilibrium position, which is very weakly damped given the large amplitude that persists up to 6 ps as shown in Fig. 3(a). Fitting the data with a damped sine function yields a period of (457 $\pm$ 2) fs or frequency, $f \approx 2.19$ THz, which is in very close agreement with the intense 72.4 cm$^{-1}$ (2.17 THz) mode with $A_{1g}$ symmetry measured by Raman spectroscopy at 77 K [31]. We note that the frequency of this mode is significantly temperature-dependent and therefore such a close agreement suggests that laser-induced heating of the sample at this fluence is entirely negligible. An extrapolation of the fit suggests that the oscillations may last up to 15 ps where the amplitude becomes $\leq$ 2 meV [31]. Such long-lived oscillations have also been observed in the low temperature phase of $1T$-$TaS_2$ [14, 15] belonging to the CDW amplitude mode and is related to the breathing mode of the stars-of-David in the distorted lattice [33]. This result confirms a direct modulation of the binding edge of the VB edge ($\Delta_{MIT}$) by interaction with the CDW amplitude in $1T$-$TaSe_2$.

To investigate the origin of the coherent phonon oscillations further, we performed time-resolved reflectivity (TRR) and Raman spectroscopy measurements as a

function of temperature. Figs. 3(a) and (b) compare the oscillatory component of the VB edge from TR-ARPES to the TRR signal, $\Delta R/R$ in the low-temperature phase. Using 0.09 mJ cm$^{-2}$ fluence, there is only a small change in $\Delta R/R$ and the signal is instead dominated by large oscillations. The inset of Fig. 3(b) shows that the modulation lasts up to at least 20 ps. Importantly, the oscillations in TRR clearly consist of multiple frequencies, in stark contrast to the single frequency VB data from TR-ARPES. This is highlighted by the Fourier transform (FT) of the oscillatory components shown in Fig. 3(c), together with a Raman spectrum at the same temperature for comparison. FT of the VB shift data shows only a single frequency present at $\sim$ 2.2 THz in agreement with the damped sine fit previously. Whereas the TRR signal is comprised of multiple frequencies with greatest amplitude at $\sim$ 1.8, 2.2 and 2.9 THz, and closely resembles the Raman spectrum. We note that the 1.8 THz cannot be seen in the latter since it is below the notch filter cut-off. Since both TR-ARPES and TRR experiments utilise a similar optical pump, it is likely that multiple modes are triggered in both cases and relate to the Raman-active phonon modes of the distorted CCDW lattice, including the CDW amplitude mode. These appear in the TRR signal since it represents the average response of electrons without energy-momentum selectivity. Instead, TR-ARPES directly probes the local electronic structure of the VB at $\bar{\Gamma}$ and therefore our results suggest a selective electron-phonon coupling, whereby the binding energy of the VB related to $\Delta_{\mathrm{MIT}}$ is modulated by a single frequency belonging to the CDW amplitude mode.

We now focus on the dynamics in the CCDW phase at room temperature and higher (i.e. in the absence of the MIT) measured by TRR. Shown in Fig. 4 is a FT analysis of the $\Delta R/R$ signal for various sample temperatures in the range (295 - 478) K compared to Raman spectroscopy measurements. Similar to the 77 K data, multiple frequency components are seen at 295 K in Fig. 4(a). The greatest peaks in FT amplitude belong to the highest intensity modes determined previously in TRR, although they are found at slightly lower frequencies of 2.0 and 2.7 THz because of the higher sample temperature, in agreement with Raman spectroscopy. We note that the damping of the oscillatory component of $\Delta R/R$ at this temperature is much greater and the modulation only lasts up to $\sim$ (5 - 6) ps. As the temperature is increased in the range (295 - 410) K, we see the intensity of the amplitude mode decreases sharply together with a shift to lower frequencies until the mode becomes absent for $T \geq 450$ K. By comparison, the Raman measurements show that all modes remain clearly visible at higher temperatures until there is a sudden change in the spectra when heating above the first order ICCDW-CCDW phase transition at $T_{\mathrm{CDW}} = 473$ K and all modes merge into a broad background, similar to previous reports in the Ta-based compounds [34, 35]. The somewhat softer (i.e.

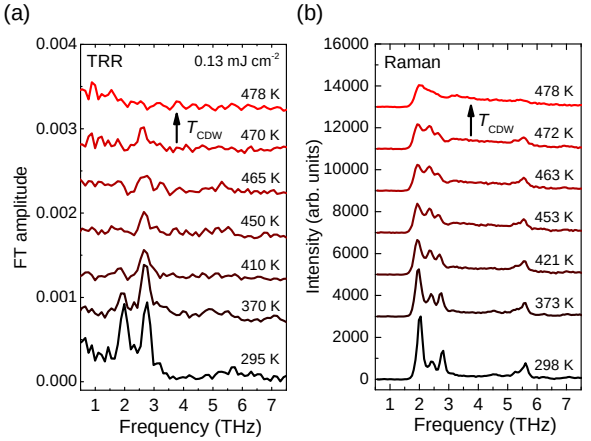


FIG. 4: Temperature dependence of coherent phonon oscillations. (a) Fourier transform (FT) of the transient reflectivity, $\Delta R/R$ signal measured by TRR (0.13 mJ cm$^{-2}$) at sample temperatures in the range (295 - 478) K as indicated. (c) Raman spectra measured over a similar temperature range as panel (a) for comparison. The data in both panels is offset for clarity.

second order) behaviour of the $A_{1g}$ amplitude mode in TRR could suggest a transient melting of the CDW order parameter by the optical pump which is completely suppressed at 450 K using 0.13 mJ cm$^{-2}$ fluence. Instead, the 2.7 THz mode, which is related to phonon modes of the PLD, appears to remain robust until it suddenly becomes absent above $T_{\mathrm{CDW}} = 473$ K similar to the Raman spectra. Thus our results reveal an induced metastable state in $1T$-$TaSe_2$ whereby the lattice-order persists following the collapse of the order parameter. In addition, we have demonstrated the manipulation of a phase transition which is typically first-order that becomes second-order in out-of-equilibrium conditions.

## CONCLUSION

We investigated electron dynamics in the low-temperature phase of $1T$-$TaSe_2$ using a combination of TR-ARPES and TRR. At 77 K, we find an electronic gap at the $\bar{\Gamma}$-point related to the metal-insulator transition (MIT), $\Delta_{\mathrm{MIT}} \approx 260$ meV below $E_{\mathrm{F}}$ in good agreement with previous reports [10]. Perturbation by an intense femtosecond laser pulse triggers coherent oscillations of the VB edge ($\Delta_{\mathrm{MIT}}$) which is modulated by a single frequency consistent with the CDW amplitude mode ($f \approx 2.2$ THz), similar to the related compound $1T$-$TaS_2$ [14, 15]. TRR measurements using a similar pump pulse instead show modulations comprised of multiple frequencies. Therefore, we suggest a selective electron-phonon coupling linking the electron dynamics of the VB binding energy at $\bar{\Gamma}$-point with the CDW

amplitude mode based on the direct measurements of the band structure, shedding light on the interplay between strongly-correlated phases in this complex material. Above room temperature, we are able to induce a metastable state in $1T$-$TaSe_2$ by transiently suppressing the CDW order parameter (amplitude mode) below $T_{CDW}$, whilst the lattice-order appears to remain robust. More generally, our results contribute to the understanding of CDW systems that exhibit metastable [7, 29, 36] or hidden states [18] in out-of-equilibrium conditions. The orders-of-magnitude change in resistivity between the CDW and insulating phases of the Ta-based TMDs has already been suggested as a potential use in so-called memresistive devices [37] which could be manipulated using short laser pulses [8].

**Acknowledgements**

The authors acknowledge funding and support from the EPSRC Centre for Doctoral Training in Condensed Matter Physics (CDT-CMP), Grant No. EP/L015544/1.

* Corresponding author: c.j.sayers@bath.ac.uk

[1] L. J. Li, E. C. T. O'Farrell, K. P. Loh, G. Eda, B. Ozyilmaz, and A. H. C. Neto, Controlling many-body states by the electric field effect in a two-dimensional material, Nature. **529**, 185 (2016).

[2] H. H. da Silva Neto, P. Aynajian, A. Frano, R. Comin, E. Schierle, E. Weschke, A. Gyenis, J. Wen, J. Schneeloch, Z. Xu, S. Ono, G. Gu, M. Le Tacon, Mathieu A. Yazdani, Ubiquitous Interplay Between Charge Ordering and High-Temperature Superconductivity in Cuprates, Science. **343**, 393 (2014).

[3] A. Kogar, Observation of a Charge Density Wave Incommensuration Near the Superconducting Dome in $Cu_xTiSe_2$, Phys. Rev. Lett. **118**, 027002 (2017).

[4] C. Giannetti, M. Capone, D. Fausti, M. Fabrizio, F. Parmigiani and D. Mihailovic, Ultrafast optical spectroscopy of strongly correlated materials and high-temperature superconductors: A non-equilibrium approach, Adv. Phys. **65**, 58 (2016).

[5] S. Hellmann, T. Rohwer, M. Kalläne, K. Hanff, C. Sohrt, A. Stange, A. Carr, M. M. Murnane, H. C. Kapteyn, L. Kipp, M. Bauer, and K. Rossnagel, Time-domain classification of charge-density-wave insulators, Natt. Comms. **3**, 1069 (2012).

[6] F. Boschini, E. H. da Silva Neto, E. Razzoli, M. Zonno, S. Peli, R. P. Day, M. Michiardi, M. Schneider, B. Zwartsenberg, P. Nigge, R. D. Zhong, J. Schneeloch, G. D. Gu, S. Zhdanovich, A. K. Mills, G. Levy, D. J. Jones, C. Giannetti and A. Damascelli, Collapse of superconductivity in cuprates via ultrafast quenching of phase coherence, Nat. Mat. **17**, 416 (2018).

[7] H. Hedayat, C. J. Sayers, D. Bugini, C. Dallera, D. Wolverson, T. Batten, S. Karbassi, S. Friedemann, G. Cerullo, J. van Wezel, S. R. Clark, E. Carpene, and E. Da Como, Excitonic and lattice contributions to the charge density wave in $1T$-$TiSe_2$ revealed by a phonon bottleneck, Phys. Rev. Research. **1**, 023029 (2019).

[8] K. Sun, S. Sun, C. Zhu, H. Tian, H. Yang and J. Li, Hidden CDW states and insulator-to-metal transition after a pulsed femtosecond laser excitation in layered chalcogenide $1T$-$TaS_{2-x}Se_x$, Sci. Adv. **4**, eaas9660 (2018).

[9] J. A. Wilson, F. J. Di Salvo, and S. Mahajan, Charge-density waves and superlattices in the metallic layered transition metal dichalcogenides, Adv. Phys. **24**, 117 (1975).

[10] L. Perfetti, A. Georges, S. Florens, S. Biermann, S. Mitrovic, H. Berger, Y. Tomm, H. Höchst, and M. Grioni, Spectroscopic Signatures of a Bandwidth-Controlled Mott Transition at the Surface of $1T$-$TaSe_2$, Phys. Rev. Lett. **90**, 166401 (2003).

[11] K. T. Law and P. A. Lee, $1T$-$TaS_2$ as a quantum spin liquid, PNAS. **114**, 6996 (2017).

[12] B. Sipos, A. F. Kusmartseva, A. Akrap, H. Berger, L. Forró and E. Tutiš, From Mott state to superconductivity in 1T-$TaS_2$, Nat. Mat. **7**, 960 (2008).

[13] Y. Liu, D. F. Shao, L. J. Li, W. J. Lu, X. D. Zhu, P. Tong, R. C. Xiao, L. S. Ling, C. Y. Xi, L. Pi, H. F. Tian, H. X. Yang, J. Q. Li, W. H. Song, X. B. Zhu, and Y. P. Sun, Nature of charge density waves and superconductivity in $1T$-$TaSe_{2-x}$-$Te_x$, Phys. Rev. B. **94**, 045131 (2016).

[14] L. Perfetti, P. A. Loukakos, M. Lisowski, U. Bovensiepen, H. Berger, S. Biermann, P. S. Cornaglia, A. Georges, and M. Wolf, Time Evolution of the Electronic Structure of $1T$-$TaS_2$ through the Insulator-Metal Transition, Phys. Rev. Lett. **97**, 067402 (2006).

[15] L. Perfetti, P. A. Loukakos, M. Lisowski, U. Bovensiepen, M. Wolf, H. Berger, S. Biermann and A. Georges, Femtosecond dynamics of electronic states in the Mott insulator 1T-$TaS_2$ by time resolved photoelectron spectroscopy, New. J. Phys. **10**, 053019 (2008).

[16] J. C. Petersen, S. Kaiser, N. Dean, A. Simoncig, H. Y. Liu, A. L. Cavalieri, C. Cacho, I. C. E. Turcu, E. Springate, F. Frassetto, L. Poletto, S. S. Dhesi, H. Berger, and A. Cavalleri, Clocking the Melting Transition of Charge and Lattice Order in $1T$-$TaS_2$ with Ultrafast Extreme-Ultraviolet Angle-Resolved Photoemission Spectroscopy, Phys. Rev. Lett. **107**, 177402 (2011).

[17] M. Eichberger, H. Schäfer, M. Krumova, M. Beyer, J. Demsar, H, Berger, G. Moriena, G. Sciaini and R. J. D. Miller, Snapshots of cooperative atomic motions in the optical suppression of charge density waves, Nature **468**, 799 (2010).

[18] L. Stojchevska, I. Vaskivskyi, T. Mertelj, P. Kusar, D. Svetin, S. Brazovskii and D. Mihailovic, Ultrafast switching to a stable hidden quantum state in an electronic crystal, Science **11**, 177 (2014).

[19] C. Sohrt, A. Stange, M. Bauer and K. Rossnagel, How fast can a Peierls-Mott insulator be melted?, Fara. Dis. **171**, 243 (2014).

[20] P. Fazekas and E. Tosatti, Charge carrier localization in pure and doped $1T$-$TaS_2$, Physica B + C **99**, 183 (1980).

[21] T. Ritschel, J. Trinckauf, K. Koepernik, B. Büchner, M. v. Zimmermann, H. Berger, Y. I. Joe, P. Abbamonte and J. Geck, Orbital textures and charge density waves in transition metal dichalcogenides, Nat. Phys. **11**, 328 (2015)

[22] T. Ritschel, H. Berger, and J. Geck, Stacking-driven gap formation in layered $1T$-$TaS_2$, Phys. Rev. B. **98**, 195134

(2018)

[23] S.-H. Lee, J. S. Goh, and D. Cho, Origin of the Insulating Phase and First-Order Metal-Insulator Transition in $1T$-$TaS_2$, Phys. Rev. Lett. **122**, 106404 (2019).

[24] F. J. Di Salvo, R. G. Maines, J. V. Waszczak, and R. E. Schwall, Preparation and properties of $1T$-$TaSe_2$, Solid. State. Comms. **14**, 497 (1974).

[25] M. Bovet, D. Popović, F. Clerc, C. Koitzsch, U. Probst, E. Bucher, H. Berger, D. Naumović, and P. Aebi, Pseudogapped Fermi surfaces of $1T$-$TaS_2$ and $1T$-$TaSe_2$: A charge density wave effect, Phys. Rev. B. **69**, 125117 (2004).

[26] P. Aebi, T. Pillo, H. Berger and F. Lévy, On the search for Fermi surface nesting in quasi-2D materials, J. Electron. Spec. Rela. Phenom. **117**, 433 (2001).

[27] S. Colonna, F. Ronci, A. Cricenti, L. Perfetti, H. Berger, and M. Grioni, Mott Phase at the Surface of $1T$-$TaSe_2$ Observed by Scanning Tunneling Microscopy, Phys. Rev. Lett. **94**, 036405 (2005).

[28] S. Colonna, F. Ronci, A. Cricenti, L. Perfetti, H. Berger, and M. Grioni, Scanning Tunneling Microscopy Observation of a Mott-Insulator Phase at the $1T$-$TaSe_2$ Surface, Jpn. J. Appl. Phys. **45**, 1950 (2006).

[29] X. Shi, W. You, Y. Zhang, Z. Tao, P. M. Oppeneer, X. Wu, R. Thomale, K. Rossnagel, M. Bauer, H. Kapteyn and M. Murnane, Ultrafast electron calorimetry uncovers a new long-lived metastable state in $1T$-$TaSe_2$ mediated by mode-selective electron-phonon coupling, Sci. Adv. **5**, eaav449 (2019).

[30] F. Boschini, H. Hedayat, C. Dallera, P. Farinello, C. Manzoni, A. Magrez, H. Berger, G. Cerullo, and E. Carpene, An innovative Yb-based ultrafast deep ultraviolet source for time-resolved photoemission experiments, Rev. Sci. Inst. **85**, 123903 (2014)

[31] See Supplemental Material at http://link.aps.org/ for details of crystal growth, electronic transport measurements, temperature-dependent Raman spectroscopy, full-wavevector ARPES (21.2 eV) and further analysis of the time-resolved spectroscopy data.

[32] F. Clerc, M. Bovet, H. Berger, L. Despont, C. Koitzsch, O. Gallus, L. Patthey, M. Shi, J. Krempasky, M. G. Garnier, P. Aebi, Spin–orbit splitting in the valence bands of $1T$-$TaS_2$ and $1T$-$TaSe_2$, J. Phys: Condens. Matter. **16**, 3721 (2004).

[33] J. Demsar, L. Forro, H. Berger and D. Mihailovic, Femtosecond snapshots of gap-forming charge-density-wave correlations in quasi-two-dimensional dichalcogenides $1T$-$TaS_2$ and $2H$-$TaSe_2$, Phys. Rev. B. **66**, 041101(R) (2002)

[34] J. E. Smith, Jr. J. C. Tsang, and M. W. Shafer, Raman spectra of several layer compounds with charge density waves, Solid. State. Comms. **19**, 283 (1976)

[35] J. C. Tsang, J. E. Smith Jr., M. Shafer and S. F. Meyer, Raman spectroscopy of the charge-density-wave state in $1T$- and $2H-TaSe_2$, Phys. Rev. B. **16**, 4239 (1977).

[36] M. Porer, U. Leierseder, J.-M. Ménard, H. Dachraoui, L. Mouchliadis, I. E. Perakis, U. Heinzmann, J. Demsar, K. Rossnagel and R. Huber, Non-thermal separation of electronic and structural orders in a persisting charge density wave, Nat. Mat. **13**, 857 (2014).

[37] M. Yoshida, R. Suzuki, Y. Zhang, M. Nakano and Y. Iwasa, Memresistive phase switching in two-dimensional in $1T$-$TaS_2$ crystals, Sci. Adv. **1**, e1500606 (2015).

# Supplemental material for: "Selective electron-phonon coupling in the insulating phase of $1\,T$-$TaSe_2$"

C. J. Sayers,[1,*] H. Hedayat,[2] A. Ceraso,[2] F. Museur,[3] M. Cattelan,[4]
L. S. Hart,[1] D. Wolverson,[1] L. S. Farrar,[1] S. Dal Conte,[2]
G. Cerullo,[2] C. Dallera,[2] E. Carpene,[5] and E. Da Como[1]

[1]*Centre for Nanoscience and Nanotechnology, Department of Physics, University of Bath, Bath, BA2 7AY, UK*
[2]*Dipartimento di Fisica, Politecnico di Milano, 20133 Milano, Italy*
[3]*Laboratoire de Physique, Ecole Normale Supérieure de Lyon, CNRS 69364 Lyon Cedex 07, France*
[4]*School of Chemistry, University of Bristol, Cantocks Close, Bristol BS8 1TS, UK*
[5]*IFN-CNR, Dipartimento di Fisica, Politecnico di Milano, 20133 Milano, Italy*

## CRYSTAL GROWTH

Single crystals of $1T$-$TaSe_2$ were grown using the chemical vapour transport (CVT) technique inside an evacuated quartz ampoule. The starting materials consisted of high-purity tantalum (99.9%) and selenium (99.9%) powders, together with anhydrous iodine pellets (99.9%) which acts as the transport agent. Crystals were grown in a slight excess of selenium ($\sim$ 3 mg cm$^{-3}$) to encourage ideal stoichiometry. A growth temperature of $T_g$ = 960°C was maintained for $\sim$ 21 days before the ampoule was quenched rapidly in water from high temperature in order to retain the metastable $1T$ phase, similar to the methods of Ref. [1]. The resulting crystals were up to (4 x 4) mm across with regular hexagonal edges and had a metallic gold colour characteristic of $1T$-$TaSe_2$, as shown in Fig. S1.

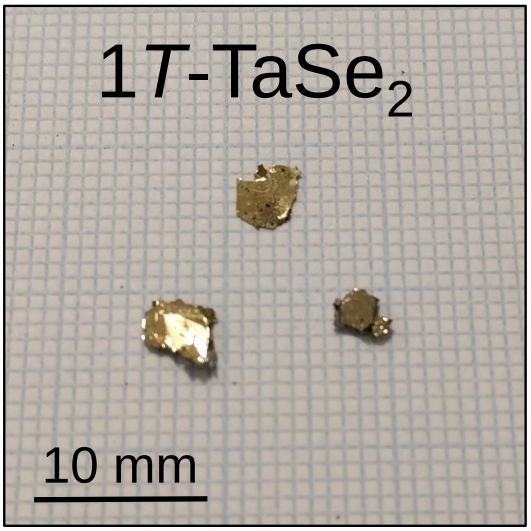


FIG. S1: Single crystals of $1T$-$TaSe_2$. Samples were grown by the chemical vapour transport (CVT) method. The image shows typical crystals which were selected for TR-ARPES measurements.

**ELECTRONIC TRANSPORT**

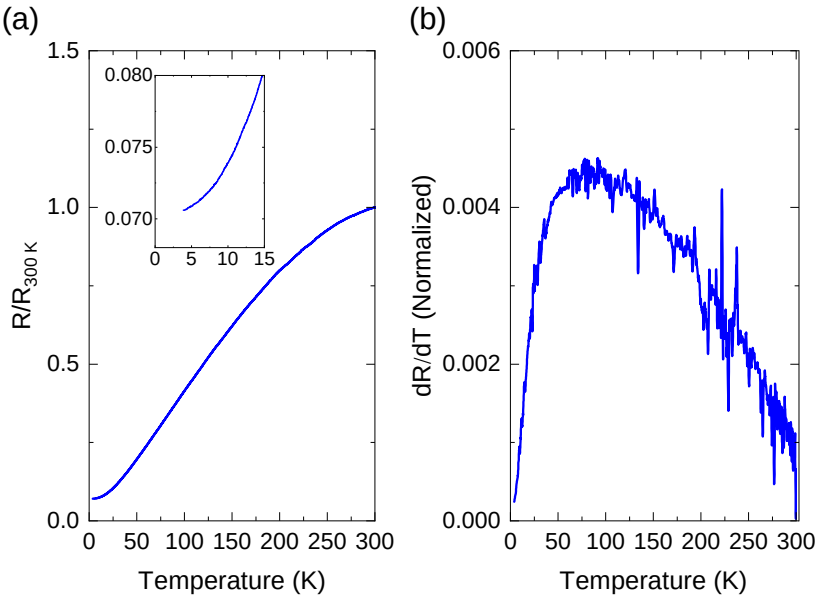


FIG. S2: Electronic transport. (a) Normalized resistance as a function of temperature. The inset shows the low temperature range (< 15 K). (b) First derivative of resistance.

Fig. S2(a) shows resistance as a function of temperature for $1T$-$TaSe_2$ crystals selected from the same batch as those used for TR-ARPES measurements. The shape of the curve is typical for this compound across the measured temperature range of (300 - 4) K with overall metallic behaviour. At 473 K, the first-order CCDW transition is expected where there is a sharp increase in the resistance upon cooling i.e from the ICCDW to the CCDW state [1].

By analysing the first derivative of resistance, $\mathrm{d}R/\mathrm{d}T$ in Fig. S2(b), there are no obvious signatures of phase transitions occurring in this range and the sample remains metallic to 4 K. This is in stark contrast to the clear metal-insulator transition (MIT) observed by TR-ARPES, whereby a significant gap of $\sim$ 260 meV below $E_\mathrm{F}$ develops upon cooling from 300 K to 77 K, as discussed in the main text. This MIT was also observed by full-wavevector ARPES ($h\nu = 21.2$ eV) and shows that the entire Fermi surface (FS) is gapped at 40 K [see Fig. S5(f)] evidenced by a loss of intensity across the Brillouin zone (BZ). Following such a substantial loss of FS, one would expect a large increase in the resistance near the MIT onset temperature [$T \approx$ (220 - 260) K [2]], and possibly a switch to insulating behaviour.

The contrasting results between these techniques could provide support for the hypothesis of Perfetti *et al.* [2] that the MIT in $1T$-$TaSe_2$ is only a surface effect, since we are sensitive to this in ARPES (surface probe) but not in the electronic transport measurements (bulk probe).

The residual resistance ratio (RRR), $R_{300K}/R_{4K}$ allows an estimation of the crystal quality (specifically the scattering of carriers with defects and/or impurities). We find a range of RRR $\approx$ (14 - 16) within the batch, which indicates reasonable purity compared to previous reports [1]. The inset of Fig. S2(a) shows that there is no upturn at low temperatures which one would expect if there was a significant defect scattering.

## RAMAN SPECTROSCOPY

In order to determine the CCDW phase transition and to monitor the temperature dependence of phonon modes in $1T$-$TaSe_2$, Raman spectroscopy was performed in the range (77 - 486) K as shown in Fig. S3. The low temperature data (77 - 270 K) was measured on a bulk crystal mounted inside a flow cryostat under vacuum. Instead, the high temperature data (298 - 486 K) was acquired from a sample mounted on a heating plate in air. To avoid oxidation at high temperature in the latter case, the $1T$-$TaSe_2$ sample was encapsulated in hexagonal boron nitride (h-BN). A bulk-like $1T$-$TaSe_2$ flake was obtained by exfoliation from single crystals ($>$ 20 layers based on optical contrast) which was then encapsulated between two flakes of h-BN (2D-semiconductors.com) on a $Si/SiO_2$ substrate using a dry transfer technique [3] in an oxygen-free environment ($<$ 0.5 ppm). The final result is shown in the inset of Fig. S3(a). Measurements were made using a Renishaw InVia Raman spectrometer operating in backscattering geometry. The laser excitation wavelength was 532 nm and the grating was 1800 l/mm. A long working-distance 50x objective lens (N.A. = 0.5) was used. The overall spectral resolution was better than 1 $cm^{-1}$. The laser power was kept sufficiently low to minimize heating effects, and was measured to be (65 $\pm$ 1) $\mu$W on the sample.

Similar to the other TMDs with trigonal ($1T$) structure, $1T$-$TaSe_2$ has only two Raman-active modes in the normal phase (undistorted lattice) with $A_g$ and $E_g$ symmetry. In the CCDW phase, the distorted structure is triclinic and there are 114 optical modes in total of which 57 are Raman-active with $A_g$ symmetry [4]. Shown in Fig. S3(a) is a high signal-to-

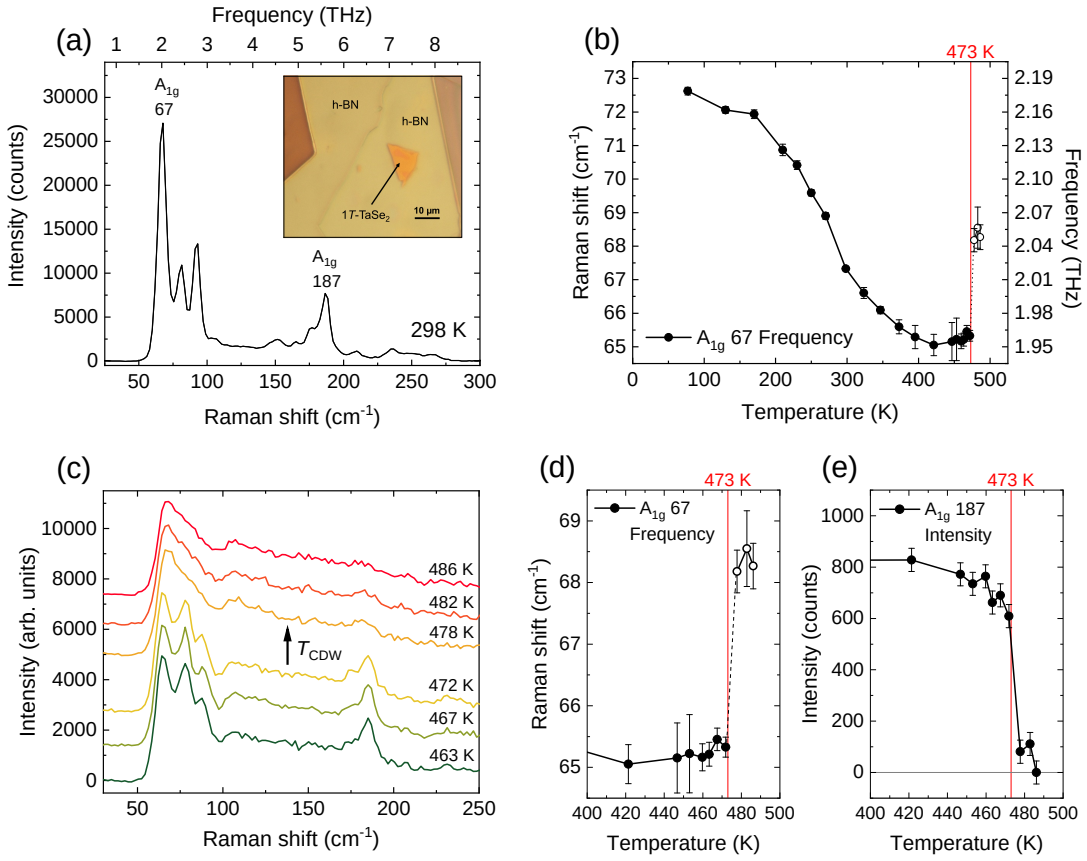


FIG. S3: Temperature dependence of phonon modes in 1$T$-$TaSe_2$ measured by Raman spectroscopy. (a) Raman spectrum at room temperature (298 K). The inset shows a bulk-like 1$T$-$TaSe_2$ flake encapsulated between sheets of h-BN which was used to measure the high-temperature range (298 - 486) K. (b) Temperature dependence of the $A_{1g}$ 67 mode in the range (77 - 486) K. (c) Raman spectra near the expected CDW phase transition ($T_{CDW} \approx 473$ K). (d) Frequency of the $A_{1g}$ 67 mode near the expected phase transition. Error bars are the standard deviation from the Voigt fitting only. (e) Intensity of the $A_{1g}$ 187 mode above the background level. The error bars represent the magnitude of the background noise in the spectra near $A_{1g}$ 187.

noise ratio spectrum of 1$T$-$TaSe_2$ in the CCDW phase at room temperature (298 K). From this data, it is possible to identify 12 individual modes. Two particular modes are labelled according to their peak centre at room temperature, namely $A_{1g}$ 67 and $A_{1g}$ 187.

In Fig. S3(b), the frequency of the $A_{1g}$ 67 ($\sim$ 2 THz) mode is shown as a function of tem-

perature. This mode is very strongly temperature-dependent and shifts $> 7$ cm$^{-1}$ between 77 K and 470 K. By contrast, the frequency of the $A_{1g}$ 187 mode is almost temperature independent. Shown in Fig. S3(c) are the Raman spectra near the expected CCDW phase transition ($T_{CDW} \approx 473$ K). Here, there is a sudden change in the spectrum upon heating between 472 and 478 K. A loss of definition of all the modes occurs and only a broad background remains below 100 cm$^{-1}$, which is similar to previous reports and indicates the sample has passed from the CCDW to ICCDW phase [5]. We note also that this behaviour is similar to $1T$-$TaS_2$ when passing from the CCDW to the NCCDW [6]. A sudden loss of CDW order across a narrow temperature range is characteristic of a first-order phase transition in these compounds [1, 4, 5]. By contrast, other $1T$-TMDs such as $1T$-$TiSe_2$ and $1T$-$VSe_2$ exhibit softer development of the CDW phase (i.e. second-order) whereby the phonons of the distorted lattice are only well-resolved far below the transition temperature (60 - 80 K $< T_{CDW}$) [7, 8]. Fig. S3(d) and (e) show the temperature dependence of the $A_{1g}$ 67 frequency and the $A_{1g}$ 187 intensity respectively over the range (400 - 500) K. The sudden change near 473 K (red vertical line) confirms the expected phase transition temperature in our samples. In Fig. S3(d), the dashed line joining the data points above and below $T_{CDW}$ indicates that the plotted frequency is the peak of the well-defined $A_{1g}$ mode below $T_{CDW}$, whereas it is the peak of the broad feature above $T_{CDW}$, which can no longer be unambiguously identified as the same mode.

**LEED**

Prior to TR-ARPES measurements, a low-energy electron diffraction (LEED) pattern of the $1T$-$TaSe_2$ sample was acquired in order to determine the orientation of the crystal with respect to the lab frame as shown in Fig. S4. This allowed an estimation of the measured momentum direction, $\mathbf{k}_{||}$ which is aligned with the lab horizontal as illustrated by the dashed line. Based on this, we obtained TR-ARPES spectra approximately along the $\overline{\text{M}}$-$\overline{\Gamma}$-$\overline{\text{M}}$ direction.

The hexagonal symmetry (red sketch) of $1T$-$TaSe_2$ is clearly visible from the diffraction spot pattern. On each of the corners of this main feature, weak secondary spots were observed with the same symmetry (blue sketch). The ratio of the spot separation between these features gives 720 pxl / 200 pxl = $3.6 \approx \sqrt{13}$. The secondary feature is also rotated by $\sim 13^\circ$ with respect to the primary. Hence, the secondary spots come from the $\sqrt{13}a_0$ x $\sqrt{13}a_0$ superlattice structure with 13° rotation as expected for the CCDW phase [10, 11, 14]. These features were clearly visible both at room temperature and 77 K.

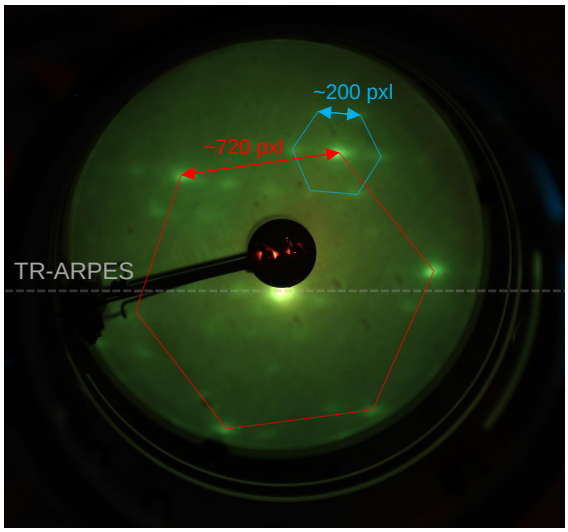


FIG. S4: Low-energy electron diffraction (LEED). The pattern is from the $1T$-$TaSe_2$ single crystal mounted in the analysis chamber prior to TR-ARPES measurements.

**FULL-WAVEVECTOR ARPES**

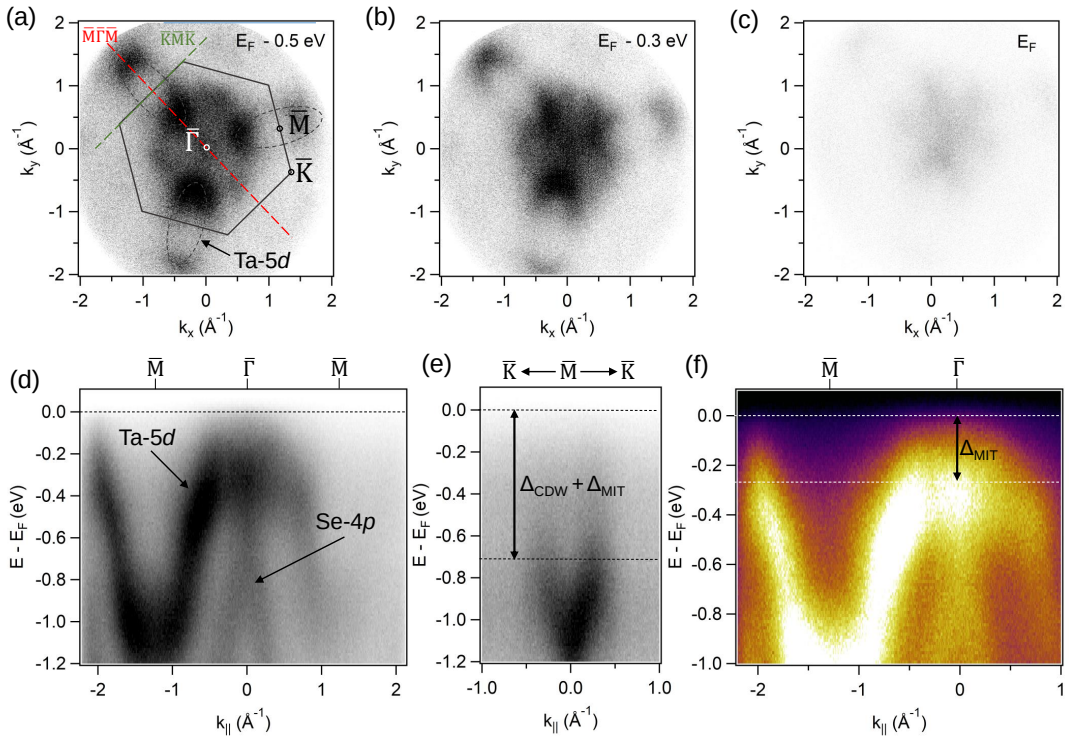


FIG. S5: Full-wavevector ARPES at 40 K using He-I$\alpha$ radiation ($h\nu = 21.2$ eV). (a) - (c) ARPES images at specific binding energies (indicated). Panel (a) includes a sketch of the BZ (black hexagon) and an outline of the Ta-5$d$ derived electron pockets (grey dashed ellipse). The labelled high-symmetry points are a projection onto the experimental $k_z$. Directions of the momentum cuts through the BZ for the data in panels (d) - (f) are indicated by the red and green dashed lines. (d) Dispersion along the $\overline{\text{M}}$-$\overline{\Gamma}$-$\overline{\text{M}}$ direction (e) Dispersion through the centre of the electron pocket along the $\overline{\text{K}}$-$\overline{\text{M}}$-$\overline{\text{K}}$ direction. The CDW and MIT gap is indicated. (f) Same data as panel (a) displayed in a alternative colour scale in order to highlight the MIT gap.

Due to the photon energy of the probe in TR-ARPES ($\sim$ 6 eV), there is a limited access to momentum space of $\mathbf{k}_{||} \approx \pm$ 0.2 Å$^{-1}$. Therefore, to study the electronic structure at larger momenta, we performed ARPES measurements of $1T$-$TaSe_2$ single crystals using He-I$\alpha$ radiation ($h\nu = 21.2$ eV) at the NanoESCA facility, Bristol. Here, the instrument is capable of obtaining full-wavevector ARPES images (simultaneous $k_x$ and $k_y$) at a given

binding energy. A scan in the range $E$ - $E_F$ = (-1.2 − 0.1) eV with 12.5 meV step size was made using 25 eV pass energy and an overall energy resolution of ∼ 50 meV. The sample temperature was maintained at 40 K.

Fig. S5(a) - (c) shows the full-wavevector ARPES images at specific binding energies. At ($E_F$ - 0.5) eV in panel (a), the electronic structure of $1T$-$TaSe_2$ is clear and a sketch of the hexagonal BZ is overlaid with the high-symmetry points labelled. There is an obvious similarity to other group-V TMDs with $1T$ symmetry such as $1T$-$VSe_2$ [12]. On the edges of the BZ around the $\overline{M}$-point, the elliptical electron pockets originating from the Ta-5$d$ states are seen. At 40 K, far below the CCDW temperature (473 K), there is a loss of intensity on the parallel arms of these pockets where the CDW gap is excepted to occur. At the BZ centre ($\overline{\Gamma}$-point), a weak spot is visible which originates from the top of the Se-4$p$ derived hole pocket. In addition, there is a broad *pancake* feature which extends across a large portion of the BZ from the centre to the inner corners of the electron pockets. At ($E_F$ - 0.3) eV in panel (b), the electronic structure is still clearly visible however at the Fermi level, $E_F$ in panel (c), there is almost a complete loss of intensity. This provides evidence that the entire FS is gapped at 40 K as a result of the metal-insulator transition (MIT).

Panel (d) shows the dispersion along the $\overline{M}$-$\overline{\Gamma}$-$\overline{M}$ direction [red dashed line in panel (a)] and the key features are highlighted, including the Ta-5$d$ and Se-4$p$ derived bands. Overall, our results are most similar to the low temperature data from Perfetti *et al.* [2]. We are not able to resolve the separate Ta and Se bands at $\overline{\Gamma}$ in this data, although we note that they have been observed previously from high energy resolution (<10 meV) ARPES measurements [13]. Instead, we observe only a broad feature where the Ta-5$d$ band flattens and merges with Se-4$p$ band. The dispersion through the electron pocket along the $\overline{K}$-$\overline{M}$-$\overline{K}$ direction is shown in panel (e) where the CCDW gap is expected to occur. Here, there is a loss of intensity which extends ∼ 0.7 eV below $E_F$ which we suggest is the CCDW gap enhanced by the MIT. Panel (f) highlights the MIT gap across the entire BZ in that direction. In particular, we note that near the $\overline{\Gamma}$-point, the Ta- and Se-derived bands are shifted considerably below $E_F$ (∼ 250 meV) which can only be explained by a gap opening due to the MIT as the CCDW is not expected to have any influence on states near $\overline{\Gamma}$ since the CDW $q$-vector is believed to only link parallel portions of the electron pocket at the $\overline{M}$-point [14].

## ANALYSIS OF BAND EDGE DYNAMICS

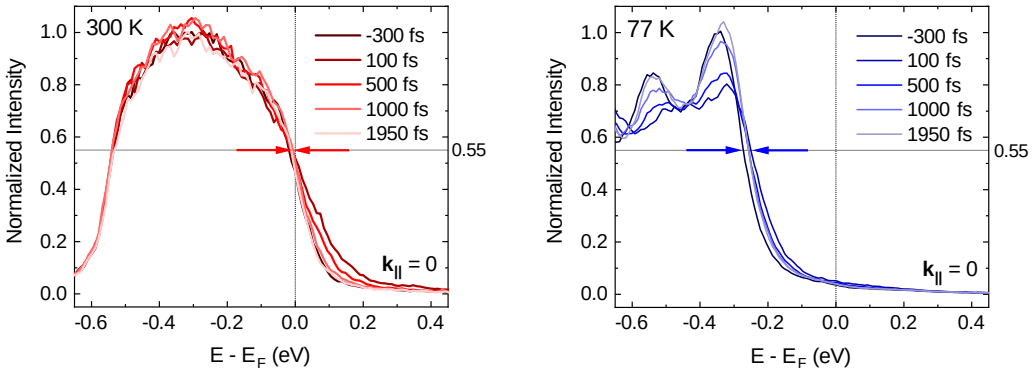


FIG. S6: TR-ARPES dynamics at 300 K and 77 K. Normalized EDCs at $\bar{\Gamma}$ for select pump-probe delays in the CCDW phase (300 K) and CCDW + MIT phase (77 K). The horizontal line is the 0.55 intensity level which corresponds to the nodal point of all spectra at 300 K.

Fig. S6 shows the dynamical evolution of the TR-ARPES spectra at 300 and 77 K. A nodal point is identified between all spectra at 300 K (0.55 normalized intensity), indicated by the red horizontal arrows, and occurs close to the experimentally determined Fermi level, $E_F$. At positive delay, there is a noticeable broadening of the photoemission intensity across the Fermi level due to the out-of-equilibrium electron distribution created by the pump. However there is no upshift in the band edge (0 eV) or band peak ($\sim$ -0.3 eV), which is expected since $\bar{\Gamma}$ is far away from the development of CDW order near the $\bar{M}$-point and is therefore not gapped. At 77 K however, the equilibrium (-300 fs) band edge is $\sim$ 260 meV lower in energy compared to 300 K as a result of a gap opening due to the MIT. Upon pumping, there is a positive shift of the band edge along the 0.55 intensity line as indicated by the blue horizontal arrows. This region was used for the band edge dynamics analysis presented in the main text.

## LONG-LIVED COHERENT OSCILLATIONS

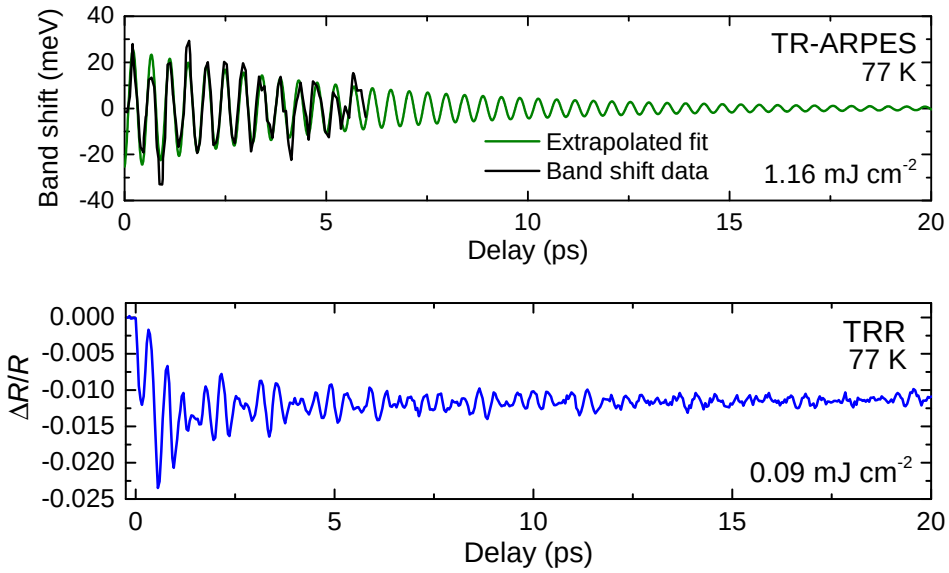


FIG. S7: Long-lived coherent oscillations in the MIT phase of $1T$-$TaSe_2$. Comparison of the VB shift (TR-ARPES) and transient reflectivity (TRR) up to 20 ps.

Fig. S7 demonstrates the weak damping of coherent oscillations in the MIT phase (77 K) of $1T$-$TaSe_2$. The data presented here is the same as the main text. Oscillations of the VB edge from TR-ARPES are fitted with a damped single-frequency sine function which gives a period, $T = (457 \pm 2)$ fs or frequency, $f \sim 2.19$ THz. This is in close agreement with the 72.4 $cm^{-1}$ mode (2.17 THz) with $A_{1g}$ symmetry at 77 K found by temperature-dependent Raman spectroscopy [see Fig. S3(b)]. Although the data only extends up to 6 ps, extrapolation of the fit reveals that the oscillations are extremely long-lived with only a very weak damping. By 15 ps, the amplitude of the fit is $\leq 2$ meV. Comparison with the time-resolved reflectivity (TRR) data (blue line) confirms that the oscillations can last to 20 ps. Although in the latter case, the signal is comprised of multiple frequencies as discussed in the main text.

* Corresponding author: c.j.sayers@bath.ac.uk

[1] F. J. Di Salvo, R. G. Maines, J. V. Waszczak, and R. E. Schwall, Preparation and properties of $1T$-$TaSe_2$, Solid. State. Comms. **14**, 497 (1974).

[2] L. Perfetti, A. Georges, S. Florens, S. Biermann, S. Mitrovic, H. Berger, Y. Tomm, H. Höchst, and M. Grioni, Spectroscopic Signatures of a Bandwidth-Controlled Mott Transition at the Surface of $1T$-$TaSe_2$, Phys. Rev. Lett. **90**, 166401 (2003).

[3] A. Castellanos-Gomez, M. Buscema, R. Molenaar, V. Singh, L. Janssen, H. S. J. van der Zant and G. A. Steele, Deterministic transfer of two-dimensional materials by all-dry viscoelastic stamping, 2D. Mat. **1**, 011002 (2014).

[4] S. Sugai, K. Murase, S. Uchida, and S.Tanaka, Comparison of the soft modes in tantalum dichalcogenides, Physica. B+C **105**, 405 (1981).

[5] J. C. Tsang, J. E. Smith Jr., M. Shafer and S. F. Meyer, Raman spectroscopy of the charge-density-wave state in $1T$- and $2H-TaSe_2$, Phys. Rev. B. **16**, 4239 (1977).

[6] J. E. Smith, Jr. J. C. Tsang, and M. W. Shafer, Raman spectra of several layer compounds with charge density waves, Solid. State. Comms. **19**, 283 (1976)

[7] J. A. Holy, K. C. Woo, M. V. Klein and F. C. Brown, Raman and infrared studies of superlattice formation in $TiSe_2$, Phys. Rev. B. **16**, 3628 (1977).

[8] H. Hedayat, C. J. Sayers, D. Bugini, C. Dallera, D. Wolverson, T. Batten, S. Karbassi, S. Friedemann, G. Cerullo, J. van Wezel, S. R. Clark, E. Carpene, and E. Da Como, Excitonic and lattice contributions to the charge density wave in $1T$-$TiSe_2$ revealed by a phonon bottleneck, Phys. Rev. Research. **1**, 023029 (2019).

[9] J. A. Wilson, F. J. Di Salvo, and S. Mahajan, Charge-density waves and superlattices in the metallic layered transition metal dichalcogenides, Adv. Phys. **24**, 117 (1975).

[10] M. Bovet, D. Popović, F. Clerc, C. Koitzsch, U. Probst, E. Bucher, H. Berger, D. Naumović, and P. Aebi, Pseudogapped Fermi surfaces of $1T$-$TaS_2$ and $1T$-$TaSe_2$: A charge density wave effect, Phys. Rev. B. **69**, 125117 (2004).

[11] P. Aebi, T. Pillo, H. Berger and F. Lévy, On the search for Fermi surface nesting in quasi-2D materials, J. Electron. Spec. Rela. Phenom. **117**, 433 (2001).

[12] A. J. H. Jones, C. J. Sayers, M. Cattelan, L. S. Farrar, S. J. Bending, N. A. Fox, E. Da Como, and J. Laverock, Charge Density Wave Gap in $1T$-$VSe_2$: Momentum and Temperature Dependence, *Unpublished*.

[13] F. Clerc, M. Bovet, H. Berger, L. Despont, C. Koitzsch, O. Gallus, L. Patthey, M. Shi, J.

Krempasky, M. G. Garnier, P. Aebi, Spin–orbit splitting in the valence bands of $1T$-$TaS_2$ and $1T$-$TaSe_2$, J. Phys: Condens. Matter. **16**, 3721 (2004).

[14] J. A. Wilson, F. J. Di Salvo, and S. Mahajan, Charge-density waves and superlattices in the metallic layered transition metal dichalcogenides, Adv. Phys. **24**, 117 (1975).

## 7.4 Discussion & concluding remarks

The work in Section 7.3 presented measurements of the low temperature phase (77 K) of 1 $T$-$TaSe_2$. A combination of TR-ARPES and TRR was used to investigate the response of the system following perturbation from an intense laser pulse in an attempt to further the understanding of the metal-insulator transition (MIT) and its interplay with CDW order.

Between 300 K and 77 K, a large gap of $\Delta_{\mathrm{MIT}} \approx 260$ meV was found to open at the $\bar{\Gamma}$-point in TR-ARPES, evidenced by a lowering of the valence band (VB) edge below $E_{\mathrm{F}}$ in good agreement with the metal-insulator transition observed previously [167]. This was confirmed by full-wavevector ARPES ($h\nu = 21.2$ eV) of the full BZ which revealed that the entire FS is removed at 40 K. This observation is in contrast to bulk-sensitive electronic transport measurements which show metallic behaviour at all temperatures. Therefore it seems plausible that the MIT occurs only at the surface as suggested previously [167,168,170]. Using moderate-high pump fluence, it was found that the gap, $\Delta_{\mathrm{MIT}}$ is only weakly perturbed and there is no evidence for collapse of the MIT phase. Instead, the pump triggers extremely strong and long-lasting coherent oscillations which manifest as a modulation of the VB binding energy. The oscillations appear to be comprised of a single frequency belonging to the CDW amplitude mode [197] with $A_{1g}$-symmetry ($\sim$ 2.2 THz), similar to that observed in time-resolved studies of 1 $T$-$TaS_2$ [175–177]. In order to investigate the coherent oscillations in more detail, complimentary TRR and Raman spectroscopy measurements were performed as a function of temperature. The optical pump in TRR was also found to trigger strong oscillations which last up to $\sim$ 20 ps. However, in stark contrast to the single-frequency VB modulation in TR-ARPES, the $\Delta R/R$ signal was clearly comprised of multiple frequencies ($\sim$ 1.8, 2.2 and 2.9 THz). A comparison of the fourier transform amplitude of oscillatory signals from the different experimental techniques showed an excellent agreement between TRR and Raman spectroscopy, suggesting that the optical pump triggers many of the Raman-active phonons of the distorted lattice. Since TR-ARPES and TRR experiments utilise similar optical pump pulses, it is likely that multiple phonons are also triggered in TR-ARPES. However, the clear single-frequency CDW amplitude mode modulations of the VB binding energy, related to the order parameter ($\Delta_{\mathrm{MIT}}$), suggests a selective electron-phonon coupling in the MIT phase. In addition, a comparison between temperature-dependent Raman spectroscopy and TRR

measurements reveal an induced metastable state in 1 $T$-$TaSe_2$ related to CDW order. Above room temperature, it was found that the amplitude mode can be suppressed by the optical pump and displays a softer temperature dependence (i.e. second-order), whilst the phonons of the distorted lattice remain robust until the first-order transition at $T_{CDW}$, similar to Raman spectroscopy measurements.

These results shed light on the interplay between CDWs and the MIT in the 1 $T$ Ta-based TMDs, a class of materials which exhibit highly-diverse and rich strongly correlated behaviour. As suggested previously, 1 $T$-$TaSe_2$ is the better suited compound to investigate this phenomenon because of its reduced complexity compared to 1 $T$-$TaS_2$ [174]. Since the 6 eV photon energy only provides access to a narrow region of momentum space around $\bar{\Gamma}$, an important extension to this work could be investigate the electron dynamics in the low-temperature phase using TR-ARPES at higher momenta. In this way, the dynamics of the CDW gap at the $\overline{\text{M}}$-point could be monitored simultaneously in the same experiment as the MIT gap at $\bar{\Gamma}$. It would also be interesting to test the limit of perturbation required for the complete collapse of either the MIT or CDW phase.

Aided by recent developments in the field of 2D materials, future studies of 1 $T$-$TaSe_2$ in the monolayer limit may also help to elucidate the origin of the MIT. If there in fact a Mott insulating state only at the surface [167], reducing dimensionality may have a profound effect as the ratio of surface to bulk increases. The growth of monolayer materials by in-situ molecular beam epitaxy (MBE) systems has already demonstrated strong enhancements or modifications to existing properties in TMDs [103], including the emergence of Mott phases [198] in systems which do not exhibit such behaviour in the bulk.

More generally, these results contribute to the understanding of ultrafast phase switching in these materials, the establishment of metastable states [79,132,182] and the possibility of unlocking usually hidden phases [179]. The orders-of-magnitude change in resistivity between the CDW and insulating phases of the Ta-based TMDs has already been suggested as a potential use in so-called memresistive devices [162] which could be manipulated using short laser pulses [199].

# Chapter 8

## Conclusions & Outlook

This thesis has presented a study of charge density wave (CDW) phenomena in the metallic transition metal dichalcogenides (TMDs) [2, 16]. Within this class of materials, there is an ongoing debate about the physical origin of CDWs and various scenarios have been proposed for the dominant driving mechanism in each compound [20]. Specifically in this work, the isostructural selenium-based compounds with trigonal ($1\,T$) symmetry were investigated, namely; $1\,T$-$TiSe_2$, $1\,T$-$VSe_2$ and $1\,T$-$TaSe_2$. The only physical difference between these materials is the transition metal (Ti, V or Ta), yet they exhibit vastly different CDW properties including; transition temperature, distorted lattice periodicity and commensurability. As such, the expectation was that the underlying driving mechanism may be fundamentally different in each case. Given their nearly identical physical structure, these compounds provided an ideal platform with which to compare these key differences in CDW phenomena.

Multiple experimental and theoretical techniques were used in each case to study signatures of CDW formation in both the electronic and lattice structure of these materials. Primarily, angle-resolved photoemission spectroscopy (ARPES) and variants thereof were used to search for gaps, $\Delta$ in the electronic band dispersion and identify their location on the Fermi surface (FS). The evolution of these electronic features with temperature and their response to external perturbation, together with the behaviour of phonons belonging to the distorted crystal lattice, enabled a likely CDW mechanism to be proposed in each case.

## 8.1 Summary of the main findings

Chapter 3 provided a detailed description of the methods to grow high quality single crystal TMDs by chemical vapour transport (CVT), which was used to produce all of the samples studied in this thesis. The influence of crystal growth conditions on the CDW properties of TMDs was then investigated in Chapter 4 by electronic transport measurements of 1$T$-$VSe_2$. Specifically, six different crystal batches were produced by CVT with growth temperatures in the range $T_g$ = (550 - 700)°C. Resistance measurements were used to determine the CDW transition temperature, $T_{CDW}$ and the residual resistance ratio (RRR), which is related to the density of defects or impurities in metals. Overall, it was found that both $T_{CDW}$ and RRR were reduced with increasing growth temperature. The samples were characterised mainly by synchrotron-based XPS and exhibited a rigid shift of Se-3$d$ core levels to deeper binding energies, which correlated with the transport behaviour. This effect was attributed to an overall effective electron doping as 1$T$-$VSe_2$ becomes Se-deficient at elevated temperatures, and thus the relative amount of V to Se increases. Although this doping effect is in general agreement with previous studies of 1$T$-$VSe_2$ and related compounds [42, 87, 89], the presence of metal interstitials was not observed. Instead, the defects were determined to be predominately Se vacancies. By optimising the crystal growth conditions, 1$T$-$VSe_2$ samples were produced with unprecedented purity (RRR ≈ 49) and an increased transition temperature of $T_{CDW}$ = (112 - 113) K compared to the typically reported value of ∼ 110 K.

In Chapter 5, ultrafast spectroscopy techniques were used to investigate the photo-induced CDW suppression and recovery dynamics in 1$T$-$TiSe_2$ in order to disentangle the contribution of excitons and phonons, which are both believed to be important in driving the phase [131, 132]. Time- and -angle resolved photoemission spectroscopy (TR-ARPES) was used to directly track the dynamics of the valence band maximum close to the $\bar{\Gamma}$-point, related to the CDW gap, $\Delta_{CDW}$. It was found that perturbation of the CDW order occurs on relatively short timescales ($\leq$ 200 fs) and nearly complete suppression is achieved at low fluence, suggestive of a primarily exciton driven CDW mechanism [42, 146, 147] as free carriers promoted by the pump pulse rapidly screen the coulomb potential and reduce the exciton binding energy [28]. A detailed pump fluence dependence over the range (31 - 250 $\mu$J cm$^{-2}$) revealed several different out-of-equilibrium regimes. At low fluence, the CDW gap, $\Delta_{CDW}$ was able to recover completely to its initial

condition within ∼2 ps. However, above a threshold fluence of $F_{\text{th}} = 60$ $\mu$J cm$^{-2}$, the recovery was impeded and the valence band remained up-shifted within the experimentally explored time window. The observation of coherent oscillations of the CDW gap in TR-ARPES at low fluence, related to the $A_{1g}^{*}$ CDW amplitude mode (∼ 3.4 THz) [136], became absent above $F_{\text{th}}$ which promoted further investigation. As such, detailed time-resolved reflectivity (TRR) was performed over a similar fluence range and utilised the same pump pulse as TR-ARPES. A progressive switching of the dominant oscillation frequency from the $A_{1g}^{*}$ CDW mode to the $A_{1g}$ mode of the normal phase structure was found to occur precisely at the threshold fluence, $F_{\text{th}}$, revealing the important role of phonons. Simulations of the quasiparticle dynamics using a modified Rothwarf-Taylor (R-T) model [78, 141] were performed to gain further insight into the interaction of excitons with strongly coupled phonons, SCPs. Excellent agreement with experiments were found across the entire fluence range and a crossover to the *bottleneck* regime [78] was found beyond $F_{\text{th}}$, related to the exciton dissociation rate and the anharmonic decay of SCPs to the thermal bath.

In Chapter 6, the role of electronic instabilities in 1$T$-$VSe_2$ was investigated by acquiring high resolution full-wavevector ARPES images of the FS. These measurements revealed a quasi-2D FS topology with notably large parallel portions along the arms of the V-3$d$ electron pockets centred at the $\overline{\text{M}}$-point. Based purely on symmetry arguments with regards to the FS images, the length of the expected in-plane wavevector, $\mathbf{q}_{\text{CDW}} = 1/4a_0$ [48] effectively links parallel portions of FS at the $\overline{\text{M}}$-point as discussed previously in the group-V TMDs [2]. A maximum gap of $\Delta_{\text{CDW}}(30\text{ K}) = 10$ meV was found to open along these central portions of FS. Further analysis of the momentum-dependence of the gap showed that the gap varies continuously around the elliptical pocket and is minimum at the apex, where the FS separation becomes $\leq \mathbf{q}_{\text{CDW}}$. Hence, these measurements represent a direct observation of CDW order in 1$T$-$VSe_2$, and is highly suggestive of a FS nesting type scenario. This hypothesis was supported by a comparison of the experimental results with DFT calculations of the electronic susceptibility, $\chi^0(\mathbf{q})$ which showed a divergence near $\mathbf{q}_{\text{CDW}} = (1/4a_0,\ 0.314c_0)$, thus agreeing closely with the nesting vector identified in ARPES. Signatures of two phase transitions at $T_{\text{c1}} = 110$ K and $T_{\text{c2}} =$83 K were observed in electronic transport and Raman spectroscopy measurements, similar to that reported from previous electron [107] and x-ray [48] scattering measurements. Surprisingly, the gap in ARPES was found to open at $T_{\text{c2}}$, and not the well-known transition

at $T_{c1}$. This unexpected behaviour was investigated further by considering the effect on the electronic susceptibility, $\chi^0(\mathbf{q})$ of separate $3q$ and $2q$ CDW states corresponding to the transitions at $T_{c1}$ and $T_{c2}$ according to Eaglesham *et al.* [107]. From this, it was found that $2q$ is responsible for gapping the majority of states on the FS for which the $3q$ competes.

In Chapter 7, the interplay between the metal-insulator transition (MIT) and the CDW in $1\,T$-$TaSe_2$ was investigated using complementary TR-ARPES and TRR measurements. It was found that a large gap at the $\bar{\Gamma}$-point opens between 300 K and 77 K on the order of $\Delta_{MIT} \approx 260$ meV, reminiscent of a MIT in this compound. Full-wavevector ARPES showed that there is an entire loss of FS (40 K) as a result of this transition. Comparing this insulating behaviour observed in surface-sensitive ARPES measurements to the metallic behaviour seen in bulk-sensitive electronic transport suggests a MIT which occurs only at the surface, as mentioned previously [167,168]. The MIT phase is extremely robust and $\Delta_{MIT}$ was only weakly perturbed at the highest laser fluence (1.16 mJ cm$^{-2}$). Instead, the pump triggered extremely strong and long-lasting coherent oscillations of the VB edge comprised of a single frequency belonging to the CDW amplitude mode with $A_{1g}$ symmetry ($\sim$ 2.2 THz) [197]. By contrast, the TRR signal, $\Delta R/R$ was clearly modulated by multiple frequencies belonging to phonons of the distorted lattice. Since both experiments utilised similar optical pump pulses, it is likely that multiple phonons were also triggered in TR-ARPES. Since they were not observed in the VB modulations, it was determined that the MIT may be selectively coupled only to the CDW amplitude mode. In addition, measurements of the coherent oscillations by TRR as a function of temperature above 300 K showed that the CDW amplitude mode can be suppressed by the optical pump, whilst the distorted lattice structure remains in a metastable state up to $T_{CDW}$.

## 8.2 Implications for the understanding of CDW formation in TMDs

The primary motivation for this thesis was to further the understanding of CDW formation in bulk metallic TMDs, driven by the ongoing research into 2D materials and high-temperature superconductivity as outlined in Section 1.1.1. Therefore, the following briefly discusses the implications of the work summarised in Section 8.1 with regards to this effort.

Since $1T$-$TiSe_2$ belongs to the group-IV TMDs, it possesses small closed elliptical electron pockets, and therefore a nesting type mechanism can be ruled out because of the complete absence of parallel portions of FS [21]. Instead, there has been increasing support [146–148] for the *excitonic insulator* scenario [28, 42], which has culminated in recent evidence for exciton condensation in this material [27]. In general, the results in Chapter 5 are in agreement with a primarily exciton-driven CDW in $1T$-$TiSe_2$ based on the response to perturbation from a laser pulse. However, the lattice has also been shown to be important based on the role of CDW phonons in the recovery dynamics, whereby the maximum CDW order parameter, $\Delta_{\mathrm{CDW}}$ is only established when both excitonic correlations and lattice order are present [79]. To determine these contributions unambiguously may require novel experimental or theoretical approaches, or perhaps information can be gained by studying other potential excitonic insulator systems [200–202]. The complimentary ultrafast spectroscopy techniques of TR-ARPES and TRR could be used to disentangle important processes in other CDW systems since typically both electronic and structural signatures are present, and appear concomitantly when studied by the majority of experimental probes.

$1T$-$VSe_2$ belongs to the group-V TMDs and therefore possesses larger open elliptical electron pockets with considerable portions of parallel quasi-2D FS which historically has been related to nesting instabilities [2, 50–52]. On the other hand, the predictions of a relatively weak response of the electron subsystem in such a high-dimension scenario has led to the belief than FS nesting may not be applicable to anything other than strictly 1D systems [22,23], including TMDs [21]. However, the combination of ARPES measurements and calculations of the electronic susceptibility in Chapter 5 strongly suggest a FS nesting scenario in this compound, evidenced by a divergence in both the real and imaginary parts of $\chi^0(\mathbf{q}, k)$ [22,23,33] near the expected CDW wavevector which agrees closely with symmetry arguments from experiment. Thus, these results reaffirm the importance of electronic instabilities in the group-V TMDs [2]. Given the resemblance of the FS in $1T$-$VSe_2$ to $1T$-$TaSe_2$, a similar mechanism may be responsible for the CDW in the latter [2], and could be investigated using a similar approach [100, 122]. However the high temperature of the ICCDW-CCDW phase transition, $T_{\mathrm{CDW}} = 473$ K [49] may be problematic for ARPES studies due to excessive thermal broadening of bands, whilst the normal-ICCDW phase transition is completely inaccessible experimentally since an interpolytypic transformation ($1T \rightarrow 3R$) occurs first.

## 8.3 Looking ahead

### 8.3.1 Growth of TMDs

It is well known that TMDs produced at the lowest growth temperatures ($T_g \leq 600°C$) typically exhibit the highest CDW transition temperatures, $T_{CDW}$ [42,87,89]. This effect is related to the presence of defects which results in an overall electron doping as shown in Chapter 4. The lower limit explored in that work was comparable to previous studies at $T_g = 550°C$ [89]. However, it was shown that the RRR, related to the crystal purity, seemed likely to continue increasing for samples prepared at even lower temperatures. It is anticipated that there will be a critical temperature below which there will be insufficient energy for crystallisation to occur or the required growth time would become impractically long. However given the possible gain in crystal purity, it would be interesting to explore this lower limit.

Doping TMDs with metals or chalcogens [88,91] allows manipulation of their properties, such as induced superconductivity [10], commensurability effects [125], and control over the entire phase diagram of strongly-correlated behaviour [203,204]. Hence, doping is a promising route to further understand the CDW driving mechanisms in these materials. Since early experiments of 1$T$-$TiSe_2$, there has been questions surrounding the origin of the anomalous transport behaviour [42,135] whereby there is an insulator-like region of increasing resistivity which onsets far above $T_{CDW}$, followed by a steep increase at the phase transition, before peaking around $\sim$ 165 K and returning to metallic-like behaviour down to the lowest temperatures (see Section 5.3.3). In the *excitonic insulator* scenario, it would be expected that 1$T$-$TiSe_2$ should become completely insulating for all temperatures below $T_{CDW}$. This anomalous behaviour has been explained by the seemingly unavoidable electron doping [42] in 1$T$-$TiSe_2$ crystals and in-situ grown films, such that there are always small regions of FS (electron pockets) remaining after CDW formation. The close proximity of band edges to $E_F$ has resulted in a debate about whether 1$T$-$TiSe_2$ is either a semiconductor [142,143] or a semimetal [42,144], and it is likely that this material is extremely sensitive to the delicate balance between electron and hole carrier densities [42]. Based on this knowledge, research efforts to produce pure (stoichiometric) or slightly hole-doped 1$T$-$TiSe_2$ could be extremely enlightening with regards to its CDW formation. As of yet, there are no obvious routes with which to achieve this aim. However, recent ob-

servations of an intrinsic insulating ground state have been made in $1T$-$TiSe_2$ crystals grown under high gas pressure, and ARPES measurements show complete removal of the electron pockets from the FS in the CDW phase [205].

### 8.3.2 2D materials

Recent advances in the preparation of 2D materials by dry transfer of exfoliated flakes [206] or in-situ growth of films by MBE [102, 207] and CVD [208, 209] has already allowed an investigation into the effects of dimensionality on the properties of TMDs at the monolayer limit, including CDW systems. The in-situ growth of metallic TMD films in UHV is important since their properties are particularity sensitive to oxidation. Studying these materials with probes of the electronic structure such as STM and ARPES has already led to important discoveries of dramatically enhanced charge order [102], control of the distorted lattice periodicity by strain [207] and emergent phases of matter which are not normally found in their bulk counterparts; such as CDWs [198], ferromagnetism [105] and Mott insulating states [198], amongst numerous others. A dramatic enhancement of the CDW transition temperature, $T_{\mathrm{CDW}}$ has been observed in monolayer samples of many metallic TMDs; including $1T$-$TiSe_2$ [210], $1T$-$VSe_2$ [103] and $2H$-$NbSe_2$ [211], where the latter is $\geq 4$ times its bulk value.

With regards to the origin of the MIT in $1T$-$TaSe_2$ (see Section 7.4), the suggested Mott phase [167] has not only been found to persist in 2D [212] but is also enhanced in the monolayer limit [213]. Future investigation of the unusual orbital ordering [171–173, 213] is required to fully understand the complex phase diagrams of the Ta-based TMDs.

The next challenge will be the preparation of van der Waals heterostructures [39] in which stacks of 2D materials are organised in a particular fashion to achieve desired properties. The first step will be identifying the strength and types of interactions between layers in these devices. Thus far, significant hybridisation of the electronic structure between layers of semiconducting TMDs has already been observed [214] and recently superconductivity has been discovered in twisted bilayer graphene at the so-called *magic angle* of $\sim 1.1°$ [215, 216]. Similarly, it will be interesting to study the possible interaction between layers of different CDW-bearing TMDs. Suitable candidates could be systems with similar CDW wavevectors such as $2H$-$NbSe_2$ and $2H$-$TaS_2$ [217]. Another possibility is a combination of $1T$ and $2H$ compound layers which should lead to an inversion symmetry breaking and has previously introduced anomalies in experiments of $2H$-$TaSe_2$ [218]

for example. Finally, it is plausible to think that, given sufficient interlayer coupling, a rotation of two identical layers with strong nesting characteristics (e.g. $1\,T$-$VSe_2$) may allow an engineering of the lattice periodicity at particular angles as the size of the CDW wavevector varies. In the same way, it may be possible to induce nesting between pockets of FS in systems which do not usually normally support this behaviour (e.g. $1\,T$-$TiSe_2$).

### 8.3.3 Importance of CDWs to superconductivity

Although this thesis has not directly focused on the interplay between CDWs and superconductivity, the relationship between other correlated states [183] and forms of electronic and lattice order [79] has been investigated by utilising intense ultrashort laser pulses to suppress charge order. If CDWs are in competition with superconductivity in TMDs [10, 14, 15], then an understanding of the suppression of charge order could help in the search for high temperature superconductivity in other systems such as the cuprates [8, 9]. In TMDs, future investigation into CDW incommensurability effects and the presence of superconductivity close to domain walls may provide further insights [125, 219, 220].

# Bibliography


[1] R. E. Peierls. *Quantum Theory of Solids*. Oxford University Press, (1955).

[2] J. A. Wilson, F. J. Di Salvo, and S. Mahajan. Charge-density waves and superlattices in the metallic layered transition metal dichalcogenides. Advances in Physics, **24**, 117, (1975).

[3] R. H. Friend and D. Jérome. Periodic lattice distortions and charge density waves in one- and two-dimensional metals. Journal of Physics C: Solid State Physics **12**, 1442 (1979).

[4] M. Sato, H. Fujishita, S. Sato, and S. Hoshino. Neutron inelastic scattering and x-ray structural study of the charge density wave state in $K_{0.3}MoO_3$. Journal of Physics C: Solid State Physics **18**, 2603 (1985).

[5] J. M. Tranquada, B. J. Sternlieb, J. D. Axe, Y. Nakamura, and S. Uchida. Evidence for stripe correlations of spins and holes in copper oxide superconductors. Nature **375**, 561 (1995).

[6] P. Fazekas and E. Tosatti. Charge carrier localization in pure and doped $1\,T$-$TaS_2$. Physica B + C, **99**, 183 (1980).

[7] E. Revolinsky, E. P. Lautenschlager, and C. H. Armitage. Layer structure superconductor. Solid State Communications, **1**, 59 (1963).

[8] G. Ghiringhelli, M. Le Tacon, M. Minola, S. Blanco-Canosa, C. Mazzoli, N. B. Brookes, G. M. De Luca, A. Frano, D. G. Hawthorn, F. He, T. Loew, M. Moretti Sala, D. C. Peets, M. Salluzzo, E. Schierle, R. Sutarto, G. A. Sawatzky, E. Weschke, B. Keimer, and L. Braicovich. Long-Range Incommensurate Charge Fluctuations in (Y,Nd)$Ba_2Cu_3O_{6+x}$. Science, **337**, 821 (2012).

[9] E. H. da Silva Neto, P. Aynajian, A. Frano, R. Comin, E. Schierle, E. Weschke, A. Gyenis, J. Wen, J. Schneeloch, Z. Xu, S. Ono, G. Gu, M. Le Tacon, and A. Yazdani. Ubiquitous Interplay Between Charge Ordering and High-Temperature Superconductivity in Cuprates. Science **343**, 393 (2014).

[10] E. Morosan, H. W. Zandbergen, B. S. Dennis, J. W. G. Bos, Y. Onose, T. Klimczuk, A. P. Ramirez, N. P. Ong, and R. J. Cava. Superconductivity in $Cu_xTiSe_2$. Nature Physics, **2**, 544, (2006).

[11] M. M. Ugeda, A. J. Bradley, Y. Zhang, S. Onishi, Y. Chen, W. Ruan, C. Ojeda-Aristizabal, H. Ryu, M. T. Edmonds, H. Z. Tsai, A. Riss, S. K. Mo, D. Lee, A. Zettl, Z. Hussain, Z. X. Shen, and M. F. Crommie. Characterization of collective ground states in single-layer $NbSe_2$. Nature Physics, **12**, 92, (2016).

[12] A. M. Gabovich, A. I. Voitenko, J. F. Annett, and M. Ausloos. Charge- and spin-density-wave superconductors. Superconductor Science and Technology, **14**, R1 (2001).

[13] J. Choe C. W. Chen and E. Morosan. Charge density waves in strongly correlated electron systems. Reports on Progress in Physics **79**, 084505 (2016).

[14] L. J. Li, E. C. T. O'Farrell, K. P. Loh, G. Eda, B. Özyilmaz, and A. H. C. Neto. Controlling many-body states by the electric field-effect in a two-dimensional material. Nature **529**, 185 (2016).

[15] K. Cho, M. Kończykowski, S. Teknowijoyo, M. A. Tanatar, J. Guss, P. B. Gartin, J. M. Wilde, A. Kreyssig, R. J. McQueeney, A. I. Goldman, V. Mishra, P. J. Hirschfeld, and R. Prozorov. Using controlled disorder to probe the interplay between charge order and superconductivity in $NbSe_2$. Nature Communications, **9**, 2796 (2018).

[16] J. A. Wilson and A. D. Yoffe. The transition metal dichalcogenides: Discussion and interpretation of the observed optical, electrical and structural properties. Advances in Physics, **18**, 193 (1969).

[17] R. F. Frindt. Superconductivity in ultrathin $NbSe_2$ layers. Physical Review Letters, **28**, 299 (1972).

[18] K. S. Novoselov, A. K. Geim, S. V. Morozov, D. Jiang, Y. Zhang, S. V. Dubonos, I. V. Grigorieva, and A. A. Firsov. Electric Field Effect in Atomically Thin Carbon Films. Science, **306**, 666 (2004).

[19] K. F. Mak, C. Lee, J. Hone, J. Shan, and T. F. Heinz. Atomically thin $MoS_2$: a new direct-gap semiconductor. Physical Review Letters, **105**, 136805, (2010).

[20] K. Rossnagel. On the origin of charge-density waves in select layered transition-metal dichalcogenides. Journal of Physics: Condensed Matter, **23**, 213001, (2011).

[21] P. Aebi, Th. Pillo, H. Berger, and F. Levy. On the search for Fermi surface nesting in quasi-2D materials. Journal of Electron Spectroscopy and Related Phenomena, **117**, 433 (2001).

[22] M. D. Johannes and I. I. Mazin. Fermi surface nesting and the origin of charge density waves in metals. Physical Review B **77**, 165135 (2008).

[23] X. Zhu, J. Guo, J. Zhang, and E. W. Plummer. Misconceptions associated with the origin of charge density waves. Advances in Physics: X **2**, 622 (2017).

[24] M. C. M. O'Brien and C. C. Chancey. The Jahn-Teller effect: An introduction and current review. American Journal of Physics, **61**, 688 (1993).

[25] Y. Ge and A. Y. Liu. First-principles investigation of the charge-density-wave instability in 1$T$-$TaSe_2$. Physical Review B **82**, 155133 (2010).

[26] F. Weber, S. Rosenkranz, J. P. Castellan, R. Osborn, G. Karapetrov, R. Hott, R. Heid, K. P. Bohnen, and A. Alatas. Electron-phonon coupling and the soft phonon mode in $TiSe_2$. Physical Review Letters, **107**, 266401, (2011).

[27] A. Kogar, M. S. Rak, S. Vig, A. A. Husain, F. Flicker, Y. I. Joe, L. Venema, G. J. MacDougall, T. C. Chiang, E. Fradkin, J. van Wezel, and P. Abbamonte. Signatures of exciton condensation in a transition metal dichalcogenide. Science **358**, 1314 (2017).

[28] D. Jérome, T. M. Rice, and W. Kohn. Excitonic insulator. Physical Review, **158**, 462 (1967).

[29] G. Grüner. The dynamics of charge-density waves. Reviews of Modern Physics, **60**, 1129, (1988).

[30] C. Kittel. *Introduction to solid state physics*. Wiley, (2005).

[31] J. Singleton. *Band theory and electronic properties of solids*. Oxford University Press, (2001).

[32] G. Grüner. *Density Waves in Solids*. Perseus Publishing, (1994).

[33] S. B. Dugdale. Life on the edge: A beginner's guide to the Fermi surface. Physica Scripta **91**, 053009 (2016).

[34] W. Kohn. Image of the Fermi Surface in the Vibration Spectrum of a Metal. Physical Review Letters **2**, 393 (1959).

[35] A. K. Geim and K. S. Novoselov. The rise of graphene. Nature Materials, **6**, 183, (2007).

[36] R. Lv, J. A. Robinson, R. E. Schaak, D. Sun, Y. Sun, T. E. Mallouk, and M. Terrones. Transition Metal Dichalcogenides and Beyond: Synthesis, Properties, and Applications of Single- and Few-Layer Nanosheets. Accounts of Chemical Research, **48**, 56, (2015).

[37] Y. Lin, D. Dumcenco, Y. Huang, and K. Suenaga. Atomic mechanism of the semiconducting-to-metallic phase transition in single-layered $MoS_2$. Nature Nanotechnology, **9**, 391 (2014).

[38] G. Fiori, F. Bonaccorso, G. Iannaccone, T. Palacios, D. Neumaier, A. Seabaugh, S. K. Banerjee, and L. Colombo. Electronics based on two-dimensional materials. Nature Nanotechnology, **9**, 768, (2014).

[39] A. K. Geim and I. V. Grigorieva. Van der Waals heterostructures. Nature, **499**, 419 (2013).

[40] H. Katzke, P. Tolédano, and W. Depmeier. Phase transitions between polytypes and intralayer superstructures in transition metal dichalcogenides. Physical Review B **69**, 134111 (2004).

[41] A. V. Kolobov and J. Tominaga. *Two-Dimensional Transition-Metal Dichalcogenides*. Springer, (2016).

[42] F. J. Di Salvo, D. E. Moncton, and J. V. Waszczak. Electronic properties and superlattice formation in the semimetal $TiSe_2$. Physical Review B, **14**, 4321 (1976).

[43] J. R. Long, S. P. Bowen, and N. E. Lewis. Anomalous resistivity of ioine-free 2H-$NbSe_2$. Solid State Communications **22**, 363 (1977).

[44] C. F. van Bruggen and C. Haas. Magnetic susceptibility and electrical properties of $VSe_2$ single crystals. Solid State Communications **20**, 251 (1976).

[45] A. H. Thompson and B. G. Silbernagel. Correlated magnetic and transport properties in the charge-density-wave states of $VSe_2$. Physical Review B, **19**, 3420 (1979).

[46] D. E. Moncton, J. D. Axe, and F. J. DiSalvo. Study of superlattice formation in $2H$-$NbSe_2$ and $2H$-$TaSe_2$ by neutron scattering. Physical Review Letters, **34**, 734 (1975).

[47] J. A. Wilson. Questions concerning the form taken by the charge-density wave and the accompanying periodic-structural distortions in $2H$-$TaSe_2$ and closely related materials. Physical Review B, **17**, 3880 (1978).

[48] K. Tsutsumi. X-ray-diffraction study of the periodic lattice distortion associated with a charge-density wave in $1T$-$VSe_2$. Physical Review B, **26** 5756 (1982).

[49] F. J. Di Salvo, R. G. Maines, J. V. Waszczak, and R. E. Schwall. Preparation and properties of $1T$-$TaSe_2$. Solid State Communications, **14**, 497 (1974).

[50] A. M. Woolley and G. Wexler. Band structures and Fermi surfaces for $1T$-$TaS_2$, $1T$-$TaSe_2$ and $1T$-$VSe_2$. Journal of Physics C: Solid State Physics **10**, 2601 (1977).

[51] V. Grasso. *Electronic structure and electronic transitions in layered materials*. Reidel, (1986).

[52] K. Motizuki. *Structural phase transitions in layered transition metal compounds*. Reidel, (1986).

[53] M. Bovet, D. Popović, D. F. Clerc, C. Koitzsch, U. Probst, E. Bucher, H. Berger, D Naumović, and P. Aebi. Pseudogapped Fermi surfaces of $1T$-$TaS_2$ and $1T$-$TaSe_2$: A charge density wave effect. Physical Review B, **69**, 125117 (2004).

[54] G. Lucovsky, R. M. White, J. A. Benda, and J. F. Revelli. Infrared-Reflectance Spectra of Layered Group-IV and Group-VI Transition-Metal Dichalcogenides. Physical Review B **7**, 3859 (1973).

[55] J. A. Holy, K. C. Woo, M. V. Klein, and F. C. Brown. Raman and infrared studies of superlattice formation in $TiSe_2$. Physical Review B, **16**, 3628 (1977).

[56] H. Hertz. Über einen Einfluß des ultravioletten Lichtes auf die electrische Entladung. Annalen der Physik, **267**, 938 (1887).

[57] A. Einstein. Über einen die Erzeugung und Verwandlung des Lichtes betreffenden heuristischen Gesichtspunkt. Annalen der Physik, **322**, 132 (1905).

[58] S. Hüfner. *Photoelectron Spectroscopy: Principles and Applications*. Springer-Verlag, (1995).

[59] C. N. Berglund and W. E. Spicer. Photoemission Studies of Copper and Silver: Theory. Physical Review **136**, A1030 (1964).

[60] A. Damascelli. Probing the Electronic Structure of Complex Systems by ARPES. Physica Scripta, **109**, 61 (2004).

[61] G. D. Mahan. Theory of Photoemission in Simple Metals. Physical Review B **2**, 4334 (1970).

[62] C. Tusche, Y. J. Chen, C. M. Schneider, and J. Kirschner. Imaging properties of hemispherical electrostatic energy analyzers for high resolution momentum microscopy. Ultramicroscopy **206**, 112815 (2019).

[63] D. O'Connor, B. A. Sexton, and R. St. C. Smart. *Surface Analysis Methods in Materials Science*. Springer, (2003).

[64] E. Carpene, E. Mancini, C. Dallera, G. Ghiringhelli, C. Manzoni, G. Cerullo, and S. De Silvestri. A versatile apparatus for time-resolved photoemission spectroscopy via femtosecond pump-probe experiments. Review of Scientific Instruments, **80**, 055101 (2009).

[65] M. Cattelan and N. Fox. A Perspective on the Application of Spatially Resolved ARPES for 2D Materials. Nanomaterials, **8**, 284 (2018).

[66] M. Escher, N. Weber, M. Merkel, C. Ziethen, P. Bernhard, G. Schönhense, S. Schmidt, F. Forster, F. Reinert, B. Krömker, and D. Funnemann. NanoESCA: A novel energy filter for imaging x-ray photoemission spectroscopy. Journal of Physics: Condensed Matter **17**, S1329 (2005).

[67] M. P. Seah and W. A. Dench. Quantitative electron spectroscopy of surfaces: A standard data base for electron inelastic mean free paths in solids. Surface and Interface Analysis **1**, 2 (1979).

[68] S. Nannarone, F. Borgatti, A. DeLuisa, B. P. Doyle, G. C. Gazzadi, A. Giglia, P. Finetti, N. Mahne, L. Pasquali, M. Pedio, G. Selvaggi, G. Naletto, M. G. Pelizzo, and S. Tondello. The BEAR Beamline at Elettra. AIP Conference Proceedings, **705**, 450 (2004).

[69] L. Pasquali, A. De Luisa, and S. Nannarone. The UHV Experimental Chamber For Optical Measurements (Reflectivity and Absorption) and Angle Resolved Photoemission of the BEAR Beamline at Elettra. AIP Conference Proceedings, **705**, 1142 (2004).

[70] D. C. Koningsberger and R. Prins. *X-Ray Absorption: Principles, Applications, Techniques of EXAFS, SEXAFS and XANES*. Wiley & Sons, (1988).

[71] J. Als-Nielsen and D. McMorrow. *Elements of Modern X-ray Physics*. Wiley & Sons, (2011).

[72] J. Stöhr. *NEXAFS Spectroscopy*. Springer, (1992).

[73] F. Boschini, H. Hedayat, C. Dallera, P. Farinello, C. Manzoni, A. Magrez, H. Berger, G. Cerullo, and E. Carpene. An innovative Yb-based ultrafast deep ultraviolet source for time-resolved photoemission experiments. Review of Scientific Instruments, **85**, 123903 (2014).

[74] S. Passlack, S. Mathias, O. Andreyev, D. Mittnacht, M. Aeschlimann, and M. Bauer. Space charge effects in photoemission with a low repetition, high intensity femtosecond laser source. Journal of Applied Physics **100**, 024912 (2006).

[75] A. Verna, G. Greco, V. Lollobrigida, F. Offi, and G. Stefani. Space-charge effects in high-energy photoemission. Journal of Electron Spectroscopy and Related Phenomena **209**, 14 (2016).

[76] L. C. Smallwood, C. Jozwiak, W. Zhang, and A. Lanzara. An ultrafast angle-resolved photoemission apparatus for measuring complex materials. Review of Scientific Instruments, **83** 123904 (2012).

[77] J. Faure, J. Mauchain, E. Papalazarou, W. Yan, J. Pinon, M. Marsi, and L. Perfetti. Full characterization and optimization of a femtosecond ultraviolet laser source for time and angle-resolved photoemission on solid surfaces. Review of Scientific Instruments, **83**, 043109 (2012).

[78] C. Giannetti, M. Capone, D. Fausti, M. Fabrizio, F. Parmigiani, and D. Mihailovic. Ultrafast optical spectroscopy of strongly correlated materials and high-temperature superconductors: A non-equilibrium approach. Advances in Physics **65**, 58 (2016).

[79] H. Hedayat, C. J. Sayers, D. Bugini, C. Dallera, D. Wolverson, T. Batten, S. Karbassi, S. Friedemann, G. Cerullo, J. van Wezel, S. R. Clark, E. Carpene, and E. Da Como. Excitonic and lattice contributions to the charge density wave in $1T$-$TiSe_2$ revealed by a phonon bottleneck. Physical Review Research, **1**, 023029 (2019).

[80] Y. Suzaki and A. Tachibana. Measurement of the $\mu$m sized radius of Gaussian laser beam using the scanning knife-edge. Applied Optics **14**, 2809 (1975).

[81] C. V. Raman. A new radiation. Indian Journal of Physics **2**, 387 (1928).

[82] C. Lamberti. *Characterization of Semiconductor Heterostructures and Nanostructures*. Elsevier Science, (2008).

[83] M. Fox. *Optical properties of solids*. Oxford University Press, (2001).

[84] D. B. Lioi, D. J. Gosztola, G. P. Wiederrecht, and G. Karapetrov. Photon-induced selenium migration in $TiSe_2$. Applied Physics Letters **110**, 081901 (2017).

[85] 2D semiconductors. https://www.2dsemiconductors.com.

[86] HQ graphene. http://www.hqgraphene.com.

[87] F. J. Di Salvo and J. V. Waszczak. Magnetic studies of $VSe_2$. Physical Review B, **23**, 457 (1981).

[88] H. P. B. Rimmington and A. A. Balchin. The growth by iodine vapour transport techniques and the crystal structures of layer compounds in the series $TiS_xSe_{2-x}$ , $TiS_xTe_{2-x}$, $TiSe_xTe_{2-x}$. Journal of Crystal Growth, **21**, 171, (1974).

[89] F. Levy and Y. Froidevaux. Structural and electrical properties of layered transition metal selenides $V_xTi_{1-x}Se_2$ and $Ta_xTi_{1-x}Se_2$. Journal of Physiscs C: Solid State Physics **12**, 473 (1979).

[90] F. J. Di Salvo and J. V. Waszczak. Transport properties and the phase transition in $Ti_{1-x}M_xSe_2$ ($M$ = Ta or V). Physical Review B, **17**, 3801 (1978).

[91] F. J. Di Salvo, J. A. Wilson, B. G. Bagley, and J. V. Waszczak. Effects of doping on charge-density waves in layer compounds. Physical Review B, **12**, 2220 (1975).

[92] H. Schafer. Chemische Transportreaktionen. VCH Weinheim (1962).

[93] R. M. A. Lieth. *Preparation and crystal growth of materials with layered structures.* D. Reidel, (1977).

[94] F. Levy. *Crystallography and crystal chemistry of materials with layered structures.* D. Reidel, (1976).

[95] A. Ubaldini and E. Giannini. Improved chemical vapor transport growth of transition metal dichalcogenides. Journal of Crystal Growth, **401**, 878, (2014).

[96] R. Samnakay, D. Wickramaratne, T. R. Pope, R. K. Lake, T. T. Salguero, and A. A. Balandin. Zone-Folded Phonons and the Commensurate–Incommensurate Charge-Density-Wave Transition in 1$T$-$TaSe_2$ Thin Films. Nano Letters, **15**, 2965, (2015).

[97] G. Leicht, H. Berger, and F. Levy. The growth of $n$- and $p$-type $ReS_2$ and $ReSe_2$ single crystals and their electrical properties. Solid State Communications **61**, 531 (1987).

[98] E. Giannini. *Private Communication* (2016).

[99] V. N. Strocov, M. Shi, M. Kobayashi, C. Monney, X. Wang, J. Krempasky, T. Schmitt, L. Patthey, H. Berger, and P. Blaha. Three-Dimensional Electron Realm in $VSe_2$ by Soft-X-Ray Photoelectron Spectroscopy: Origin of Charge-Density Waves. Physical Review Letters, **109**, 086401 (2012).

[100] A. J. H. Jones, C. J. Sayers, M. Cattelan, L. S. Farrar, S. J. Bending, N. A. Fox, E. Da Como, and J. Laverock. Charge Density Wave Gap in 1 $T$-$VSe_2$: Momentum and Temperature Dependence. *In preparation* (2020).

[101] W. Jolie, T. Knispel, N. Ehlen, K. Nikonov, C. Busse, A. Grüneis, and T. Michely. Charge density wave phase of $VSe_2$ revisited. Physical Review B, **99** 115417 (2019).

[102] J. Feng, D. Biswas, A. Rajan, M. D. Watson, F. Mazzola, O. J. Clark, K. Underwood, I. Marković, M. McLaren, A. Hunter, D. M. Burn, L. B. Duffy, S. Barua, G. Balakrishnan, F Bertran, P. Le Fèvre, T. K. Kim, G. van der Laan, T. Hesjedal, P. Wahl, and P. D. C. King. Electronic Structure and Enhanced Charge-Density Wave Order of Monolayer $VSe_2$. Nano Letters, **18**, 4493 (2018).

[103] P. Chen, W. W. Pai, Y. H. Chan, V. Madhavan, M. Y. Chou, S. K. Mo, A. V. Federov, and T. C. Chiang. Unique Gap Structure and Symmetry of the Charge Density Wave in Single-Layer $VSe_2$. Physical Review Letters, **121**, 196402 (2018).

[104] Y. Ma, Y. Dai, M. Guo, C. Niu, Y. Zhu, and B. Huang. Evidence of the Existence of Magnetism in Pristine $VX_2$ Monolayers (X = S, Se) and Their Strain-Induced Tunable Magnetic Properties. ACS Nano, **6**, 1695 (2012).

[105] M. Bonilla, S. Kolekar, Y. Ma, H. C. Diaz, V. Kalappattil, R. Das, T. Eggers, H. R. Gutierrez, M. H. Phan, and M. Batzill. Strong room-temperature ferromagnetism in $VSe_2$ monolayers on van der Waals substrates. Nature Nanotechnology, **13**, 289 (2018).

[106] Z. L. Liu, X. Wu, Y. Shao, J. Qi, Y. Cao, L. Huang, C. Liu, J. O. Wang, Q. Zheng, Z. L. Zhu, K. Ibrahim, Y. L. Wang, and H. J. Gao. Epitaxially grown monolayer $VSe_2$: an air-stable magnetic two-dimensional material with low work function at edges. Science Bulletin **63**, 419 (2018).

[107] D. J. Eaglesham, R. L. Withers, and D. M. Bird. Charge-density-wave transitions in 1T-$VSe_2$. Journal of Physics C: Solid State Physics, **19** 359 (1986).

[108] S. Barua, M. C. Hatnean, M. R. Lees, and G. Balakrishnan. Signatures of the Kondo effect in $VSe_2$. Scientific Reports, **7**, 10964 (2017).

[109] M Bayard and M. J. Sienko. Anomalous electrical and magnetic properties of vanadium diselenide. Journal of Solid State Chemistry, **19**, 325 (1976).

[110] A. Toriumi and S. Tanaka. Galvanomagnetic properties of 1T-$VSe_2$. Physica B + C, **105**, 141 (1981).

[111] C. S. Yadav and A. K. Rastogi. Electronic transport and specfiic heat of 1T-$VSe_2$. Solid State Communications, **150**, 648 (2010).

[112] K. Hayashi and M. Nakahira. Stability and the equilibrium selenium vapor pressure of the $VSe_2$ phase. Journal of Solid State Chemistry **24**, 153 (1978).

[113] J.-P. Peng, J.-Q. Guan, H.-M. Zhang, C.-L. Song, L. Wang, K. He, Q.-K. Xue, and X.-C. Ma. Molecular beam epitaxy growth and scanning tunneling microscopy study of $TiSe_2$ ultrathin films. Physical Review B **91**, 121113(R) (2015).

[114] B. Hildebrand, C. Didiot, A. M. Novello, G. Monney, A. Scarfato, A. Ubaldini, H. Berger, D. R. Bowler, C. Renner, and P. Aebi. Doping nature of native defects in 1$T$-$TiSe_2$. Physical Review Letters **112**, 197001 (2014).

[115] S. H. Huang, G. J. Shu, W. W. Pai, H. L. Liu, and F. C. Chou. Tunable Se vacancy defects and the unconventional charge density wave in 1$T$-$TiSe_{2-\delta}$. Physical Review B **95**, 045310 (2017).

[116] C. J. Sayers, L. S. Farrar, S. J. Bending, M. Cattelan, , A. J. H. Jones, N. A. Fox, G. Kociok-Köhn, K. Koshmak, J. Laverock, L. Pasquali, and E. Da Como. Correlation between crystal purity and the charge density wave in 1$T$-$VSe_2$. Physical Review Materials (2020).

[117] J. F. Moulder, W. F. Stickle, P. E. Sobol, and K. D. Bomben. *Handbook of X-ray Photoelectron Spectroscopy*. Perkin-Elmer Corporation, (1992).

[118] J. J. Yeh and I. Lindau. Atomic subshell and photoionization cross sections and asymmetry parameters $1 \leq Z \geq 103$. Atomic Data and Nuclear Data Tables **32**, 1 (1985).

[119] P Knowles, B. Yang, T. Muramatsu, O. Moulding, J. Buhot, C. Sayers, E. Da Como, and S. Friedemann. Fermi surface reconstruction and electron dynamics at the charge-density-wave transition in $TiSe_2$. arXiv:1911.01945 (2019).

[120] T. Sato, K. Terashima, S. Souma, H. Matsui, T. Takahashi, H. Yang, S. Wang, H. Ding, N. Maeda, and K. Hayashi. Three-Dimensional Fermi-Surface Nesting in

1T-$VSe_2$ Studied by Angle-Resolved Photoemission Spectroscopy. Journal of the Physical Society of Japan, **73**, 3331 (2004).

[121] K. Terashima, T. Sato, H. Komatsu, T. Takahashi, N. Maeda, and K. Hayashi. Charge-density wave transition of $1T$-$VSe_2$ studied by angle-resolved photoemission spectroscopy. Physical Review B **68**, 155108 (2003).

[122] J. Laverock, D. Newby Jr., E. Abreu, R. Averitt, K. E. Smith, R. P. Singh, G. Balakrishnan, J. Adell, and T. Balasubramanian. **k**-resolved susceptibility function of $2H$-$TaSe_2$ from angle-resolved photoemission. Physical Review B **88**, 035108 (2013).

[123] R. A. Craven, F. J. Di Salvo, and F. S. L. Hsu. Mechanisms for the 200 K transition in $TiSe_2$: A measurement of the specific heat. Solid State Communications, **25** 39 (1978).

[124] A.F. Kusmartseva, B. Sipos, H. Berger, L. Forro, and E. Tutis. Pressure Induced Superconductivity in Pristine $1T$-$TiSe_2$. Physical Review Letters **103**, 236401 (2009).

[125] A. Kogar, G. A. de la Pena, S. Lee, Y. Fang, S. X. L. Sun, D. B. Lioi, G. Karapetrov, K. D. Finkelstein, J. P. C. Ruff, P. Abbamonte, and S. Rosenkranz. Observation of a Charge Density Wave Incommensuration Near the Superconducting Dome in $Cu_xTiSe_2$. Physical Review Letters **118**, 027002 (2017).

[126] J. Ishioka, Y. H. Liu, K. Shimatake, T. Kurosawa, K. Ichimura, Y. Toda, M. Oda, and S. Tanda. Chiral charge-density waves. Physical Review Letters, **105**, 176401, (2010).

[127] J. van Wezel. The chiral charge density wave transition in 1T-$TiSe_2$. Journal of Physics: Conference Series, **391**, 012167 (2012).

[128] J. P. Castellan, S. Rosenkranz, R. Osborn, Q. Li, K. E. Gray, X. Luo, U. Welp, G. Karapetrov, J. P. C. Ruff, and J. van Wezel. Chiral phase transition in charge ordered $1T$-$TiSe_2$. Physical Review Letters, **110**, 196404, (2013).

[129] M. Gradhand and J. van Wezel. Optical gyrotropy and the nonlocal Hall effect in chiral charge-ordered $TiSe_2$. Physical Review B, **92** 041111(R) (2015).

[130] H. P. Hughes. Structural distortion in $TiSe_2$ and related materials - a possible Jahn-Teller effect? Journal of Physics C: Solid State Physics, **10**, L319 (1977).

[131] J. van Wezel, P. Nahai-Williamson, and S. S. Saxena. Exciton-phonon-driven charge density wave in $TiSe_2$. Physical Review B, **81** 165109 (2010).

[132] M. Porer, U. Leierseder, J.-M. Ménard, H. Dachraoui, L. Mouchliadis, I. E. Perakis, U. Heinzmann, J. Demsar, K. Rossnagel, and R. Huber. Non-thermal separation of electronic and structural orders in a persisting charge density wave. Nature materials, **13**, 857, (2014).

[133] C. Monney, M. Puppin, C. W. Nicholson, M. Hoesch, R. T. Chapman, E. Springate, H. Berger, A. Magrez, C. Cacho, R. Ernstorfer, and M. Wolf. Revealing the role of electrons and phonons in the ultrafast recovery of charge density wave correlations in 1$T$-$TiSe_2$. Physical Review B, **94**, 165165 (2016).

[134] T. Kaneko, Y. Ohta, and S. Yunoki. Exciton-phonon cooperative mechanism of the triple-$q$ charge-density-wave and antiferroelectric electron polarization in $TiSe_2$. Physical Review B **97**, 155131 (2018).

[135] M. D. Watson, O. J. Clark, F. Mazzola, I. Marković, V. Sunko, T. K. Kim, K. Rossnagel, and P. D. C. King. Orbital- and kz-Selective Hybridization of Se 4$p$ and Ti 3$d$ States in the Charge Density Wave Phase of $TiSe_2$. Physical Review Letters **122**, 076404 (2019).

[136] E. Möhr-Vorobeva, S. L. Johnson, P. Beaud, U. Staub, R. De Souza, C. Milne, G. Ingold, J. Demsar, H. Schaefer, and A. Titov. Nonthermal melting of a charge density wave in $TiSe_2$. Physical Review Letters, **107**, 036403,(2011).

[137] T. Rohwer, S. Hellmann, M. Wiesenmayer, C. Sohrt, A. Stange, B. Slomski, A. Carr, Y. Liu, L. M. Avila, M. Kalläne, S. Mathias, L. Kipp, K. Rossnagel, and M. Bauer. Collapse of long-range charge order tracked by time-resolved photoemission at high momenta. Nature, **471** 490 (2011).

[138] G. Rohde, T. Rohwer, C. Sohrt, A. Stange, S. Hellmann, L. X. Yang, K. Hanff, A. Carr, M. M. Murnane, H. Kapteyn, L. Kipp, K. Rossnagel, and M. Bauer. Tracking the relaxation pathway of photoexcited electrons in 1$T$-$TiSe_2$. The European Physical Journal Special Topics **222**, 997 (2013).

[139] S. Mathias, S. Eich, J. Urbancic, S. Michael, A. V. Carr, S. Emmerich, A. Stange, T. Popmintchev, T. Rohwer, M. Wiesenmayer, A. Ruffing, S. Jakobs, S. Hellmann,

P. Matyba, C. Chen, L. Kipp, M. Bauer, H. C. Kapteyn, H. C. Schneider, K. Rossnagel, M. M. Murnane, and M. Aeschlimann. Self-amplified photo-induced gap quenching in a correlated electron material. Nature Communications, **7**, 12902 (2016).

[140] S. Hellmann, T. Rohwer, M. Kalläne, K. Hanff, C. Sohrt, A. Stange, A. Carr, M.M. Murnane, H.C. Kapteyn, L. Kipp, M. Bauer, and K. Rossnagel. Time-domain classification of charge-density-wave insulators. Nature Communications, **3**, 1069 (2012).

[141] A. Rothwarf and B. N. Taylor. Measurement of Recombination Lifetimes in Superconductors. Physical Review Letters **19**, 27 (1967).

[142] T. E. Kidd, T. Miller, M. Y. Chou, and T. C. Chiang. Electron-Hole Coupling and the Charge Density Wave Transition in $TiSe_2$. Physical Review Letters, **88**, 226402 (2002).

[143] G. Monney, C. Monney, B. Hildebrand, P. Aebi, and H. Beck. Impact of Electron-Hole Correlations on the $1T$-$TiSe_2$ Electronic Structure. Physical Review Letters, **114**, 086402,(2015).

[144] G. Li, W. Z. Hu, D. Qian, D. Hsieh, M. Z. Hasan, E. Morosan, R. J. Cava, and N. L. Wang. Semimetal-to-Semimetal Charge Density Wave Transition in $1T$-$TiSe_2$. Physical Review Letters, **99**, 027404, (2007).

[145] A. Zunger and A. J. Freeman. Band structure and lattice instability of $TiSe_2$. Physical Review B, **17** 1839 (1978).

[146] H. Cercellier, C. Monney, F. Clerc, C. Battaglia, L. Despont, M. G. Garnier, H. Beck, P. Aebi, L. Patthey, H. Berger, and L. Forró. Evidence for an excitonic insulator phase in $1T$-$TiSe_2$. Physical Review Letters, **99**, 146403 (2007).

[147] C. Monney, E. F. Schwier, M. G. Garnier, N. Mariotti, C. Didiot, H. Cercellier, J. Marcus, H. Berger, A. N. Titov, H. Beck, and P. Aebi. Probing the exciton condensate phase in $1T$-$TiSe_2$ with photoemission. New Journal of Physics, **12**, 125019, (2010).

[148] C. Monney, C. Battaglia, H. Cercellier, P. Aebi, and H. Beck. Exciton Condensation Driving the Periodic Lattice Distortion of $1T$-$TiSe_2$. Physical Review Letters, **106**, 106404, (2011).

[149] C. Monney, H. Cercellier, F. Clerc, C. Battaglia, E. F. Schwier, C. Didiot, M. G. Garnier, H. Beck, P. Aebi, H. Berger, L. Forró, and L. Patthey. Spontaneous exciton condensation in 1T-$TiSe_2$: BCS-like approach. Physical Review B, **79**, 045116,(2009).

[150] K. Rossnagel, L. Kipp, and M. Skibowski. Charge-density wave phase transition in 1$T$-TiSe2: Excitonic insulator versus band-type Jahn-Teller mechanism. Physical Review B **65**, 235101 (2002).

[151] T. Pillo, J. Hayoz, H. Berger, F. Levy, L. Schlapbach, and P. Aebi. Photoemission of bands above the Fermi level: The excitonic insulator phase transition in 1$T$-$TiSe_2$. Physical Review B **61**, 16213 (2000).

[152] P. Chen, Y. H. Chan, X. Y. Fang, S. K. Mo, Z. Hussain, A. V. Fedorov, M. Y. Chou, and T. C. Chiang. Hidden Order and Dimensional Crossover of the Charge Density Waves in $TiSe_2$. Scientific Reports, **6**, 37910, (2016).

[153] M. Cazzaniga, H. Cercellier, M. Holzmann, C. Monney, P. Aebi, G. Onida, and V. Olevano. *Ab initio* many-body effects in $TiSe_2$: A possible excitonic insulator scenario from GW band-shape renormalization. Physical Review B, **85**, 195111 (2012).

[154] S. Sugai, K. Murase, S. Uchida, and S. Tanaka. Raman studies of lattice dynamics in 1$T$-$TiSe_2$. Solid State Communications, **88**, 433 (1980).

[155] G. P. Segre, N. Gedik, J. Orenstein, D. A. Bonn, R. Liang, and W. N. Hardy. Photoinduced Changes of Reflectivity in Single Crystals of $YBa_2Cu_3O_{6.5}$ (Ortho II). Physical Review Letters, **88**, 137001 (2002).

[156] B. Giambattista, C. G. Slough, W. W. McNairy, and R. V. Coleman. Scanning tunneling microscopy of atoms and charge-density waves in 1$T$-$TaS_2$, 1$T$-$TaSe_2$ and 1$T$-$VSe_2$. Physical Review B, **41** 10082 (1990).

[157] M. Calandra, I. I. Mazin, and F. Mauri. Effect of dimensionality on the charge-density wave in few-layer 2$H$-$NbSe_2$. Physical Review B **80**, 241108(R) (2009).

[158] J. Yang, W. Wang, Y. Liu, H. Du, W. Ning, G. Zheng, C. Jin, Y. Han, N. Wang, Z. Yang, M. Tian, and Y. Zhang. Thickness dependence of the charge-density-wave transition temperature in $VSe_2$. Applied Physics Letters, **105**, 063109 (2014).

[159] A. Pásztor, A. Scarfato, C. Barreteau, E. Giannini, and C. Renner. Dimensional crossover of the charge density wave transition in thin exfoliated $VSe_2$. 2D Materials, **4**, 041005 (2017).

[160] R. H. Friend, D. Jérome, D. M. Schleich, and P. Molinié. Pressure enhancement of charge density wave formation in $VSe_2$; The role of coulomb correlations. Solid State Communications **27**, 169 (1978).

[161] M. Yoshida, Y. Zhang, J. Ye, R. Suzuki, Y. Imai, S. Kimura, A. Fujiwara, and Y. Iwasa. Controlling charge-density-wave states in nano-thick crystals of $1\,T$-$TaS_2$. Scientific Reports **4**, 7302 (2014).

[162] M. Yoshida, R. Suzuki, Y. Zhang, M. Nakano, and Y. Iwasa. Memresistive phase switching in two-dimensional in $1\,T$-$TaS_2$ crystals. Science Advances **1**, e1500606 (2015).

[163] S. Sugai, M. Murase, S. Uchida, and S. Tanaka. Investigation of the charge densit waves in $1\,T$-$VSe_2$ by Raman scattering. Journal de Physique Colloques, **42**, C6 (1981).

[164] S. Sugai. Lattice Vibrations in the Charge-Density-Wave States of Layered Transition Metal Dichalcogenides. Physica Status Solidi B, **129**, 13 (1985).

[165] S. Uchida and S. Sugai. Infrared and Raman studies on commensurate CDW states in transition metal dichalcogenides. Physica B+C, **105** 393 (1981).

[166] A. Soumyanarayanan, M. M. Yee, Y. He, J. van Wezel, D. J. Rahn, K. Rossnagel, E. W. Hudson, M. R. Norman, and J. E. Hoffman. Quantum phase transition from triangular to stripe charge order in $NbSe_2$. Proceedings of the National Academy of Sciences of the United States of America **110**, 1623 (2013).

[167] L. Perfetti, A. Georges, S. Florens, S. Biermann, S. Mitrovic, H. Berger, Y. Tomm, H. Höchst, and M. Grioni. Spectroscopic Signatures of a Bandwidth-Controlled Mott Transition at the Surface of $1\,T$-$TaSe_2$. Physical Review Letters, **90**, 166401 (2003).

[168] S. Colonna, F. Ronci, A. Cricenti, L. Perfetti, H. Berger, and M. Grioni. Mott Phase at the Surface of $1\,T$-$TaSe_2$ Observed by Scanning Tunneling Microscopy. Physical Review Letters **94**, 036405 (2005).

[169] J. A. Wilson, F. J. Di Salvo, and S. Mahajan. Charge-Density Waves in Metallic, Layered, Transition-Metal Dichalcogenides. Physical Review Letters, **32**, 882 (1974).

[170] S. Colonna, F. Ronci, A. Cricenti, L. Perfetti, H. Berger, and M. Grioni. Scanning Tunneling Microscopy Observation of a Mott-Insulator Phase at the 1 $T$-$TaSe_2$ Surface. Japanese Journal of Applied Physics **45**, 1950 (2006).

[171] T. Ritschel, J. Trinckauf, K. Koepernika, B. Büchner, M. v. Zimmermann, H. Berger, Y. I. Joe, P. Abbamonte, and J. Geck. Orbital textures and charge density waves intransition metal dichalcogenides. Nature Physics **11**, 328 (2015).

[172] T. Ritschel, H. Berger, and J. Geck. Stacking-driven gap formation in layered 1 $T$-$S_2$. Physical Review B **98**, 195134 (2018).

[173] S.-H Lee, J. S. Goha, and D. Cho. Origin of the Insulating Phase and First-Order Metal-Insulator Transition in 1 $T$-$TaS_2$. Physical Review Letters **122**, 106404 (2019).

[174] C. Sohrt, A. Stange, M. Bauer, and K. Rossnagel. How fast can a Peierls-Mott insulator be melted? Faraday Discussions, **171**, 243 (2014).

[175] L. Perfetti, P. A. Loukakos, M. Lisowski, U. Bovensiepen, H. Berger, S. Biermann, P. S. Cornaglia, A. Georges, and M. Wolf. Time Evolution of the Electronic Structure of 1 $T$-$TaS_2$ through the Insulator-Metal Transition. Physical Review Letters, **97**, 067402 (2006).

[176] L. Perfetti, P. A. Loukakos, M. Lisowski, U. Bovensiepen, M. Wolf, H. Berger, S. Biermann, and A. Georges. Femtosecond dynamics of electronic states in the Mott insulator 1T-$TaS_2$ by time resolved photoelectron spectroscopy. New Journal of Physics, **10**, 053019 (2008).

[177] J. C. Petersen, S. Kaiser, N. Dean, A. Simoncig, H. Y. Liu, A. L. Cavalieri, C. Cacho, I. C. E. Turcu, E. Springate, F. Frassetto, L. Poletto, S. S. Dhesi, H. Berger, and A. Cavalleri. Clocking the Melting Transition of Charge and Lattice Order in 1 $T$-$TaS_2$ with Ultrafast Extreme-Ultraviolet Angle-Resolved Photoemission Spectroscopy. Physical Review Letters, **107**, 177402 (2011).

[178] M. Eichberger, H. Schäfer, M. Krumova, M. Beyer, J. Demsar, H. Berger, G. Moriena, G. Sciaini, and R. J. D. Miller. Snapshots of cooperative atomic motions in the optical suppression of charge density waves. Nature, **468**, 799 (2010).

[179] L. Stojchevska, I. Vaskivskyi, T. Mertelj, P. Kusar, D. Svetin, S. Brazovskii, and D. Mihailovic. Ultrafast switching to a stable hidden quantum state in an electronic crystal, Science, **344**, 177 (2014).

[180] I. Avigo, P. Zhou, M. Kalläne, K. Rossnagel, U. Bovensiepen, and M. Ligges. Excitation and Relaxation Dynamics of the Photo-Perturbed Correlated Electron System 1$T$-$TaS_2$. Applied Sciences **9**, 44 (2019).

[181] F. Boschini, E. H. da Silva Neto, E. Razzoli, M. Zonno, S. Peli, R. P. Day, M. Michiardi, M. Schneider, B. Zwartsenberg, P. Nigge, R. D. Zhong, J. Schneeloch, G. D. Gu, S. Zhdanovich, A. K. Mills, G. Levy, D. J. Jones, C. Giannetti, and A. Damascelli. Collapse of superconductivity in cuprates via ultrafast quenching of phase coherence. Nature Materials **17**, 416 (2018).

[182] X. Shi, W. You, Y. Zhang, Z. Tao, P. N. Oppeneer, X. Wu, R. Thomale, K. Rossnagel, M. Bauer, H. Kapteyn, and M. Murnane. Ultrafast electron calorimetry uncovers a new long-lived metastable state in 1$T$-$TaSe_2$ mediated by mode-selective electron-phonon coupling. Science Advances, **5**, eaav4449 (2019).

[183] C. J. Sayers, H. Hedayat, A. Cersaso, F. Museur, M. Cattelan, L. S. Hart, D. Wolverson, L. S. Farrar, S. Dal Conte, G. Cerullo, C. Dallera, E. Carpene, and E. Da Como. Selective electron-phonon coupling in the insulating phase of 1$T$-$TaSe_2$. *In preparation* (2020).

[184] S. Nagata, T. Aochi, T. Abe, S. Ebisu, T. Hagino, Y. Seki, and K. Tsutsumi. Superconductivity in the layered compound 2H-$TaS_2$. Journal of Physics and Chemistry of Solids, **53**, 1259 (1992).

[185] K. Yokota, G. Kurata, T. Matsui, and H. Fukuyama. Superconductivity in the quasi-two-dimensional conductor 2$H$-$TaSe_2$. Physica B **284**, 551 (2000).

[186] B. Sipos, A. F. Kusmartseva, A. Akrap, H. Berger, L. Forró, and E. Tutiš. From Mott state to superconductivity in 1T-$TaS_2$. Nature Materials, **7**, 960 (2008).

[187] Y. Liu, D. F. Shao, L. J. Li, W. J. Lu, X. D. Zhu, P. Tong, R. C. Xiao, L. S. Ling, C. Y. Xi, L. Pi, H. F. Tian, H. X. Yang, J. Q. Li, W. H. Song, X. B. Zhu, and Y. P. Sun. Nature of charge density waves and superconductivity in 1$T$-$TaSe_{2-x}Te_x$. Physical Review B **94**, 045131 (2016).

[188] R. Huisman and F. Jellinek. On the polymorphism of tantalum diselenide. Journal of Less Common Metals, **17**, 111 (1969).

[189] H. W. Myron, J. Rath, and A. J. Freeman. Generalized electronic susceptibility and charge-density waves in 1$T$-$TaS_2$ and 1$T$-$TaSe_2$. Physical Review B **15**, 885 (1977).

[190] R. Brouwer and F. Jellinek. The low-temperature superstructures of 1T-$TaSe_2$ and 2H-$TaSe_2$. Physica B+C, **99**, 51 (1980).

[191] S. Sugai, K. Murase, S. Uchida, and S. Tanaka. Comparison of the soft modes in tantalum dichalcogenides. Physica B+C, **105**, 405 (1981).

[192] J. E. Smith, J. C. Jr. Tsang, and M. W. Shafer. Raman spectra of several layer compounds with charge density waves. Solid State Communications **19**, 283 (1976).

[193] N. F. Mott. The Basis of the Electron Theory of Metals, with Special Reference to the Transition Metals. Proceedings of the Physical Society, Section A **62**, 416 (1949).

[194] N. F. Mott. Metal-insulator transition. Reviews of Modern Physics **40**, 677 (1968).

[195] M. Imada, A. Fujimori, and Y. Tokura. Metal-insulator transitions. Reviews of Modern Physics **70**, 1039 (1998).

[196] L. Perfetti, T. A. Gloor, F. Mila, H. Berger, and M. Grioni. Unexpected periodicity in the quasi-two-dimensional Mott insulator 1$T$-$TaS_2$ revealed by angle-resolved photoemission. Physical Review B, **71**, 153101 (2005).

[197] J. Demsar, L. Forro, H. Berger, and D. Mihailovic. Femtosecond snapshots of gap-forming charge-density-wave correlations in quasi-two-dimensional dichalcogenides 1$T$-$TaS_2$ and 2$H$-$TaSe_2$. Physical Review B **66**, 041101(R) (2002).

[198] Y. Nakata, K. Sugawara, R. Shimizu, Y. Okada, P. Han, T. Hitosugi, K. Ueno, T. Sato, and T. Takahashi. Monolayer 1$T$-$NbSe_2$ as a Mott insulator. NPG Asia Materials **8**, e321 (2016).

[199] K. Sun, S. Sun, C. Zhu, H. Tian, H. Yang, and J. Li. Hidden CDW states and insulator-to-metal transition after a pulsed femtosecond laser excitation in layered chalcogenide 1$T$-$TaS_{2-x}Se_x$. Science Advances **4**, eaas9660 (2018).

[200] Y. F. Lu, H. Kono, T. I. Larkin, A. W. Rost, T. Takayama, A. V. Boris, B. Keimer, and H. Takagi. Zero-gap semiconductor to excitonic insulator transition in $Ta_2NiSe_5$. Nature Communications, **8**, 14408 (2017).

[201] D. Werdehausen, T. Takayama, G. Albrecht, Y. Lu, H. Takagi, and S. Kaiser. Photo-excited dynamics in the excitonic insulator in $Ta_2NiSe_5$. Journal of Physics: Condensed Matter, **30**, 305602 (2018).

[202] D. Werdehausen, T. Takayama, M. Höppner, G. Albrecht, A. W. Rost, Y. Lu, D. Manske, H. Takagi, and S. Kaiser. Coherent order parameter oscillations in the ground state of the excitonic insulator $Ta_2NiSe_5$. Science Advances, **4**, eaap8652 (2018).

[203] R. Ang, Y. Miyata, E. Ieki, K. Nakayama, T. Sato, Y. Liu, W. J. Lu, Y. P. Sun, and T. Takahashi. Superconductivity and bandwidth-controlled Mott metal-insulator transition in $1T$-$TaS_{2-x}Se_x$. Physical Review B, **88**, 115145 (2013).

[204] R. Ang, Z. C. Wang, C. L. Chen, J. Tang, N. Liu, Y. Liu, W. J. Lu, Y. P. Sun, T. Mori, and Y. Ikuhara. Atomistic origin of an ordered superstructure induced superconductivity in layered chalcogenides. Nature Communications, **6**, 6091 (2015).

[205] D. J. Campbell, C. Eckberg, P. Y. Zavalij, H. H. Kung, E. Razzoli, M. Michiardi, C. Jozwiak, A. Bostwick, E. Rotenberg, A. Damascelli, and J. Paglione. Intrinsic insulating ground state in transition metal dichalcogenide $TiSe_2$. Physical Review Materials, **3**, 053402 (2019).

[206] A. Castellanos-Gomez, M. Buscema, R. Molenaar, V. Singh, L. Janssen, H. S. J. van der Zant, and G. A. Steele. Deterministic transfer of two-dimensional materials by all-dry viscoelastic stamping. 2D Materials, **1**, 011002 (2014).

[207] D. Zhang, J. Ha, H. Baek, Y-. H-. Chan, F. D. Natterer, A. F. Myers, J. D. Schumacher, W. G. Cullen, A. V. Davydov, Y. Kuk, M. Y. Chou, N. B. Zhitenev, and J. A. Stroscio. Strain engineering a $4a \times \sqrt{3}a$ charge-density-wave phase in transition metal dichalcogenide 1T-$VSe_2$. Physical Review Materials, **1**, 024005 (2017).

[208] H. Wang, X. Huang, J. Lin, J. Cui, Y. Chen, C. Zhu, F. Liu, Q. Zeng, Z. Zhou, P. Yu, X. Wang, H. He, S. H. Tsang, W. Gao, K. Suenaga, F. Ma, C. Yang, L. Lu, T. Yu,

E. H. T. Teo, G. Liu, and Z. Liu. High-quality monolayer superconductor $NbSe_2$ grown by chemical vapour deposition. Nature Communications, **8**, 394 (2017).

[209] W. Fu, Y. Chen, J. Lin, X. Wang, Q. Zeng, J. Zhou, L. Zheng, H. Wang, Y. He, H. He, Q. Fu, K. Suenaga, T. Yu, and Z. Liu. Controlled Synthesis of Atomically Thin 1T-$TaS_2$ for Tunable Charge Density Wave Phase Transitions. Chemistry of Materials, **28**, 7613 (2016).

[210] P. Chen, Y. H. Chan, X. Y. Fang, Y. Zhang, M. Y. Chou, S. K. Mo, Z. Hussain, A. V. Fedorov, and T. C. Chiang. Charge density wave transition in single-layer titanium diselenide. Nature Communications, **6**, 8943, (2015).

[211] X. Xi, L. Zhao, Z. Wang, H. Berger, L. Forró, J. Shan, and K. F. Mak. Strongly enhanced charge-density-wave order in monolayer $NbSe_2$. Nature Nanotechnology, **9**, 765, (2015).

[212] H. Ryu, Y. Chen, H. Kim, H. Z. Tsai, S. Tang, J. Jiang, F. Liou, S. Kahn, C. Jia, A. A. Omrani, J. H. Shim, Z. Hussain, Z. X. Shen, K. Kim, B. I. Min, C. Hwang, M. F. Crommie, and S. K. Mo. Persistent Charge-Density-Wave Order in Single-Layer $TaSe_2$. Nano Letters, **18**, 689 (2018).

[213] Y. Chen, W. Ruan, M. Wu, S. Tang, H. Ryu, H. Z. Tsai, R. Lee, S. Kahn, F. Liou, C. Jia, O. R. Albertini, H. Xiong, T. Jia, Z. Liu, J. A. Sobota, A. Y. Liu, J. E. Moore, Z. X. Shen, S. G. Louie, S. K. Mo, and M. F. Crommie. Strong correlations and orbital texture in single-layer 1$T$-$TaSe_2$. Nature Physics, (2020).

[214] N. R. Wilson, P. V. Nguyen, K. Seyler, P. Rivera, A. J. Marsden, Z. P. L. Laker, G. C. Constantinescu, V. Kandyba, A. Barinov, N. D. M. Hine, X. Xu, and D. H. Cobden. Determination of band offsets, hybridization, and exciton binding in 2D semiconductor heterostructures. Science Advances, **3**, e1601832 (2017).

[215] Y. Cao, V. Fatemi, S. Fang, K. Watanabe, T. Taniguchi, E. Kaxiras, and P. Jarillo-Herrero. Unconventional superconductivity in magic-angle graphene superlattices. Nature, **556**, 43 (2018).

[216] Y. Cao, V. Fatemi, A. Demir, S. Fang, S. L. Tomarken, J. Y. Luo, J. D. Sanchez-Yamagishi, K. Watanabe, T. Taniguchi, E. Kaxiras, R. C. Ashoori, and P. Jarillo-

Herrero. Correlated insulator behaviour at half-filling in magic-angle graphene superlattices. Nature, **556**, 80 (2018).

[217] J. van Wezel. *Private Communication* (2017).

[218] J. A. Galvis, P. Rodière, I. Guillamon, M. R. Osorio, J. G. Rodrigo, L. Cario, E. Navarro-Moratalla, E. Coronado, S. Vieira, and H. Suderow. Scanning tunneling measurements of layers of superconducting $2H$-$TaSe_2$: Evidence for a zero-bias anomaly in single layers. Physical Review B, **87**, 094502 (2013).

[219] Y. I. Joe, X. M. Chen, P. Ghaemi, K. D. Finkelstein, G. A. de la Peña, Y. Gan, J. C. T. Lee, S. Yuan, J. Geck, G. J. MacDougall, T. C. Chiang, S. L. Cooper, E. Fradkin, and P. Abbamonte. Emergence of charge density wave domain walls above the superconducting dome in $1T$-$TiSe_2$. Nature Physics, **10**, 421, (2014).

[220] S. Yan, D. Iaia, E. Morosan, E. Fradkin, P. Abbamonte, and V. Madhavan. Influence of Domain Walls in the Incommensurate Charge Density Wave State of Cu Intercalated $1T$-$TiSe_2$. Physical Review Letters **118**, 106405 (2017).